An investigation of photoelectron angular distributions and circular dichroism of chiral molecules

Dissertation zur Erlangung des Doktorgrades

der Naturwissenschaften vorgelegt beim Fachbereich Physik

der Johann Wolfgang Goethe-Universität in Frankfurt am Main

von

Giammarco Nalin

aus Verona

Frankfurt am Main, 2021

(D30)

vom Fachbereich Physik der Johann Wolfgang Goethe-Universität als Dissertation angenommen.

Dekan: Prof. Dr. Harald Appelshäuser

1. Gutachter: Prof. Dr. Reinhard Dörner

2. Gutachter: Prof. Dr. Till Jahnke

Datum der Disputation: 14.02.2022

Die vorliegende Version unterscheidet sich geringfügig von der Version, die in der Universitätsbibliothek veröffentlicht wurde. Einige Tippfehler etc. wurden korrigiert und der Lebenslauf ist nicht enthalten.

Datum der aktuellen Version: 09.08.2022

This version differs slightly from the version published in the University Library. Some typos, etc. have been corrected and the curriculum vitae is not included.

Date of the current version: 09/08/2022

क्लेश कर्म विपाकाशयैःपरामृष्टः पुरुषविशेष ईश्वरः ॥२४॥

"Klesa Karma Vipaka Asayaih Aparmrstah Purusavisesah Isvarah"

Yoga Sutras 1, 24

To my family,

To my friends,

May love always guide us.

INHALTSANGABE

Die vorliegende Arbeit demonstriert das Potenzial aus verschiedene Arten von Photoelektronenemissionswinkelverteilungen im molekularen Bezugssystem (engl. *Molecular frame photoelectron angular distrbibution* – MFPAD) und dem mit ihnen verknüpften chiral-optischen Phänomen des Photoelektronen-Zirkulardichroismus (engl. *photoelectron circular dichroism* – PECD) Informationen über die molekulare Geometrie polyatomarer, chiraler Moleküle zu erhalten, und die hierbei auftretende Abhängigkeit von der Photoelektronenenergie zu untersuchen. Um den Einfluss des molekularen Potentials auf die Winkelverteilungen zu aufzuzeigen, wurden zwei chirale Moleküle untersucht: 2-(Methyl)oxiran (C_3H_6O, MOx, m = 58,08 uma) und 2-(Trifluoromethyl)oxiran ($C_3H_3F_3O$, TFMOx, m = 112,03 uma). Die beiden Moleküle unterscheiden sich in einer Substituentengruppe während sie in ihrer Oxirane-Gruppe identisch sind. Das O(1s) Elektron wurde durch Absorption eines Synchrotron-Photons ionisiert. Diese direkte Photoionisation eines K-Schalen-Elektrons geschieht im Molekül an einer klar lokalisierten Stelle und das (nach der Ionisation hochangeregte Molekül) zerfällt hierauf elektronisch unter Emission von weiteren Elektronen und fragmentiert in verschiedene geladene (und neutrale) Bruchstücke in einer sogenannten Coulomb-Explosion. Die entstehenden Elektronen und ionischen Fragmente werden mittels der COLd Target Recoil Ion Momentum Spectroscopy (COLTRIMS) Methode detektiert und die Impulsvektoren aller Fragmente werden für jedes einzelne Ionisationsereignis aus der Messung bestimmt. Mithilfe der COLTRIMS-Methode kann die räumliche Orientierung des in der Gasphase vorliegenden Moleküls im Laborsystem über die Emissionsrichtungen seiner Bruchstücke im Nachhinein festgestellt werden. Dadurch (und durch eine koinzidente Messung des Photoelektronenimpulses) ergibt sich die Möglichkeit die Emissionsrichtung des Photoelektrons im molekularen Bezugssystem zu bestimmen und man erhält Zugang zu den o.g. MFPADs (und dem mit ihnen verknüpften PECD) für unterschiedliche Orientierungen zwischen Molekül und Lichtausbreitungsrichtung.

Unter „Stereochemie" (vom griechischem $\sigma\tau\varepsilon\rho\varepsilon o$, *stereo*: fest) versteht man die Chemie dreidimensionaler Systeme. Da die meisten Moleküle eine dreidimensionale Struktur aufweisen, deckt die Stereochemie große Bereiche der Chemie im Allgemeinen ab und ist offensichtlicher Weise auch für die Biologie von Relevanz. Sie ist von fundamentaler Bedeutung für das Verständnis von chemischen Strukturen, molekularer Dynamik und molekularen Reaktionen. Z.B. sind grundlegende Phänomene belebter Materie mit wesentlichen Entdeckungen der Stereochemie unmittelbar verknüpft. Die Stereochemie ist seit ihrer Einführung im späten 18. Jahrhundert ein reges Forschungsgebiet, so dass ihr tiefergehendes Verständnis in der Vergangenheit großen technischen Fortschritt ausgelöst hat. Chiralität ist ein Unteraspekt der Stereochemie. Hierbei liegt der Fokus auf Objekten mit der besonderen Eigenschaft, dass sie nicht mit ihrem Spiegelbild durch Translation und/oder Rotation in Übereinstimmung gebracht werden können. Das Wort „chiral" leitet sich aus dem griechischen Wort $\chi\varepsilon\iota\rho$ für „Hand" ab. Die erste Verwendung dieses Begriffs wird typischerweise Lord Kelvin zugesprochen, der während einer Vorlesung des Oxford Universität Junior Scientific Clubs in 1893 feststellte: „...any geometrical figure, or group of points, 'chiral', and say that it has chirality if its image in a plane mirror, ideally realized, cannot be brought to coincide with itself.". Obwohl dies typischerweise als Geburtsstunde des Wortes „Chiralität" angesehen wird, war das zugrundeliegende Konzept bereits in vielerlei Forschungsgebieten vertreten (vor allem in der Mathematik), welches die weitreichende Relevanz des Konzepts der Chiralität in vielen Feldern der Wissenschaft hervorhebt. In der Natur existieren über viele Größenordnungen hinweg zahlreiche Beispiele für chirale Symmetrien. Chiralität ist von makroskopischen (bspw. die Verteilung der Rotationen von Galaxien) bis mikroskopischen Maßstäben (bspw. die Struktur mancher Planktonarten) beobachtbar. Im molekularen Bereich ist die Anzahl auftretender chiraler Systeme sehr beachtlich: tatsächlich sind die meisten pharmazeutischen Verbindungen, Lebensmitteldüfte, Pheromone, Enzyme, Aminosäuren und DNA-Moleküle chiral. Das Konzept der Chiralität geht weit über die reine geometrische Symmetrie von Objekten hinaus, es ist ein zentraler Bestandteil der fundamentalsten

Eigenschaften der physikalischen Kräfte in der Natur. Es wird vermutet, dass die Symmetriebrechung, die durch unterschiedliches physikalisches Verhalten eines chiralen Systems unter denselben Stimuli auftritt, eine mögliche Erklärungen der „Homochiralität des biologischen Lebens" ist. Unser Organismus weist eine große enantiomerer Selektivität verschiedener organischer Verbindungen auf (z.B. bezüglich der Wirkung von Medikamenten bis hin zu o.g. Duftstoffen). Über 800 der in der Lebensmittel- und Duftmittelindustrie häufig verwendeten Stoffe wurden als chiral identifiziert, wobei ihre Enantiomere mit deutlich unterschiedlichen Gerüchen wahrgenommen werden. Als weit bekanntes Beispiel sei hier der unterschiedliche Geruch von D- und L-Limonen genannt. Ebenso kann die Reaktion auf pharmazeutische Substanzen enantiomer-spezifisch ausfallen. In der Tat bestehen etwa 60 % aller aktuell verkäuflichen Medikamente aus chiralen Verbindungen, wobei allerdings etwa 90 % dieser als Razemat verkauft werden. Einen ähnlichen Grad an Enantiomer-Selektion wird in Kommunikationssystemen von Pflanzen und Insekten beobachtet. Pflanzen produzieren lipophile Flüssigkeiten mit hohem Dampfdruck, flüchtige Blattduftstoffe, welche aus verschiedenen, typischerweise chiralen Enzymen synthetisiert werden. Chirale Moleküle und chirale Effekte haben einen großen Einfluss auf viele Forschungsgebiete von, nur um einige zu nennen, stereo-sensitiver Synthese auf Grundlage heterogener enantioselektiver Katalyse, über Optoelektronik bis hin zu photochemischer asymmetrischer Synthese und chiraler Oberflächenforschung.

Ein chirales Molekül kommt in Form von zwei Enantiomeren vor. Ihre nahezu identischen chemischen und physischen Eigenschaften sorgen auch heutzutage noch für technische Herausforderungen in der Trrennung von razemischen Mischungen, der Bestimmung des Enantiomerenüberschusses und der direkten Bestimmung der absoluten Konfiguration eines Moleküls. In den letzten Jahrzehnten wurden allerdings große Fortschritte erzielt. Aufgrund der pharmazeutischen Relevanz und/oder der technologischen und wirtschaftlichen Bedeutung vieler chiraler Verbindungen, erlebten Detektionssysteme für chiral-spezifische Phänomenen ein stets ansteigendes Interesse. Probleme, wie etwa die

geringe Separationsausbeute und die hohen Kosten existierender Prozesse, sowie das limitierte Zusammenwirken mit bekannten chiralen Referenzreagenzen sind allerdings immernoch allgegenwärtig. Die in dieser Arbeit vorgestellten Untersuchungen und die hier angewandte Messmethode können hier eventuell neue Impulse geben.

Ein durch Photoionisation emittiertes Elektron besitzt eine charakteristische Emissionswinkelverteilung. Im Falle der Ionisation eines Moleküls, ist diese Winkelverteilung das Resultat von konstruktiver und destruktiver Interferenzen von direkt emittierten und am molekularen Potential gestreuten Photoelektronpartialwellen verschiedener Drehimpulsbeiträge und Symmetrie. Das volle Streumuster der Elektronenwelle wird dann im oben bereits erwähnten molekularen Bezugsystem als „MFPAD" sichtbar.

Ein Dichroismus beschreibt den Unterschied in der Absorption (oder Emission) von monochromatischem Licht durch ein optisch aktives Medium, wenn die Polarisationeigenschaften des Lichts verändert werden. Ein solcher Effekt wurde zunächst von Haidinger (1847) und später von Cotton (1895) beobachtet, woraufhin ursprünglich der Term „Cotton Effekt" verwendet wurde. Er wurde theoretisch erst von Rosenfeld im Jahr 1928 diskutiert. Der oben bereits erwähnte *Zirkular*dichroismus (CD, aus dem englischen *circular dichroism*) kann z.B. in flüssigen oder gasförmigen chiralen Substanzen beobachtet werden, wenn diese mit zirkular polarisiertem Licht interagieren und man die Helizität des Lichtes ändert. Mit der Entwicklung von Synchrotronanlagen, die fast monochromatische, teilweise kohärente Photonenstrahlen mit hoher Brillanz und hohem Fluss bereitstellen, sind detaillierte Untersuchungen zutem Zirkulardichroismus an chiralen Molekülen in der Gasphase möglich geworden. In Kombination mit der COLTRIMS-Technik, also der koinzidenten Vermessung der ionischen und elektronischen Photoionisationsfragmente, ab-initio Modellierunen des Ionisations- und Fragmentationsprozesses, lassen sich mit solchen CD-Messungen Rückschlüsse auf die (absolute) Konfiguration von Molekülen und ihre molekulare Ionisationsdynamik gewinnen. So weist z.B. der

Photoelektronenzirkulardichroismus (PECD, aus dem englischen *photoelectron circular dichroism*), der bei der Photoionisation von chiralen Molekülen mit unterschiedlicher Licht-Helizität auftreten kann, einige Charakteristika auf, welche ihn zu einer geeigneten Observablen machen, um die absolute Struktur von einzelnen, chiralen Molekülen zu bestimmen. PECD ein universeller optischer Prozess. Er zeigt eine komplexe Abhängigkeit vom elektronischen Zustand des Moleküls, seinem Vibrationszustand, und der Energie der eingestrahlten Photonen. Diese Sensitivität wurde bereits zur Untersuchung von ultra-schneller Moleklardynamik verwendet, z.B. in Arbeiten zur zeitaufgelösten molekularen Relaxation. PECD wird verwendet, um den Enantiomerenüberschuss in Razematen in Echtzeit zu bestimmen. Als differentielle Observable sind PECD-Effekte oftmals mehrere Größenordnungen stärker als der natürlichen Absorptions-CD, beispielsweise tritt ein PECD von bis zu 10 % für zufällig im Raum orientierte Moleküle auf und bis zu 20–30 % Signalstärke sind beobachtbar für Moleküle, welche in der Polarisationsebene des einlaufenden Photons ausgerichtet sind. Diesem Anstieg liegt zugrunde, dass PECD im Rahmen der elektrischen Dipolwechselwirkung auftritt, während CD durch Interferenz von elektrischen und magnetischen Dipol-Beiträgen entsteht.

Die in dieser Arbeit vorgestellten Experimente wurden mittels der COLTRIMS-Messtechik durchgeführt. Eine COLTRIMS-Apparatur ist in der Lage ionische Fragmente und Photoelektronen mit einem vollständigen Raumwinkel von 4π in Koinzidenz zu detektieren. Sie wurde ursprünglich entwickelt um Kollisionen von Atomen mit schnellen, hochgeladenen Ionen zu untersuchen. In den letzten 25 Jahren wurde die Messtechnik weiter verfeinert und ihr Geltungsbereich ausgeweitet. Heutzutage sind Messungen an einzelnen Atomen und Molekülen, Dimeren und Clustern, bis hin zu verdampften Flüssigkeiten möglich und üblich. Die Technik wurde außerdem für den Einsatz mit verschiedenen Photonenquellen angepasst, beispielsweise mit Synchrotronstrahlung, mit Starkfeld-Lasern oder mit freien Elektronenlasern. Einige grundlegende Arbeiten zur Ionisations- und Zerfalldynamik von Atomen und kleinen Molekülen wurden mit ihre durchgeführt.

Die COLTRIMS-Methode ermöglicht es außerdem Photoelektronenemissionswinkelverteilungen im Molekülsystem zu messen. Die Messmethode basiert auf einer Kombination einer Flugzeitmessung der dem Abbilden des Impulsraumes von Teilchen auf einem ortsauflösenden Detektor. Die Impulse der Reaktionsfragmente werden aus ihrem Auftreffort auf dem Detektor und ihrer Flugzeit berechnet. Aus den Impulsen können auch alle abgeleiteten Größen (bspw. Emissionswinkel, Energie, etc.) bestimmt werden und kinematisch vollständige Experimente sind mit COLTRIMS realisierbar. Die in dieser Arbeit präsentierten Experimente wurden mit zirkular polarisierten Licht des SEXTANT-Strahlrohrs an der SOLEIL Synchrotronanlage (Saint-Aubin, Frankreich) durchgeführt. Durch die koinzidente Messung der ionischen Impulse konnte die räumliche Orientierung einzelner Moleküle entweder teilweise (bei Fragmentation in zwei Fragmente) oder vollständig (bei Fragmentation in drei oder mehr Fragmente) bestimmt werden, wodurch eine Messung von MFPADs für verschiede Orientierungen zwischen Photonenstrahl und Molekül möglich war.

Im Folgenden wird eine Zusammenfassung der Ergebnisse dieser Arbeit gegeben. Der PECD von zufällig im Raum orientierten TFMOx Molekülen erreicht ein Maximalwert von ca. 2 %, was eine Signalstärke darstellt, die bereits einige Größenordnungen größer ist, als sie mit anderen etablierten chiral-optischen Techniken erreicht wird. Die in dieser Arbeit beobachteten Ergebnisse sind außerdem vergleichbar mit vorhergehenden Ergebnissen für das MOx Molekül. Eine räumliche Ausrichtung des Moleküls zeigte einen dramatischen Anstieg auf bis zu 20 % im winkel-integrierten PECD für spezifische Relativwinkel zwischen Photonenpolarisationsebene und Molekül. Die Winkelverteilung zeigte die erwartete Symmetrien mit der Eigenschaft PECD($\pi-\theta$, $\pi-\varphi$) = $-$ PECD(θ, φ). Der maximale PECD sollte also für parallele oder orthogonale Orientierung des Moleküls in der/zur Polarisationsebene auftreten. Der vollständig differentielle PECD im molekularen Bezugsystem wurde ebenfalls gemessen, wodurch sich für manche Molekülorientierungen ein weiterer Anstieg des PECD auf bis zu 45 % zeigte. Betrachtet man die dem PECD zugrundeliegenden MFPADs, so zeigen sie

eine Inversion des Vorzeichens beim Wechsel der Helizität (gemäß der Definition des PECD), und eine qualitative, progressive Inversion des Vorzeichens bei der schrittweisen Umkehrung der Lichtausbreitungsrichtung relativ zur Molekülorientierung. Dies bestätigte den chiralen Ursprung des Effekts. Es zeigte sich außerdem, dass der sowohl der integrierte als auch der vollständig differentielle PECD eine starke Abhängigkeit von der Photoelektronenenergie aufweist: der integrierte PECD zeigt zusätzliche/andere Charakteristika für kleine Energien, der vollständig differentielle PECD zeigt eine progressive Verschiebung seiner Maxima und Minima (für verschiedene Lichtausbreitungsrichtungen) in Abhängigkeit von der Photoelektronenenergie. Die maximale Stärke des PECD-Effekts ist mir relativ geringen Schwankungen bis hin zu Werten von 50 % bei 6 eV Photoelektronenenergie beobachtbar. Ein in dieser Arbeit durchgeführter Vergleich von TFMOx und MOx (letzteres wurde in vorangegangenen Experimenten untersucht), ermöglichte eine systematische Quantifizierung des Einflusses der verschiedenen Substituentengruppen (CF_3 bzw. CH_3) auf die Emissionswinkelverteilungen der Photoelektronen und dem zugehörigen PECD bei 11,5 eV Photonelektronenenergie. Die Experimente zeigten überraschenderweise eine vollständige Vorzeicheninversion aller drei PECD Varianten für zufällig, teilweise und vollständig im Raum ausgerichtete Moleküle auf, und einen quantitativ stärkeren Effekt für TFMOx. Dies legt nahe, dass es einen messbaren Einfluss der schwereren Streuzentren (der F-Atome) auf die gemessenen Streumuster gibt. Der Trend des PECD für zufällig orientierte Moleküle und die Merkmale des winkel-integrierten PECD sind für beide Systeme ähnlich, der vollständig differentielle PECD weist jedoch feinere Unterschiede bezüglich der Abhängigkeit von der Lichtausbreitungsrichtung auf.

Die vorliegende Arbeit zeigt einen weiteren Weg für die „Verwendung" der MFPADs einzelner Moleküle in der Gasphase auf: Durch einen iterativen Vergleich mit theoretisch modellierten MFPADs und einem Rückkopplungs-basierten Ansatz lassen sich sogar einzelne Feinheiten der Molekülgeometrie aus den Messdaten extrahieren. Darüber hinaus zeigte sich in diesem Zusammenhang, dass es auch

möglich ist, über den gemessenen PECD die absolute Konfiguration chiraler Moleküle zu bestimmen. Die Ergebnisse dieser Arbeit und eine kürzlich zur Publikation eingereichte Folgestudie setzen hier einen neuen Maßstab bezüglich der Komplexität der untersuchten Moleküle. Die Nutzung von MFPADs (und PECD) für detaillierte Geometrie-Bestimmung ist insofern von Interesse, da diese Methode auch eine Erweiterung bezüglich zeitaufgelöster Untersuchungen erlaubt.

Table of Contents

1. INTRODUCTION

Stereochemistry (from the Greek στερεο-, *stereo-*, meaning solid) refers to chemistry in three dimensions. Since most molecules show a three-dimensional structure (3D), stereochemistry pervades all fields of chemistry and biology, and it is an essential discipline for the understanding of chemical structure, molecular dynamics and molecular reactions. Stereochemistry is a keystone for the understanding of the chemistry of biological life since its revolutionary introduction in late 18th century, starting from the early observations of the interaction of organic compounds with light, to one of the most groundbreaking scientific discoveries of the last century such as to the observation of the double helix structure of deoxyribonucleic acid (DNA) [1]. The research on stereochemistry shed light on fundamental questions about the origin of life in the Universe, triggering tremendous technical advancements, and therefore making it a flourishing field of research.

In chemistry, chirality is an important topic of stereochemistry which it is the peculiar geometrical property of an object of not being superimposable to its mirror-image. The word chirality is derived from the Greek χειρ for "hand", and the first use of this term in chemistry is usually attributed to Lord Kelvin who called during a lecture at the Oxford University Junior Scientific Club in 1893 "any geometrical figure, or group of points, 'chiral', and say that it has chirality if its image in a plane mirror, ideally realized, cannot be brought to coincide with itself." [2]. Although the latter is usually considered as the birth of the word chirality, the

concept underlying it was already present in several fields of science (above all mathematics), already proving the multidisciplinary relevance of chirality across many field of science and beyond [3].

Nature shows great examples of chiral symmetry on all scales. Empirically, it is possible to observe it at macroscopic scale (e.g., distribution of rotations of galaxies [4]), down to the microscopic scale (e.g., structure of some plankton species [5]), but it is at the molecular level where the number of chiral systems gets remarkable: most of the pharmaceutical drugs, food fragrances, pheromones, enzymes, amino acids and the DNA molecule, in fact, are chiral. Moreover, the concept of chirality goes far beyond the mere spatial symmetry of objects being crucially interwoven as e.g., with the fundamental properties of physical forces in nature. The symmetry breaking, namely the different physical behaviour of two enantiomers (from the Greek ἐναντίος, *enantios,* meaning opposite[1]) of a chiral system upon the same stimuli, is considered to be one of the best explanation for the long-standing questions of homochirality in biological life, and ultimately to the chemical origin of life on Earth as we know it [6]–[8].

The concept of chirality challenged and inspired scientists for over a century, and it is perhaps surprising how recently the concept has been developed, despite being at the interface between biological life and the laws of Nature and present at virtually all scales. An early poetical intuition of the holistic implications of chirality could be found in the famous *Through the Looking-Glass and What Alice Found There* from Charles L. Dodgson (best known as Lewis Carroll) first published in December 1871, when Alice said to her cat: "How would you like to live in a looking-glass house, Kitty? ... Perhaps looking-glass milk isn't good to drink."

---

1 In chemistry, *isomers* are molecules with the same chemical formula; *stereoisomers* are isomers with the same arrangements of atoms (i.e., bonds), which differ in their spatial orientation of substitutional groups; *conformers* are stereoisomers with high symmetry. A molecule can have infinite stereoisomers. Enantiomers are stereoisomers that show inversion symmetry, and must always come in pairs, although their natural abundance can be very different. A molecule can have multiple "pairs" or enantiomers.

1.1 Historical background

The first documented observations of chiroptical phenomena can be appointed to the French physicists F. Arago and J.-B. Biot, who separately studied the interaction of linearly polarized light with quartz in 1811 and 1812, respectively. It was already known that quartz crystals exhibit the phenomenon of hemihedrism, therefore come in two enantiomeric forms: the α and β quartz, as shown in Figure 1.1. It has been observed that, when illuminated with polarized light, two plates made from the two quartz enantiomers rotate the polarization plane light with respect to its propagation direction of an angle proportional to the thickness of the plate itself, but into opposite directions depending on the enantiomer. In 1815, J.-B. Biot alone extended these observations to organic substances both in liquid form such as turpentine (a mixture of terpenes, primarily α and β pinene), and solid solutions such as sucrose ($C_{12}H_{22}O_{11}$, α-D-glucopyranoside), camphor ($C_{10}H_{16}O$, 1,7,7-Trimethylbicyclo[2.2.1]heptan-2-one), and tartaric acid ($C_4H_6O_6$, 2,3-Dihydroxybutanedioic acid), showing a similar optical activity for each compound in its physical phases as quartz, but without being able to fully interpret the results of his observation.
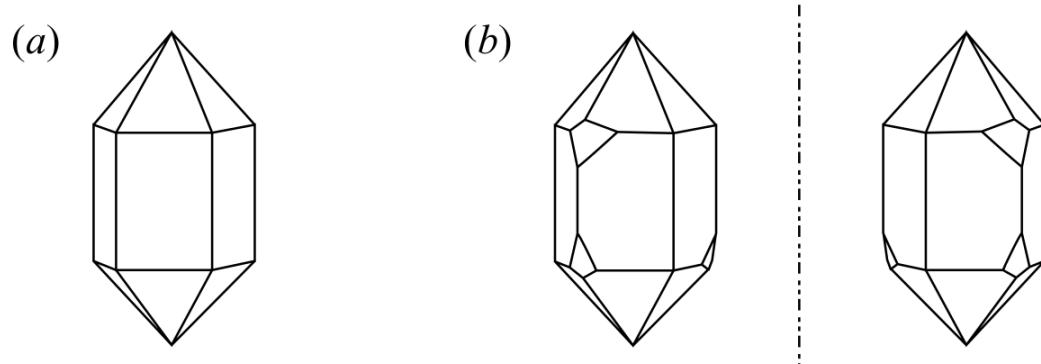
Figure 1.1: Comparison between high symmetry and hemihedral. a) high symmetry holohedral hexagonal crystal structure; (b) hemihedral hexagonal crystal and its mirror image. This two enantiomers are the prototypical structures for α and β quartz, respectively. Image reproduced from [27].

In 1848, inspired by the work of J.-B. Biot and under his supervision, L. Pasteur decided to further compare the properties of specific salts of the (+)-tartaric acid, depicted in the B) panel of Figure 1.2 (see appendix B.3 for the meaning of "+"), with its optically inactive isomer the paratartrate (also called paratartatic acid). In particular, he was interested in the liquid solution of double sodium-ammonium

tartrate whose macroscopic crystalline forms display, like quartz, a hemihedral morphology as shown in A) and C) panels of Figure 1.2. At first, he induced crystallization of a mixture of the two compounds by slow evaporation, obtaining two types of large crystals which could be mechanically separated with a pair of tweezers. When the obtained crystals were separately redissolved in a solvent, and illuminated with linearly polarized light, the two solutions rotate the polarization direction of the light into opposite directions by a certain degree. Finally, replicating the same experiment with the paratartrate alone, he surprisingly obtained an equal amount of two complementary hemihedral crystals typical of the tartaric acid, showing that the paratartrate is not a pure compound, thus explaining its optically inactivity in liquid phase. He was therefore able to *resolve* the paratartrate conglomerate into its two enantiomers, the (+)-tartaric acid and the (-)-tartaric acid, the latter had never been purified and observed alone before. Despite the lack of the modern concept of molecule, Pasteur associated what he called the "molecular dissymmetry" to what he macroscopically observed in crystalline forms, addressing the link to some unknown "dissymmetric forces of Nature" [9].
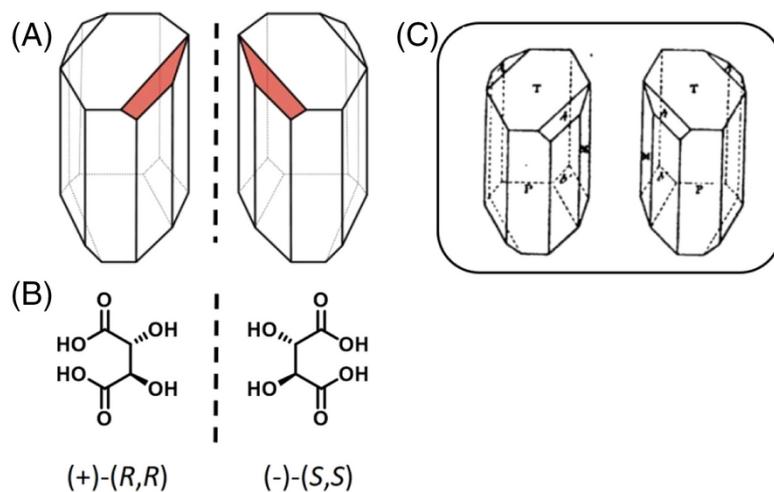
Figure 1.2: A) Hemihedral crystals of double sodium-ammonium tartrate, and C) the crystals as drawn by Pasteur; B) chemical structures of enantiomeric tartaric acids. Image reproduced from [10].

The fundamental roots of the observed asymmetry remained unclear until 1874 when J. H. van't Hoff and J. A. Le Bel independently introduced the concept of physical geometry for the carbon atom, and in particular its asymmetries in space. This new interpretation pictures a carbon atom with four different substituents as

disposed on a regular tetramer, and radically changed the conventional symbolic language of chemistry to more visually based language. With this new approach, it was possible to visually identify enantiomers as mirror images of each other, thus bridging the gap between the empirical observation of optical activity and its molecular nature. Modern chiroptical experiments on molecules such as studies on circular dichroism (CD), and birefringence effects were performed starting from 1895 by the French physicist A. Cotton using polarized light, and will be discussed in more detail in chapter 2.

1.2 Chirality in everyday life

Restricting the view to the molecular world, the discovery, and quantification of homochirality in the biological realm [6] has been a groundbreaking discovery across many scientific disciplines, and it shows the central role of chirality on the origin of biological life. The two main pillars of homochirality are first that the ribose sugar ($C_5H_{10}O_5$), the building block of nucleotides and of nucleic acids, occurs in nature just as D-type enantiomer, and second that 19 out of 20 of the most common amino acids [11], the building blocks of polypeptide chains such as proteins, are chiral and exclusively L-type[2] enantiomers. These two well-known aspects imply a signature of homochirality on higher-order structures such as in DNA and RNA, whose secondary structure has the form of an α-helix i.e., right hand-helix.

Therefore, it is intuitive to understand why our organism as well as the one of other animals show high enantio-selectivity towards specific compounds ranging from drugs, to fragrances. The way in which each enantiomer binds with the sense organs could be different and, as a result, the perceived smell and taste is different [12]. Over 800 odour molecules commonly used in industry in food and as fragrance are indeed chiral; a well-know examples are the striking difference

---

2   D and L descriptors are based on Fischer projection, are often used in the nomenclature of amminoacids, and are relative descriptors. Absolute descriptors are instead S and R, further described in appendix B.3.

between (4R)- and (4S)-carvone, or the more peculiar one between D- and L-limonene [13]. Similarly, biological responses to pharmaceuticals drugs can be enantiomer specific, and in fact about 60% the drugs currently on the market are chiral compounds, and nearly 90% of them are sold as racemates[3] [14]. In some cases, the complex interaction of racemates with the human body could lead to tragic outcomes, as the use in the past century of a medicament containing a racemic mixture of thalidomide ($C_{13}H_{10}N_2O_4$) sadly showed [15].

The same degree of enantio-selectivity is observed in the communications systems of plants and insects. Plants produce lipophilic liquids with high vapour pressure called plant volatiles (PVs) which are synthesized via different enzymes called terpene synthases that are usually chiral [16]. One example is the α-terpene studied from J.-B. Biot in his early experiments (see chapter 1.1). The two enantiomers of terpene are released in the atmosphere, triggering different biological activities to communicate to predators, pollinators and neighbouring plants [17]. Among insects, pheromones play a similar role, and a better understanding of the interaction with pheromone could lead to an effective control of species population and pollination cycles without negatively affecting the biodiversity [18], [19]. The use of chiral molecules and the exploitation of related chiral effects have a crucial impact on a growing number of branches of science and technology, with exciting developments ranging from stereo-selective synthesis based on heterogeneous enantioselective catalysis [20], to optoelctronics [21], to photochemical asymmetric synthesis [22], and chiral surface science [23], just to cite a few.

The almost identical chemical and physical properties of enantiomers continue to pose technical challenges concerning the resolution of racemic mixtures, the determination of the enantiomeric excess[4], and the direct determination of the absolute configuration of an enantiomer. Huge improvements have been achieved

---

3   The term *racemate* indicates a 50:50 mixture of two enantiomers. From Latin *racemus,* meaning a bunch of grapes; it is related to the *acidum racemicum* (tartaric acid) which is known from centuries in the context of wine-making.

4   The enantiomeric excess (ee) quantifies the purity of a chiral compound. It represents the relative content one enantiomer compared to the other. A racemic mixture has an ee of 0%, while a pure enantiomer has an ee of 100%.

in the last decades, and analytical systems for chiral detection based on chiral-specific phenomena are increasingly gaining interest for their technological and economic impact, especially for pharmaceutically relevant compounds. Many limitations such the low separation yields and the high cost of the process, and the restricted interaction to known chiral reference reagent are still restricting advanced detection and separation techniques to be use on many chiral compounds of interest.

1.3 Structural symmetry and true chirality

The property of an enantiomer of "not being superimposable to its mirror image" can be more rigorously described using symmetry operations and elements of group theory. Symmetry operations are spatial manipulations of a molecular structure which signify the equivalence of two configurations, namely the manipulated and the original. Symmetry operations are performed on a symmetry element: an axis, a plane, or a point. According to the symmetry operation, if a molecule belongs to a symmetry element, then its structure is the same as the original after the transformation, thus it displays a particular symmetry. For molecules to be chiral, a combination of the point group *centre of inversion i* and *reflection planes σ* (both vertical and horizontal) must *be missing*. The latter implies that the structures (e.g., enantiomers) are different (i.e., "not superimposable") before and after either manipulation. More generally, chiral molecules should *lack* any improper rotation axis of the point group S_n that converts a point (x, y, z) into (-x, y, z)[5]. Hence, chirality is supported by the point groups with proper rotations, namely the axial groups C_n, D_n, and the polyhedral groups O, T and I.

How can these structural considerations be translated into the language of symmetries and conservation laws of physics? An improper rotation S_n is

---

5   A reflection is defined relative to a plane: by definition, it will leave all the points on that plane unvaried. In this example, the reflection is performed relative to the z-y plane, therefore inverting just the x-axis. It is worth noticing that the sense of rotation of an object rotating around the x-axis is unaffected by the parity operator $\hat{P}$.

equivalent to applying the parity operation $\hat{P}$ [6], which simply inverts all spatial coordinates of a point in space $r \xrightarrow{\hat{P}} -r$ (therefore called space inversion), followed by a π rotation around an axis orthogonal to the reflection plane. Vectors are classified according to their transformation with respect to $\hat{P}$: *polar* or true vectors are reversed by $\hat{P}$ (e.g., the position vector **r**), while *axial* or pseudo vectors are not (e.g., the angular momentum vector **L**), as shown in the equations (1.1). What is usually measured in chiroptical experiments are *pseudo scalar:* scalars that change sign with $\hat{P}$ such as the optical rotation angle α and the circular intensity difference of the CD.

$$ r \xrightarrow{\hat{P}} (-r) \quad ; \quad L = r \times p \xrightarrow{\hat{P}} (-r) \times (-p) = L \tag{1.1}$$

A chiral object lacks of parity because the parity operator $\hat{P}$ transforms it into its enantiomer of *opposite* chirality: when the term "chiral" is referred to a *static* object as perhaps to molecule, it implies the existence of two distinguishable enantiomers. Therefore, a chiral molecule has a lower symmetry than its associated Hamiltonian, which still commutes with the parity operator $[\hat{P}, \hat{H}] = 0$, thus conserving parity. This fact is called parity breaking, also called mirror symmetry breaking, and it differs from parity violation as described in the following chapter [24].
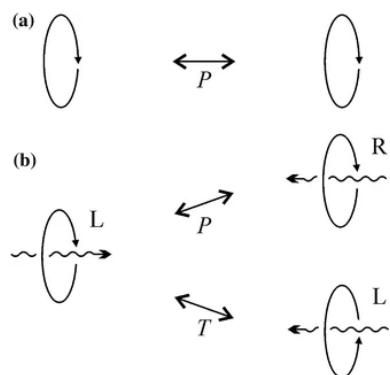
Figure 1.3: Effect of the parity P̂ and time T̂ operators on a) a single axial vector (e.g., stationary spinning particle); b) a combination of axial and polar vectors. Sketch reproduced from [27].

Despite the clear parity breaking emerging using chiral molecules, further symmetries should be considered to correctly describe phenomena like magnetic

---

6   It is possible to use either the "active" or "passive" convention: "active" implies the particle has changes position in space; "passive" implies that the coordinate system is linearly transformed to display the same position of the particle.

or electrically induced chirality in achiral systems (e.g., Faraday effect). In a *dynamic* system the symmetry can be further tested under the time reversal operator $\hat{T}$ which reverse the time $t \overset{\hat{T}}{\rightarrow} -t$ [7]. Applying the time reversal operator $\hat{T}$, *polar* or true vectors are not reversed (e.g., position vector **r**), while *axial* or pseudo vectors are (e.g., angular momentum vector **L**), as stated in the set of equations (1.2). When the sign of a vector is changed by $\hat{T}$, the vector is called *time-odd* otherwise *time-even*. A summary of the effect of the parity operators $\hat{P}$ and $\hat{T}$ on axial and polar vectors (and a combination of them) is sketched in Figure 1.3.

When a system shows *false chirality* it has neither $\hat{P}$ nor $\hat{T}$ symmetry operations alone, but their combination $\hat{P}\hat{T}$ is a symmetry operation, therefore reproducing the original configuration. On the contrary, a system shows *true chirality* when the system symmetry is broken applying both $\hat{P}$ and $\hat{T}$ symmetry operations alone, as well as their combination $\hat{P}\hat{T}$.

$$r \overset{\hat{T}}{\rightarrow} r \quad ; \quad v = \frac{d\,r}{dt} \overset{\hat{T}}{\rightarrow} \frac{d\,r}{d(-t)} = -v \quad ; \quad L = r \times p \overset{\hat{T}}{\rightarrow} r \times (-p) = -L \qquad (1.2)$$

Consequently, the electric filed **E** is polar time-even vector, and the magnetic B-filed is axial time-odd vector, and any processes involving static and uniform electromagnetic interactions must conserve parity and reversibility. Therefore, the use of circularly polarized light (CPL) ensures the parity breaking, because the rotating and propagating **E** and **B** vectors of a plane wave define two non-superimposable states, namely the left and right circularly polarized [25]. Since CPL defines a true chiral system, it can be used to convert achiral molecules into a chiral excited state, as recently demonstrated by K. Fehre and co-workers [26].

A state of polarization *p* can be thought as a superimposition of two linearly polarized orthogonal components lying on a plane perpendicular to the light's propagation direction. For components with equal magnitudes, the phase-shift

---

7   The test could be extended to the charge conjugation operator Ĉ, although not relevant for the present work.

determines the overall polarization: for a phase shift of ±π/2, the light is circularly polarized. The sign of the phase difference determines the handedness of the rotation. From the point of view of an observer looking at the photon source along the propagation direction, a clockwise rotation corresponds to a phase shift of -π/2 and is a right-hand circular polarization state (RCP), while a counter-clockwise rotation has a phase shift of +π/2, and refers to left-hand circular polarization state (LCP), as summarized in Table 1 in chapter 3.2.

1.4 Symmetry violation

According to the CPT theorem, it is possible to define, in the words of L. D. Barron, "a mirror universe where, all particle positions are reflected about some plane (parity inversion operator $\hat{P}$), all particles are replaced by their anti-particles (charge conjugation operator $\hat{C}$) and all momenta are reversed (time reversal operator $\hat{T}$), will evolve according to the same physical laws as the present universe" [27]. Symmetry is conserved by the four fundamental forces (i.e., gravitation, electromagnetic, strong and weak), but individual symmetries may be violated as proposed by T. D. Lee and C. N. Yang in 1956 [28], although the idea had already been criticized for long time[8]. Although enantiomers show identical chemical and physical properties, it has been predicted that their ground energy levels should be different [30], [31]. For an isomerization reaction of large chiral molecules at its apparent equilibrium $S \rightleftharpoons R$, modern theoretical calculations predict an extremely small difference in Gibbs standard free energy $\Delta_R G^0$ of about 10^{-16} to 10^{-14} $k_b T$ at 25 °C, thus a consequent equilibrium constant K < 1, giving an excess of to $10^6 - 10^8$ molecules per mol of the energetically favoured enantiomer under thermodynamic equilibrium at 25 °C [32]. The debate about the validity of the calculations is still going on today,

---

8   "Wolfgang Pauli is said to have bet large amounts of champagne against it when the suggestion of parity violation first appeared. Similarly, as reported in the December 2001 news of the American Physical Society, Richard Feynman considered at the time the notion of parity violation to be "unlikely, but possible, and a very exciting possibility", and he made a $50 bet with a friend that parity would not be violated. However, Feynman lost that bet and experimental proof of parity violation was swift and complete." citation integrally reported from [29].

especially because the sensitivity of all spectroscopic techniques used to probe the former difference is, at the present moment, several order of magnitude higher than the theoretical proposed values.

Despite the lack of experimental evidence, the difference in energy is thought to originate from the weak interaction, which is know to violate the CP symmetry; in particular, it seems to emerge from the spin-orbit coupling, a weak magnetic interaction between the spin of the electrons and their orbital motion which slightly splits the degenerate energy of the two spin configurations, mirrored in each enantiomer [29]. The weak interaction was proven to violate the P symmetry by Madame Chien-Shiung Wu in her famous experiment on β decay on polarized Co-60 atoms [33] for which the Nobel Prize in physics 1957 was awarded jointly to C. N. Yang and T. D. Lee. Further investigation in the physics of the decay of K-mesons [34], lead to prove the violation of the combination of the CP symmetry, a discovery worth the Nobel Prize in physics 1980 to J. W. Cronin, and V. L. Fitch.

1.5 Absolute configuration

The analytic techniques capable of assigning the absolute configuration of two enantiomers are the crucial tool to allow further developments in the research on chiral molecules and chiral compounds. During the last century, X-ray crystallography and vibrational circular dichroism (VCD) have been the mostly used techniques to assign the absolute configuration of two enantiomers using CPL as a probe, as explained in the previous chapter 1.4.

X-ray crystallography is the most used technique capable of determining the absolute configuration of chiral molecules, since the relationship between macroscopic chirality and chirality at the molecular level was established, in 1951, through anomalous X-ray scattering[9] [35]. Despite its tremendous success, it is

---

9   In contrast to elastic scattering, the anomalous X-ray diffraction makes use of an additional phase shift for resonant scattering, making it sensitive to the space inversion of a target.

necessary for large molecules to provide theoretical models to compute the angular distribution of a given structure *ab initio*. The technique has more limitations: the target molecule has to be in a single crystal form, a condition difficult to achieve for many biological samples, but most importantly where the influence of the nearest neighbours on the signal is very strong and influences the accuracy of the calculations. Furthermore, the technique relies on the stronger scattering from heavier atoms in the crystal lattice, which are usually missing in many organic molecules, introducing another constrain in the sample preparation [36].

Two other benchmark techniques to determine the absolute structure of a chiral molecule are nuclear magnetic resonance (NMR) spectroscopy and high-performance liquid chromatography (HPLC). NMR is a powerful technique routinely used to prove the structure of complex biological molecules and proteins of mass up to 25 kDa, but the measurements have to be backed up by sophisticated quantum chemical calculations of the measured sample. Furthermore, the sample preparation usually requires the formation of diastereomeric complexes between the chiral analyte and a known solvated chiral resolving agent [37]. Likewise, HPLC can be particularly effective on small organic molecules as amino acid, but as for NMR, the formation of diastereomers with chiral agents is a tight requirement [38].

Other techniques like VCD and coherent three-wave mixing have been successfully used to resolve specific racemic mixtures, but they both rely on demanding *ab initio* calculations, and the very low intrinsic sensitivity hinder the use for a immediate broader adoption as routine techniques and scalability [39]–[41]. Novel techniques based on Coulomb explosion imaging (CEI) were proven to allow addressing absolute configuration on small single molecules in the gas phase, overcoming some of the previously mentioned limitation. The chapter 2.3 will give an overview on the state of the art.

1.6 Motivations and goals

The intrinsic limitations of most of the techniques capable of chiral recognition represent an opportunity for the development of an alternative and novel approach for directly determining the molecular geometry and assigning the absolute configuration of chiral molecules. The technique used in this work, a momentum microscopy technique capable of performing kinematically complete scattering experiments (up to electron spins) in coincidence for single molecules in gas phase, has the capability of benchmarking sophisticated theoretical models, helping the development of fundamental understanding of electron dynamics in molecules. The high sensitivity of chiroptical phenomena is used as a effective probe for structural determination of chiral molecules.

The goal of this work is to investigate a particular chiroptical phenomena, the photoelectron circular dichroism (PECD) in combination with CEI, both extensively described in chapter 3.2, to probe the molecular structure of single chiral molecules in gas phase, and potentially of much larger molecules with the backup of computational simulations. The ultimate goal is to provide a robust, extremely sensitive to photoelectron energy and reference-free technique to investigate absolute configurations of chiral molecules, opening the way to a new form of single molecule X-ray crystallography. To achieve this goal, molecular frame photoelectron angular distributions (MFPADs) of unknown enantiomers obtained for different molecular orientations were analysed and compared to theoretical predictions which can be used to investigate the geometrical structure of the associated target, as described in chapter 3.3. An MFPAD is the result of the interference patterns of photoelectrons scattering on the molecular potential in which much information of the scattering, interferences and ionization dynamics are embedded, thus extremely sensitive to all parameters defining the molecular structure at the instant of photoionization. The PECD phenomenon, which is extensively discussed in chapter 3.2, quantifies the forward-backward asymmetry of photoelectrons along the light's propagation direction uniquely generated from

chiral molecules, and it is computed starting from the MFPAD from which it inherits a great sensitivity to the molecular potential.
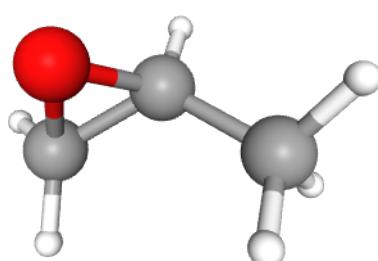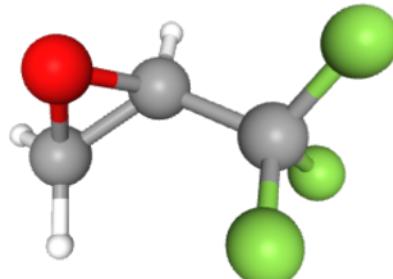
Figure 1.4: Left S-MOx and right R-TFMOx. The Cahn, Ingold and Prelog (CIP) rule is used to assigned the descriptors S and R, as described in appendix B.3.

The experiments presented in chapter 5 were conducted using the COLd Target Recoil Ion Momentum Spectroscopy (COLTRIMS) technique (chapter 4.3) and they systematically explored the influence of photoelectron energy and of substitutional groups on integral and fully-differential PECD for a direct ionization dynamics upon orienting and fixing the target molecule in space, respectively. The orientation of the targets molecules in space was obtained taking advantage of the COLTRIMS microscope using momentum vectors associated to two fragments (e.g., partial orientation chapter 5.2) or three fragments (e.g., complete orientation, chapter 5.3), thus accessing the MFPADs as function of photon propagation direction.

The molecules used for this work are the 2-(methyl)oxirane C_3H_6O (MOx, m = 58.08 uma), commonly called propylene oxide, and the 2-(trifluoromethyl)oxirane $C_3H_3F_3O$ (TFMOx, m = 112.03 uma), both shown in Figure 1.4. In both systems, the targeted electron is in the O(1s) shell because of its outstanding binding energy, making it easier to ionize compared to the three C(1s) electrons in the molecule which differ of just few eV due to chemical shift. All the experiments presented in this work have been conducted using highly-polarized synchrotron radiation at the SOLEIL Synchrotron facility (Saint-Aubin, France) at the SEXTANT beamline, described in details in chapter 4.1.

2. CIRCULAR DICHROISM AND STRUCTURAL DETERMINATION

The dichroism is an effect which describes the difference in the absorption (or emission) by an optically active medium of monochromatic light depending on the light polarization. This effect has been initially observed by Haidinger (1847) and later Cotton (1895), and thus termed the "Cotton effect", but has been theoretically and systematically discussed by Rosenfeld just in 1928 [42]. The name dichroism comes from the Greek word *dikhroos*, meaning "two-coloured", and it refers to early experiments on crystals such as tourmaline which show different transmitted wavelengths upon the rotation of a polarizer (i.e., dichroic dispersion and birefringence). The circular dichroism (CD) makes use of circularly polarized light (CPL) and the medium for its observation is a randomly oriented chiral substance in liquid or gas phase. Despite the strict requirement for a chiral medium, CD has been recently shown to emerge from achiral molecules both theoretically e.g., in perovskites, and experimentally e.g., in controlling and shaping the photon angular momentum [43], [44].

For the scope of this work, it is useful to consider separately the CD in absorption (e.g., excitation) from the CD in photoelectron emission (e.g., core-ionization). The former includes effects as natural CD, optical rotary dispersion (ORD) [45], vibrational CD (VCD) [46], and Raman optical activity (ROA) [36], and it is usually investigated in the infrared (IR) − visible (VIS) − ultraviolet (UV) and vacuum ultraviolet (VUV) part of the photon spectrum; the latter includes the

circular dichroism in the angular distribution (CDAD), the photoelectron circular dichroism (PECD) induced by soft or hard X-ray photons instead[10] which are the main focus of this work.

The usual signal strength of the natural CD in absorbance are in the range of 10^{-3} for the electronic, and $10^{-4} - 10^{-5}$ for the vibronic case. CD in absorption relies on the quantum mechanical interferences between the electric dipole (E1), the electric quadrupole (E2), and the magnetic dipole (M1) transition moments of a molecule. From spectroscopy, it is known that the pure magnetic dipole M1 is dominant in virtually all the valence-to-valence electron transitions (from THz to UV photon energy). On the contrary, core electron transitions happen in the range of VUV and X-ray photon energy, where the most common interference mechanisms are the magnetic dipole – electric dipole (M1*E1) and the magnetic dipole – electric quadrupole (M1*E2) ones [49].

Despite the small differential signals, CD in absorption provides a well-established technique, suited to investigate with great accuracy the electronic configuration and eventually the conformation of solvated large biological molecules in liquid or gas phase. These families of techniques were particularly successful in the investigation of the secondary structures of protein (UV), in the study of the vibronic spectra of several proteins and DNA helices (IR), and specific electrochemical reactions as charge transfer transitions in metal-protein complexes (UV-VIS) [8].

2.1 Photoelectron circular dichroism (PECD)

The advent of 3rd generation synchrotrons made high brilliance, high flux, high monochromatic, and partially coherent X-ray photons available to a broader

---

10   The magnetic circular dichroism (MCD) [47], and its equivalent in ionization x-ray magnetic dichroism (XMCD) [48] are left aside from the present short introduction on CD because they are field-induced dichroic effects and therefore do not require the target molecule to be chiral. Nevertheless, it is worth mentioning them because of the dramatic impact they had in the understanding of physical properties of inorganic magnetic materials as well as biological compounds.

scientific community [51]. Synchrotron radiation and dramatic technological advances in undulators and toroidal gratings opened the possibility to excite and/or ionize selectively core electrons, with the use of partially coherent highly polarized X-ray photons (see chapter 4.1). These tools made CD in photoelectron emission, in combinations with *ab initio* calculations, an extremely powerful technique to investigate optical properties with high-accuracy, to determine the (absolute) configuration of molecules, and to probe molecular dynamics of single chiral and non-chiral molecules in the gas-phase to an unprecedented degree of detail.

The photoelectron circular dichroism (PECD) effect is defined as the normalized difference in emission of a photoelectron along the photon propagation direction in the laboratory frame (LF), and it is observed when two chiral objects interact, as in the case of a chiral molecule and a circularly polarized photon. The effect is a consequence of the intrinsic symmetry breaking of chiral molecular system, and the first theoretical formulation was given by B. Ritchie in 1976 [52], [53], refined by N. A. Cherepkov in 1982 [54]. The PECD show characteristics that make it a suitable observable for a technique with the aim of directly determining the absolute configuration of chiral molecules, as described in the followings.

First, PECD is a chiroptical phenomenon observed in all ionization regimes, therefore universal [55]. Experiments have been conducted from single to multiple photoionization [56] and even in the strong-field ionization [57], and the majority of them were performed so far on valence electrons of randomly oriented molecules [58]–[62]. PECD has a complex dependency on the electronic [63] and vibronic [64] molecular configuration, the molecular conformation [65], [66], dimerization [67], clustering [68] and the energy of the outgoing photoelectron [69]. The high sensitivity of PECD made possible to study ultra-fast molecular dynamics [70], in particular time-resolved molecular relaxation [71]. In parallel with more traditional chiroptical techniques, racemic mixtures can be resolved in real-time with the use of PECD, accessing their enantiomeric content
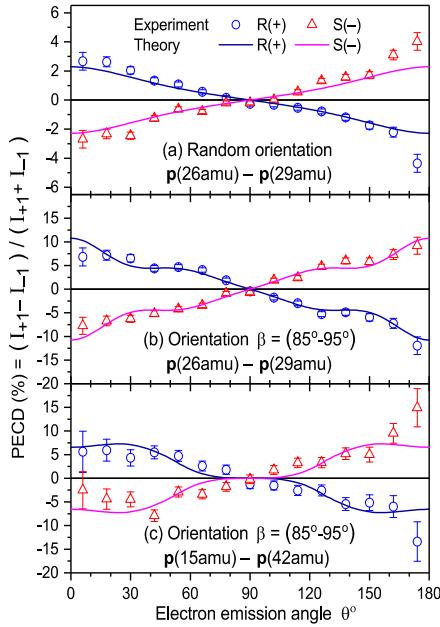
Figure 2.1: PECD as function of the photoelectron emission angle θ for the O(1s) photoelectron in MOx with a kinetic energy of 11.5 eV. The solid lines are the theoretical calculations. β is the angle between the relative momentum vector of two ionic fragments and the photon propagation direction. a) integrated over all molecular orientations; b) molecule aligned to the polarization plane; c) a second fragmentation channel for comparison. Image reproduced from [74].

[72]. Only a few experiments have been conducted using core ionization, as shown in the pioneering study from V. Ulrich et al. [73]. Nevertheless, the latter ionization regime is crucial to use CEI in order to determine *a posteriori* the alignment of the molecular target at the ionization instant, having a localized source of the scattering photoelectron, as described in chapter 2.3.

Second, the differential signal of PECD is several orders of magnitude higher than natural CD in absorption, e.g., up to 10% for randomly oriented molecules, and up to 20 − 30% when the molecule is aligned to the polarization plane of the incoming photon, as shown in Figure 2.1. The reason of such a considerable increase lies in the facts that for PECD the symmetry breaking upon switching photon polarization is completely addressed to a pure electric dipole E1, in contrast with CD, a difference described in greater detail in chapter 3.2.

A pioneering work on the sensitivity of PECD to the molecular orientation has been recently done by Tia et al. [74] who have investigated the PECD of an O(1s) core ionized electron of a MOx molecule. The molecular orientation has been

obtained through the coincident measurement of two photoions and photoelectrons in a COLTRIMS experiment, described in greater details in chapters 4.6.1.1 and 5.
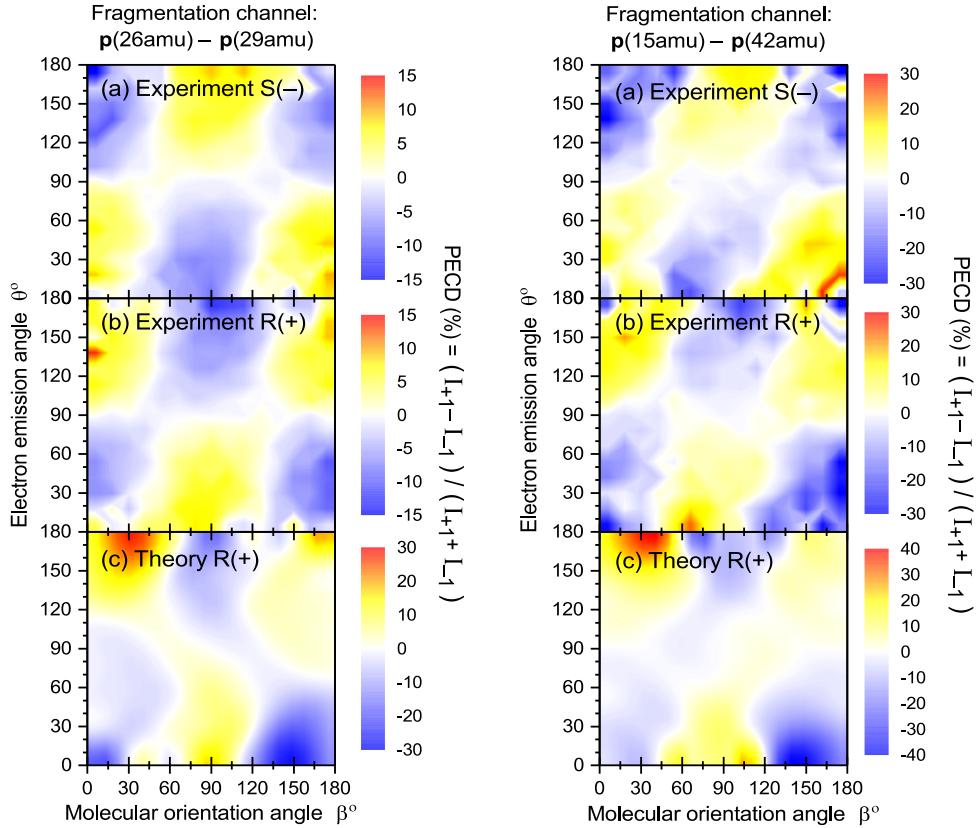
Figure 2.2: PECD (colour coded) as function of molecular orientation β (horizontal axis) and electron emission angle θ (vertical axis) of O(1s) photoelectron of MOx with kinetic energy 11.5 eV: PECD maps. The two columns represent two different fragmentation channels. a) experimental asymmetry for the S(−) enantiomer; b) experimental asymmetry for the R(+)-MOx enantiomer; c) theoretical predictions for the R(+)-MOx enantiomer. The PECD computed for the S(−)-MOx enantiomer has an opposite sign of asymmetry. Image adapted from [74].

The results of the former experiment suggest that the electron wave scatters at the molecular potential, a picture supported by comparison with theoretical calculations. This scattering results into complex angular distribution of the photoelectrons in the molecular frame ("Molecular Frame Photoelectron Angular Distribution", MFPAD) as described in chapter 3.3. The reported PECD was obtained considering the integrated MFPADs over the unresolved molecular axis, since is not possible to completely determine the orientation of a molecule in space with just two fragments, but it was enough to determine the fragmentation axis with respect to the photon propagation direction, as shown in Figure 2.2.

Within the validity of the axial-recoil approximation, the photoions emission direction is assumed to coincide with the molecular fragmentation axis. The former assumption holds when very fast fragmentation dynamics occurs, such as rapid Auger decay of an inner-shell vacancy and which result in a CE of a molecular dication. An increase of PECD by a factor of 10 compared to randomly oriented molecules (i.e., integrating the MFPADs across all molecular orientations) can be retrieved by selecting specific fragmentation directions with respect to the light's propagation direction, as shown for MOx by Tia et al. [74]

This latter experiment proves that the PECD is indeed extremely sensitive to the geometry of the molecular potential and therefore the molecular structure of a chiral molecule, its orientation in relation to the direction of light's propagation, and the helicity of the ionizing photon. The PECD is therefore a promising phenomenon to determine the absolute structure of single molecules in the gas-phase, in good agreement with *ab initio* theoretical calculations, without using any reference compounds.

2.2 Circular dichroism in the angular distribution (CDAD)

The circular dichroism in the angular distribution (CDAD) is another chiroptical phenomenon in photoemission closely related to the PECD effect, and it was theoretically predicted along with it by B. Ritchie in 1976. The CDAD occurs with spatially-oriented, achiral high-symmetry molecules irradiated with CPL, and it is measured in the polarization plane (i.e., perpendicular to the photon propagation direction). Initially, the CDAD seemed to emerge from beyond the dipole approximation [75], or to require a strong spin-orbit interaction [76], but R. L. Dubs et al. in 1985 demonstrated that it stems instead from the pure dipole contribution E1, as in the case of PECD, and it occurs in linear molecules [77]. Finally, the CDAD was experimentally proven by C. Westphal in 1989 [78].

The CDAD has a similar quantum mechanical derivation with respect to PECD [79], but it occurs with fixed-in-space achiral molecules: the handedness is induced by the experimental geometry, namely using the photon propagation direction of right and left CPL and a molecular axis vector (i.e., "recoil") to define the system of reference and detecting the photoelectron momentum vector [80]. Therefore, the CDAD will not occur in an angle-integrated observation, and, in contrast to PECD, it is enantiomer-insensitive [80].
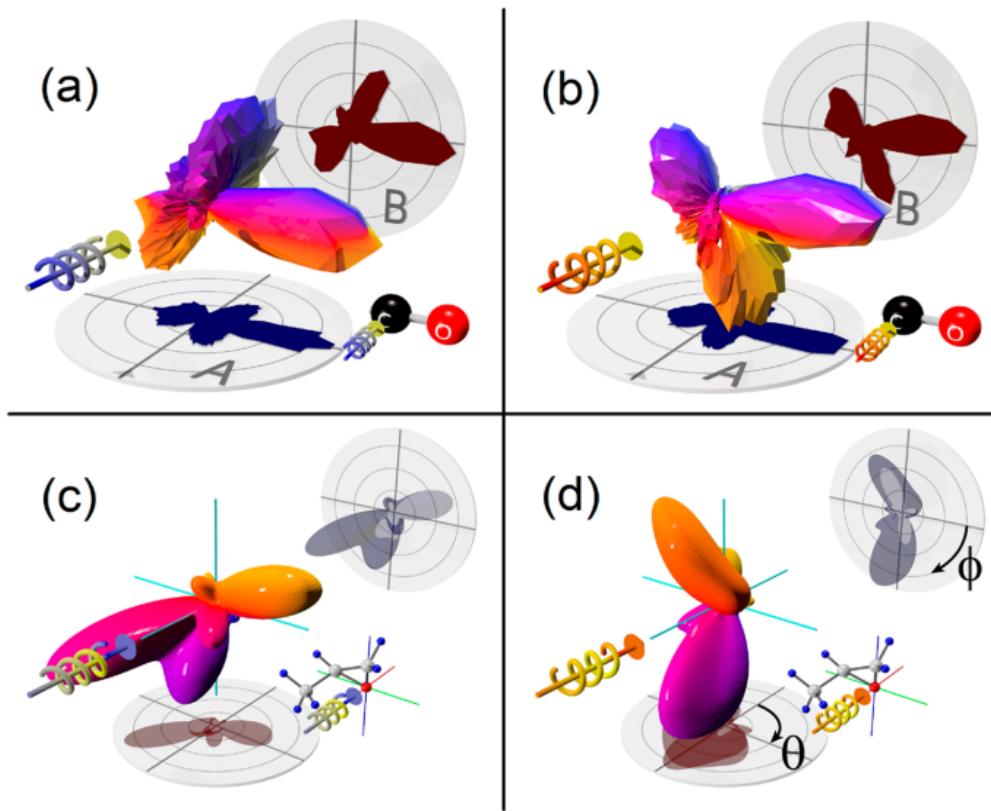
Figure 2.3: Comparison of MFPAD between CO and MOx for LCP and RCP light, first and second column respectively a),b) experimental data for CO; c), d) theoretical calculations for MOx. Therefore, CO shows just CDAD contrast, and MOx shows both PECD and CDAD. In the insert in panel d) the angle φ, and the angle θ are highlighted. Image reproduced from [74].

Moreover, the CDAD is observed in directions mutually perpendicular to the photon propagation direction and the molecular axis (i.e., in the polarization plane). Therefore, the CDAD is absent along the photon propagation direction [81]. In the system of reference shown in paned d) of Figure 2.3, for a fixed-in-space molecule, the CDAD is calculated as the asymmetry upon switching CPL in photoelectron emission in the photon polarization plane (i.e., up/down) described by the angle φ.

The CDAD is usually calculated using the equation (2.1). By contrast, the PECD is calculated as the asymmetry with respect to the photon propagation direction along the x-axis (i.e., forward/backward), describe by the angle θ. The PECD can be observed for both randomly oriented and fixed-in-space molecules [82].

$$CDAD(\varphi) = \frac{I_{+1}(\varphi) - I_{-1}(\varphi)}{I_{+1}(\varphi) + I_{-1}(\varphi)}$$ (2.1)

   In Figure 2.3, it is possible to observe the difference of photoelectron angular distribution upon switching light helicity for fixed-in-space CO (i.e., a linear molecule) in panel a) and b) (i.e., first row) and fixed-in-space MOx (i.e., a chiral molecule) in panel c) and d) (i.e., second row). In the case of CO, the distributions are oriented unambiguously with a lobe pointing along the molecular axis toward the O atom, forming with the helicity a unique system of reference, and are symmetric along the photon propagation direction. The change in helicity induces a clear flip about the cosφ = 0 axis (see projections on the B disks for each panel), giving a CDAD of about 60% for some φ angles [81]. In the case of MOx, the asymmetry of the distribution appears to be more complex and present both along the photon propagation direction and in the polarization plane; the resulting PECD effect for MOx has been already shown in Figure 2.2.

   Despite the intrinsic lack of chiral sensitivity, the former experiment shows the high sensitivity of chiroptical phenomena to the molecular structure. As for the previous case of the PECD, it is possible to illuminate a molecule "from within", obtaining high contrasted PADs, in good accordance with the theoretical predictions, even for molecules randomly oriented in space [79].

2.3 Absolute configuration of polyatomic molecules

In contrast to the conventional approaches mentioned in chapter 1.5, techniques that are able to combine the high sensitivity of chiroptical phenomena with single molecule targets can lead to a strong innovation and scalability in assigning the of absolute configuration of chiral molecules.

For the first time, M. Pitzer et al. directly determined the absolute configuration of the benchmark molecule CHBrClF using Coulomb explosion imagine (CEI), i.e., without the need of theoretical modelling [74]. Unlike spectroscopic approaches, CEI can be considered a gas phase single molecule (momentum) microscopy: the molecular structure is magnified to a macroscopic scale through the acceleration of the molecular fragments induced by a multiple ionization [83]. CHBrClF is a molecule with low symmetry central chiral carbon atom with 4 different atomic substituents in a tetrahedral arrangement with different atomic mass. Using a COLTRIMS apparatus (extensively described in chapter 4.3), it was possible to resolve a racemic mixture of CHBrClF assigning the absolute configuration (i.e., handedness) of each enantiomer on a single molecule level. After each ionization event, the apparatus measures the time-of-flight (tof) and impact position on a detector of charged fragments, allowing the computation of the 3D momentum vectors of each charged fragment in coincidence; leveraging the momentum conservation for a complete kinematic ionization, it is possible to reconstruct the emission directions in momentum space of each charged fragment at the instant of ionization, as presented in Figure 2.4.

The momentum space images require recording large amount of five folds coincidence events, using high power and high repetition femtosecond LASER. The discrimination of enantiomers is done defining the angle $\cos\theta = \boldsymbol{p}_F \cdot (\boldsymbol{p}_{Cl} \times \boldsymbol{p}_{Br})(|\boldsymbol{p}_F||\boldsymbol{p}_{Cl} \times \boldsymbol{p}_{Br}|)^{-1}$, self-referenced to the molecular coordinates. The technique could determine the spatial orientation of the
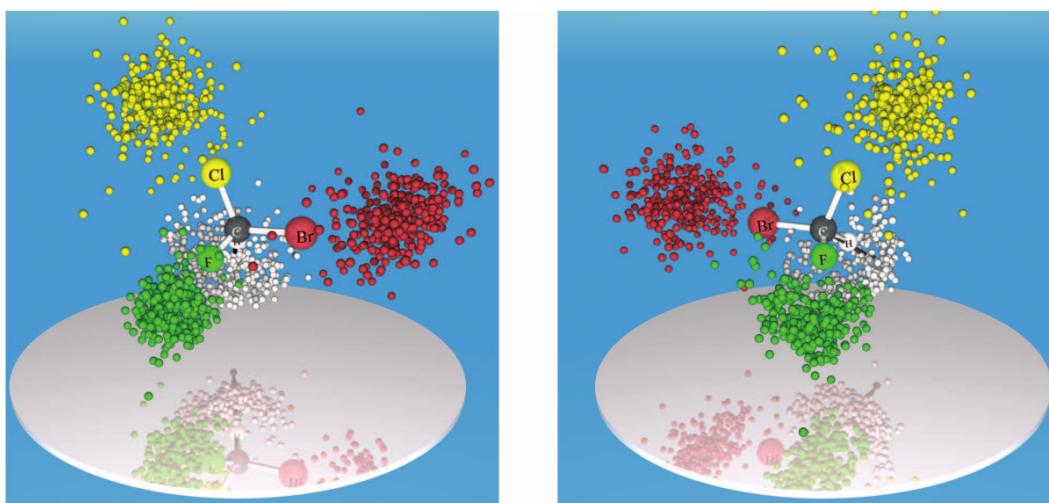
Figure 2.4: Linear momenta in five-fold fragmentation of both CHBrClF enantiomers. Left: the measured momenta for S-CHBrClF gating the θ angle to cosθ < −0.6; right the momenta of R-CHBrClF gating the angle θ to cosθ > 0.6. In both images the atom are colour coded as C atom grey, H atom white, F atom green, Cl atom yellow, and Br atom red. The MF is defined by the momentum of C atom and the momentum sum of the Br and Cl atoms, and the momenta are expressed in the MF. H atom momenta are expanded by a factor 2. The central C atom is also accelerated away from the centre of mass (c.m.) and ejected in a similar direction as H [84].

molecule with only four charged fragments or a combination of three charged fragments and a neutral (momentum conservation). The latter could increase dramatically the experimental yield as detection efficiency diminishes with the increasing number of fragments, because the multi particle coincidence count rate is proportional to the single particle detection efficiency to the power of the number of detected particles. Obtaining structural information of larger molecules with the help of pure CEI techniques poses challenges like the initial generation of high-charge states, the sharp fall of detection efficiency for the coincident detection of many particles, and uncertainties in the assignment of the different molecular fragments.

3. PHYSICS BACKGROUND

A core photoionization induces the ejection of one (or more) electron from an inner-shell (atomic-like) molecular orbital upon the absorption of photon with energy $E_\gamma = h\nu$ greater than the electron binding energy $E_{e,b}$. As a consequence, an inner-shell vacancy is created, and therefore the molecule becomes excited. The ejected electron *e* to the continuum is described by a wave vector k_e and carries a kinetic energy $E_{e,\gamma}$, dependent on the difference between the incoming photon energy and the electron binding energy $E_{e,b}$, and the difference between the final and initial vibrational state of the excited molecule, as shown in equation (3.1).

$$E_{e,\gamma} = h\nu - E_{e,b} + E_{v,i} - E_{v,f} = \frac{\hbar^2 k_e^2}{2m_e} \qquad (3.1)$$

The excited molecule can relax following several relaxation pathways, each with a typical occurrence probability, typically resulting in the ejection of electrons. Polyatomic molecules can eject electrons in multiple ways, but the focus of this work is on direct ionization (one electron), and Auger electrons (for multiple electrons in a so-called Auger cascade). Regardless of the mechanism, if more than two electrons are ejected, the molecule can photodissociate into several charged (and neutral) fragments which then will fly apart due to the charge repulsion; this process is called Coulomb explosion (CE), and it is described in greater detail in chapter 3.4 .

In the following section, the quantum mechanical model for direct photoionization of a generic quantized system using weak-field photons (i.e., from synchrotron radiation) is presented. The model is instrumental to theoretically describe the general phenomenon of circular dichroism (CD), and in particular the photoelectron circular dichroism (PECD) in the dipole approximation, based on scattering on the molecular potential. The reader will be introduced to the concept of photoelectron angular distribution (PAD) in a chiral system. The following derivation mainly follows the work of J. J. Sakurai "Modern Quantum Mechanics" [85].

3.1 Photoionization and dipole approximation

The process of photoionization can be theoretically described by the well-know non-relativistic time-dependent Schrödinger equation for a single particle

$$i\hbar \frac{d}{dt} |\psi(\boldsymbol{r},t)\rangle = \boldsymbol{H} |\psi(r,t)\rangle \qquad (3.2)$$

where **H** is the Hamilton operator for a charged particle, and ψ the position-space wave function dependent on the whole quantum system. Within the semi–classical approximation (i.e., matter described as quantum mechanical object and light described as a wave using classical physics), the Hamilton operator of an electron of charge e in an external electro-magnetic field subjected to a central molecular potential V(**r**) can be written as

$$\boldsymbol{H} = \frac{1}{2m_e}[\boldsymbol{p} - e\boldsymbol{A}(\boldsymbol{r},t)]^2 + e\varphi - V_{eff}(\boldsymbol{r}) \qquad (3.3)$$

where **A** is the magnetic vector potential in time-space coordinates, V_{eff} is the electric potential and $\boldsymbol{p}$ is the canonical momentum operator. The relationship between the magnetic vector potential **A**, the electric field **E** and the magnetic field **B** vectors is (choosing the Coulomb gauge, as described later)

$$E(\mathbf{r},t) = -\frac{1}{c}\frac{\partial \mathbf{A}(\mathbf{r},t)}{\partial t} \quad ; \quad B(\mathbf{r},t) = \nabla \times \mathbf{A}(\mathbf{r},t) \ . \tag{3.4}$$

The magnetic vector potential **A** comes in the usual non-quantized form for a single frequency ω and the photon (linear) polarization vector $\hat{\boldsymbol{\varepsilon}}$:

$$A(\mathbf{r},t) = 2A_0\hat{\boldsymbol{\varepsilon}}\cos(\mathbf{k}\mathbf{r}-\omega t) = A_0\hat{\boldsymbol{\varepsilon}}[e^{i\mathbf{k}\mathbf{r}-i\omega t}+e^{-i\mathbf{k}\mathbf{r}+i\omega t}] \tag{3.5}$$

where A_0 is a amplitude and $\mathbf{k}=\omega/c\,\hat{\boldsymbol{n}}$ is the photon's wave vector, with $\hat{\boldsymbol{n}}$ along the z-axis chosen herein as the photon propagation direction, and by definition orthogonal to polarization vector $\hat{\boldsymbol{\varepsilon}}$. The convenience of the magnetic vector potential description comes with the compulsory choice of a symmetry gauge to have a unique description of the field. For time-independent charges in a non quantized field, the Coulomb gauge is best suited: it consists in setting the divergence of the vector potential $\nabla \cdot \mathbf{A}=0$, combined with the observation that the electric potential φ = 0 because of the absence of static charges. To simplify the binomial expression in (3.3), it is worth noticing that $\mathbf{p}\cdot\mathbf{A}=\mathbf{A}\cdot\mathbf{p}$ and $\mathbf{A}^2 \ll \mathbf{A}\cdot\mathbf{p}$ which, therefore, can be dropped. The latter condition is a consequence of the weak field photons produced by perhaps synchrotron radiation due to its low intensity, as reported in chapter 4.1. Within the Born-Oppenheimer (OP) approximation (i.e., adiabatic approximation), the effective interaction Hamiltonian becomes

$$H_{\text{int}}(t) = \frac{e}{m_e c}A_0\hat{\boldsymbol{\varepsilon}}\,\mathbf{p}[e^{i\mathbf{k}r-i\omega t}+e^{-i\mathbf{k}r+i\omega t}] \tag{3.6}$$

where it worth to notice two purely quantum contributions, namely $i\mathbf{k}r-i\omega t$ for the absorption and $-i\mathbf{k}r+i\omega t$ for the stimulated emission, with respect to the molecule. The equation (3.6) can be simplified expanding the absorption term as

$$e^{i\mathbf{k}r}=1+i\mathbf{k}r-\frac{1}{2}\mathbf{k}r^2+\dots \tag{3.7}$$

noticing that, when the photon wavelength is larger than the diameter of light atoms or small molecules, the product $\mathbf{k}\cdot\mathbf{r}$ << 1, as well as for all the higher order.

Therefore, limiting the expansion (3.7) up to the zeroth order leads to the so-called *dipole approximation E1*:

$$H_{\text{int}}(t) \approx -\frac{e}{m_e} A_0 \hat{\boldsymbol{\varepsilon}} \, \boldsymbol{p} \, e^{-i\omega t} \approx -\hbar\omega[\hat{\boldsymbol{\varepsilon}} \cdot \boldsymbol{r}] \ . \tag{3.8}$$

where $\hat{\boldsymbol{\varepsilon}} \cdot \boldsymbol{r}$ is an electric dipole E1. It is important to remark that not all Maxwell equations are satisfied within the framework of the dipole approximation, and some relevant electronic transitions are completely forbidden by selection rules, a quite crude approximation. The expansion up to the second order allows more transitions to be taken into account, resulting in a more flexible approximation. This latter choice leads to the interaction Hamiltonian operator in the form of

$$H_{\text{int}}(t) \approx -\frac{e}{m_e} A_0 e^{i\boldsymbol{kr}} \hat{\boldsymbol{\varepsilon}} \, \boldsymbol{p} \, e^{-i\omega t} \approx -\hbar\omega\left[\hat{\boldsymbol{\varepsilon}} \cdot \boldsymbol{r} \pm \hat{\boldsymbol{\varepsilon}} \cdot \boldsymbol{\mu} + \frac{1}{2} i (\boldsymbol{k} \cdot \boldsymbol{r})(\boldsymbol{r} \cdot \hat{\boldsymbol{\varepsilon}})\right] \tag{3.9}$$

with three contributions put in evidence, namely the electric dipole E1 $\boldsymbol{r}$, the magnetic dipole $\boldsymbol{\mu} = \boldsymbol{r} \times \boldsymbol{p}$ also called M1, and the electric quadrupoles E2 $\propto \boldsymbol{r}^2$ [54].

It is possible to derive the transition rate $w_{i \rightarrow n}$ for the absorption term between an initial state *i* and a final state *n* (which could also be in the continuum), using the formalism of the time-dependent perturbation theory within the adiabatic approximation. The complete Hamiltonian for this problem can be written as:

$$H = \frac{p^2}{2m_e} - V_{eff}(\boldsymbol{r}) - \frac{e}{m_e} \boldsymbol{A} \, p = H_0 + H_{\text{int}}(t) \tag{3.10}$$

thus, divided into an unperturbed part H_0 and a time-dependent part $H_{int}(t)$; the latter represents the interaction of the system with the incoming photon, and it can be described with the dipole approximation E1. When the perturbation is absent (t = 0), the unperturbed state constitutes a known basis of Eigenkets *n* with relative Eigenstates E_n according to the time-independent Schrödinger equation $\widehat{H}_0|n\rangle = E_n|n\rangle$ which can be dropped in the following derivation.

The time evolution of a generic quantum state $\alpha(t)$ is defined by the ket $|\alpha(t)\rangle = \sum_n c_n(t) e^{\frac{-i E_n t}{\hbar}} |n\rangle$. The states can be described as a sum of perturbation coefficients $c_n(t) = \langle n | U_I(t, t_0) | i \rangle$ representing the influence of a generic external potential $U_I(t, t_0)$ on the state times the internal exponential temporal decay. It is relatively straightforward to show that the time partial derivative of the quantum state $\alpha(t)$ is $i\hbar \frac{\partial}{\partial t} |\alpha(t)\rangle = H_{int}(t) |\alpha(t)\rangle$, thus fully described by the interaction Hamiltonian. The latter can be further developed as

$$i\hbar \frac{\partial}{\partial t} \langle n | \alpha(t) \rangle = i\hbar \frac{d}{dt} c(t) = \sum_i \widehat{H}_{ni}^{int}(t) e^{i\omega_{ni} t} c_i(t) \tag{3.11}$$

with $\omega_{ni} = (E_n - E_i)/\hbar$ as the resonant condition to the photon absorption process. Applying the dipole approximation E1, the matrix element becomes $\widehat{H}_{ni}^{int} = \langle n | H_{int}(t) | i \rangle \propto \langle n | \hat{\varepsilon} \, \boldsymbol{p} | i \rangle$. Finally, it is possible to write the transition rate its full form

$$w_{i \to n} = \frac{2\pi}{\hbar} \frac{e^2}{m_e^2 c^2} |A_0|^2 \left[\langle n | e^{ikr} \hat{\varepsilon} \, \boldsymbol{p} | i \rangle \right]^2 \delta(E_n - E_i - \hbar\omega) \ . \tag{3.12}$$

The δ function ensures energy conservation upon the photon absorption. The transition matrix element is defined as $|V_{in}|^2 = \left[\langle n | e^{ikr} \hat{\varepsilon} \, \boldsymbol{p} | i \rangle \right]^2$, and it determines the availability of electronic transitions according to specific selection rules; its descriptive accuracy depends on approximation used, as already discussed in this chapter. If (3.12) is integrated over the density of final states, Fermi's golden rule is obtained. In general Fermi's golden rule is a transition probability in the form of

$$w_{i \to n} = \frac{d}{dt} |\langle n | U_I(t, t_0) | i \rangle|^2 \ . \tag{3.13}$$

Choosing the polarization vector $\hat{\varepsilon}$ to be along the x-axis, recalling the commutation between the position $\boldsymbol{x}$ and the momentum $\boldsymbol{p}$ operators, and recalling that the unperturbed Hamiltonian is $[\boldsymbol{x}, H_0] = \frac{i\hbar}{m_e} \boldsymbol{p}_x$, it is possible to

further simplify (3.12) in

$$\langle n | e^{ikr} \hat{\boldsymbol{\varepsilon}} \, \boldsymbol{p} | i \rangle \approx \langle n | \boldsymbol{p}_x | i \rangle = -i \hbar \, \omega_{in} \langle n | \boldsymbol{x} | i \rangle \; . \tag{3.14}$$

Fully differential cross-sections, i.e., cross-sections differential in all observables of a final state, completely characterize atomic and molecular many-particle reactions. The observables in an ionization process are the vector momenta, spins and internal excitation of all reaction products. Any integration over observables, such as the electron spin, can mask some characteristics features of the specific reaction.

Recalling that the energy of an incoming photon flux described as a classical electromagnetic radiation is $\dfrac{\omega^2}{2\pi c} |A_0|^2$, it is possible to define the absorption cross-section σ_{abs} in the dipole approximation as

$$\sigma_{abs}(\omega) = 4\pi \, \omega_{ni} \langle n | (e\,\boldsymbol{x}) | i \rangle \, \delta(\omega - \omega_{ni}) \; . \tag{3.15}$$

The quantity usually recorded in an experiment is the differential cross-section over the solid angle Ω $\dfrac{d\sigma}{d\Omega} = \dfrac{\sigma}{4\pi} I_p(\theta)$ proportional to the intensity recorded at a detector at an angle θ.

3.2 Photoelectron dynamics of chiral molecules

The intensity of a PAD within the dipole approximation for a generic light polarization *p* has the general form of equation (3.16), where P_j is the Legendre polynomial of order j, and b_j^p are the radial dipole matrix elements of order j.

$$\frac{d\sigma}{d\Omega} = \frac{\sigma}{4\pi} I_p(\theta) = \sum_{j=0} b_j^p P_j(cos\theta) \tag{3.16}$$

As derived by J. Cooper and R. N. Zare [86], for the ionization of an isotropic ensemble of atoms or for achiral molecules in the gas-phase with a linearly

polarized photon (i.e., $p = 0$) restricted to $j \leq 2$ i.e., within the dipole approximation E1, the PAD of equation (3.16) is reduced to

$$\frac{d\sigma}{d\Omega} = \frac{\sigma}{4\pi} I_0(\theta) = \frac{\sigma}{4\pi}\left[1 + b_2^0 P_2(\cos\theta)\right] \, , \qquad (3.17)$$

where θ is the angle to the photon polarization plane (see appendix B.6 for details on the convention used), b_2^0 the anisotropy or asymmetry parameter, and P_2 the Legendre polynomial of order 2. The equation (3.17) arises from the interference of partial waves with cylindrical symmetry, usually described by the cosine of the relative phase shifts associated to the angular momentum channels [87], which for linearly polarized light implies $b_1^0 = 0$, called the dichroic parameter. The anisotropy or asymmetry parameter b_2^0 is constrained between -1 and 2 to keep (3.17) positive, corresponding to pure $\sin^2$ or $\cos^2$ distributions, respectively, and an isotropic distribution is given for $b_2^0 = 0$. The latter considerations imply that the highest emission probability occurs when the electron is emitted parallel to the photon polarization vector, and it is zero when perpendicular. The emission is symmetric with respect to the light propagation direction. The asymmetry parameter b_2^0 holds information on photoionization dynamics describing the interference of s and d photoelectron partial waves, but it is neither possible to access their radial dipole matrix elements, nor their phase shift [88].

For chiral molecules at all light polarization, for given a vector **r**, the angle θ is now defined with respect to the photon propagation direction along the x-axis according to equation (3.18), therefore $b_2^{\pm 1} = -b_2^0 1/2$.

$$\theta = \cos^{-1}\left(\frac{r_x}{\sqrt{r_x + r_y + r_z}}\right) \qquad (3.18)$$

For chiral molecules, the intrinsic symmetry breaking prevents the interference terms dependent on the sine of adjacent partial waves to be averaged out over integration on all molecular orientations, giving rise to the dichroic parameter b_1, as shown in equation (3.19). The dichroic parameter b_1 shows an enhanced sensitivity to the amplitude and sign of the scattering phase of the outgoing

partial waves, therefore it is a very sensitive probe for scattering processes on a complex chiral molecular potential with respect to the light propagation direction (i.e., backward-forwards asymmetry).

$$I_{\pm 1}(\theta) \propto \frac{\sigma}{4\pi}\left[1 \pm b_1^{\pm 1}P_1(\cos\theta) - \frac{1}{2}b_2^0 P_2(\cos\theta)\right] \tag{3.19}$$

The full quantum mechanical derivation of equation (3.19) following from the conclusion of the previous chapter is carried out in the appendix B.2, and just the final form is presented here.

Table 1: Translations of polarization p into several conventions; S_3 is the Stokes parameter; to determine the rotation, a virtual observer looks along the light's propagation direction towards the light source.

Polarization p	$S_3 - helicity$	Conventional name	Rotation
0	0	Linear	Planar (h/v)
-1	+1	Rcp	Clockwise
+1	-1	Lcp	Anti-clockwise

Considering achiral molecules, for all polarizations it is true $b_1^p = 0$, therefore the dichroic parameter b_1^0 vanishes for a linearly polarized photon $p = 0$, retrieving the well-known result of equation (3.17). For chiral molecules and CPL (i.e., p = ± 1), the dichroic parameter $b_1^{\pm 1}$ is non-zero, and in particular it changes sign upon switching light helicity *or* equivalently changing enantiomer [86], as shown in equation (3.19). The mutual relation between the b_j^p coefficients depending on light polarization is summarized from set of equations (3.20) whose values are calculated in greater detail in appendix *B.2*. The polarization *p* can assume only three integer values, because a photon carries an angular momentum of $\pm\hbar$; following the handedness convention introduced at the end of chapter 1.3, the translation between conventions is reported in Table 1, and further discussed in the appendix B.1. It is important to remark that the angle θ changes definition according to the polarization *p*.

$$b_1^0 = 0 \quad ; \quad b_2^{\pm 1} = -1/2\, b_2^0 \quad ; \quad b_1^1 = -b_1^{-1} \tag{3.20}$$

Experimentally, the PECD for a single randomly oriented chiral molecule is defined as the normalized difference of two electron angular distributions generated from photons with opposite helicities of polarization *p*, as in

$$PECD(cos\theta)=\frac{I_{+1}(\theta)-I_{-1}(\theta)}{I_{+1}(\theta)+I_{-1}(\theta)}=\frac{b_1^{+1}P_1(cos\theta)}{[1-1/2\cdot b_2^0 P_2(cos\theta)]} \qquad (3.21)$$

where θ is the angle between the momentum vector of the outgoing electron and the photon propagation direction (i.e., along the x-axis). Therefore, the PECD manifests itself in a forward/backward asymmetry of the emitted electrons´ PADs with respect to the light's propagation direction upon switching the light's helicity *or equivalently* interchanging the enantiomer. This asymmetry survives averaging over all molecular orientations, and it has been shown to be higher when the molecule is either parallel or orthogonal with respect to the polarization plane of the incoming photon [74], as the contrast of any observable shrinks when integrated over other variables.

3.3 Molecular frame photoelectron angular distribution (MFPAD)

A PAD describes the angular distribution of ejected electron upon photoionization; a PAD emerges from constructive and destructive interferences between directly emitted and scattered photoelectron partial waves of different angular momenta and symmetry; the latter waves undergo changes of their angular momentum and phase shifting due to scattering on the molecular potential, describing typical patterns. In general, any wave function can be expanded in a basis of the angular momentum eigenstates, the spherical harmonics Y_{lm}; it is described by the angular momentum quantum number $l = 0, 1, 2, 3, ...$ that corresponds to an s, p, d, f, ... waves respectively, and its projection onto laboratory frame the quantum number $-l < m < l$. A PAD can be retrieved for both atomic and polyatomic systems, and it can be measured in different reference systems e.g., laboratory frame (LF) or molecular frame (MF). Thus, the most general form of a PAD can be described regardless of approximations, as

$$\frac{d\sigma}{d\Omega} = \frac{\sigma}{4\pi} I_p(\theta,\phi) \propto \sum_{L=0}^{L_{max}} \sum_{M=-L}^{L} B_{LM} Y_{LM}(\theta,\phi) \quad . \tag{3.22}$$

The coefficients B_{LM} are derived from the transition matrix element defined in equation (3.12), containing therefore the radial dipole matrix elements, along with their associated phase shifts; furthermore, they are dependent on photoionization dynamics, the experimental geometry, the electron's initial orbital, the spatial distribution of the sample, and the photoionization energy. The $Y_{LM}(\theta,\phi)$ are spherical harmonic functions, where the angles θ and φ are defined with respect to the z-axis either in the LF or in the MF (see appendix B.6).

For atoms, a PAD is always measured with respect to a LF, and just two partial waves for each orbital are required, whose sum has $|l - l'| \le L_{max} \le l + l'$. In contrast, a PAD in a molecule can be measured with respect to its MF, and because in molecules l is not any more a good quantum number[11], more than two partial waves must be used to describe the wave function of an outgoing photoelectron [88]. In the molecular case, the former sum is extended to $L_{max} = 2l_{max}$, where l_{max} is the arbitrary highest orbital angular momentum quantum number of the generated partial wave. Therefore, it is possible to compute the molecular frame photoelectron angular distribution (MFPAD) as superimposition of the outgoing partial waves as function of the angles θ and φ (i.e., spherical coordinates as in appendix B.6) with respect to a MF coordinate system defined from the photo-fragments momentum vectors, as pointed out in the pioneering work of D. Dill [89]. In the MF, odd spherical harmonics contribute to the angular distribution of a photoelectron, as in contrast with the LF, where the odd spherical harmonics can occur only if the molecules are chiral, or oriented in space.

To experimentally obtain MFPADs for molecules, several experimental approaches are commonly used: either a molecule can be first aligned with a LASER [90], or adsorbed on a surface [91] and then photoionized, or photo-fragments and photoelectrons from an ionization can be detected in

---

11   For an Hamiltonian *H* and an operator *O*, an eigenvalue is a good quantum numbers if every eigenvector remains an eigenvector of *O* with the same eigenvalue as time evolves.

coincidence. The latter method make use of the calculated momentum vectors to select *a posteriori* events belonging to specific molecular orientations, while the previous ones manipulates the target before ionization. MFPADs represent the limiting PAD when a molecule is completely aligned with respect to the LF [92]. The aim of using MFPADs is to experimentally determine all the radial dipole matrix elements and phase shifts involved in the investigated dynamics. Therefore, MFPADs are capable of directly probing the molecular geometry, and in principle the molecular dynamics too. For the latter goal, the positions of lobes and nodes in MFPADs is dependent on the specific photoelectron scattering dynamics that are strongly energy dependent, requiring sophisticated computational simulations to be interpreted. The internuclear distance of the scattering centres strongly influences the phase shift of the scattered wave, which in addition depends on the photoelectron energy.
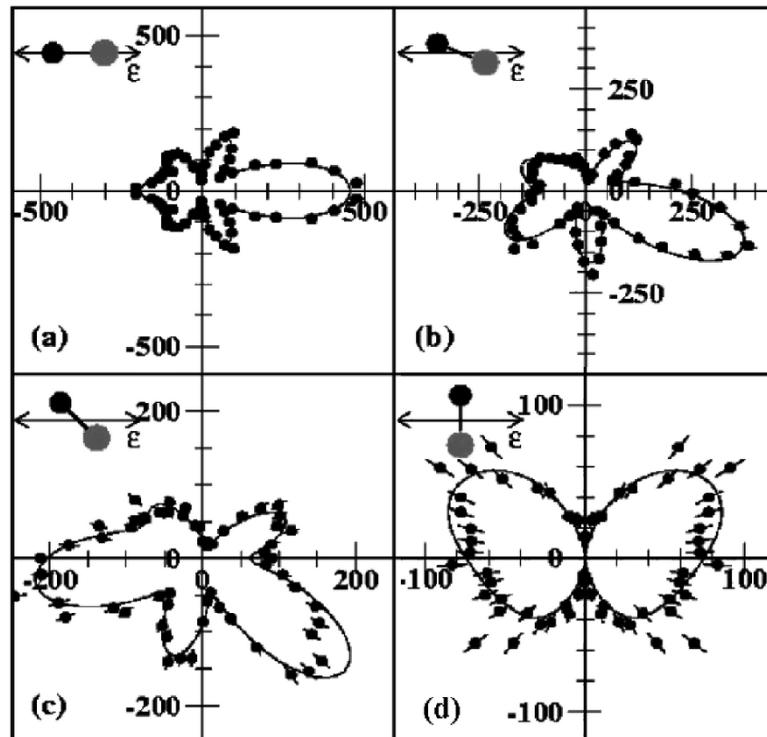
Figure 3.1: PADs of CO at 10.2 eV photoelectron energy in the frame of the incoming photon (LF), restricted to a plane parallel to the polarization one. In each panel, the orientation of the molecule (grey O, black O) relative to the photon polarization vector (arrow) is shown in the top-right corner. The solid curves represent the fit to the spherical harmonic expansion. The change in scale of a factor of 2 between (a) and (d) is due to a particular dipole transition. Image reproduced from [93].

For K-shell electrons, before scattering at the molecular potential, the initial photoelectron wave is a p-wave (i.e., dipole) with its maximum along the polarization axis. Higher angular momentum contributions to the photoelectron wave are only created by the scattering at the molecular potential. Therefore, it is often possible to recognize traces of this dipole pattern in complex MFPADs, as shown for CO in the pioneering work of A. Landers et al. [93] whose main results are reproduced in Figure 3.1; although a dipole distribution should always be the most prominent, relative angles between the polarization axis and the molecule of 0° and 90° result in a clear node with minima along the light's propagation direction (panel a and d). Nevertheless, the node tends to be filled at intermediate angles (panel b and c), suggesting a more complex interpretation. The other features in the angular distribution emerge from the aforementioned scattering on the molecular potential, and from the effect of relevant dipole selection rules [94].

Polarization-averaged MFPADs (PA-MFPADs) are MFPADs integrated over all light's propagation directions and have been shown to remove the strong contribution of the direct wave of the photoelectron due to direction-averaging, making them a suitable tool for capturing the molecular structure information. In a recent paper from Williams et al. [95] PA-MFPADs were demonstrated to capture the directions of the bonds in polyatomic molecules, and a following work from E. Plésiat et al. [96] showed the energy dependency of PA-MFPADs for several achiral molecules, attempting an explanation for the complicated trends as function of the photoelectron energy. In two recent papers, PA-MFPADs were demonstrated capable of holding information on the length of single bond [97], [98]. Very recently, G. Kastirke et al. demonstrated the possibility of using PA-MFPAD in combination with free-electron LASER (FEL) radiation to record molecular movies [99].

3.4 Coulomb explosion

As a consequence of a photoionization, the excited-state dynamics of polyatomic molecules generally involve a non-adiabatic[12] coupling of vibrational and electronic degrees of freedom which leads to conical intersections (CIs) between electronic potential energy surfaces [100]. CIs are considered the most photochemically relevant ultrafast nonradiative decay channels which can lead to photodissociation. Complex polyatomic molecules can eject multiple electrons by several mechanisms which leaves positive charges in the system. The creation of two or more static charges can lead to fragmentation, and charged (as well as neutral) fragments fly apart due to the electrostatic forces acting on the centres of the charges; the fragments share the total momentum, thus their velocities are inversely proportional to their mass. In larger molecules, many photodissociation channels occur as shown by the presence of many isolated structures in the photoion-photoion coincidence (PIPICO) diagrams in chapter 4.6.1.1. The capability of collecting the photo-fragments from a single dissociation event and obtain a momentum image has been already demonstrated in 1967, paving the way to the CEI [101]. The nuclei dynamics can be captured by the kinetic energy release (KER) defined as the energy sum of all ionic fragments in the centre of mass (c.m.) frame, as shown in equation (3.23).

$$KER = \sum_{i=0}^{n} \frac{p_i^2}{2m_i} \quad . \tag{3.23}$$

The KER distribution provides information about the final excited quantum states that was populated at the moment of photodissociation, therefore makes it possible to infer a reaction pathways. Experimentally, the KER is used to select a specific reaction channels through gating, and due to its angular invariance, it is used to calibrate detectors, as reported in chapter 4.6.1.1 using N_2 molecule.

---

12 The adiabatic approximation, also called the Born-Oppenheimer approximation, decouples the wave functions of nuclei and elections, picturing molecules as nuclei moving over a potential energy surface provided by the electrons. This is certainly a valid approximation for many chemical processes, but the time-scale of photochemical processes, and the complexity of poly atomic molecules requires going beyond this approximation for more accurate predictions.

3.5 Axial-recoil approximation

In order to experimentally obtain the photoelectron angular distribution in the molecular frame (MFPAD), momentum vectors of each photo-fragment emitted following the photoionization are measured, in this work, using a COLTRIMS apparatus described in greater detail in chapter 4.3. If the molecular dissociation takes place much faster than the rotation of the molecule, the distribution of the trajectories of the fragments, therefore the detected momentum vectors, will reflect the initial orientation of the molecule; in some cases, the vectors will point along the broken bonds. Generally speaking, the molecule should not rotate significantly before it final fragmentation. The former requirement leads to the so called "axial-recoil approximation", by which the measured momentum vectors of each fragment are correlated to the spatial configuration of the molecule before the photoionization [102].

In order to use the former approximation for polyatomic molecules, on top of the ultra-fast dissociation, the line connecting the centre of mass of the fragments and the one of the centres of charge has to coincide with the axis of the broken bond. For diatomic molecules, the former condition is intrinsically satisfied, but even for small molecules which brake into diatomic photo-fragments it could not be fulfilled. In general, the electrostatic force acts on the centre of gravity of the charges, not of the mass of the fragments. Therefore, if charges are not aligned along the broken bond axis, the measured molecular axis could not correspond to the axis of the broken bond. The CE could lead to a rotation of the individual fragments, because of the conservation of angular momentum. When the fragmentation is polyatomic, the fragmentation dynamics play a decisive role, and a theoretical modelling must be used to establish a unambiguous link between the assigned axes and the actual molecular orientation. Thus, the possible mismatch between centre of charge and the centre of mass is a crucial aspect for the comparison between simulations and experimental data, as previously discussed in chapter 3.4 .

4. THE EXPERIMENTAL SETUP

Synchrotron light sources produce synchrotron radiation (SR) from the acceleration of electrons or positrons, and they are an essential tool to investigate matter at the atomic level, and light-matter interaction [103]. The possibility of generating soft and hard X-ray photons with high energy resolution, highly polarized, with partial lateral coherency, and relatively short pulse duration (~ 100 ps) opened the road for the investigation of core electrons in molecules and the related scattering phenomena. The experimental apparatus used for this work is the Cold Target Recoil Ion Momentum Spectroscopy (COLTRIMS), or "reaction microscope" which allows 3D momentum spectroscopy in coincidence.

The following sections present the basic principles of photon generation in a synchrotron facility, and the implementation of a COLTRIMS system for the experiments conducted by the author at the SOLEIL synchrotron facility at the beamline SEXTANT in September 2018.

4.1 Synchrotron radiation (SR)

If a charged particle with charge q and rest mass m_0, accelerated to kinetic energy E_k much greater than its energy at rest E_0, is forced on a curved trajectory, it emits a strongly forward focussed radiation whose energies reaches the hard X-ray regime. This phenomenon has been independently observed by V. Veksler in

1944, and E. McMillan in 1945 [104]. The finite speed of light is independent of the system of reference, therefore the speed of an object can be expressed in relation to the speed of light using the Lorentz transformation. In the set of equation 4.1 for a particle of rest mass m_0, travelling with energy E at speed v, the relativistic factor β, and the Lorentz factor γ are defined. The former corresponds to the ratio between the actual velocity v and the speed of light c; the latter is defined as a function of β, and it is proportional to the energy E. The closer to the speed of light a particle travels, the bigger the Lorentz factor γ gets and the smaller the divergence of the emitted radiation, defined by the angle η.

$$\beta \equiv \frac{v}{c}$$
$$\gamma = \frac{E}{m_0}c^2 \equiv \frac{1}{\sqrt{(1-\beta^2)}}$$
$$E_k = E - E_0 = (\gamma - 1)m_0 c^2$$
$$\eta \propto \frac{1}{\gamma}$$

(4.1)

The ultrarelativistic regime is reached when the kinetic energy E_k of a particle is greater than its energy at rest E_0. Following from the latter simplified explanation, the most suitable elementary particles to be accelerated in terms of required energy are electrons (or positrons), due to a small $E_{0,el}$ = 512 keV [105].
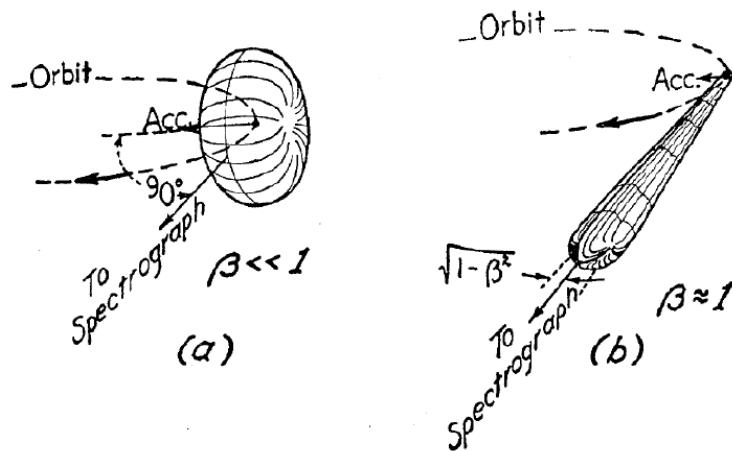
Figure 4.1: Photon angular distributions for two values of the relativistic factor β with divergence angle η in evidence: a) nonrelativistic electron in the particle rest system, η is large; b) relativistic electron in laboratory frame, η is smaller. It is possible to switch between two systems using a Lorentz transformation [105].

The radiation fields of emission of a particle subjected to an acceleration exhibits a strong vectorial dependency on the particles´ directions of motion, the magnitude and direction of the acceleration, and the direction of observation. The angular distribution of the emitted radiation resemble a Hertzian dipole at nonrelativisity velocities, as shown in the panel a of Figure 4.1: the probability of photon emission is in this case rotationally-symmetric around a centripetal acceleration vector (usually induced by a magnetic B-field). When a charged particle approaches relativistic speeds resulting in larger γ values, the emission pattern becomes highly forward collimated within an angle η of few mrad along the electron propagation direction as shown in panel b of Figure 4.1. In the latter case, the wavelength of the emitted photon becomes much shorter compare to the nonrelativistic case, due to relativistic space-time contraction. As a consequence, it is possible to emit highly collimated photons in the hard and soft X-ray regime in a reliable and continuous way.

4.2 Structure of a synchrotron facility

A synchrotron light facility produces photons over a very wide energy range, from IR (1 eV) to hard X-ray (10 keV) which are delivered to the users through specialised beamlines, as sketched in Figure 4.2 for the SOLEIL synchrotron light facility (Saint Aubin, France). New facilities output high brilliance, highly monochromatic SR, which can be arbitrarily highly-polarised; this type of SR exhibits (partially) transverse spatial coherency, and comes in pulses with length between 3 and 200 ps (shorter pulses are achievable, but at the cost of a dramatic reduction in intensity [106]). Synchrotron facilities are usually ranked according to specific figures of merit referred to the produced photons such as total flux (photons s^{-1}), spectral flux per unit of bandwidth BW (photons s^{-1} 0.1% BW^{-1}), brightness (photons s^{-1} $mrad^{-2}$ 0.1% BW^{-1}), brilliance (photons s^{-1} $mrad^{-2}$ mm^{-2}), where the bandwidth BW is defined as $\Delta\lambda/\lambda$. The intensity at the sample per unit of BW (photons s^{-1} mm^{-2} 0.1% BW^{-1}) is the result of a combination of the

synchrotron specifications and the efficiency of the specific beamline optics. The brilliance for the SOLEIL synchrotron light facility is reported in Figure 4.3 for all the beamlines.
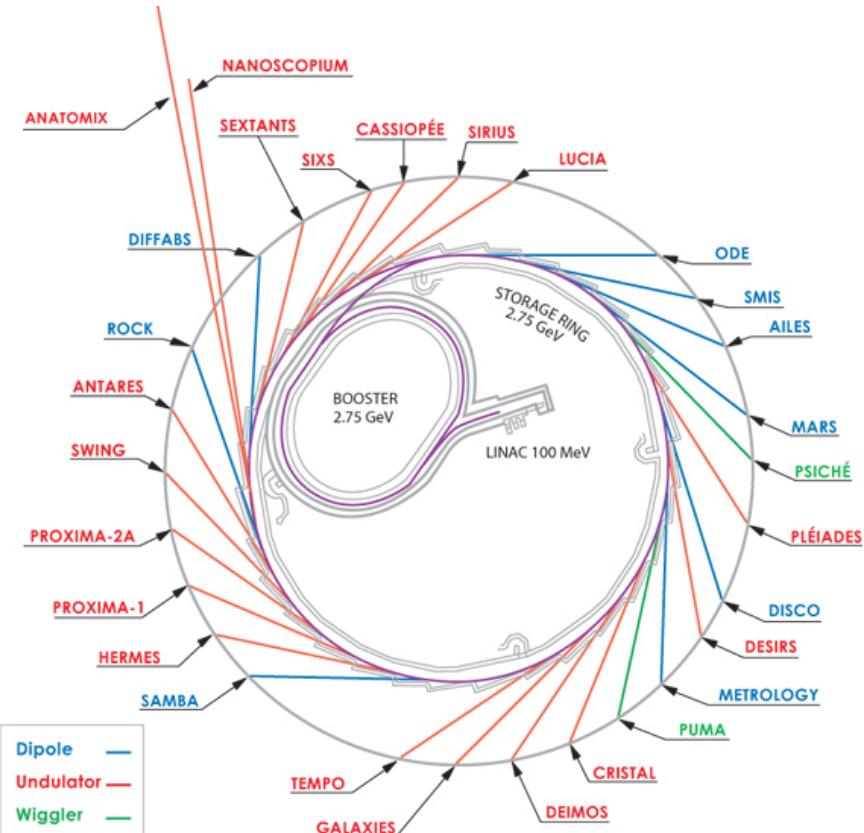
Figure 4.2: Sketch of SOLEIL synchrotron light facility. Each beamline is colour coded with the respective type of insertion device magnet. Some beamlines have more than one insertion device to cover larger ranges of photon energies. The acceleration and boosting devices are operating at 2.75 GeV, feeding a storage ring of 113 m diameter. Image courtesy of SOLEIL.

In a synchrotron facility, the electrons are initially created by an electron gun and modulated into bunches. At first, a linear accelerator (LINAC) accelerates each bunch by using a strong electric E-fields parallel to the electrons' propagation direction. In the LINAC, the electrons are accelerated by a series of radiofrequency (RF) cavities to $\gamma = 100$ corresponding to a speed of 99,9995% of c and E_k in the MeV range, already above the transition value for electrons. Then the electrons are injected into a circular device composed of a custom RF cavities and several bending magnets called the booster ring; here electrons are accelerated by just a small percentage (at about 99,999995% of c), which corresponds to a large γ, resulting in an increase of E_k to a range of $1 - 8$ GeV. However, beams at higher

energy are prone to beam divergence which reduces the brightness of the emitted SR, requiring stronger and more expensive magnets and a larger RF system to replace SR energy losses.

Subsequently, the electrons go into the storage ring and are kept circulating at ultrarelativistic speed. Several more RF cavities and several types of bending/correcting magnets are placed along the storage ring to impose and maintain the trajectory of the electrons (e.g., transversal momentum) such as dipole, quadrupole and sextupoles magnets. The first type of magnet keeps the electron trajectory within a tolerance value, the former is used as electromagnetic focussing lenses, the latter corrects aberrations occurring from electrons with different energies; for more complex corrections, octupoles could be implemented [105]. The interaction with magnets and the collisions of electrons with the residual gas and within the same bunch induce the electrons to radiate, deviating from the optimal trajectory and eventually escaping the bunch. Therefore, the ring is constantly refilled of electrons to keep the ring current up to of approximately 35 mA.

The primary source of SR are arrays of insertion devices e.g., wigglers and undulators, but dipole magnets could be used as well. Insertion devices have two parallel planes of multiple metre long arrays of magnets, arranged in periodic patterns, usually separated by a small gap. Electrons coming from the storage ring are forced through a sinusoidal magnetic B-field of period λ_0 under the influence of high static magnetic B-field between $1 - 2$ T. In Figure 4.4 the most advanced type of undulator, the Advance Planar Polarized Light Emitter II (APPLE II), is sketched along with some polarization schemes described later in this chapter.

Insertion devices are characterized by a deflection parameter K, alternately called strength parameter, described as

$$K = \frac{e}{2\pi m_e c} B \lambda_0 \quad .$$

(4.2)
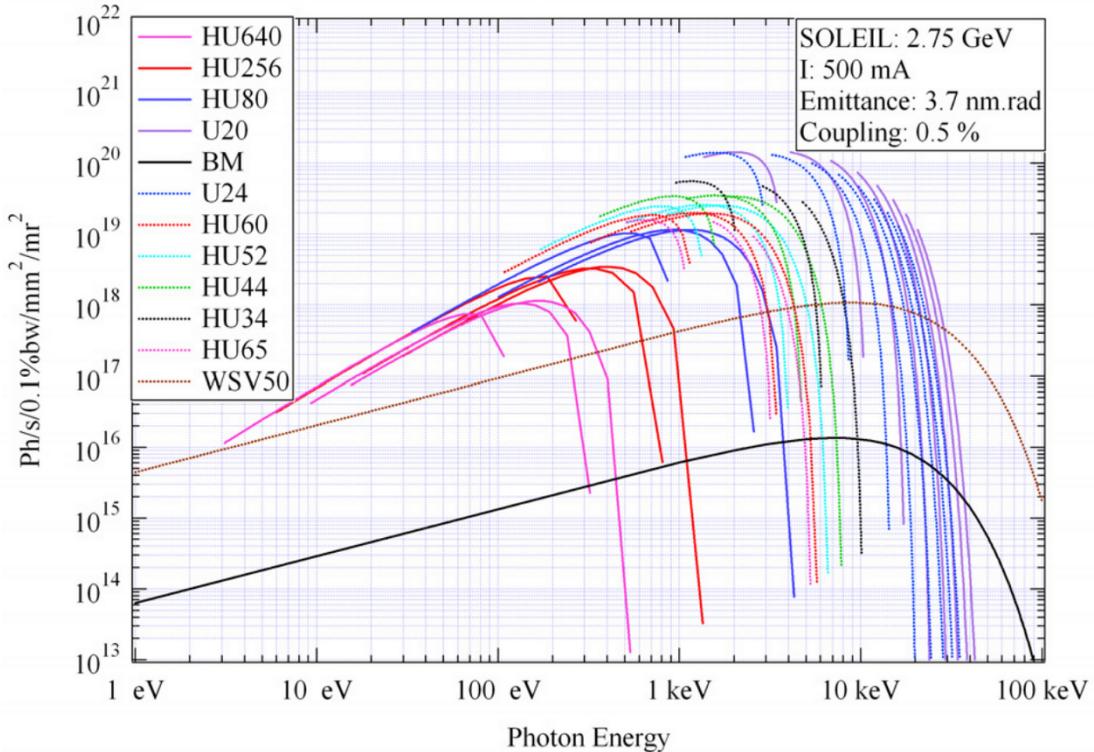
Figure 4.3: average predicted brilliance of the SOLEIL insertion devices: HU640, HU256 electromagnetic undulators of 640 mm and 256 mm periods for the long wavelength region; HU80 to HU36 elliptically polarized undulators of 80 to 36 mm periods for the VUV and soft X-ray region; U20, U24 in-vacuum undulators with shorter periods 20 and 24 mm; for radiation at several keV; U18 cryogenic in-vacuum undulator operating at 77 K for higher remanent field and coercivity; WSV 50 in-vacuum wiggler of 50 mm period for extension to higher energies; W164 out of-vacuum wiggler for 164 mm period. SRW calculations performed with an emittance of 3.9 nm rad, 1% coupling, 0.1% energy spread. Image reproduced from [16].

Values of $K \gg 1$ are typical for wigglers, and imply large deflections of electrons which appear to be independent emitters: their emission is completely incoherent at all frequencies and therefore the emission spectrum is almost continuous peaking in brilliance at the critical wavelength. On the contrary, values $K < 1$ are typical for undulators and the smaller deflection allows the electrons to emit preferentially in their propagation (forward) direction, inducing constructive interference of the partially coherent emitted waves. The final spectrum associated with an undulators has several orders of outstanding odd harmonics, which are several orders of magnitude higher in brilliance compared to the one merging from a wiggler.

By longitudinally moving two opposing arrays of magnets with respect to each other, the strengths of the vertical and horizontal magnetic B-field components

can be varied, inducing a phase shift between the respective components of the electron wave. Tuning the relative position of magnets, the produced photons can be polarized vertically, horizontally, and circularly as briefly sketched in Figure 4.4 (for more details about CPL polarization see appendix B.1).
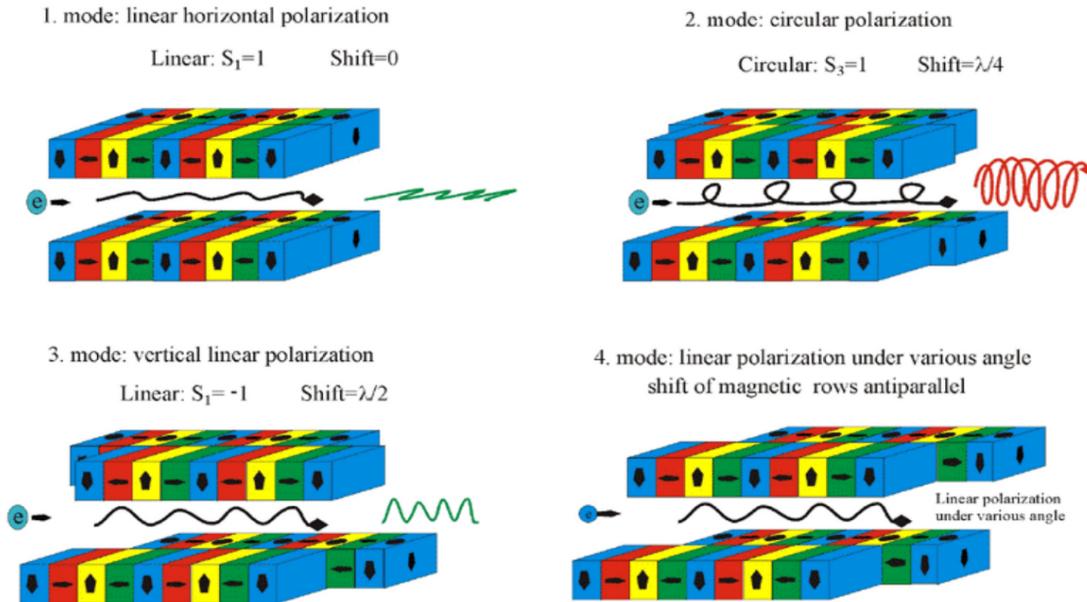
Figure 4.4: sketch of APPLE II undulator polarization schemes and corresponding arrangement of the magnetic arrays. For a description of the degree of polarization P and Stoke´s parameters see B.1. Image reproduce from [107]

Along each beamline there are dedicated optical elements. The desired photon energy can be adjusted using monochromators using diffraction gratings with tunable resolving power $R = \lambda / \Delta \lambda$ from 10^1 up to 10^6 [108]. The position and the focus of the photon beam can be tuned using water cooled switching and refocusing mirrors, and horizontal and vertical slits are used to reduce the absolute beam intensity.

There are several time structures for the electron bunches, called filling modes or patterns, which consist in the disposition of electron bunches along the storage ring. The most used scheme for tof spectroscopy is the n-bunch mode with n bunches of electrons regularly spaced along the storage ring with n = 1, 8, or 16, usually. The time in between to bunches is the period of the so-called "bunch marker", a signal generated when a bunch is passing through a specific cavity and

continuously recorded to determine the tof of particles. For experiments performed with a COLTRIMS apparatus, it is particularly important to provide a mode with n ≤ 16 to correctly correlate the tof of electrons and the much longer tof of ions for a given ionization event, thus providing a sufficiently long time between two bunches; further details on the synchrotron parameters are given in chapter 4.5.3.

4.2.1 Coherency

In undulators, the highly forward directed emission of the photon in combination with only weak deflections of electrons allows for a certain degree of spatial coherence, although usually electrons in bunches are independent emitters (i.e., uncorrelated) and the resulting emitted photons are usually incoherent, too. Two types of coherency exist: spatial (or transversal) coherence, and temporal (or longitudinal) coherence. The spatial coherence is related to the distribution of the electrons of a bunch in momentum-position space, the so-called phase-space: the smaller the size of the source and the more forward-focussed the emission, the higher the degree of spacial coherence, down to the diffraction limit. This lower limit constrains the achievable wavelengths for a desired spatial coherence value. The temporal coherence is proportional to the ratio of the emitted wavelength and the length of the electron bunch: the shorter the wavelength with respect to the length of the bunch, the lower the degree of temporal coherence [109]. Therefore, for X-rays (both soft and hard), the degree of spatial coherency that can be achieved is limited. The smooth transition between different degrees of coherence is described practically by the coherence length: the distance over which the phase difference between two photons is small enough to keep the waves interfering. A typical spatial coherence length for SR in the soft X-ray regime can be several micrometres in the horizontal and more than 100 µm in the vertical direction [109], but the degree of coherence is 1% and 40% for the horizontal and vertical directions respectively [109]. Compared to SR, fourth-generation free-electron LASERs (FELs) provide a full coherence (both

spatial and temporal) thanks to the small size of micro-bunching of the electrons kept below the diffraction limit [110]. The latter condition is achieved by particular settings in a custom LINAC while preparing the electron bunches for a progressive micro-bunching occurring in the long undulators used.
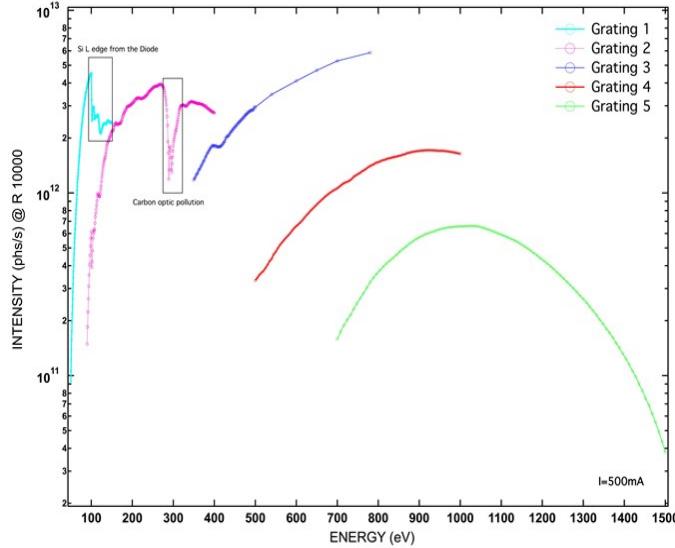

Figure 4.5: Intensity of the photon flux at different energies provided by different gratings (1 – 5) at a ring current of 500 mA; typical value for the 8-bunch mode is 100 mA. Image reproduced from [111]

4.2.2   Beamline SEXTANT

The present work has been conducted at the synchrotron facility SOLEIL at the SEXTANT beamline sketched in Figure 4.2 and Figure 4.6, respectively. During all experiments, the facility worked in "8-bunch" mode with a bunch spacing t_{BM} = 147.5363 ns. Details on the specific measuring schemes for each experiment are reported in chapter 4.5.3.

The SEXTANT beamline is dedicated to polarized soft X-ray scattering experiments, and it covers the range 50 – 1000 eV range with two different undulators (HU44 or HU80) with a high resolving power greater than 10^4. The intensity of the photon flux as function of the photon energy is reported in Figure 4.23. At the waist of the focus with the horizontal and vertical slits opened at h = 40 μm, and v = 10 μm respectively, the full width at half maximum (FWHM) of the beam is horizontal 17.3 μm and vertical 7.4 μm [112]. The degree of circular polarization is estimated to be S_3 > 90% [112]. The experiments presented in this

work use both slits opened in the range 75 – 100 μm to increase the count rates, but slightly decreasing the resolution along the tof direction (see chapter 4.7).
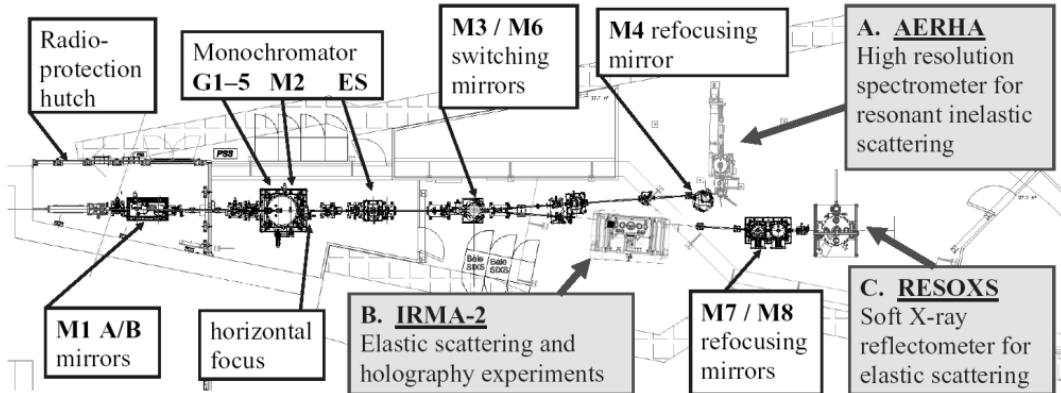
**Figure 4.6:** Sketch of the structure of SEXTANT beamline. Image reproduced from [112].

4.3 COLTRIMS

The COLTRIMS technique has been originally developed to measure the momentum transfer in collisions of fast, highly charged ions with atoms [113]. COLTRIMS has been used to study targets ranging from single atoms [114], dimers and tetramers [115], [116], up to molecular liquids [117]. This technique can be used in combination with a wide range of photon sources as SR [118], strong-field LASERs [57], [119]–[121] and free-electron LASERs (FEL) [99], [122]. For molecular targets, COLTRIMS has been used to investigate ionization dynamics in multiple regimes such as direct ionization [81], double-ionization [123], [124] and Auger electron emission [125], [126] achieving fully resolved PADs in molecular frame [74], [127], [128] and the determination of the absolute molecular structure of small chiral molecules [129]. The selected citations can be complemented with an in-depth review of the last 30 years of developments of COLTRIMS [130]; for a focus on the challenges of the transition from atomic to molecular targets the reader is invited to refer to [131].

The apparatus is based on time-of-flight (tof) spectroscopy principles, and it is capable of indirectly measuring the enlarged 3D momentum spheres (e.g., Newton spheres) of both electrons and ions emerging from an ionization or

a scattering process in coincidence [132]. Particles' momenta are obtained by measuring the position of impact on a detector and tof of each particle. The measured momentum gives access to many derived quantities (e.g., emission angles, energies, etc.) measured in coincidence. The technique is capable of kinematically complete experiments up to the spin of electrons, and it is often included to the realm of electron momentum spectroscopic imaging techniques [133].

A common alternative technique to COLTRIMS is the Velocity Map Imaging (VMI), which is often used due to its high energy resolution and simple implementation. In contrast to COLTRIMS, VMI relies on a 2D-projection of the particle's Newton spheres, as described more extensively elsewhere [134].
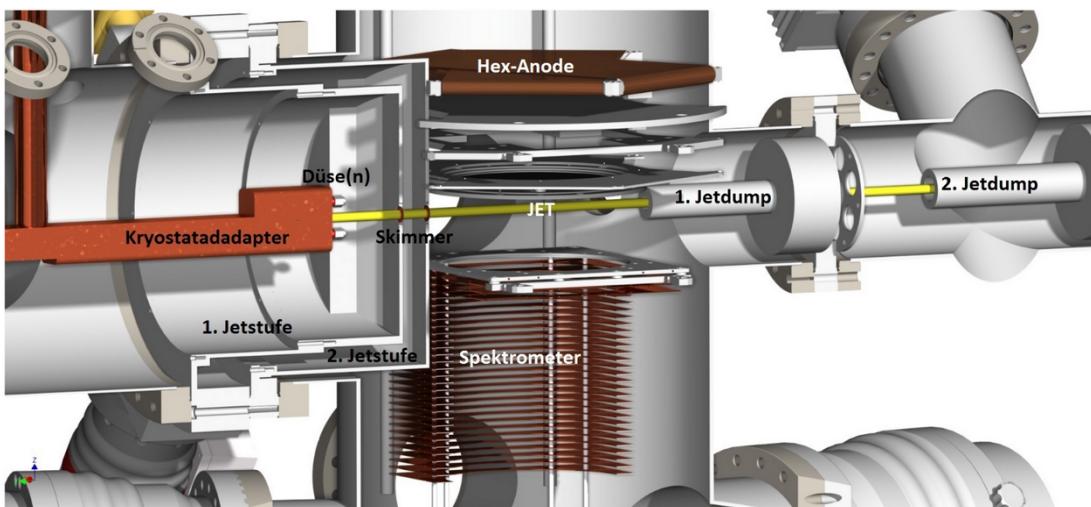
Figure 4.7: Section of the COLTRIMS chamber (from left to right): cryogenic arm from the reservoir with nozzle; two expansion stages with skimmers; main chamber with spectrometer and detectors; two dump stages. All stages are served by turbopumps of various pumping speeds. Image reproduced from [135].

4.3.1 Supersonic jet

A COLTRIMS system typically employs a thermalized supersonic molecular beam with a narrow velocity distribution. As shown in Figure 4.7, a target gas passes from a high-pressure reservoir $p_0 = 1 - 30$ bar into an expansion chamber kept at pressure $p = 10^{-3} - 10^{-6}$ mbar through a small nozzle with a diameter of 10 to 100 μm. In such conditions, an adiabatic expansion of the gas symmetric around the propagation axis occurs, as at first observed by Otto Stern in 1922 [136].

If the difference of pressure between the reservoir and the expansion stage is high enough, the volume in front of the nozzle will be characterized by an essentially laminar-supersonic regime with Mach number[13] M >> 1, where the effect of the lateral and frontal shock waves on the core of the volume is negligible. The latter volume extends for a distance proportional to the ratio of the pressure (7-mm nozzle-skimmer distance) and it is called the zone of silence, as presented in panel a in Figure 4.8. The resulting molecular jet has a well-defined Maxwell-Boltzmann distribution around supersonic translational velocities, whilst the internal temperature on all degree of freedom can reach few K without further cryogenic external cooling of the nozzle.

For the experiment presented in this work the nozzle diameter was 100 μm and two skimmers were used for collimation of the jet, each with a 300 μm diameter.

4.3.2   Adiabatic expansion

If the size of the nozzle is bigger than the mean free-path of the molecule in a gas at temperature T_0 (i.e., non-effusive gas), an adiabatic cooling of all degrees of freedom[14] takes place due to the high rate of collisions in the expansion region. Enthalpy is therefore converted into kinetic energy during the adiabatic expansion, leading to supersonic beam of translational supersonic velocity v at temperature T. as described in equation (4.3).

$$\frac{1}{2}mv^2 = H_0 - H = m\int_{T}^{T_0} C_p \, dT \qquad (4.3)$$

Assuming a constant thermal capacity at constant pressure c_p, it is possible to define the adiabatic coefficient $\gamma = C_p/C_v = (f+2)/f$ where f is the number of degrees of freedom of the molecular system. Due to the difficulties in measuring

---

13   The Mach number M is defined as the ratio of the transnational speed of particles and the local speed of sound.

14   The effective cross-sections of the energy transfers of the elastic collisions and the rotational and vibrational excitations due to inelastic collisions are different: the various degrees of freedom have different degree of cooling: T translation <T rotation <T vibration.

the density and the exact translational velocity v of the jet, it is convenient to define the speed ratio S, used instead of M, as

$$S \equiv \frac{v}{\sqrt{2 k_b T / m}} \quad .$$

(4.4)

The relationship between the nozzle diameter d, the reservoir pressure p_0, and the speed ratio S can be empirically determined [137]. It is therefore possible to estimate the final temperature after the expansion as

$$T = T_0 \left(1 + \frac{\gamma - 1}{\gamma} S^2\right)^{-1} = T_0 \left(1 + \frac{2}{f+2} S^2\right)^{-1}$$

(4.5)

from whom in the zone of silence S >> 1, for the case of an atom with three degrees of freedom f = 3 the approximation $T \simeq 2,5 \, T_0 S^{-2}$ can be derived.
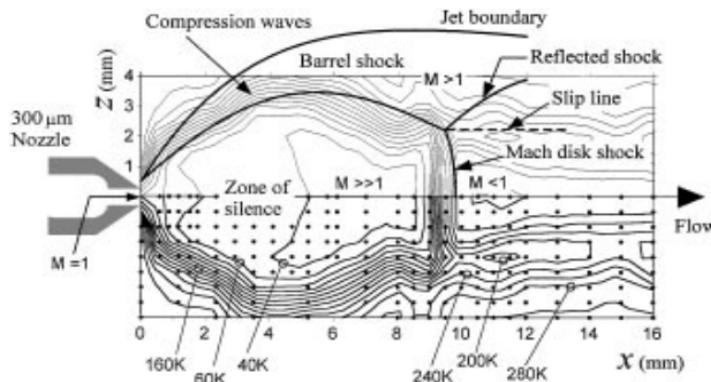
Figure 4.8: Raman mapping of rotational temperatures in a supersonic jet of CO_2 under a stagnation pressure of 2 bars in proximity of the nozzle. Isothermal lines are depicted at steps of 20 K. Several areas are identified by the value Mach number M. The skimmer has to be mounted closer than the Mach disc shock which then gets deformed in the real usage. Images reproduced from [138].

However, the heat capacity c_p for molecules is generally not constant during an irreversible expansion because the lower the temperature, the fewer degrees of freedom for rotational and vibrational excitations can be occupied. For the molecules investigated in the present work, it is therefore difficult to precisely calculate the thermal contribution to the momentum broadening, and it will decrease the final momentum resolution. In many experiments performed with COLTRIMS, the nozzle can be cooled with the aid of a cryostat to lower the final temperature T and achieve an higher jet density. For molecules whose vapour pressure at room temperature is already below the atmospheric pressure

(e.g., both MOx and TFMOx), further cooling would clog the nozzle because of solidification. To select the central part of the jet, the tip of a first skimmer (300 μm diameter) reaches directly the zone of silence. A second (and eventually a third) skimmer is used to further refine the temperature profile perpendicular to the propagation direction, ensuring a sharper Maxwell-Boltzmann distribution around the selected translational velocity, at the expense of a lower density of the beam at the target region.
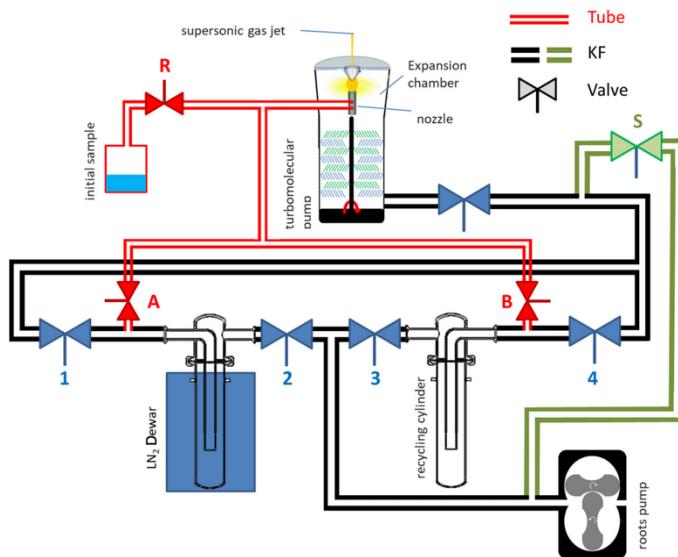
Figure 4.9: Sketch of a cold trap recycling system. The circuit in red is the reservoir: the first run (and refilling) uses the initial sample and after A or B valve are alternatively open. The circuit in black is connected to the exhaust and works alternatively with one of the cylinders after the valve 1 or 4. At any given time after the first cycle, one cylinder in a Dewar flask with liquid N_2 is collecting the sample (black circuit) and the other one left at T_R is the new reservoir (red circuit). Valves 2 and 3 are connect the system to a roots pump used to remove the carrier gas after solidification of the sample and are alternatively close (i.e., black and red circuit are in a loop). The nature of the samples used in this work allow to run the recycling without the roots pump turned on. Image reproduced from [139].

The nozzle can be moved in all three spatial directions in respect to the skimmers using manipulators for alignment purposes, maximizing the target density and pressure. In the weak-field regime of SR, the higher the density of the target, the higher the detection count rates, without limitations[15]. After the second skimmer, the molecular jet crosses the photon beam with a typical target density between $10^{11} - 10^{12}$ cm^{-3}, and a local pressure between $10^{-5} - 10^{-4}$ mbar.

---

15   Using sources such as LASER and XFEL in the strong-field regime, the density of the target has to be carefully controlled through the design of the apparatus to avoid the complete ionization of the residual gas and the consequent dramatic increase of the background signal.

The cylindrical overlapping geometry depends on the size of the beam and photon beam (see chapter 4.2.2).

4.3.3 Recycling system

When running at typical pumping speeds to maintain the ultra-high vacuum, the turbopumps at the expansion stages of COLTRIMS account for more than 99.9% of the total gas load of sample, which is removed from the apparatus. The consumption of custom-made, rare and toxic samples as the TFMOx is usually the bottleneck for long experimental campaigns. The COLTRIMS system used is equipped with a recycling system connected to the turbopumps at the expansion stages, sketched in Figure 4.9. The gas extracted by the turbopumps passes through a cold trap made of glass cooled in a liquid nitrogen and undergoes solidification. When the initial sample is used up, a condition determined by a detection of lower event rates on the detectors, the traps are left at room temperature and become the new reservoirs. The process has a recycling efficiency per cycle of more than 95% [139].

4.4 Spectrometer design principles

The core of the COLTRIMS apparatus is a spectrometer with two position sensitive detectors (PSD) for ions and electrons, respectively. In the simplest scenario, after a target is photoionized and a CE occurs, the emerging photoelectrons and positively charged ionic fragments are projected separately onto the detectors using tunable homogeneous electric E and magnetic B-fields. The initial momentum of the photoelectrons depends on the energy of the incoming photon, and the ionic fragments have the same momenta, thus their velocities are inversely proportional to their masses, as described in chapter 3.4. A general goal of the spectrometer design is to maximise the illuminated area onto each detector, and for a kinematically complete experiment, to achieve 4π solid

angle of detection for all fragments. The design of the spectrometer can greatly vary upon the physics of the system under investigation and the minimum required resolution for both detectors, but usually is based on time and space focusing (i.e., 3D focusing) geometry. As already mentioned, oppositely charged particles are accelerated in two opposite directions along the two arms of the spectrometer. Each arm can be subdivided in a custom arrangement of regions, namely acceleration (deceleration), drift and possibly deceleration. In the acceleration (deceleration) region, a voltage is imposed across a stack of equidistant copper plates, each connected by 1 MΩ resistors, creating a homogeneous E-field with the right polarity to accelerate (decelerate) particles. The drift region is E-field-free, and it is used to magnify the Newton spheres to macroscopic dimensions.

In general, very energetic (i.e., fast) electrons need a homogeneous B-field to be confined in the spectrometer volume and to be guided to the detectors along the tof direction (for details on the system of reference see appendix B.6). The B-field is generated by a pair of Helmholtz coils mounted outside the vacuum chamber, has a magnitude up to 10 Gauss, and it is applied parallel to the E-field. The resulting Lorentz force guides the electrons on a gyration movement of period T_{gy} on a plane parallel to the detector (i.e., x- and y-axis), with an increasing higher pace on the tof direction (i.e., z-axis). The gyration period T_{gy} is independent of the initial momentum in x and y direction, therefore at tofs which are integers multiples of T_{gy} there is no momentum resolution along these axes. To overcome this problem, the expected electron tof distribution should lie entirely within a single gyration period T_{gy}. To achieve this condition, a complex combination of spectrometer design and a careful tuning of the B-field is required, which lets achieving a 4π geometrical solid angle of detection of photoelectrons for a fairly broad range of electron's kinetic energies. In some specific cases, the use of a B-field can be avoided, and an electrostatic lens combined with carefully designed E-field can be used. In general, using a B-field (either weak or strong) in combination with electrostatic lenses induces non-linear distortions due to

coupling of E- and B-field. The coupling is proportional to the angle between E- and B-field: the strength of the distortion increases radially from the axis of the spectrometer because of the lens curvature, as described in detail in chapter 4.7.

In general, the tof depends on the initial particles' momentum and their starting position within the interaction volume. To let particles with equal momentum but different starting positions arriving at the same time at the detectors, a time-focusing geometry is used. A common geometry is the Wiley-McLaren focusing which consists in a length-ratio 1:2 of acceleration and drift regions [140]. As already pointed out in chapter 4.2.2, the photon beam has a Gaussian distribution with lengths measured FWHM of h = 40 μm and v = 10 μm; both lengths are directly proportional to the aperture of the beamline slits, and the interaction volume can be approximated to a thin rectangular cuboid instead of an ellipsoid.

In the direction parallel to the position sensitive detector, the impact position of a particle depends on its velocity and its initial position within the ionization volume. The dependence on the initial position can be reduced by inserting an electrostatic lens: a spatial focusing geometry is in fact used to focus particles with the same kinetic energy, and it is implemented with the use of electrostatic lenses. A perfect lens has a focusing force that is linear with the radial distance from its symmetry axis, i.e., the centre of the lens. Because of the nature of the electrodes, the curvature of the equipotential potential surfaces orthogonal to the E-field is not perfectly radial. Such electrostatic lenses can cause spherical aberrations on high kinetic energies particles (i.e., further away from the lens' axis), a phenomenon especially relevant for strong lenses (i.e., high voltage difference between two subsequent electrodes). Therefore, the use of lenses should therefore be restricted to particles with little kinetic energy (i.e., travelling in a region close to the centre of the lens). Further electrostatic distortions appear when the B- and E-field are not parallel (i.e., E-B coupling), a condition naturally occurring in proximity of the electrodes (i.e., far from the axis of the lens). Such types of distortions are extremely decremental for the extraction of the electron

momenta and are difficult, if not impossible, to be corrected during the analysis (see chapter 4.7 for details on the lens correction).

A focusing lens is usually followed by a custom compensation acceleration (i.e., $\Delta V > 0$) and/or deceleration (i.e., $\Delta V < 0$) sections. It is worth to mention that the presence of an electrostatic lens increases the length of the drift section which compensate for the particles´ acceleration gained across the lens itself. A common way to separate regions with different E-fields is to use meshes. In fact, a thin stainless steel metal mesh (30 – 100 μm hole size) could be installed between acceleration and drift regions avoiding a lens effects at the interface between two regions. Meshes can be also installed few millimetres in front of the front MCP to allow for a high post-accelleration field, sensibly increasing the detector efficiency (see chapter 4.4.3). Although meshes have a transmission efficiency of 80 — 85%, they cause micro-lensing effects that lower the particles' position resolution, and in general could lead to a insufficient multi-hit detection efficiency. Other sources of distortions arise from inhomogeneities in the spectrometer field usually due to tolerances of about 1 mm in the mounting process, unstable spectrometer voltages due to instability of the high-voltage power suppliers, a shift of the reaction volume along the z-axis due to misalignments with the waist of the photon beam (see chapter 4.7), and electric mirroring of electrical signal across the spectrometer (e.g., "cross-talking").

4.4.1 Spectrometer SEXTANT

The spectrometer used in this work has a Wiley-McLaren time-focusing geometry and an electrostatic lens for each arm, sketched in panel a of Figure 4.10 along with equipotential curves and calculated trajectories for both electron and one ion (m = 69 amu). At the electron side there is an extra deceleration section after the electrostatic lens, followed by a short drift. The spectrometer is mesh-free to maximise the multi hit capability, and it is designed to work without B-field. The voltage scheme is presented in panel b of Figure 4.10.
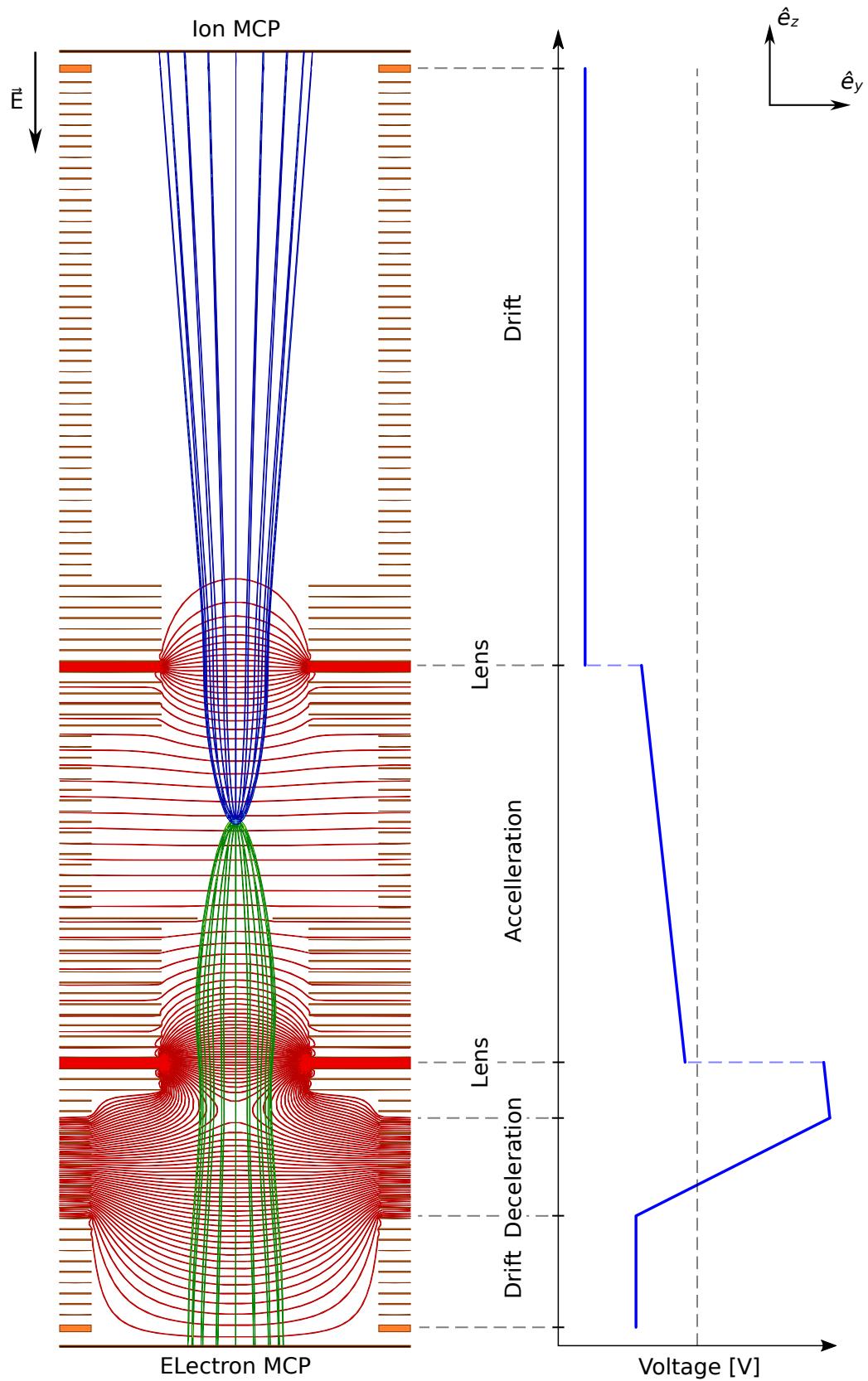
Figure 4.10: Spectrometer designed by K. Fehre and S. Grundmann. Left: sketch of the particles trajectories (blue ions, green electrons) and equipotential curves (red); right: the voltage scheme of the spectrometer used for the experiments in chapter 5. The simulations were done using the SIMION® software [166].

4.4.2 Detectors

A COLTRIMS apparatus for coincidence measurements has two time- and position-sensitive detectors (PSD), each constituted by a set of two micro channel plates (MCPs) and a delay line anode (DL).

The impact of an accelerated charged particle on the MCP's surface triggers an electron avalanche which amplifies the signal by the creation of an electron cloud. Moreover, the impact generates a fast signal with a typical shape due to short breakdown of the high voltage at which the MCP are kept. The latter signal in combination with an external BM timing is used to measure the time-of-flight (tof) of a particle, as further described in chapter 4.5.3. The impact position of the particle is determined by measuring the centre of gravity of the generated electron cloud on a multi-layered delay-line (DL) system; an example scheme of the full detector system with a two-layered DL (e.g., Quadanode detectors) is shown in Figure 4.11.
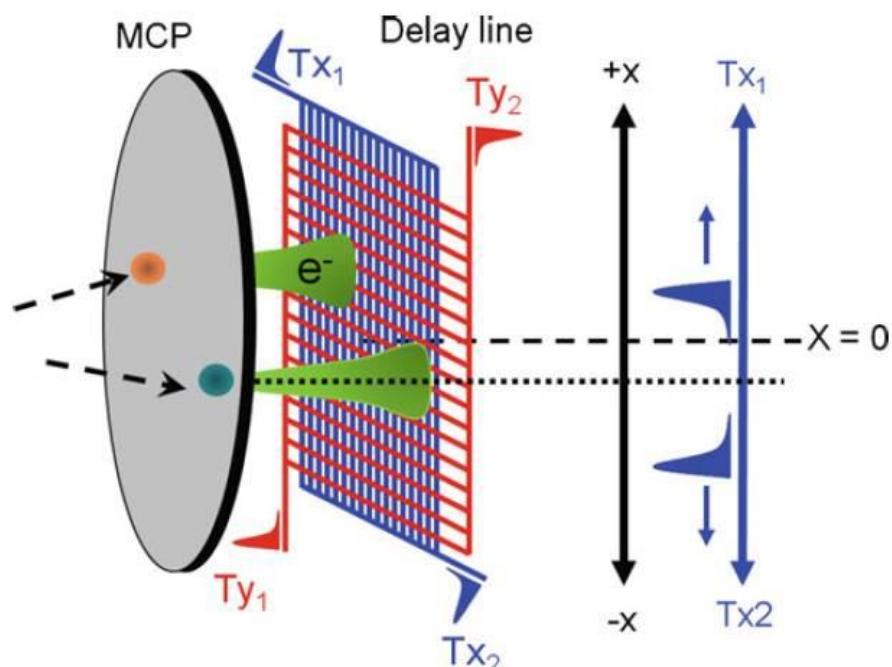
Figure 4.11: Sketch of a detector (anode). From left to right: a single MCP with two impinging particles generating two electron showers; two-layered DL (Quadanode detector) with signals sketched at their respective ends; the last two axis are an example, of the correlation between the difference in arrival times Tx_i and the absolute x position (i.e., blue layer on the DL) for one of the detected panicles. Image courtesy of RoentDek GmbH.

The detectors are internally self-calibrated due to the fixed length of each DL, but each of them is aligned arbitrarily with respect to the LF; for experiments without cylindrical symmetry, the alignment is performed after the data acquisition, using the procedure described in chapter 4.6.1. For the experiment presented in this work a mask with three indentations is mounted between the front MCP and the MCP holder to mark the absolute position of each detector, as shown in Figure 4.1. The usual aligning procedure for the ion detector relies on visualising the ionization of the residual gas along the photon beam direction; the presence of an electrostatic lens on the ion arm prevents the trace to be seen, thus the detector is aligned using the mask instead.

4.4.3   Micro channel plates (MCP)

A MCP is a silica disk made of millions of continuous micro electron multipliers (CEMs) built in parallel, coated with a semiconductor (e.g., CrNi), and kept at a voltage bias of several kV (usually $1.2 - 2.4$ kV between back and front surfaces). MCPs have been developed during the 1960s, and transversally adopted as fast, noise-free, high-gain CEMs after the declassification from military use in 1971 [141]. Charged particles[16] impacting the MCP front surface induce the ejection in the continuum of electrons from the coating material. The former electrons are then accelerated according to the MCP voltage, gaining more kinetic energy, repeating the process multiple times in a cascade effect. At the MCP back surface after a transient time of about 1 ns, an electron cloud emerges with a total gain of $10^5 - 10^8$ depending on the stacking geometry. MCPs are usually used stacked in two or three (e.g., Chevron or Z-stack, respectively), and MCPs with measuring quality grade are among the best choice for particles timing and counting purposes due to the fast response, high gains and medium lifespan; it is worth to remark that the gain of MCPs changes in time, making them consumable parts of the apparatus.

---

16   If a neutral particle (e.g., photon) has a kinetic energy high enough, it could promote an electron cascade too, but with a very low quantum efficiency.

The total gain is limited by the building up of standing currents along the walls of each pore, which is commonly referred to as the strip current of the multiplier. MCPs are non-ideal resistors of $12 - 15$ MΩ ($25 - 40$ MΩ in vacuum), therefore the strip current increases linearly with the bias voltage till a saturation point, where a further increase of bias voltage lowers the total gain. The achievable strip current is strongly influenced by the geometry of the pores, thus it should be maximized. Typically, MCPs channels have a length L = 1 mm, wit a diameter D = $2 - 25$ μm, and the aspect ratio which represents the effective channel length is $L/D = 40:1 - 80:1$. The channels are tilted with respect to the MCP surface by the bias angle α in the range of $8° - 20°$, crucial to mitigate the ion feedback effect[17] and to promote the collision of particle with the channel's walls. The higher the aspect ratio, the higher the voltage supported by the MCP and therefore the strip current (i.e., higher the gain). The former trend is limited by thermal issues due to the negative temperature coefficient typical of MCPs. Furthermore, both space- and time-resolution are proportional to the aspect ratio L/D with values smaller than 30 μm and shorter than 100 ps respectively [142]. The spatial resolution is usually limited by the DL. The maximum supported repetition rate is $1 - 10$ MHz, due to the local recovery time between $1 - 10$ ms for each pore, which nevertheless are independent.

The detection efficiency (also called quantum efficiency for electron detection) is defined as the percentage of input particles producing detectable pulses at the output. It is a complex function of many parameters like the mass and wavelength of the impinging particles, their impact kinetic energy, the bias voltage across the MCPs and the pores' geometry. To enhance the detection efficiency, particles are strongly post-accelerated to a kinetic energy of few KeV in front of the MCP. For a given particle and a bias voltage, the detection efficiency is a function of the open area ratio (OAR), which indicates the ratio of the MCP's channel open area to the total effective area. The OAR is itself a function of the pores' density and

---

17   The electron avalanche can ionize molecules of the residual gas adsorbed on the MCP's channels. Due to high voltage bias, the positively charged ions are accelerated towards the front surface (i.e., contrary to the electrons) inducing delayed secondary electron cascades, uncorrelated to the primary ones. The curvature of the electron multiplier with continuous dynode has been an attempt to mitigate the ion feedback.
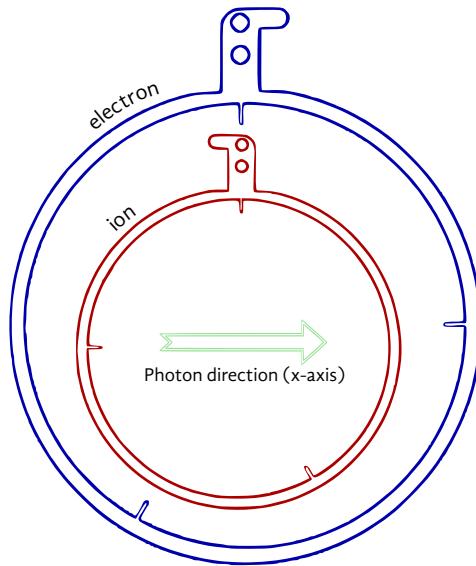
Figure 4.12: MCP masks as mounted viewed from the electron detector towards the target. The position images are produced with the same convention as shown in Figure 4.1.

diameter, as well as their geometry at the surface. For a given working voltage, the standard cylindrical apertures with OAR 70% has an absolute detection efficiency of 67%, but for a funnel geometry with OAR 90% the detection efficiency is 86% [143]. The difference between the two pore-geometries is shown in Figure 4.13. As a rule of thumb, the maximum achievable detection efficiency for any given MCP is 90% of its OAR. The detection efficiency decreases exponentially with the number of particle detected in coincidence, and it is inversely proportional to the measuring time. It is therefore crucial to maximize the multi-hit detection capability.
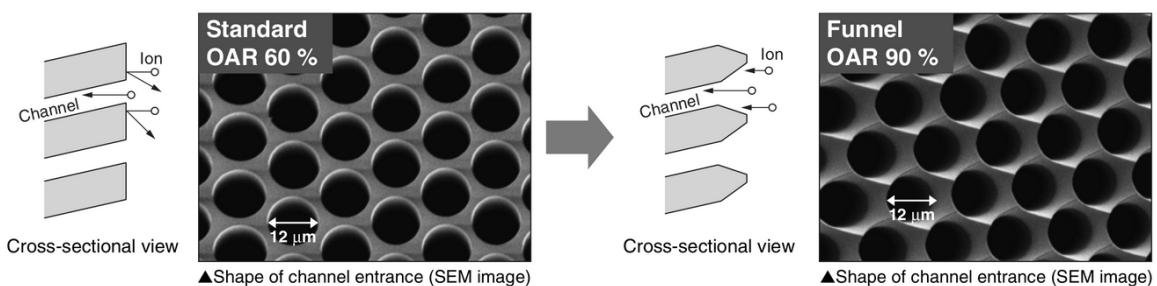
Figure 4.13: Scanning electron microscope (SEM) images ans section of standard (left) and a funnel (right) MCP surfaces. Image reproduced from [144]

For all the experiments in this work, the detectors have been built using pairs of funnel MCP from Hamamatsu, 75 mm in diameter, $D = 12$ μm; $D/L = 60{:}1$, $\alpha = 20°$ in a Chevron geometry to ensure the best multi-hit detection capability

61

[144]. In order to facilitate the mutual rotation of the detectors in the post-analysis, a thin copper mask with 3 asymmetric indentations has been mounted between the front MCP and the holder as sketched in Figure 4.12. The detectors characteristics are listed in Table 2.

Table 2: Detectors parameters for SEXTANT experiment.

	MCP parameters	**DL type**
Ion side (bottom side on chamber)	75 mm ø, F1942-01 (Mod 6) A010699 (Hamamatsu)	HEX125-Anode (batman 2/3)
Electron side (top side on chamber)	75 mm ø, 15M0023-16; 75/32/25/8; D60:1; NR60 OAR; 140 µA (Photonis)	HEX90-Anode

4.4.4 Delay lines

A delay line anode (DL) is a PSD capable of determining the x and y coordinates of a detected particle with respect to its centre measuring the difference in travelling time of two signals; it has a high position (< 50 µm) and time (< 100 ps) resolution with a theoretical throughput up to 5 MHz, typically 10 – 20 kHz in real experimental conditions. A Hexanode (RoentDek Handels GmbH [145]) is made of three layers each composed of two parallel copper wires[18] wound around a metallic support with ceramic insulators at the edges. When the electron cloud leaves the back of the MCP and lands on the DL, it generates a high-frequency electrical signal which propagates with a constant speed in both direction of the wire pairs [146]. The MCP amplification ensures that each electron cloud has a footprint much larger than the pace of the windings, therefore one signal is split into portions occurring on the same wire, but at different periods; these portions are delayed in time (circa 1 ns/mm) while travelling, merging into a single broader signal at the two ends. The final position is a centre-of-mass averaging of the sliced signals.

---

18   The wires are kept at a potential difference of ΔV = 50 V; electrons will preferentially be attracted by the more positive called the "signal", and the other one, called the "reference", is subtracted to improve the signal-to-noise ratio. For the sake of simplicity of the present discussion, just one wire will be considered.
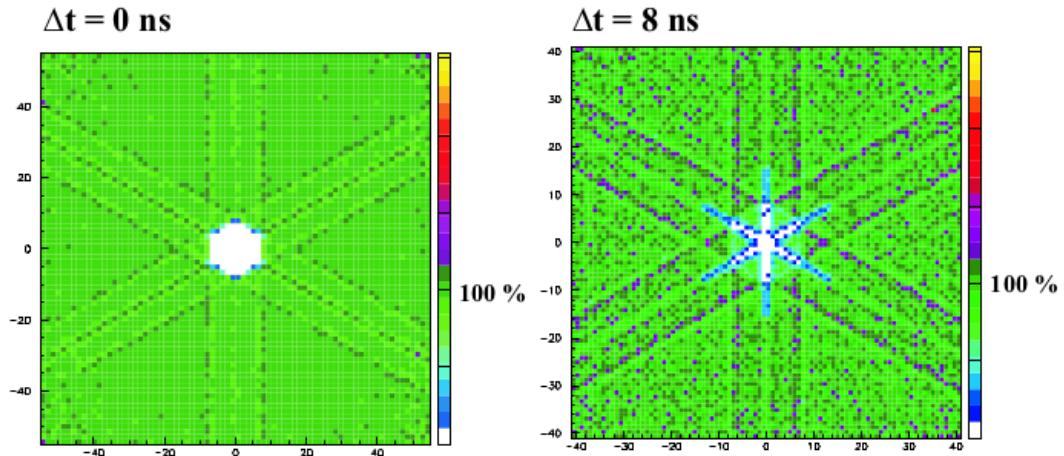
Figure 4.14: simulations of the multi hit detection capabilities of a Hexagonal DL for the case of two particles in fast succession. The first particle hits the centre, the colour coding shows the detection efficiency for a second particles that hits it after $\Delta t = 0$ ns (left), and $\Delta t = 8$ ns (right). Image reproduced from [165].

For each layer i separately, the time sum $t_{sum,i}$ is constant, and a Hexanode provides intrinsic linearity correction thanks to the redundancy of the third layer, as shown for both detectors in the left column of Figure 4.15. For each layer i, the time sum is calculated as the time difference between the measured runtime at each wire end e.g., t_{i1} and t_{i1} and the MCP time, as shown in equation (4.6)

$$t_{sum,i} = (t_{i1} - t_{MCP}) + (t_{i2} - t_{MCP}) = const \tag{4.6}$$

It is therefore possible to estimate the anode resolution as shown in the right column of Figure 4.15, whilst the remaining linearity deviations are less than 0.1 mm. Furthermore, the third layer brings the multi-hit dead-time to be less than 10 ns, greatly increasing multi-hit capabilities as summarized in the simulation of Figure 4.14. The spatial resolution of a detector using DL anodes is partly determined from the time resolution of the TDC, since the accuracy of the spatial measurement scales with the measurement of the respective signal propagation time (see chapter 4.5.2).

$$x_i = \frac{L_i}{t_{sum,i}} (t_{i1} - t_{i2}) \tag{4.7}$$

For each of the three layers i, the time difference between the two arrival times t_{i1} and t_{i2} is directly proportional to the spatial offset x_i of the centre-of-mass of each electron cloud from the middle of each winding of length L_i, as shown in

equation (4.7). The complete set of equations used to calculate the x and y coordinates of a particle using the three layers of the Hexanode are reported in appendix B.9.

In Figure 4.16 the merged results of the position calculation from the three layers are shown. It is worth to notice the homogeneity of the signal across all surface, due to the mint condition of the MCP: several factors can hinder some channels of the MCP to be active, leading to dead areas of amplification or to a leakage of electrons leading to a so-called "hot spot", here completely absent.
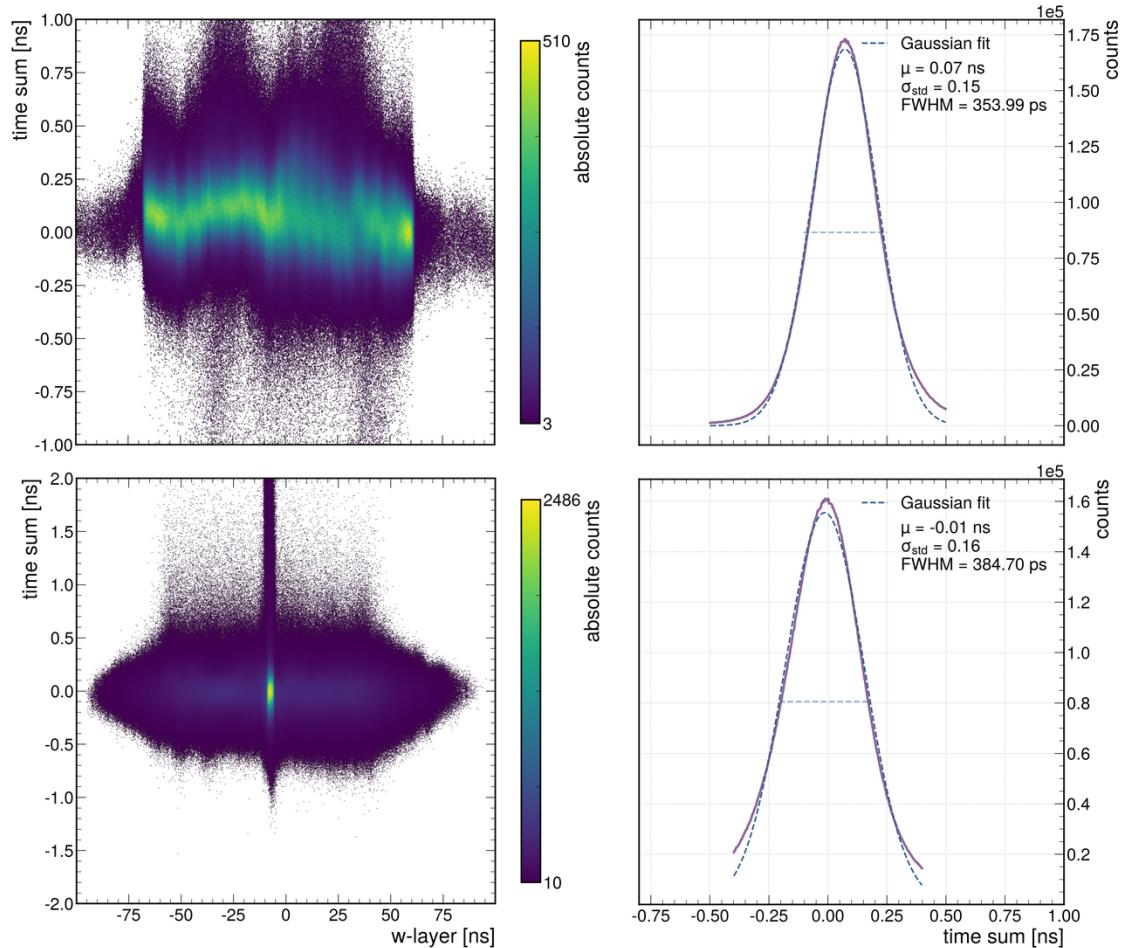
Figure 4.15: optimized time sums along the w-layer of a DL with gated projections to evaluate the time-resolution. On top the electron detector, at the bottom the recoil detector. The FWHM of the projections is the time-resolution of the w-layer, here around 354 ps, and 385 ps for electron and recoil DL, respectively. Note the strong presence of events at the centre of the distributions, especially for the recoil detector.
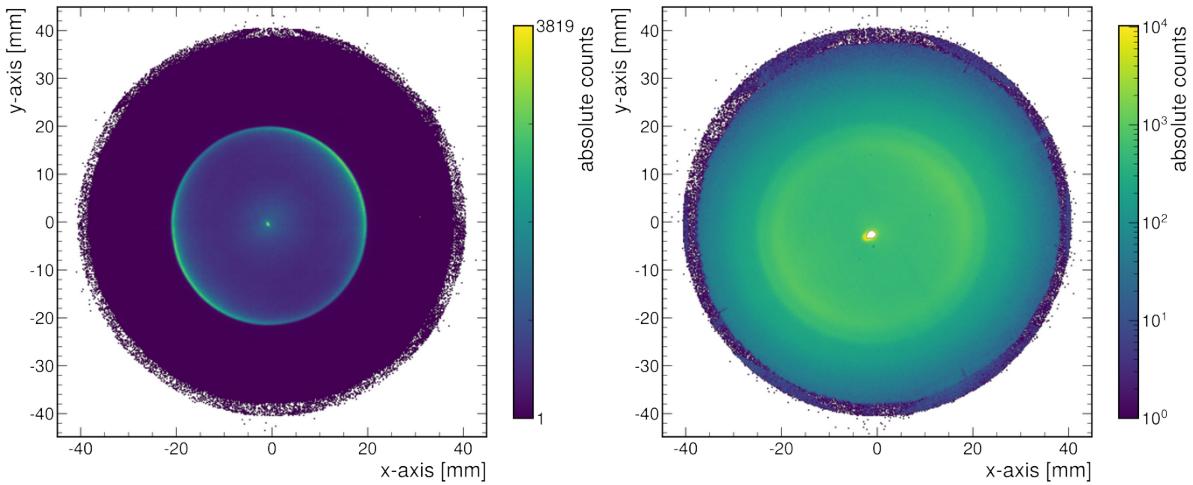
Figure 4.16: raw position image on both detectors. From left to right: electron and recoil detector. MCP marks (used for determine the detector orientation) are shown in Figure 4.22, but are already visible on the recoil detector (logarithmic scale). Note: the distribution on the recoil detector is here limited to 10^4 events.

4.5 Signal processing

The time signals for each detector are collected from the front (or back) of the MCP, and from both ends of each DL (e.g., three layers for Hexanodes), for a grand total of 7 signals (the difference between the reference and the signal is already occurred). All signals are initially amplified using the RoentDek fast amplifier FAMP6 which brings the signals with the adequate pulse-heights (i.e., any polarity) to 100 mV above the noise level with a nominal amplification factor of about 70 [145]. The front MCP signal is capacitively decoupled from the high voltage, and as the DL signal, it travels on a coaxial cable to minimize the electrical noise and to preserve the signal width. After amplification, the signals are discriminated and converted into square pulses with a Constant Fraction Discriminator (CFD) CFD8c from RoentDek [145]. The two sets of signals coming from the two anodes, and CFD processed bunch marker time t_{BM} (see chapter 4.5.3) are sent to a computer for digitization and further processing. The digitization is done by the Time to Digital Converter (TDC) TDC8HP from RoentDek through a Peripheral Component Interconnect (PCI) interface [145].

The acquisition and most of the recording parameters (e.g., the length recording window, size of the detectors, correcting tables, etc.) are controlled by a proprietary software called "CoboldPC", and the data are saved in list mode format (".lmf") which can be post-processed as it has been written.

4.5.1   Constant Fraction Discriminator (CFD)

Due to the statistical nature of the electron cloud coming from the MCP, the resulting signals have a very broad pulse height distribution. Thus, the timing (i.e., position) of the centre of gravity of the electron cloud on a DL cannot be determined by a simple threshold or leading-edge discriminator. The CFD creates a bipolar signal from the leading-edge of the monopolar input above a tunable threshold, whose zero-crossing is independent of the initial height of the input. A transition from "low" to "high" represents the zero-crossing of the bipolar signal, which can be fine-tuned from the zero-potential (different from ground) called "walk". The CFD output is a NIM signal[19] in the form of square-wave pulse with a height of -0.9 V and a width longer than 7 ns.
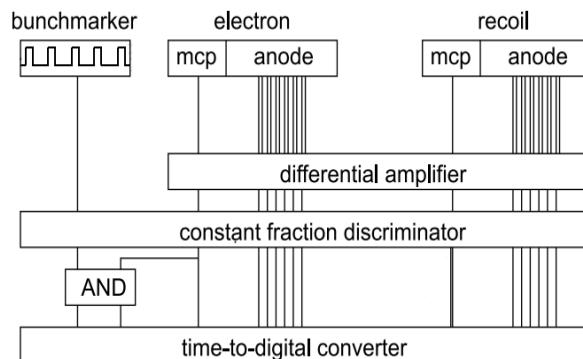
Figure 4.17: Sketch of the detection scheme of the signals with AND logic. The recoil front MCP signal is used as a general trigger signal fro the TCD.

---

19 NIM is the acronym for "Nuclear Instrumentation Module", a standard that defines mechanical and electrical specifications for electronics modules used in experimental particle and nuclear physics.

4.5.2   Time to Digital Converter (TDC)

The TDC assigns a time stamp (i.e., not the actual tof) to an event with the time elapsed between the MCP signal itself and the trigger in a specific recording time window. A TDC performs operations when triggered by a chosen external signal: in this work the trigger is the ion front MCP signal in leading edge triggering mode. The TDC card has an internal clock with 25 ps resolution for a maximum of 16 acquisition channels. After receiving the triggering signal, the TDC opens an arbitrary long time window for data acquisition, usually few µs long, to take into account the time required from the heaviest ionic fragments to be detected within the same time window.

To assign the actual tof of a detected particle, the bunch marker signal is required, as the detection scheme in Figure 4.17 shows. This timing technique is quite resource demanding, but allows the experiment to be carried out again offline during the post-analysis, allowing for a large number of experimental parameters to be optimized.

4.5.3   Time structure of the signal

When the TDC is triggered, the arbitrary length of the recording time window of several µs allows several bunch marker signals to be recorded; the bunch marker can be used as reference to determine the tof of a particle. At the SOLEIL synchrotron facility, a "8-bunch" mode corresponds to a BM period of $t_{BM} = 147.5363$ ns. The target density is designed to have much less than one ionization event per bunch to ensure the probing of a single particle ionization event, reaching an event rate of about 20 kHz in real experimental conditions.

Using a relative low bunch mode allows the BM period t_{BM} to be roughly an order of magnitude longer then the electron time-of-flight tof_e, therefore it can be used as reference of measurement. As described by equation 4.8, the tof_e is computed

as the modulo[20] of the difference between the time of arrival al an electron on the MCP $t_{MCP,e}$ and the t_{BM} corrected by an offset $t_{0,e}$ which is calculated in the calibration (see chapter 4.6.1). The $t_{MCP,e}$ is used as a reference point to calculate the time-of-flight of an ion tof_{ion} for which just the electron time-of-flight tof_e has to be added in order to have the same reference t_{BM} for both particles.

$$tof_e = mod\left((t_{MCP,e} - t_{BM}), \Delta \tau_{BM}\right) + t_{0,e}$$
$$tof_{ion} = t_{MCP,ion} - t_{MCP,e} + tof_e$$

(4.8)

4.6 Momentum calculation

During the post-analysis, the recorded data are used to compute first the position of the events at the MCP surface, and afterwards the momentum vectors of the particles at the instant of ionization. The simplified equations governing the particle´s motion in a full 3D focused spectrometers are presented in the set of equations 4.9. The former are valid for a particle whose energy is smaller compared to kinetic energy gained from the electric field in the spectrometer, the so-called "linear approximation".

$$p_{r,x} = \frac{m_r x_r}{tof_r} \cdot c_x$$
$$p_{r,y} = \frac{m_r y_r}{tof_r} \cdot c_y$$
$$p_{r,z} = \frac{E \cdot q \cdot \Delta t}{124,38} \left[\frac{V}{cm} \cdot a.u. \cdot ns\right]$$
$$\Delta t = tof_r - t_{r,mean}$$

(4.9)

The mass and the elementary charge of an electron in atomic units (a.u.) are by definition $m_e = e = 1$ a.u.; the equivalent electric E-field of the spectrometer can be derived by a calibration using known references as described in chapter 4.6.1.1, and the $t_{r,mean}$ is the centre of the momentum sphere for a specific particle.

When the total momentum $p_{i,r} = p_{r,x} + p_{r,y} + p_{r,z}$ of a particle i of mass m_i is reconstructed, its kinetic energy can be calculated as $E_{k,i} = |p_i|^2 / 2 m_i$ both for

---

20   The modulo operation returns the signed remainder of a division.

electrons $E_{k,e}$ and for each of the ionic fragments $E_{k,i}$. For a diatomic CE, the KER introduced in chapter 3.4 is calculated from equation (3.23) leading to equation (4.10) using the relative momentum vector between two detected fragments $\boldsymbol{p}_{rel} = \boldsymbol{p}_1 - \boldsymbol{p}_0$.

$$KER = |\boldsymbol{p}_{rel}|^2 / 2\mu_R \quad \text{with} \quad \mu_R = (m_0 \cdot m_1)/(m_0 + m_1) \tag{4.10}$$

In the case of a symmetrical breakup, e.g., N_2, with $m_1 = m_2 = m$ the reduced mass is equal to $\mu_R = m/2$.

All the event detected in coincidence can be represented using the so-called photoion-photoion coincidence spectrum (PIPICO), which shows correlations of the tof of two or more fragments detected in coincidence. A background signal is produced from the interaction of photons with residual gas molecules (mainly N_2, O_2 and H_2O for synchrotron experiments) and electronic noise (e.g., ringing and crosstalk of detectors), and when inevitably detected it can either trigger the opening of a time window, or be recorded among real events. During the signal post-processing, it becomes crucial to separate the signals of interest from the background, thus telling apart the real coincidence events from the false ones; to filter out most false coincidences, each event has to satisfy momentum and energy conservation rules in 3D (e.g., in 3D momentum space).

The PIPICO spectrum is the tof coincidence map of (at least) two fragments emerging from a CE [147], [148]. The tof_1 of the fastest ion is plotted along the x-axis, letting the lower half of the spectrum empty by definition. The brighter areas represent fragments belonging to the same ionization reaction; compared to a traditional tof spectrum (i.e., not in coincidence), the PIPICO spectrum makes it possible to highlight correlations between particles belonging to the same ionization event. Furthermore, it is possible to distinguish between fragmentation with multiple fragments/neutrals and with higher charges. Linear features represent breakup channels involving two or more fragments; their shape is due to the momentum conservation, with the tips corresponding to the backwards and forward emission (with respect to the direction of the electric field of the

spectrometer) respectively, and the length proportional to the KER of the breakup. In a two-body breakup, the bigger is the mass difference between fragments, the more tilted and detached from the main PIPICO diagonal the line is: more generally, the tilting reflects the fragment mass-to-charge ratio. The thickness of a line is related to the number of particles described (and proportional to the momentum resolution): the higher the number of charged fragments (or even neutrals), the thicker the lines. To better visualize these latter multi-fragments events, tri-photoion coincidence spectra (TRIPICO) can be used.
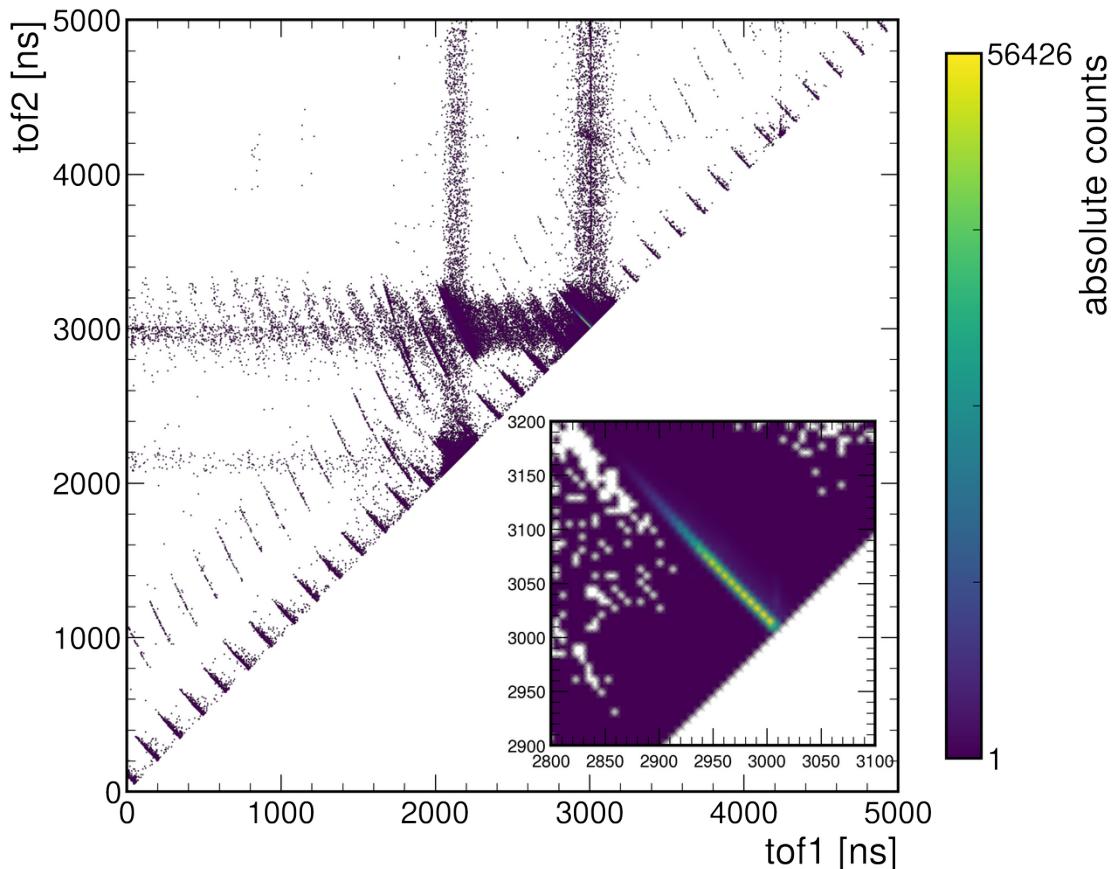
Figure 4.18: PIPICO spectrum of N_2 molecule with momentum conservation applied. The insert is a zoom-in of the strongest feature, the line with origin at $tof_1 = tof_2 = 3000$ ns orthogonal to the diagonal of the spectrum, the N^+–N^+ breakup channel. A second longer line, away from the diagonal, at shorter tof, and tilted, represents the N^{2+}-N^{2+} breakup channel. The very small area (i.e., no breakup, therefore no KER) at tof = 4100 ns (roughly twice the N^+–N^+ breakup channel) corresponds to the singly ionized parent ion N_2^+. Note how all the described features are repeated across several periods of the BM due to the so-called false coincidence. The straight lines (±45° to the diagonal) correspond to the standard tof spectroscopy and are correlated to the detected charged fragments.

4.6.1 Calibration

The calibration procedure aims to determine both the time delay $t_{0,e}$, and some internal parameters for the momentum vectors extraction such as the strength of the B-field, the E-field for equation (4.9), the relative rotation of the detectors, and the absolute value of the photoelectron and ion energies.
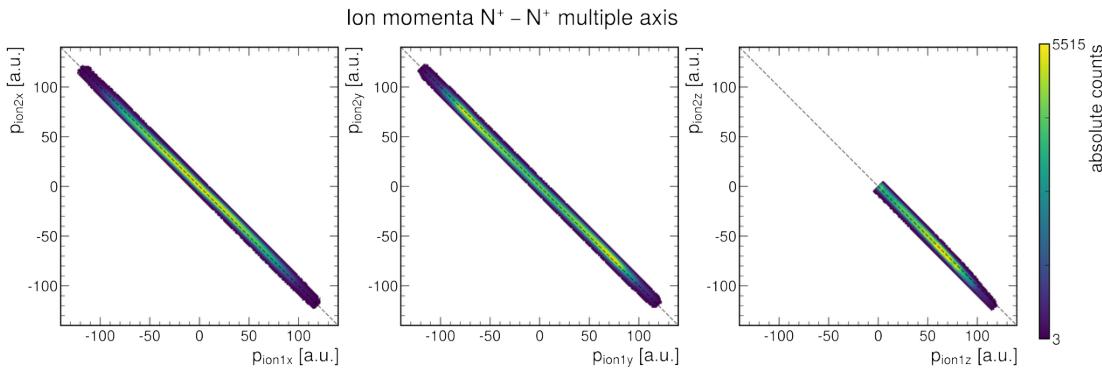

Figure 4.19: experimental values for the ion momenta in N^+–N^+ breakup in x, y and z directions. The distribution lies along the x = -y line. The distribution in the tof direction along the z-axis appears cut, because it is not possible to distinguish between the two identical ions.

As already shown in equation (4.8), a constant offset due to transit times of signals in the electronics, and the length of cabling must be taken into account. The $t_{0,e}$ is usually determined extrapolating the constant term of a regression of the nodes of the electron gyration period T_{gy} induced by an B-field. When no B-field is present, it is possible to retrieve the $t_{0,e}$ either as the difference between the mean tof of a measured electron $t_{e,mean}$ and a simulated one, or looking at the tof of photons, which are supposed to be the fastest particle to be detected.

4.6.1.1 Calibration using N_2

To both calibrate the value of the electric E-field of the spectrometer and the relative orientation of the detectors, the breakup reaction $N_2 + \hbar\nu \rightarrow N^+ + N^+ + 2e^-$ is used. The K-shell photoionization of N_2 with a right circularly polarized photon of energy 420 eV produces a back-to-back
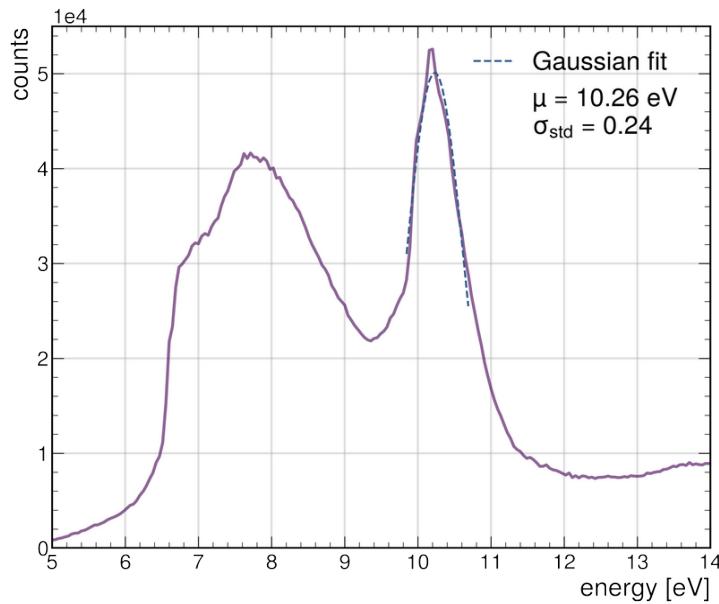
Figure 4.20: Calibrated KER spectrum for breakups that occurred parallel to the tof axis. The peak for the $D^1\Sigma_u^+ \rightarrow N^+(^3P) + N^+(^1D)$ breakup is located at 10.35 eV. The used electric field is E = 116.7 V/cm.

fragmentation of two charged ionic fragments, each with atom mass 14 amu shown in the main line of the PIPICO histogram in Figure 4.18. For a diatomic molecule, a diatomic breakup channel obeys to the simple momentum conservation law $\boldsymbol{p}_{1,i} + \boldsymbol{p}_{2,i} = 0$, valid for each direction i = x, y, and z, and it can be used as a gate on the momentum during the post-analysis. The validity of the momentum conservation for the N^+–N^+ channel is confirmed by the sharp diagonal momentum distribution shown in Figure 4.19; the width of the distribution of about 2 a.u. is due to both the momentum resolution, and the recoil of the Auger electron on the centre of mass of N_2. For more complex molecules, additional gates should be implemented e.g., on the sum of momenta.

According to the linear approximation, the momentum calculated in tof direction (i.e., z-axis) is directly proportional to the E-filed of the spectrometer as shown in the p_z equation (4.9) in chapter 4.9; therefore, the E-field can be calibrated using the KER. The KER spectrum for the electronic state $D^1\Sigma_u^+$ of the N_2^{2+} ionic state which dissociates into the optically active $N^+(^3P) + N^+(^1D)$ has been measured with high energy resolution by M. Lundqvist et al. [149]. For the vibrational level v = 1, the KER spectrum reported in Figure 4.20 shows a sharp

peak at KER = 10.316 eV that was used to scale the E-field to the final experimental value E = 116.7 V/cm.
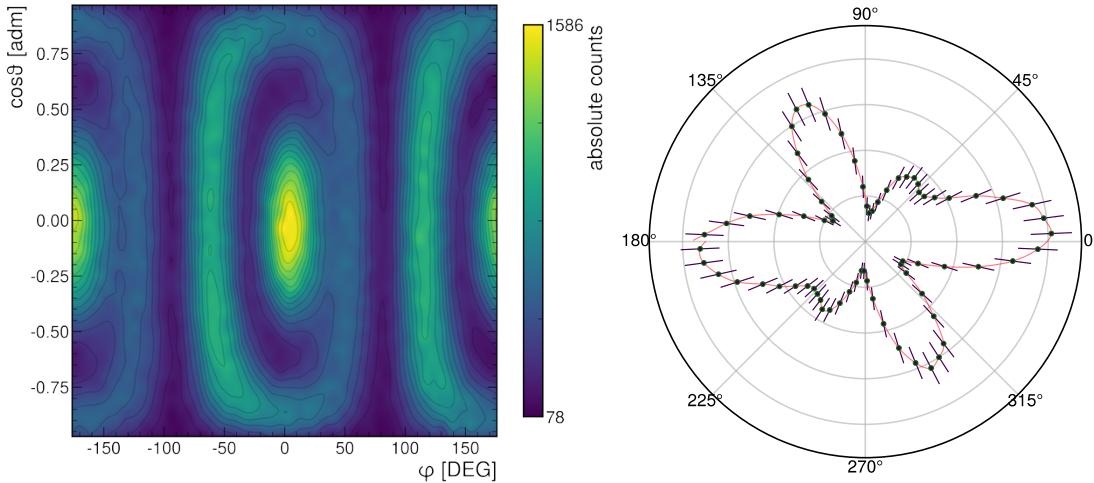
Figure 4.21: single MFPAD restricted to the polarization plane for N_2. Left: MFPAD in spherical coordinates defined by equation (4.12). Right: polar plot of the single MFPAD integrated over the angle φ; the red curve is a B-spline fit with and each data point has error bars.

A relative rotation of the detectors implies a mismatch between their internal coordinate systems with respect to the LF of integer multiple of π/3 rotation, due to the hexagonal shape of the detectors. The relative rotation angle of the electron detector is found calculating the single MFPAD of the N^+–N^+ breakup channel matching them with the reference experiments of T. Jahnke et al. [79], [81]. The MFPAD is obtained by transforming the electron momentum vectors from LF into MF and aligning the molecule along the polarization plane; the MF is defined from the set of equation (4.11) with respect of the photon propagation direction $x = (1,0,0)^T$ in the LF. The ion momentum vectors p_1 and p_2 must lie on the breakup molecular axis, and their difference $p_{rel} = p_2 - p_1$ is used to define the z'-axis in the MF, thus to orient the molecule in space. For the homonuclear N_2 the axial-recoil approximation holds as shown by Weber et al. [150] (see chapter 3.4).

$$\hat{z}' = \frac{p_2 - p_1}{\|z'\|}$$
$$\hat{y}' = \frac{(p_2 - p_1) \times \hat{x}}{\|y'\|} \quad (4.11)$$
$$\hat{x}' = \frac{\hat{y}' \times (p_2 - p_1)}{\|x'\|}$$

The MF normalized vectors are used to project the electron momentum vectors p_{el} from LF onto the MF, obtaining p'_{el} .

$$\varphi = atan2\left(p'_{e,y}, p'_{e,x}\right)$$
$$\theta = \cos^{-1}\left(\frac{p'_{e,z}}{\sqrt{p'_{e,x} + p'_{e,y} + p'_{e,z}}}\right) \tag{4.12}$$

The MFPAD of Figure 4.21 is obtained calculating the spherical coordinates of p'_{el} using equations (4.12) according to the convention described in appendix B.6, and restricting the molecular orientation to the polarization plane ± 10°. Note that in this particular case the θ angle is defined with respect to p_{rel} which is parallel to the z'-axis. The results are in good accordance with the reference for the right circularly polarized (RCP) light when the electron detector is flipped over the y-axis and then rotated by π/3 radiants clockwise. The validity of the mutual rotation of the detector is confirmed from the rotation of the marks on the MCP recorded from the raw images of the detectors as shown in Figure 4.22.
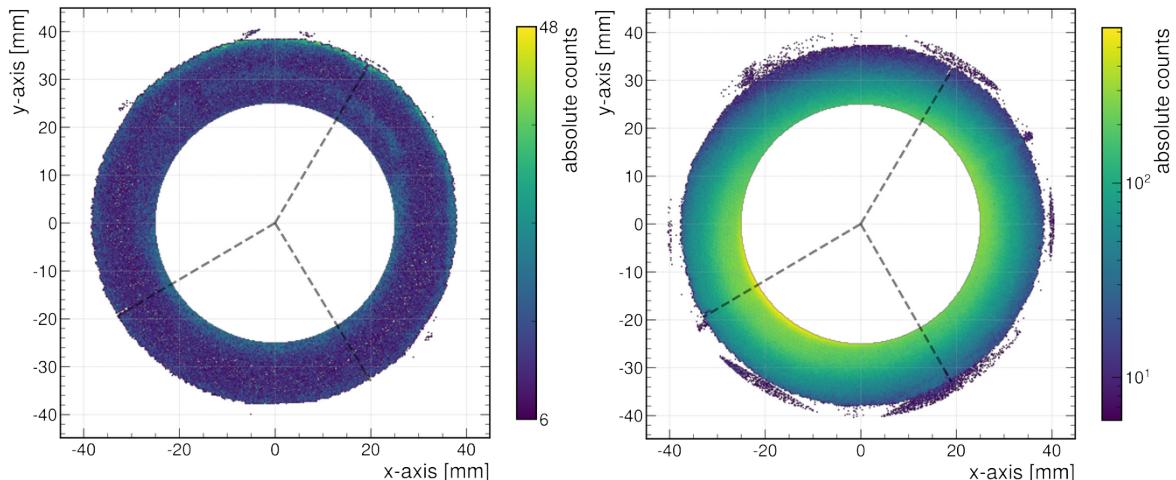

Figure 4.22: masked raw position images on both detectors from Figure 4.16. From left to right electron and recoil detector. The MCP notches are located at the end of the dotted lines.

4.6.1.2 Calibration using Ar

It is possible to exploit the high precision and accuracy of undulators on the delivered photon energy to determine the absolute energy of a detected photoelectron. For such energy calibration procedure, an Ar atom is ionized with photons at several known energies, chosen to generate photoelectrons that span

most of the detector surface, as shown in Figure 4.26. The ionization process is well-above the ionization threshold, and the $2p^{1/2}$ and $2p^{3/2}$ electrons are by definition constantly 2.15 eV apart.
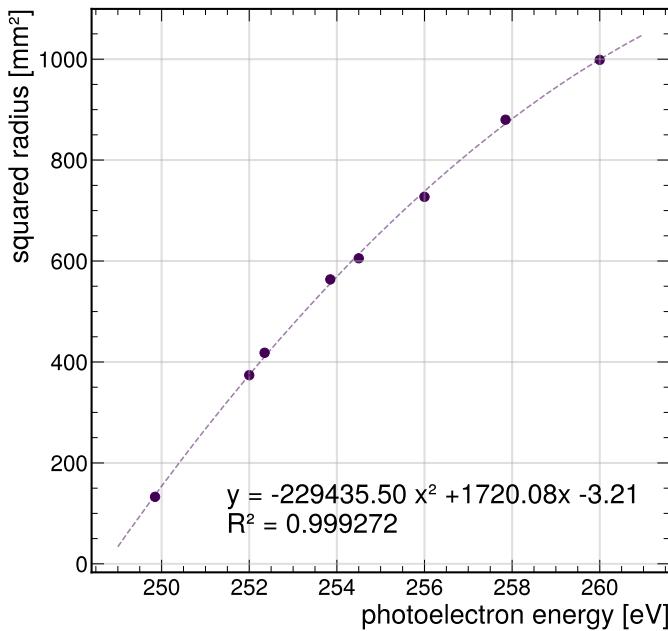
Figure 4.23: Interpolation curve and coefficient of determination R^2 for the photon energies read from the undulator and the square of the detected radius on the electron detector for Ar. The extrapolated energy offset at $r^2 = 0$ for the absolute energy determination is E(r=0) = 248.34 eV.

According to the PAD equation (3.22) in chapter 3.3, the Ar PAD for np electrons is expected to have an asymmetry parameter β dependent on the photoelectron energy. A linear increase of the photon energy above the ionization threshold results in a proportionally larger photoelectron momentum spheres, due to the monotonic increase of β for photoelectron energies below 20 eV in Ar [151]. The diameter of spheres at 260 eV, 256 eV, 254.5 eV and 252 eV photon energy is measured on the electron detector (Figure 4.26 or projections of Figure 4.24), and the squared radius is fitted with a polynomial of second order as plotted in Figure 4.23; the extrapolation returns the Ar ionization threshold E(r=0) = 248.34 eV. The inverse function, net of the offset, can be used to calculate the absolute energy of the photoelectron for other targets upon measuring their radius on the detector.
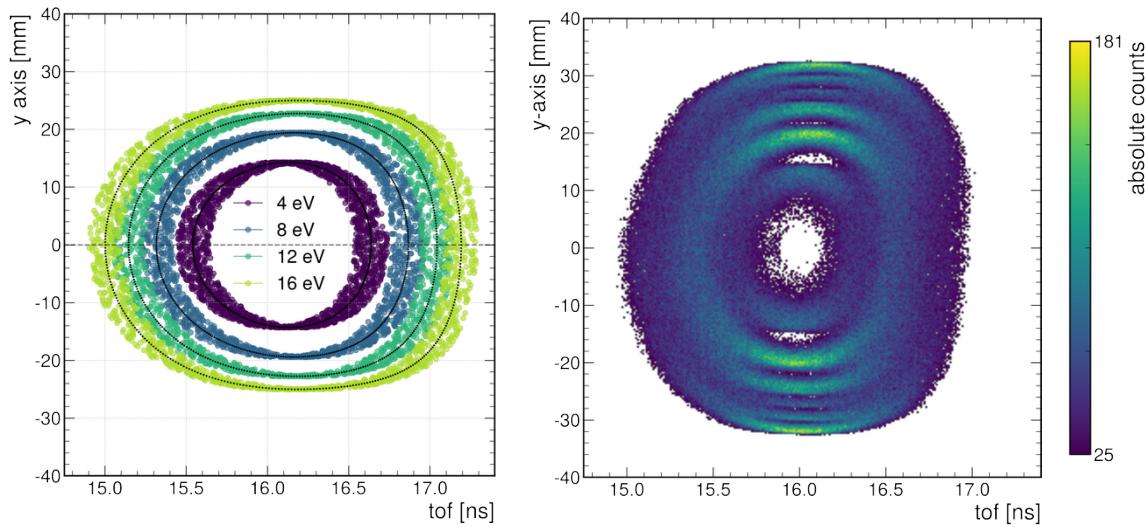
Figure 4.24: Ar 2p electrons fish fillet along y direction. Left: SIMION® simulated position along y-axis and tof at impact of four absolute electron kinetic energies, the black dots are without tof uncertainty; right: superimposition of experimental data at all photon energies with scaled detectors for both on x- and y-axis.

The section of the projected momentum spheres shown in Figure 4.24 can be obtained restricting along either x or y direction, but the former shows higher resolution due to the smaller interaction region.

4.7 Effect of electrostatic lenses

An electrostatic lens can defocus particles along the tof direction which are travelling far away from the lens centre, resulting in a lower momentum resolution; the latter phenomenon is particularly relevant for electrons because of their low charge-to-mass ratio. Four electrons with $E_{k,e}$ = 4 eV, 8 eV, 12 eV and 16 eV were simulated with SIMION®, and the momentum vectors were calculated using the set of equations (4.9). The lens effect can be simulated introducing an uncertainty of 200 ps in the tof of the electrons (12.5% of the expected electron tof) due to the loss of time focussing, as shown both in panel b Figure 4.24 for the position, and in panel b of Figure 4.25 for the KER angular distribution around the z-axis in the LF. In both figures, the black dotted lines represent the theoretical distributions with no lens perturbation.
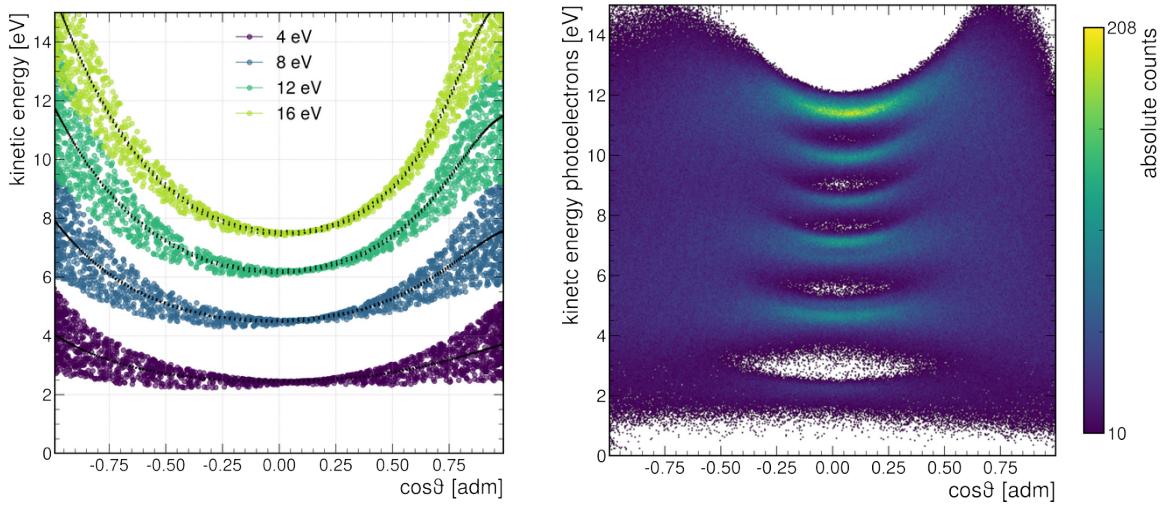
Figure 4.25: Ar 2p electrons photoelectron energy angular distribution, comparison between SIMION® simulations (left) and experimental data (right). The electron energies are reported in chapter 4.6.1.2. The optimal distribution is an horizontal line representing a perfect spherical momentum distribution, and it is achieved tuning the size of the detector (e.g., stretching the x-y plane). Although the detector on the left is not stretched, it is possible to see the quadratic progression of the linearly-spaced energies along the tof direction, independent from the stretching parameter. On the right, it is possible to see the effect of the lens both on lack of resolution along the tof direction, and on the progressive deviation from a linear distribution increasing the energy.

Due to the small distribution of the photon beam along the x direction (see chapter 4.2.2), the volume of interaction is approximated in the computations with a rectangle (instead of an ellipsoid) on the y-z plane whose four vertexes and centre are the sources of electrons. To investigate the effect of misalignment of the interaction volume with respect to the axis of the spectrometer in the simulation, the vertexes in y direction are symmetric the respect to the absolute centre of the interaction volume, but shifted of 0.1 mm along the z direction. The two edges of the rectangle have a ratio 1:15 due to the shorter FWHM of the photon beam compare to the molecular jet. From each source, 180 electrons are ejected with a 2° angular resolution with respect to the tof direction and no elevation with respect to other directions (i.e., a thin slice of the momentum sphere is obtained).

The comparison with the experimental data for the tof along the y direction in Figure 4.24 shows that the resolution along the tof direction decreases dramatically due to the effect of the electrostatic lens. Figure 4.25 shows the

consequent lack of resolution in the angular distribution (i.e., function of polar angle θ) of a photoelectron kinetic energy $E_{k,e}$.

During the calibration, the scaling parameters c_x and c_y in (4.9) were empirically determined to straighten the angular distributions in right panel b) of Figure 4.25, letting the projection of the radius of the momentum sphere along x- and y-axis of the detector matching the radius of the along the z-axis. The left panel a) in the same figure shows the effect of the target misalignment along the z-axis as an asymmetric distribution respect to θ = ± π/2 that can be partially accommodate introducing a t_0 correction factor along the tof direction in the analysis.
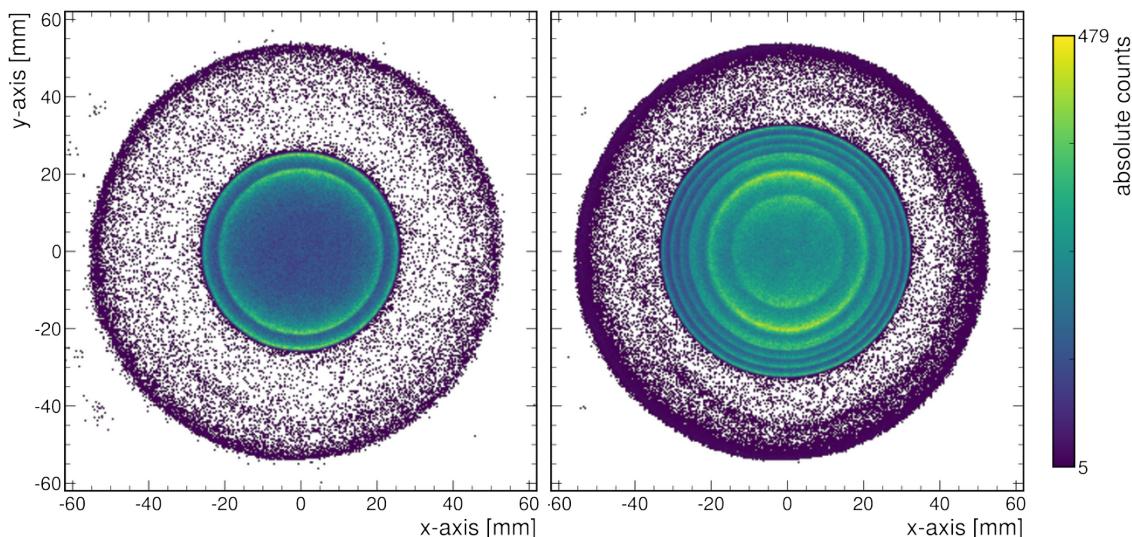
Figure 4.26: Ar 2p electrons raw position images (i.e. Newton spheres) on the electron detector. Left: single intermediate 254 eV photon energy with the two electrons visible; right: all measured energies superimposed where some lines belonging to the intermediate energies almost overlap. Note the parabolic progression of the spheres' diameter.

5. EXPERIMENTAL RESULTS

In the following chapters, the results for the experiments conducted at the SEXTANT beamline in 2018 are presented. The aim of the experiments was to explore the capability of MFPAD, and its related PECD, of giving an insight on the structure of chiral molecules such as TFMOx. During the experiments, the photoelectron energy was varied as a parameter, and a comparison with MOx was carried out to investigate the effect of the molecular structure upon changing a substitutional group (e.g., CF_3 vs. CH_3). By increasing the amount of information on the spatial molecular orientation, the results are presented for randomly oriented, oriented along an axis (i.e., from a diatomic breakup), and fully fixed in space molecules (i.e., from a polyatomic breakup). Taking advantage of the data recording structure of the COLTRIMS apparatus, it was possible to gate the raw data during the analysis to select only the events of interest for both purely diatomic and polyatomic breakups. For each molecular breakup KER, relative and sum-momenta were gated, and in case of the polyatomic breakups further restriction on the Newton plots were applied.

All results from both molecules are compared for validation with numerical calculations done with the Single Centre (SC) method and code developed by P. V. Demekhin et al. [152]: for MOx the relaxed-core Hartree-Fock (HF-RCHF) approximation [153], and for TFMOx the frozen-core Hartree-Fock (HF-FCHF) approximation were used, respectively. The RCHF used shows the major effect emerging from the monopole relaxation of molecular orbitals which is induced by

the creation of the inner-shell vacancy due to the ionization. Furthermore, the partial harmonics of the SC expansion used to describe the occupied orbitals have been increased from $l_c, |m_c| \leq 59$, to $l_c, |m_c| \leq 79$ for the experiments involving TFMOx compared to MOx, leaving the partial photoelectron continuum waves the same equal to $l_e, |m_e| \leq 29$. All calculations were performed at the equilibrium of the energy-optimized molecular geometry of the neutral ground electronic state.

5.1 Trifluoromethyloxirane

For all the experiments presented in this work, the two enantiomers of TFMOx used were commercially synthesized by SynQuest Laboratories. The purity of both samples has been tested using NRM and HPLC giving 96% and 98% purity for S-TFMOx and R-TFMOx, respectively (see appendix B.10). For each enantiomer, the O(1s) electron of the K-shell was photoionized with photon of energies of 541.5 eV, 542.5 eV, 544.5 eV, 546 eV, and 550 eV, corresponding to a photoelectron kinetic energies of 3.1 eV, 4.1 eV, 6.1 eV, and 8.1 eV, and 11.7 eV respectively (for the energy calibration, see chapter 4.6.1.2). The O(1s) electron is technically an ideal ionization site to target because of its higher ionization energy compared to the C(1s) = 285 eV[21] which makes the ionization very selective without drastically reducing the cross-section; as a consequence of the latter the location of the emerging photoelectron is unambiguous. The photon's helicity was switched every 2 hours between left circularly polarized (LCP) and left circularly polarized (RCP). The enantiomers were switched at roughly the half of the 7 days long experimental campaign to have roughly the same amount of events for each enantiomer across all photon energies. The rate at which the data were recorded were 6 kHz on the ion detector, and 10 kHz on the electron detector. A recycling system has been used to exploit all the limited experimental time at the beamline (see chapter 4.3.3).

---

21   The absolute ionization energy value varies slightly for the three C(1s) due the chemical shift.
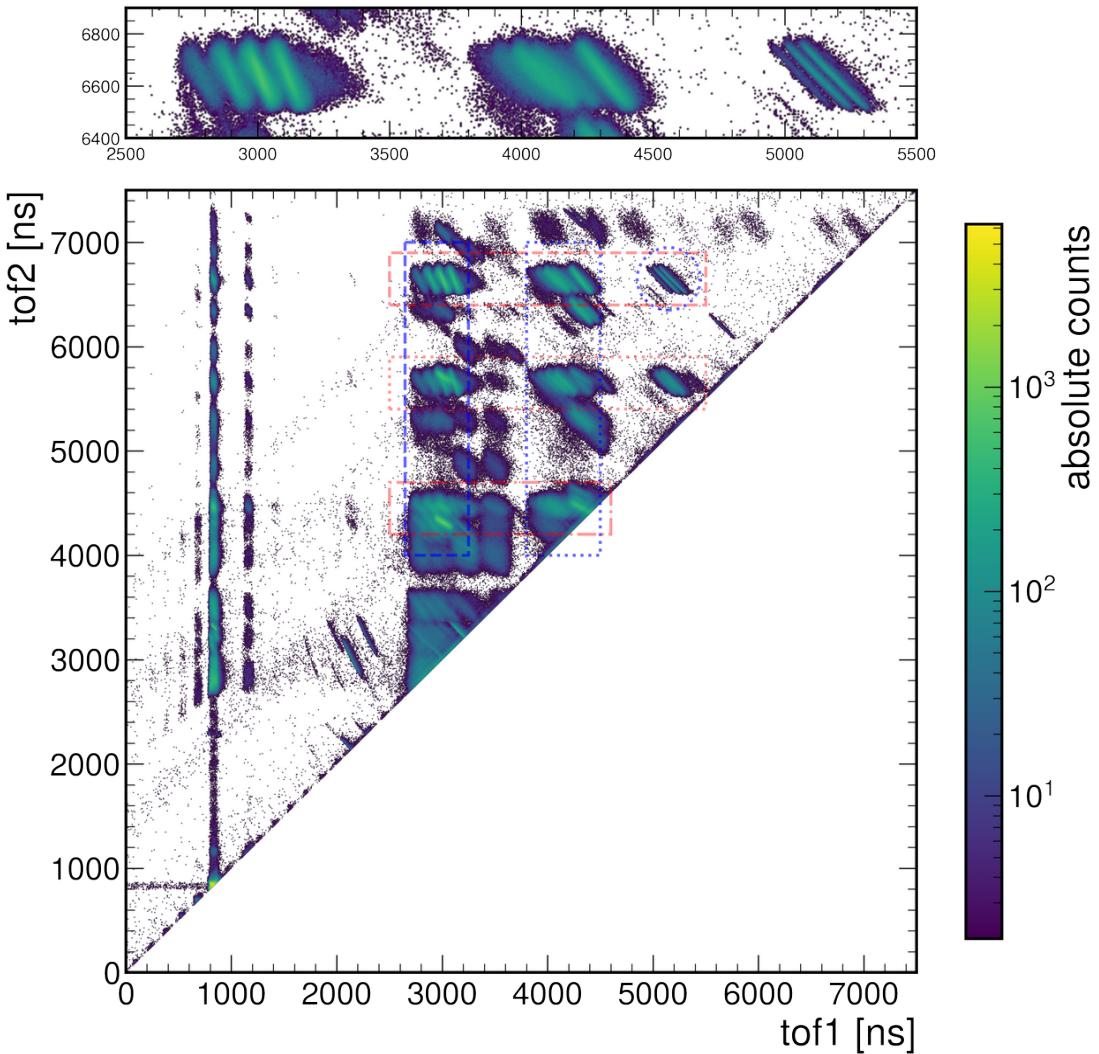
Figure 5.1: PIPICO histogram for R-TFMOx, both panels in logarithmic scale, gate on 3D momentum conservation. Bottom: the rectangular boxes are highlighting polyatomic breakup channels with one of the two fragments' mass kept constant: the red squares identify the sequential loss of a F atom from the constant CF_3^+ fragments (top-bottom direction), and the blue squares the sequential loss of one C and one O atoms from the constant $C_2H_3O^+$ (right-left direction), respectively; the blue circle highlights the only diatomic (and complete) breakup channel. The top panel is a magnification of the top red square, and shows the three main areas analysed in the present work. From left to right: CH9, CH11, CH12, and CH14.

5.1.1 Channels selection

As already mentioned in chapter 4.6.1.1 for the N_2 molecule, the PIPICO histogram of polyatomic molecules is richer in features compared to smaller molecules. The corresponding spectrum for R-TFMOx is shown in Figure 5.1, and the expected tof of the most relevant fragments are listed in Table 3. The total mass of TFMOx is m = 112 amu, and the breakup channels selected for the

analysis belong to the three areas reported in the top-insert in Figure 5.1, corresponding to the first top red rectangle in the main panel. Each of the red horizontal rectangles identify a loss of an F atom from the CF_3 fragment from top to bottom; the first two channels from the left are incomplete (i.e., one neutral fragment was not detected) polyatomic, and only the last one is a complete diatomic one. The selection criteria applied choosing the features of interest of PIPICO spectrum were to keep the CF_3 as the heaviest fragment, due its larger mass compared to the other fragments and therefore its distinct tof signal, and selecting the complementary fragments accordingly.

Table 3: tof and m/q ration for the most relevant fragments. The tof are calculated using the set of equations (4.9) with the linear approximation for the p = 0 point.

| Ion	m/q	tof (p=0) [ns]
H^+	1	801
C^+	12	2765
CH^+	13	2888
CH_2^+ / N^+	14	2997
CH_3^+	15	3102
O^+	16	3199
F^+	19	3485
C_2H^+	25	4238
$C_2H_2^+$	26	4313
$C_2H_3^+$	27	4386
COH_2^+	30	4386
C_2OH^+	41	5128
$C_2OH_2^+$	42	5190
$C_2OH_3^+$	43	5252
CF_2^+	50	5663
CF_3^+	69	6653
$C_3H_3OF_3^+$	112	8476

5.1.2 Diatomic breakup channels

The only complete diatomic breakup channel corresponds to the direct photoionization reaction with subsequent Auger decay (5.1), clearly visible in the PIPICO histogram of Figure 5.1.

$$C_3H_3F_3O + \hbar\omega \rightarrow CF_3^+ + C_2H_{i=1,2,3}O^+ + e_{ph}^- + e_{Auger}^- \qquad (5.1)$$
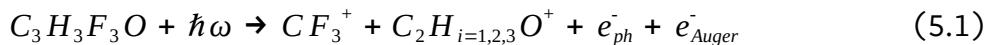
The PIPICO spectrum for the fragments CF_3^+ (m/q = 69) and $C_2H_{i\,=\,1,2,3}O^+$ (m/q = 41, 42, 43) are shown in Figure 5.2 with gating on their relative (i.e., the difference of the momentum vectors of the two fragments) and sum momenta (which sum up to zero by definition of single photoionization event) in order to select only the recorded events belonging to the breakup. The presence of three lines is due to hydrogens progressively leaving the fragment as neutrals; the constant inclination of the PIPICO lines in Figure 5.2 shows that the hydrogens do not carry away much momentum. Thus, it is possible to combine the recorded data of all three breakup channels to one, called $\mathbf{p}(69\,\text{amu}) - \mathbf{p}(43\,\text{amu})$ for brevity. The former channel contains roughly $2.5 \cdot 10^5$ valid events after gating for each enantiomer, light-helicity and photon energy.
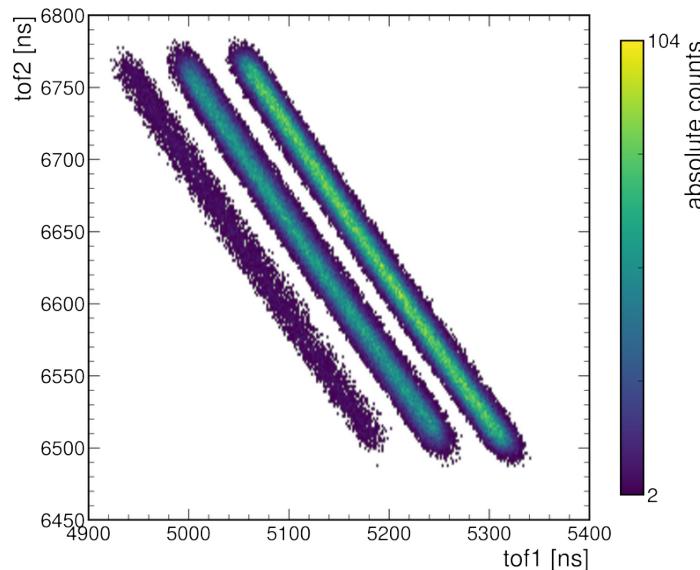
Figure 5.2: Gated PIPICO lines for three diatomic channels called $\mathbf{p}(69\,\text{amu}) - \mathbf{p}(43\,\text{amu})$.
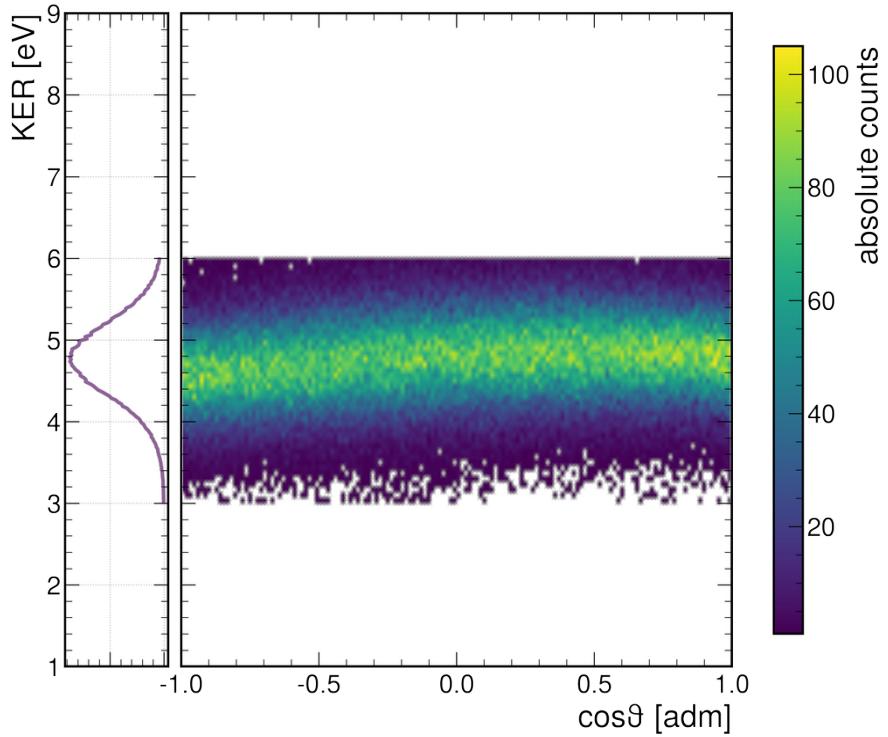
Figure 5.3: KER angular distribution. The theta angle is defined as the angle between the fragments' relative momentum and the tof direction (i.e., z-axis in LF). The hard limits of KER = 3 eV and KER = 6 eV correspond to the arbitrary chosen gating.

One important histogram used as a sanity check-up for each breakup channels is based on the KER and the emission angular distribution of the fragments shown in Figure 5.3. For the very nature of the breakup reactions considered, the KER is typically independent of the angle θ. The small deviations from linearity visible in Figure 5.3 are a consequence of the effect of strong electrostatic lenses, and it could be further corrected with the use of lookup tables during the momentum calculation. The present deviation is, however, acceptable, and does not affect the results.

5.2 Direct ionization: diatomic breakup

For the diatomic fragmentation channel **p**(69 amu) − **p**(43 amu), it is possible to use the fragments' relative momentum to define a fragmentation axis. Using the former vector, it is possible to uniaxially orient the molecule in space defining a MF, using the light's propagation direction x in the LF and the relative momentum vector. The former orientation is defined with respect to the Euler angle β, and it has one degree of freedom corresponding to the Euler angle α; the Euler angle γ (i.e., rotation around the light's propagation axis in LF because of the rotation chain) is irrelevant because of the symmetry of the CPL, and because the desired observable is a forward-backward asymmetry along the light's propagation direction (see image Figure B.4 in appendix B.6). Both the integral PECD (i.e., 1D, averaged over all molecular directions) described by equation (3.21), and the differential PECD (i.e., 2D as function of the uniaxial molecular orientation $\beta = p_{rel} / \|p_{rel}\|$ with $p_{rel} = p_1 - p_0$) described by equation (5.2) are calculated with respect to the photon's propagation direction in the LF according to the equation (3.18). As already implemented in previous experiments [74], the degree of freedom due to the molecular orientation is neglected by integrating the photoelectron momentum vectors over the α Euler angle for the calculation of the differential PECD.

$$PECD(cos\theta, \beta) = \frac{I_{+1}(\theta, \beta) - I_{-1}(\theta, \beta)}{I_{+1}(\theta, \beta) + I_{-1}(\theta, \beta)}$$

(5.2)

The PECD effect is inverted in sign upon switching the polarization of the light *or* changing the enantiomer, therefore the two datasets obtained for the two polarizations RCP and LCP have been added together after flipping the photoelectron momentum vector of the RCP dataset along the light's propagation direction axis x (i.e., cosθ) resulting in an increase of statistics of roughly a factor 2 for each enantiomer. As a consequence, the PECD is calculated as the normalized difference between the two enantiomers with respect to R

e.g., (R − S) / (R + S). The former equivalence between inverting the light helicity and exchanging the enantiomer holds only for enantiomeric pure samples and perfectly CPL, conditions ensured from the undulator and diagnosed at the beamline SEXTANT (see chapter 4.2.2). Contrary to using perfectly CPL, the values of PECD using elliptical polarized light are function of φ angle as shown in strong field regime from K. Fehre at al. [57].

5.2.1 Theoretical predictions

A mismatch of the uniaxial molecular orientation between the experimental and theoretical data is due to an arbitrary choice of the references for the coordinate frame. The experimental and theoretical MF can be brought to coincidence upon small variations of the Euler angle β (i.e., the inclination of the molecular orientation axis at the instant of the photoionization). The Euler angle β is used as a free parameter in the calculations, and the convergence criterium is the best visual fit between the computed and measured 1D PECD; the former method has been already used and extensively described in [74]. The fragmentation mechanism is thought to obey the axial-recoil approximation (see chapter 3.5). Under the former assumption in the case of MOx, the optimal Euler angle β corresponds to a molecular axis connecting the O atom with the C atom of the methyl group (results from [74]). In contrast, for the TFMOx the best-matching fragmentation axis connects the O atom with the CH_2 group on the oxirane ring, for all five photoelectron energies within a solid angle of about 0.2 sr, a result from the theoretical prediction. Because of the relatively large rotation between the experimental relative momentum and the calculated fragmentation axis, the axial-recoil approximation for the TFMOx molecule does not completely hold: the centres of charge of the fragments do not fully coincide with their centres of mass, and therefore the asymptotic relative momenta do not accurately represent the molecular orientation at the instant of photoionization.

The latter fact creates an inevitable intrinsic difference between the theoretical calculations and the experimental data, but the severity of its influence is further evaluated by the present experiment as function of the photoelectron energy and further investigated in chapter 5.3. The phenomenon could be explained considering the larger mass of the CF_3 group in TFMOx compared to the CH_3 group in MOx, and the richer electronic structure of F atoms compared to H atoms, which lead to a considerably slower dissociation of TFMOx compared to MOx, and a more complex charge arrangement on the photomontages.
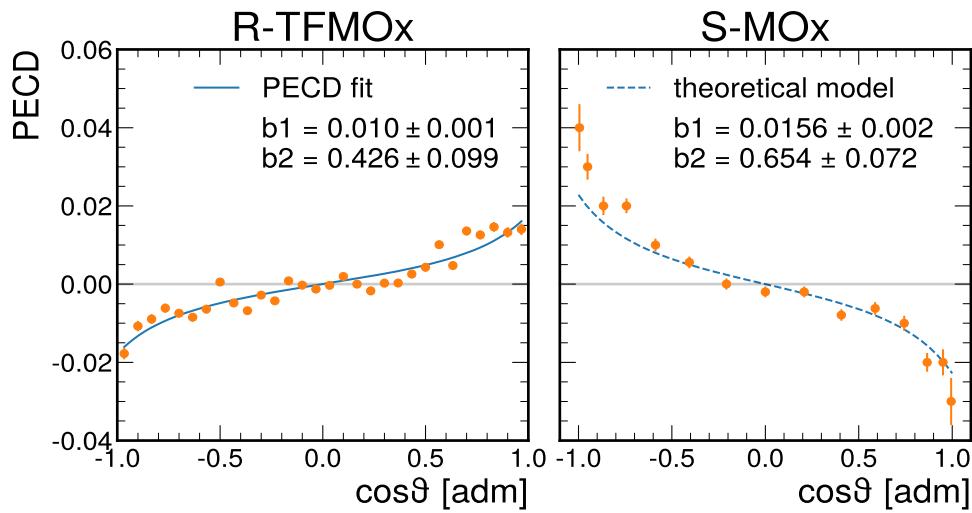

Figure 5.4: Integral PECD for randomly oriented R-TFMOx and S-MOx recorded at 11.7 eV and 11.5 eV respectively, with the anisotropy b_2 and dichroic b_1 parameters from fittings. The θ angle is defined as the angle between the photoelectron momentum vector and the light's propagation direction. The solid blue curve is a fit of the experimental data using the PECD integral equation (3.21), the dashed blue curve is retrieved from [74].

5.2.2   Influence of substitutional groups

The diatomic breakup of TFMOx is compared to a similar channel of MOx reported in [74]. For the MOx, both the integral and differential PECD were studied for O(1s) photoionization at a photoelectron kinetic energy of 11.5 eV for two fragmentation channels, of which the diatomic breakup $CH_3^+ (m/q = 15) - C_2H_2O^+ (m/q = 42)$, called $\mathbf{p}(14m) - \mathbf{p}(42m)$ for brevity, was the only complete one. Both the experimental conditions (i.e., the design of the COLTRIMS apparatus and the beamline used), and the analysis workflow are

almost identical for the MOx, and the TFMOx experiments. The MOx breakup $\mathbf{p}(14m) - \mathbf{p}(42m)$ differs from the TFMOx $\mathbf{p}(69\ amu) - \mathbf{p}(43\ amu)$ just from the nature of the first fragment, which for both molecules contains the substitutional groups attached to the carbon backbone of the oxirane molecules. As previously mentioned, the difference of one H atom between the $C_2H_iO^+$ fragments of TFMOx does not influence the breakup dynamics, therefore it is possible to compare the difference of emission patters for the two almost identical energies of 11.5 eV for MOx and 11.7 eV for TFMOx. According to the CIP rule (see appendix B.3), MOx and TFMOx are assigned to opposite descriptors R and S, therefore the direct comparison between the two molecules should be carried between opposite enantiomers (e.g., S-MOx and R-TFMOx).
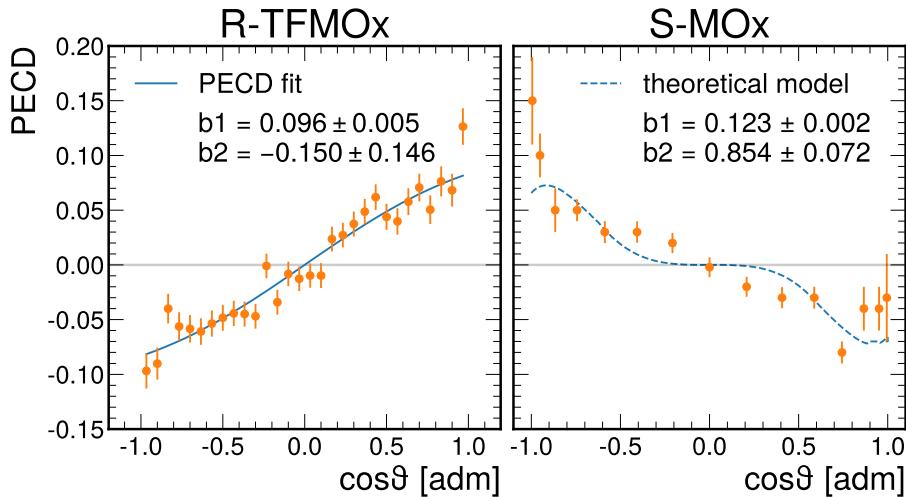
Figure 5.5: Integral PECD for uniaxially oriented R-TFMOx and S-MOx molecules along on orthogonal direction compare to the light's propagation direction recorded at 11.7 eV and 11.5 eV respectively, with the anisotropy b_2 and dichroic b_1 parameters from fittings. The solid blue curve is a fit of the experimental data using the PECD integral equation (3.21), the dashed blue curve is retrieved from [74].

According to the definition of PECD from chapter 3.2, the integral PECD (i.e., integrated over all molecular orientation) is extracted for R-TFMOx and the b_1 and b_2 parameters are calculated from a fitting using the equation (3.21) as shown in the left panel of Figure 5.4. The maximum value of the integral PECD is around 2%, several order of magnitude higher compared to dichroic observables from other traditional chiroptical techniques. The comparison with S-MOx reveals the inversion of the PECD trend with similar values for the dichroic parameter b_1. By fixing the molecular orientation to be orthogonal to the light's propagation

direction, it is possible to further enhance the PECD effect by an order of magnitude for both molecules, as shown in Figure 5.5.

$$PECD (\%) = (I_{+1} - I_{-1}) / (I_{+1} + I_{-1})$$
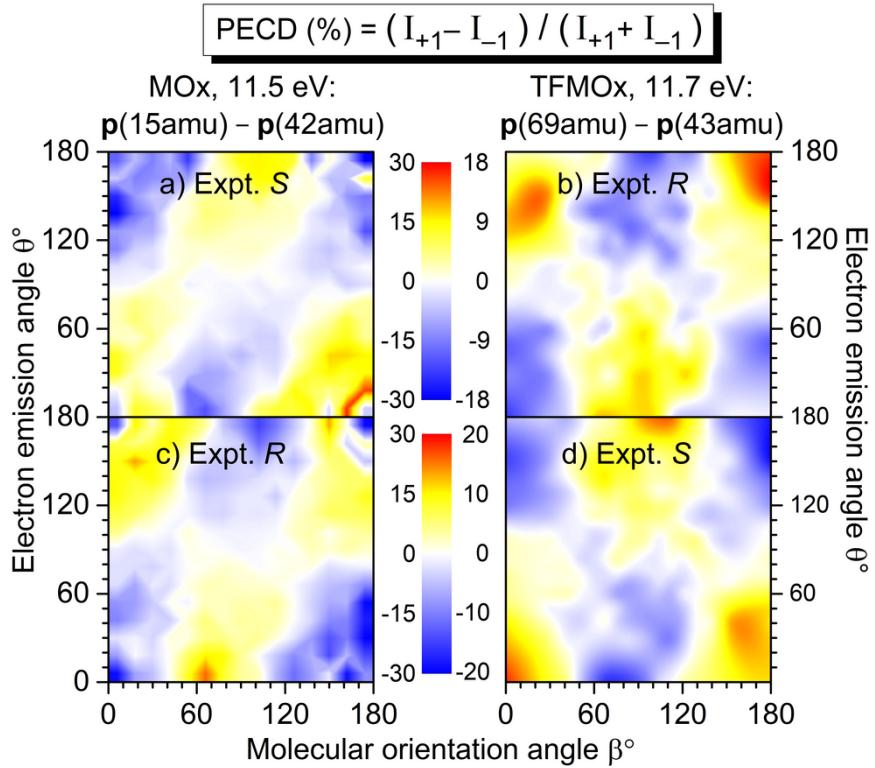
Figure 5.6: Experimental differential PECD of the uniaxially oriented enantiomers of S-MOx (left column, data from [74]) and R-TFMOx (right column) as a function of the photoelectron emission angle θ, and the molecular orientation angle β as defined in equation (5.2). According to the CIP rule (see appendix B.3), opposite enantiomers are compared in each row in order to compare identical geometrical structures. Image reproduced from [154].

The differential PECD for both R-TFMOx and S-MOx enantiomers is described as a function of the uniaxial orientation β, as shown in Figure 5.6. The direct comparison between similar molecular structures is along the rows, and the comparison upon switching enantiomer is done along the columns. For both molecules, changing the enantiomer consists in flipping the cosθ values along the light's propagation direction, which confirms the chiral origin of the PECD effect. The normalized difference also obeys the analytically-derived asymmetry property PECD(π−θ, π−β) = −PECD(θ, β), which corresponds to a flip of PECD sign upon rotation of the histograms by 180° around the normal to the picture's plane. In contrast to the integral PECD, for some molecular orientations the differential PECD reaches about 20% for R-TFMOx and 30% for S-MOx. Across the enantiomers, the differential PECD flips sign upon changing substitutional group,

as shown for the integral PECD: substituting the light CH_3 with the much heavier scatterer CF_3 results in a complete inversion of the PECD signal. Nevertheless, the distributions are similar both in intensity and arrangement of features for the correspondent fragmentation channels and photoelectron kinetic energies,thus the inner-shell PECD effect is confirmed to emerge from complex multiple scattering process by the molecular potential of the emitted photoelectron wave.

5.2.3   Effect of energy

Error: Reference source not found shows the differential PECD of R-TFMOx for all the five photoelectron kinetic energies, with maximal values of about ±16% to ±20%, values at least a factor of 10 larger than the integral PECD in Figure 5.4. There is a clear progression of the measured differential PECD with increasing photoelectron kinetic energy, although similar features occur across all energies. In particular, for the first three lower kinetic energies 3.1 eV in panel a), 4.1 eV in panel c), and the 6.1 eV in panel (e) of Error: Reference source not found, there is a sequence of stripes at about 45° propagating from top to bottom. For the two other higher kinetic energies 8.1 eV in panel g), and 11.7 eV in panel i), there is the persistence of three isolated circular areas, resembling the previously cited results of MOx in Figure 5.6. The comparison of the experimental data with the numerical calculation in the right column of Error: Reference source not found shows an overall agreement of features and signs of the differential PECD for all energies after some fine-tuning of the theoretical model. The PECD effect is indeed very sensitive to the variation of photoelectron energy.

The small discrepancies between theory and experiment in the differential PECD lead to a poor estimation of the integral b_1 parameter shown in Figure 5.8. The robustness of the experimental results is supported by the agreement with both a corresponding experiment conducted at the PETRA III synchrotron facility (DESY, Hamburg, Germany) using COLTRIMS, and the corrected version of a previous experiment conducted at the Stanford Synchrotron Radiation Lightsource (SSRL)
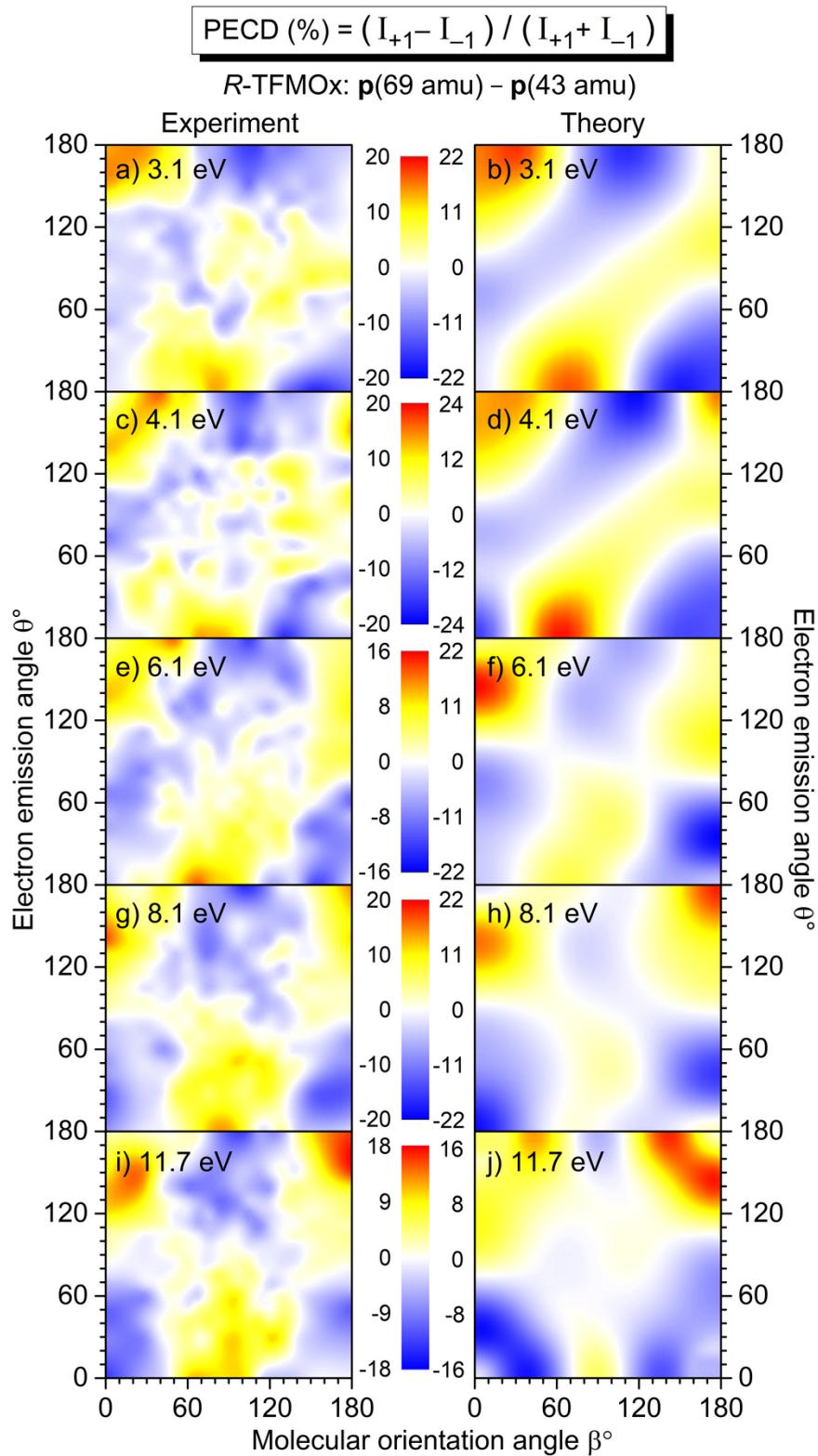
Figure 5.7: differential PECD values of uniaxially oriented R-TFMOx as a function of both the photoelectron emission angle θ, and the molecular orientation angle β for different kinetic energies of the O(1s) photoelectron as defined in equation (5.2). Left: experimental data,; right: theoretical predictions. The experimental data are the combination diatomic breakup channels CF_3^+ (m/q = 69) − $C_2H_{i=1,2,3}O^+$ (m/q = 41, 42, 43). Image reproduced from [154].

(SLAC, Menlo Park, CA, USA) with a VMI setup [155]. The results of the COLTRIMS experiments are in perfect agreement, while the VMI data shows a good agreement for low energies on averaged values, but taking into account the propagation of errors the comparison become meaningless (see appendix B.4).
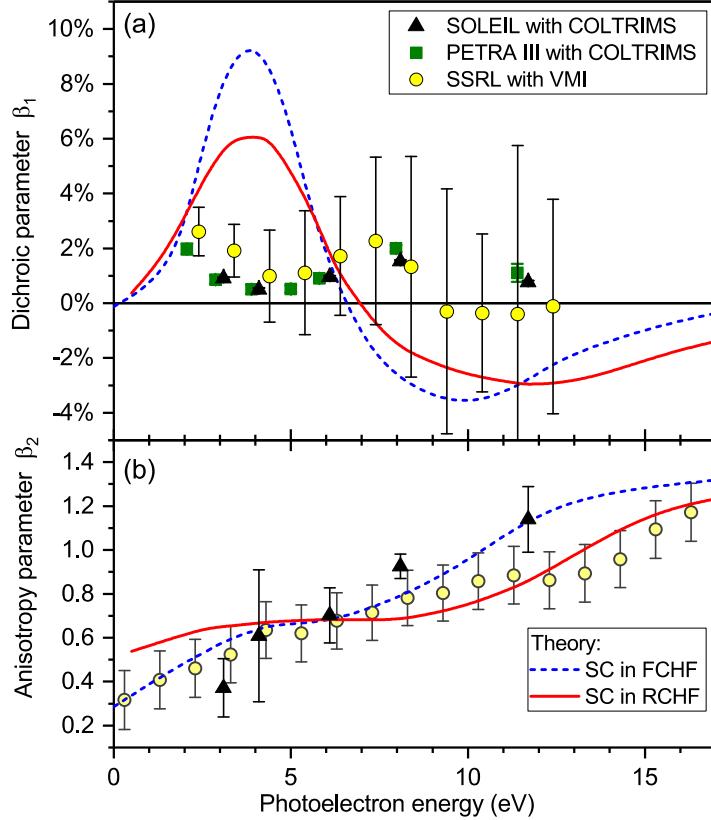
Figure 5.8: Comparison between two theoretical models (SC) and three experimental results for b_1 and b_2 parameters for randomly orientated TFMOx. The present work is represented by black triangles, the green squares represent a confirmation experiment with the same setup at a different facility, and the yellow circles the corrected value for a different setup and facility from [155]. Image adapted from [154].

The refinement of the model from using a frozen-core (FCHF) to a relaxed-core Hartree-Fock (RCHF) lowers the discrepancy between experimental and theoretical data for low energies, although the curvature is still opposite. The most striking difference is the inversion of sign for both the photoelectron energies of 8.1 eV and 11.7 eV.

Uniaxially orienting a molecule in space shows the possibility of using the PECD effect to detect and characterize chiral effects in photoelectron emission, with a great sensitivity for both the molecular structure and photoelectron energy. The

small effect of the energy could emerge from the averaging around one Euler angle, but the experimental results are in good agreement with the theoretical model.

5.3 Direct ionization: polyatomic breakup

In the following chapter, the polyatomic breakup channels mentioned in Figure 5.1 are analysed to study both the PA-MFPAD and the MFPADs from fixed-in-space molecules with their related PECD effect for TFMOx as a function of photoelectron energy. The use of at least three fragments, allows to completely fix the molecule in space. Giving access to both a PA-MFPAD, which are connected to the molecular structure, and MFPADs from fixed-in-space molecules, which are dependent on the relative angle between the molecule and the light's propagation direction. The MFPADs as function of the light's propagation direction are used to compute the fully-differential PECD histograms. Fully orienting the molecule in space is expected to strongly enhance the PECD signal, and for particular orientations the sensitivity towards the molecular structure as a function of the photoelectron energy could dramatically improve. Finally, a comparison of both the PA-MFPAD and MFPAD from fixed-in-space molecules along with their PECD effect is carried out between R-TFMOx and S-MOx, extending the results of chapter 5.2.2 regarding the influence of the substitutional group on the photoelectron interference patterns. Each enantiomer, each photoelectron energy, and each helicity have roughly the same number of recorded events: from the reactions (5.3) CH11 has $3.4 - 2.4 \cdot 10^5$, CH9 has $5.5 - 4.5 \cdot 10^5$, and CH12 has $1.9 - 1.5 \cdot 10^5$ depending on the energy considered; the MOx dataset from [156] has $3 \cdot 10^6$ events for each enantiomer and helicity for a singe photoelectron energy. All the experimental and theoretical data shown in this section are processed using a method described in appendix B.5, and the datasets from opposite helicities are combined to improve statistics employing the same procedure described in the previous chapter.

5.3.1   Polyatomic channels selection

The three incomplete polyatomic reaction channels considered in the following analysis are all ring-opening reactions summarized in (5.3), ordered by descending tof of the second fragment. The breakups in (5.3), correspond to the first two clusters of features from the left in top panel of Figure 5.1.

$$
\begin{aligned}
\text{CH12:} \quad & C_3H_3F_3O + \hbar\omega \rightarrow CF_3^+ + CH_2O^+ \quad + CH^0 \quad\quad\quad + e_{ph}^- + e_{Auger}^- \\
\text{CH11:} \quad & C_3H_3F_3O + \hbar\omega \rightarrow CF_3^+ + C_2H_{i=1,2,3}^+ + OH_{(4-i)}^0 \quad + e_{ph}^- + e_{Auger}^- \quad (5.3) \\
\text{CH9:} \quad & C_3H_3F_3O + \hbar\omega \rightarrow CF_3^+ + CH_{i=0,1,2,3}^+ + CH_{(3-i)}O^0 + e_{ph}^- + e_{Auger}^-
\end{aligned}
$$
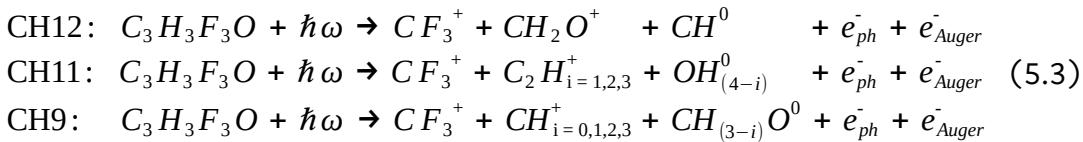
From the top of (5.3), the reactions are labelled CH12, CH11 and CH9 respectively. All reactions share the same CF_3^+ (m/q = 69) fragment as the heaviest; the CH12 has a single CH_2O^+ (m/q = 30) fragment and all possible subsequent losses of a hydrogen (e.g., CH_3O^+, CHO^+, and CO^+) are suppressed i.e., not recorded; both the CH11 and CH9 breakups show a subsequent ionization of the methyl group from the $C_2H_{i=1,2,3}^+$ (m/q = 25, 26, 27) fragment for CH11, and the $CH_{i=0,1,2,3}^+$ (m/q = 12, 13, 14, 15) one for CH9. All channels consist of an undetected neutral, and, despite the incomplete nature of the breakups, it is possible to retrieve the neutral momentum vectors from momentum conservation $\mathbf{p}_{neutral} = -(\mathbf{p}_0 + \mathbf{p}_1)$ where the two detected fragments are labelled 0 and 1 respectively, according to their flight time (i.e., mass). The PIPICO spectrum of all breakup channels is shown in Figure 4.25: the broader features compared to the purely diatomic channel of Figure 5.2 suggest the presence of a neutral fragment in the breakup reaction. Parallel lines in the histogram represent a subsequent loss of an H atom resulting in identical ionization dynamics, where each lost H atom does not carry away much momentum, thus parallel. The latter observation is confirmed by the Newton plots later considered in this chapter, and allows to group the sub-channels into a single one for the post-analysis. Different inclinations of the observed lines suggest a different redistribution of mass among the fragments, therefore potentially different fragmentation dynamics. Despite the very similar tof, a clear example of the former is the difference between the first three lines (i.e., CH11) and the last single line (i.e., CH12) in the right panel

of Figure 5.9. Usually, different channels display different fragmentation dynamics as investigated in great detail in the next chapter.

Having three coplanar momentum vectors, makes it possible to define a molecular frame MF, thus orienting the molecule in space as described in chapter 5.3 , but it does not allow assigning directly the handedness of the molecule. MFPADs are used to access the handedness of a chiral molecule instead.
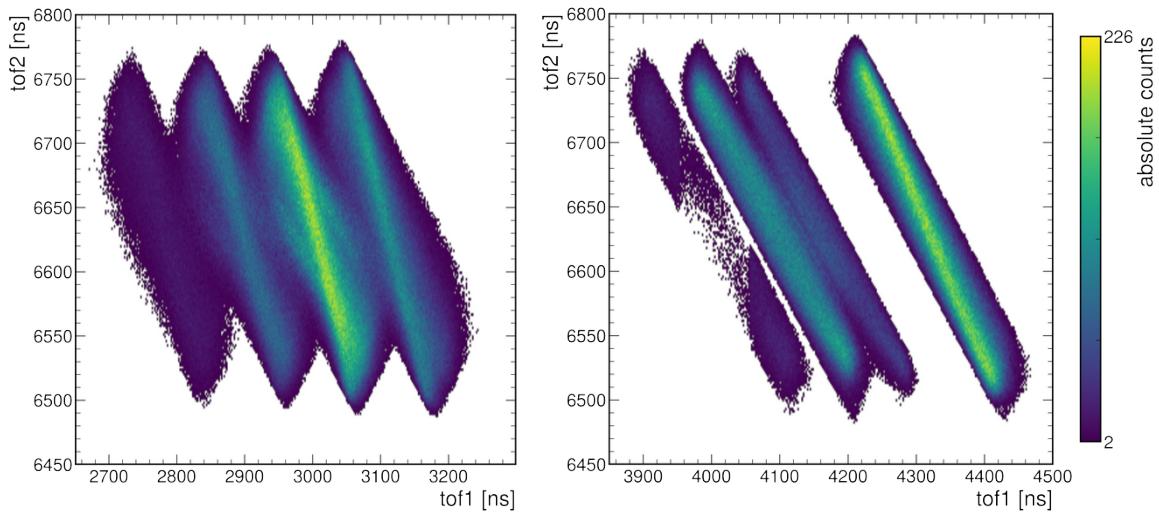
Figure 5.9: PIPICO histograms of the three polyatomic channels of R-TFMOx at 11.7 eV photoelectron energy, linear scale: left CH9, right CH11 (three lines) and CH12 (single isolated line). CH9 and CH11 show parallel lines indicating the ionization of the methyl group, in CH12 the ionization is suppressed . The first line from the left of CH11 is not complete due to gating conditions on the fragment 1 momentum distribution.

5.3.2 Molecular frame (MF) definition

Within a polyatomic breakup channel composed of three fragments, each associated with a well-defined momentum vector, it is possible to define a fragment frame (X, Y, Z) and use it to determine the orientation of the molecule in space. The fragment frame is just loosely linked to the molecular bonds which might "naturally" define the MF (x', y', z'), and the two are typically skewed by some unknown angles (α, β, and γ the Euler rotation angles with respect to the X, Y, and Z fragment axes, respectivelly) due to some rotation of the fragments frame after the breakup. The angles can be calculated by matching the position of distinct structural features of the experimental and theoretical PA-MFPAD of a molecule, as described in a recent paper by K. Fehre et al. [156]. In the case of

MOx, the recursive method implemented estimates the rotation angles to be in the order of few degrees, as qualitatively visible comparing the experimental and theoretical PA-MFPADs. Although the rotation optimization for TFMOx was not performed, the difference in the theoretical and experimental PA-MFPAD shown in Figure 5.14 suggests only a small rotation as well, therefore the fragments frame is considered to be equal to MF (i.e., x' = X, y' = Y, and z' = Z).

By definition, three non-degenerate fragment emission directions[22] lie on a plane, are enough to fully orient the correspondent molecule in space leaving only one degree of freedom for the plane versor. In principle, using the momentum vectors of at least four fragments allows to both determine the orientation of a molecule in space and its handedness in a pure CE approach [129]. In the latter condition, long data collection times for a suitable amount of valid events for each degree of freedom of the observables would be required. The reasons for longer collection times are a) the COLTRIMS detection efficiency decreases drastically with the number of charged fragments detected in coincidence, and b) polyatomic fragmentation channels with more than three charged fragments may experience more complex breakup dynamics for larger molecules. Thus, in this work, polyatomic channels with two charged fragments and a neutral have been selected to circumvent the former problems and are the only ones considered.

$$
\begin{aligned}
\hat{z}' &= \frac{p_1 \times p_0}{\|z'\|} \\
\hat{y}' &= \frac{(p_1 \times p_0) \times p_{neutral}}{\|y'\|} \\
\hat{x}' &= \frac{\hat{y}' \times (p_1 \times p_0)}{\|x'\|}
\end{aligned}
\tag{5.4}
$$

In a breakup, the momentum vector of an undetected neutral fragment can be retrieved using momentum conservation; in the following analysis the events close to zero-sum were removed to improve the quality of MF definition. The MF is by definition randomly oriented with respect to the LF. It is possible to arbitrary define the MF as described in the set of equations (5.4) with the CF_3^+ vector as p_1,

---

22   If the there fragments are degenerate, they lie on a line (or a point) in space, making it impossible to define a unique MF.

and $C_2H_i^+$ vector as $\mathbf{p_0}$, observing that: 1) the x'-axis lies along the neutral fragment's emission direction, therefore the y'-axis and the $\mathbf{p_1}$ vector are not parallel, thus the system will be optimized using a rotation. 2) the spherical coordinates θ and φ of the photoelectron are defined in the MF with respect to the z'-axis and on the x'-y' plane, respectively. Using the MF, subset of data can be selected (i.e., post-alligned) according to a specific photon propagation direction, and the z'-axis is aligned to it, as described in chapter 5.3.3.
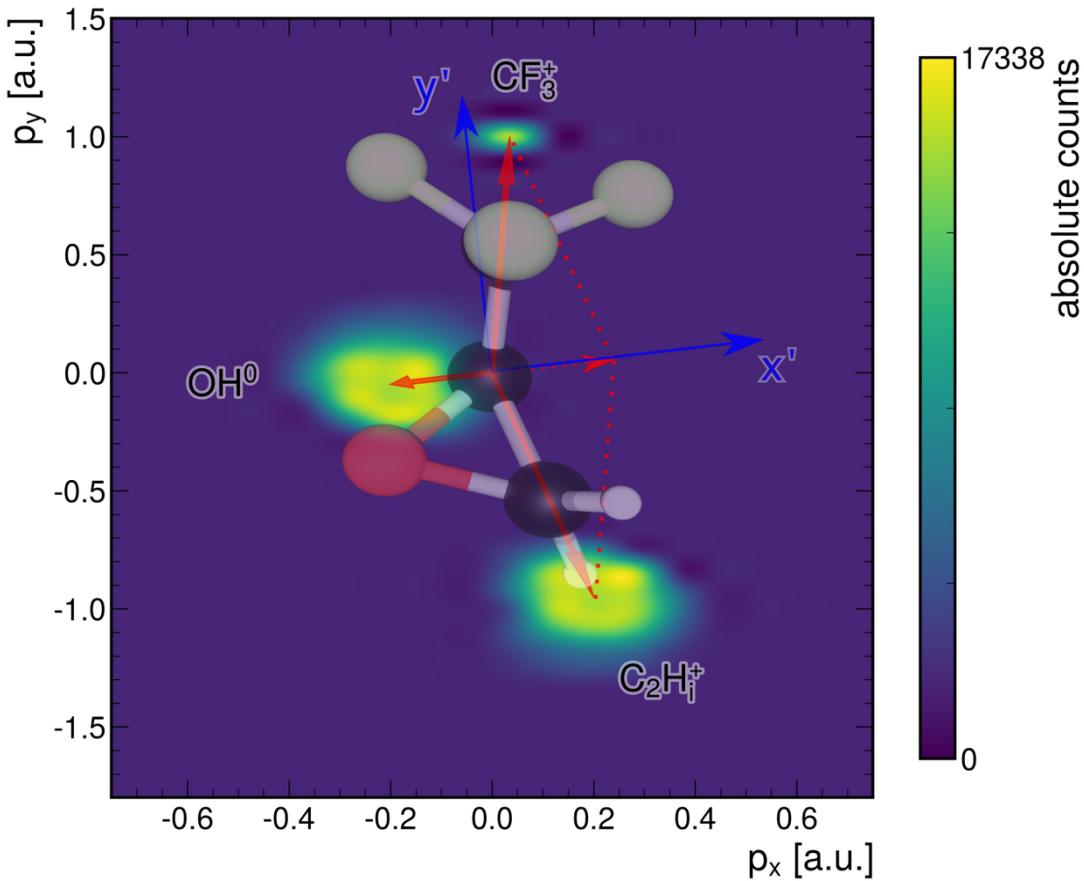
Figure 5.10: momentum vectors distribution of R-TFMOx CH11 with photoelectron energy 11.7 eV (red), and x'- and y'-axis of MF (blue). The momentum vectors are normalized to the CF_3^+ vector (i.e., $\mathbf{p_1}$), which therefore has unitary length. The momentum of the neutral fragment (i.e., OH^0, $\mathbf{p_{neutral}}$) corresponds to the opposite of the sum of the fragments' momenta; all three fragments lie on a plane. The circularly depleted area at the tip of the $C_2H_i^+$ vector (i.e., $\mathbf{p_0}$) corresponds to the elimination of the events close to zero-sum, and by definition it is replicated at the tip of the OH^0 vector. The the CF_3^+ momentum vector and the y'-axis are rotated around the z'-axis of about $\alpha = 4.6°$. By definition, the MF x'-axis and y'-axis are parallel and orthogonal to $\mathbf{p_{neutral}}$, respectively. Note: the x- and y-axis used here are a neutral system of reference.

An example of the momentum vector distribution for CH11 is shown in Figure 5.10: the distribution is normalized using the magnitude of the $\mathbf{p_1}$ vector CF_3^+, and all fragments momenta lies on the x'-y' plane. The momentum associated with the

neutral fragment lies close to the centre of the distribution, suggesting that it acquired a small amount of kinetic energy during the breakup. Within the validity of the axial-recoil approximation (see chapter 3.5), it is possible to deduce the position of the two external C atom and the O to be on the x′-y′ plane. The angle between the y′-axis and the CF_3^+ vector is used to rotate the MF around the z′-axis by the Euler angle $\alpha = -4.6°$ as a optimization. The position of the rotated and energy-optimized atomic structure for each of the two enantiomers of TFMOx is reported in spherical coordinates in Figure 5.11. The x′-y′ plane is identified in spherical coordinates, by definition, by the line $\cos\theta = 0$. In such defined system of reference, an inversion of enantiomer corresponds to mirroring with respect to the line $\cos\theta = 0$ i.e., z′-axis in Cartesian coordinates. Further rotations of the molecule around the z′-axis (e.g., the Euler angle α according to the convention described in appendix B.6) correspond in spherical coordinates to a rigid shift of the position of the atoms along the angle φ axis.
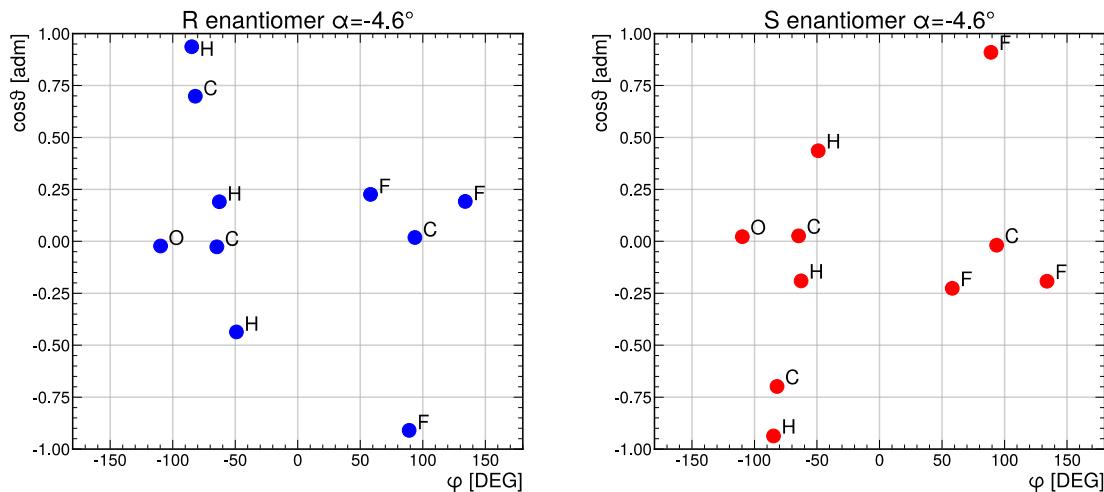

Figure 5.11: Optimized position of each atoms of R-TMOx (left) and S-TMOx (right) in spherical coordinates (defined in appendix B.6). Within the axial-recoil approximation, the two external C and O atoms lie on the x′-y′ plane i.e., $\cos\theta = 0$. The rotation of the molecule is calculated from Figure 5.10 as the angle between the y′-axis and the CF_3^+ momentum vector (i.e., $\mathbf{p_1}$) that corresponds to the Euler angle $\alpha = -4.6°$. Such rotations are mapped to a rigid translation along the φ-axis in spherical coordinates. The enantiomer inversion corresponds to mirroring the atoms' coordinates about the line $\cos\theta = 0$.

An alternative and more concise way to show the fragments' momentum vectors is using the Newton diagrams. Newton diagrams can be applied to uncover fragmentation dynamics and are closely related to the KER of the breakup. A Newton plot for polyatomic breakups shows the particles' momentum vectors

in the MF with respect to the centre of mass (c.m.) of the fragments with one of the fragments' momentum vector being used as a scaling factor. In a three-fragments breakup, the momentum vector of the first fragment is used as a scaling factor, therefore represented by a unitary vector, while the momenta of the other two fragments are mapped in the upper and lower halves of a Newton plot, respectively as shown in Figure 5.12 and Figure 5.13 for various reaction channels.

In just few cases, a Newton plot directly reveals the true fragmentation mechanism, and predictions of a model should be used to provide a comprehensive study [157], nevertheless much information of crucial interest about the type of fragmentation can be retrieved, and different fragmentations dynamics identified [158]. In a Newton representation, the more distant from the centre a feature is, the faster the fragment has been ejected. Furthermore, two opposite cases can be identified: on one side circular/arc structures indicate *sequential* or *stepwise* fragmentation processes; by the contrary well-define spots indicate a *single steps* CE. In between the latter two, an *asynchronous* type of breakup is possible in which the fragmentation occurs in one step, but it is preceded by molecular vibrations and/or rotations. For a stepwise fragmentation, if the angular velocity of the molecule after first ionization step is comparable with the fragment's ejection-time, the fragments' momentum distribution is bent describing an arc or a circle; the longer the time between the first and the second fragmentation step, the more isotropic the fragment distribution is. The validity of the axial-recoil approximation is tightly related with well-defined narrow spots in Newton plots, which provides an unambiguous definition of the MF.
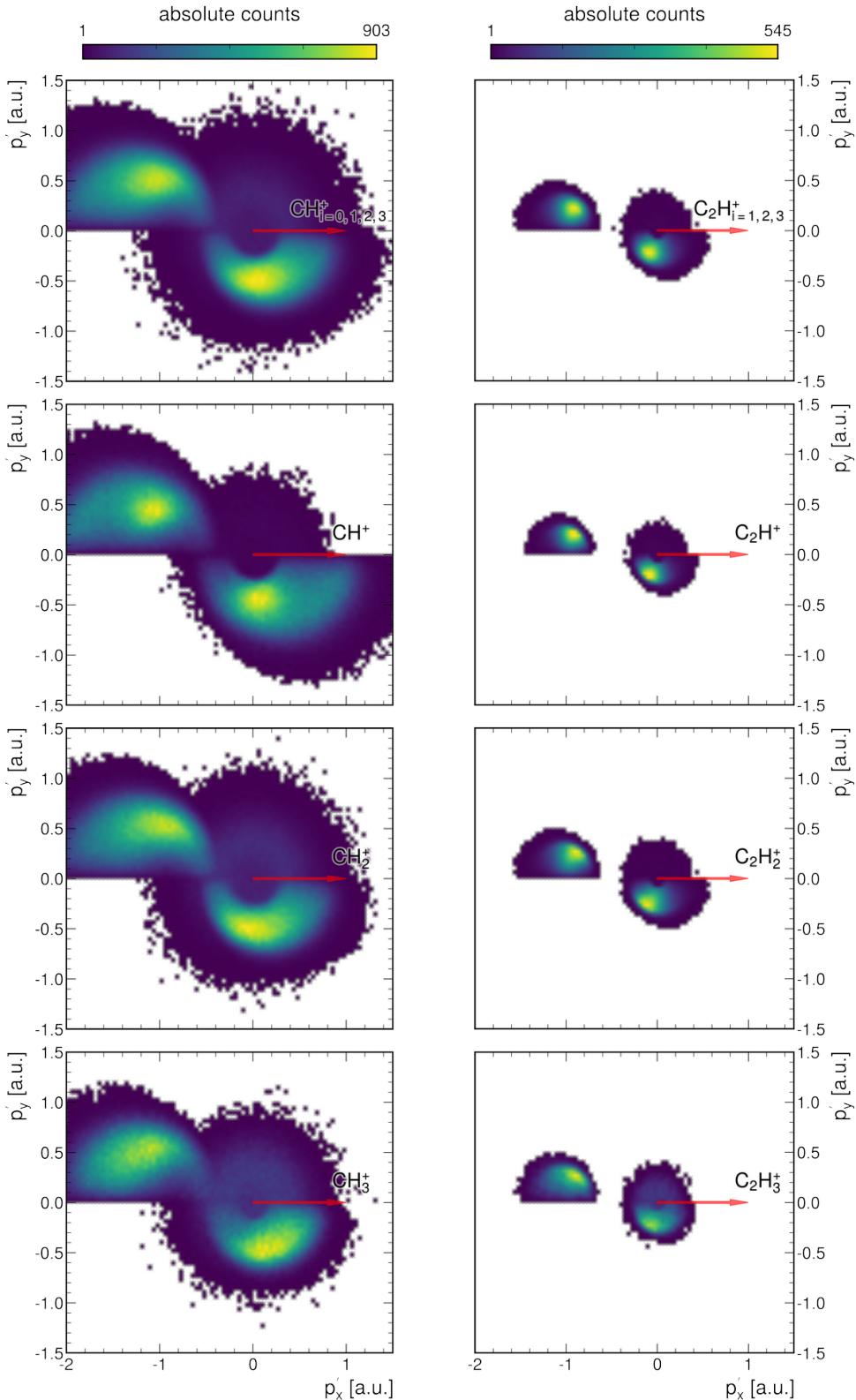
Figure 5.12: Newton diagrams for CH9 and CH11 breakup channels. First column CH9 breakup: top is the sum of all breakups, going down the single three breakups ordered by ascending mass of the reference fragment CH_i^+. Second column CH11 breakup. In contrast with CH9, the latter CH11 shows for each fragment clearly separated distributions, with low dispersion and closer to the centre of the graph; the latter are all signs of an ultrafast breakup. Note the central circular area belong to the neutral fragment of each breakup.

In both Newton diagrams in Figure 5.12 and Figure 5.13, the first detected fragment's momentum $\mathbf{p}_0$ defines the x-axis, and it is represented by the unitary red arrow. The top panel of each column in Figure 5.12 depicts collective data of all the breakups. The two columns in Figure 5.12 show two breakups channels CH9 and CH11, respectively. In the right column, the momentum distributions of each fragment for the CH11 channel are well separated, and not bent, suggesting a single step CE. By contrast, the left column the CH9 channel shows a bent distribution, suggesting a *stepwise* fragmentation: the arc is populated by events in which the molecular fragment rotates after the first one is ejected, before breaking into two fragments. Moreover, the differences for the CH11 channel across several breakup channels (i.e., panel 2 - 4) are small and overall similar to their combination (i.e., top panel 1). On the contrary, for the CH9 channel there is a significant difference of the position of the main peaks for the channels CH^+ and CH_2^+ (i.e., panel 2 and 3, respectively), and the channel CH_3^+ (i.e., panel 4): they appear to be rotated anti-clockwise compared to the latter two distributions, probably due to further vibrations or rotation occurring specifically in CH9 channel.

In Figure 5.13, the cumulative Newton plots for the CH11 channel (left) and the single ones for the CH12 channel (right) are reported. Despite both breakups show well separated distributions suggesting a direct CE fragmentation, the localization of the features for the CH12 channel is poor, and a central ring linked to the neutral fragment is present. The Newton plot for the CH12 channels suggests either a *stepwise* fragmentation, or an *asynchronous* one. In conclusion, according to the Newton plots, the CH11 channel is the only one showing a *direct* CE fragmentation, therefore displaying a sufficiently fast breakup dynamics to comply with the axial-recoil approximation. All breakup (sub)channels of the CH11 reaction show similar fragmentation dynamics, therefore can be combined together to describe the same MF i.e., not rotated with respect to each (sub)channel.
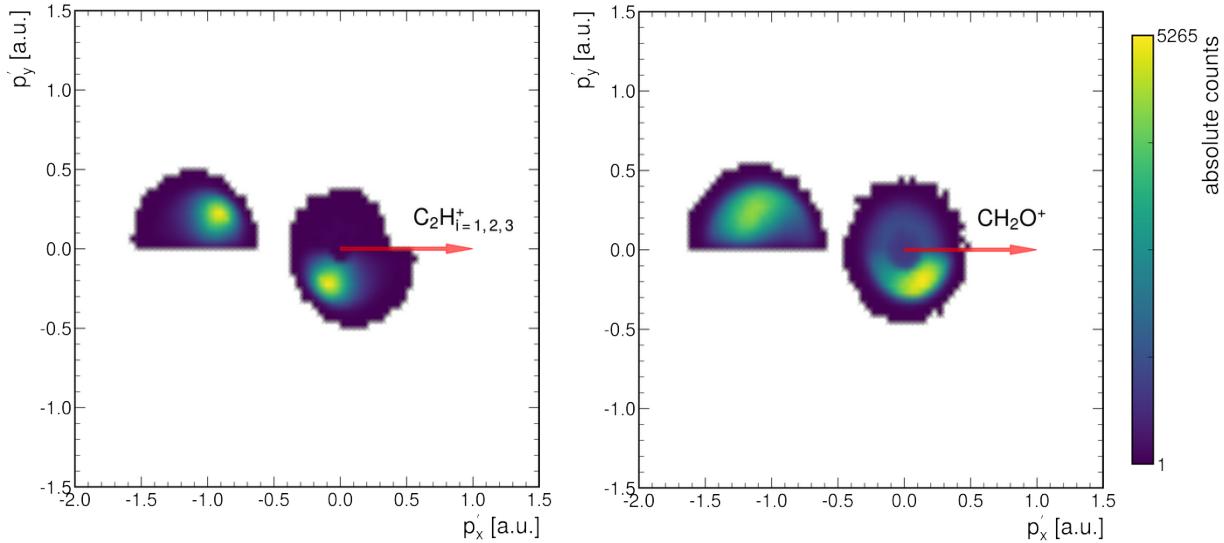
Figure 5.13: Newton plots, comparison: left the sum of all breakup channels of CH11, right the single breakup channel CH12. The only channel further analysed is the CH11 due to the higher likelihood of ultrafast breakup which is a fundamental condition for the axial-recoil approximation to hold.

The influence of the photoelectron energy on the Newton plots, thus on the MF definition, is marginal, because of the small momentum carried by the photoelectron. A complete series of Newton plots for all photoelectron energies is reported in appendix B.8.

### 5.3.3 Polarization-averaged MFPAD

For the K-shell electrons, the MFPAD often shows a reminiscence of a dipolar emission pattern with respect to the photon polarization direction [94]; other more meaningful features in the distribution to probe the molecular structure are emerging mainly from the scattering on the molecular potential (see chapter 3.1). To mitigate the influence of the dipole, a MFPAD integrated over all light's propagation directions can be examined, called polarization-averaged MFPAD (PA-MFPAD). It has been shown both theoretically and experimentally that a PA-MFPAD is very sensitive to the molecular geometry [159], and its photoelectron interference patterns vary greatly with the photoelectron energy [96]. In a recent work from K. Fehre et al., a PA-MFPAD has been successfully used to determine details of the molecular structure of MOx with a sensitivity to the C-H bond length down to 5% of the computed energy-optimized one [156].
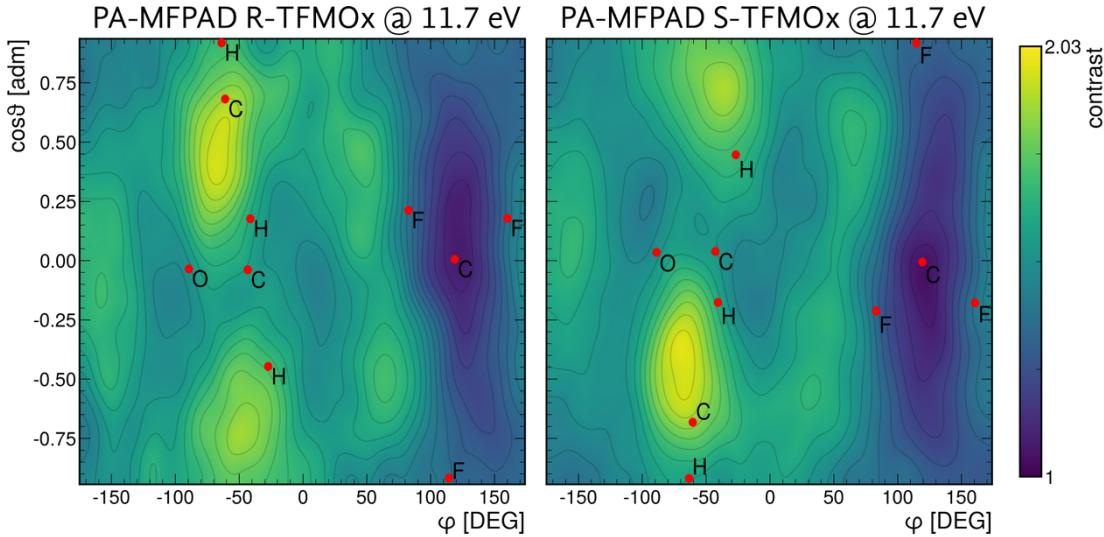
Figure 5.14: PA-MFPAD of R- and S-TFMOx for the second breakup line of CH11 at 11.5 eV, which corresponds to a photon energy of 550 eV. Both MFPADs are the sum of LCP and RCP polarization. Note the symmetry for reflection between the two histograms with respect to to $\cos\theta = 0$. The position of the atoms is taken from Figure 5.11 for both enantiomers.

By definition, a PA-MFPAD is independent of the light's polarization (i.e., linked to the light's propagation direction as described later in this chapter), and it shows a symmetry around the $\cos\theta = 0$ axis upon switching enantiomer *or* helicity as shown in Figure 5.14, confirming the chiral nature of the emerging emission pattern; a normalized difference upon switching enantiomers is computed to provide a sanity check of the chiral molecular geometry. For each of two enantiomers of TFMOx shown in Figure 5.14, the histograms are computed using the sum of LCP and flipped RCP histograms to increase statistics; the perfect flip along the $\cos\theta = 0$ axis proves the sensitivity of the PA-MFPAD to the chiral molecular potential. For the photoelectron energy 11.7 eV it is possible to further add the two enantiomers flipping one (e.g., S) along $\cos\theta = 0$ to further increase the statistics e.g., roughly 4 times compared to a single-helicity dataset, a technique used in the experimental data shown in Figure 5.15, Figure 5.16, and Figure 5.17.

The PA-MFPADs comparison between the experimental data at 11.7 eV photoelectron energy obtained as previously described, and the theoretical predictions at 11.5 eV photoelectron energy for R-TFMOx is reported in Figure 5.15, where both the absolute location, and partly the intensity of the main
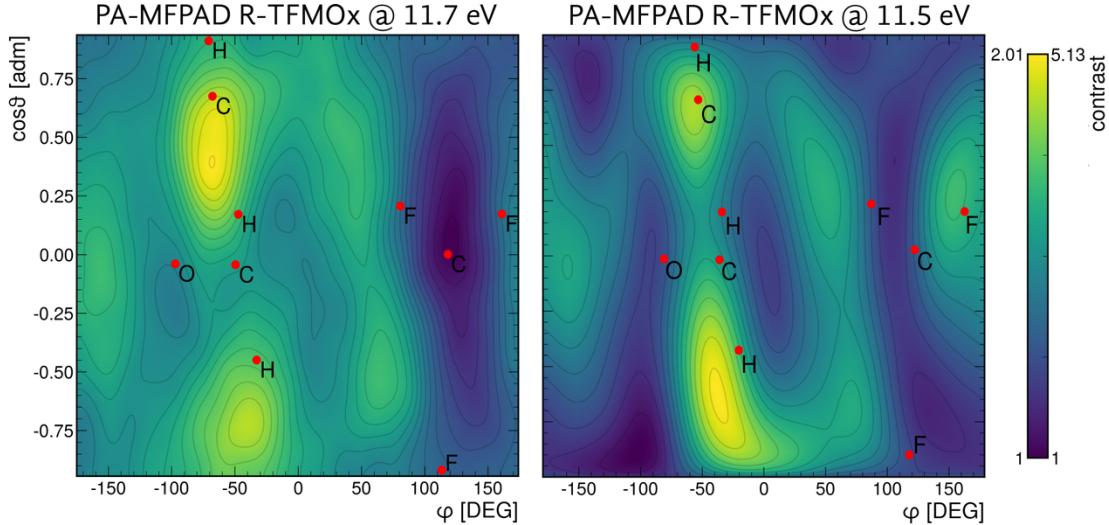
Figure 5.15: PA-MFPAD for CH11 at 11.7 eV. Left: experimental values for R + S flipped TFMOx combined, internal ticks on the colour scale; right: theoretical results for the R enantiomer, external ticks on the colour scale. All features have a good agreement, apart from the region along $\varphi = 150°$, where the CF_3 substitutional group is located. The position of the atoms is taken from Figure 5.11.

features for $\varphi < 140°$ are correctly reproduced by theory; the largest discrepancy is a peak at $\varphi > 140°$. The absolute contrast (i.e., the difference between absolute maximum and minimum) in the region $\varphi < 140°$ is more than 2 times lower for the experimental data compared to the theoretical calculations. Based on the position of the atoms in spherical coordinates shown in Figure 5.11, each area of an MFPAD and PA-MFPAD can be mapped to a specific part of the molecule, within the validity of the axial-recoil approximation and taking into account minor rotation of the MF.

The PA-MFPAD histograms in spherical coordinates can be shown in Cartesian coordinates and superimposed to the energy-optimized molecular structure of R-TFMOx to possibly identify the correlation with the molecular geometry, as shown for two photoelectron energies in Figure 5.16 and Figure 5.17, namely 11.7 eV and 3.1 eV, respectively. For both energies, the region at $\varphi < 140°$ shows features related to the oxirane ring, and the region at $\varphi > 140°$ is in close proximity to both the CF_3 group and the chiral C atom, which appears to be depleted in photoelectron emission. For the energy 11.7 eV, the former area has a typical ring structure which goes around the molecule; in the same area, for the energy 3.1 eV, most of the same features are present, but the one associated with

the C-H bond of the chiral C atoms are strongly depleted. The full energy progression is shown in Figure 5.21, and extensively discussed later in this chapter.

The PA-MFPAD directly reveals just partly the atomic bonds of the molecule, and the influence of the scattering CF_3 seems just partially reproduced by the theory. The apparent inconsistency between experimental data and theory prediction of the angular distribution from the oxirane ring and the CF_3 could be explained considering both the scattering dynamics of photoelectrons as described in chapter 3.3, and the fact the molecular vibrational modes re not averaged for the theoretical predictions. Due to the already richly structured and complex molecular potential, the interference between direct and scattered photoelectron waves are complex and sensitive to phase shifts induced by small differences in the molecular configuration (e.g., vibrational modes). The theoretical predictions are performed looking at a static energy-optimized geometrical structure: the former oxirane ring is a more rigid structure in comparison to the latter CF_3 which has several degrees of freedom. Although the timescale of molecular vibrations is much longer than the time required from the photoelectron to escape the molecular potential after direct and indirect scattering, the experimental data are the results of averaging over several conformations belonging to multiple vibrational modes. Furthermore, the reduction in contrast between experimental data and theoretical predictions can be associated with an uncertainty on the determination of the neutral fragment momentum vector and thus on MF definition. In general, performing an absolute and direct comparison between experimental and theoretical 3D-MFPADs requires the relative rotation of the MF, although small, to be corrected for as, shown in [156].
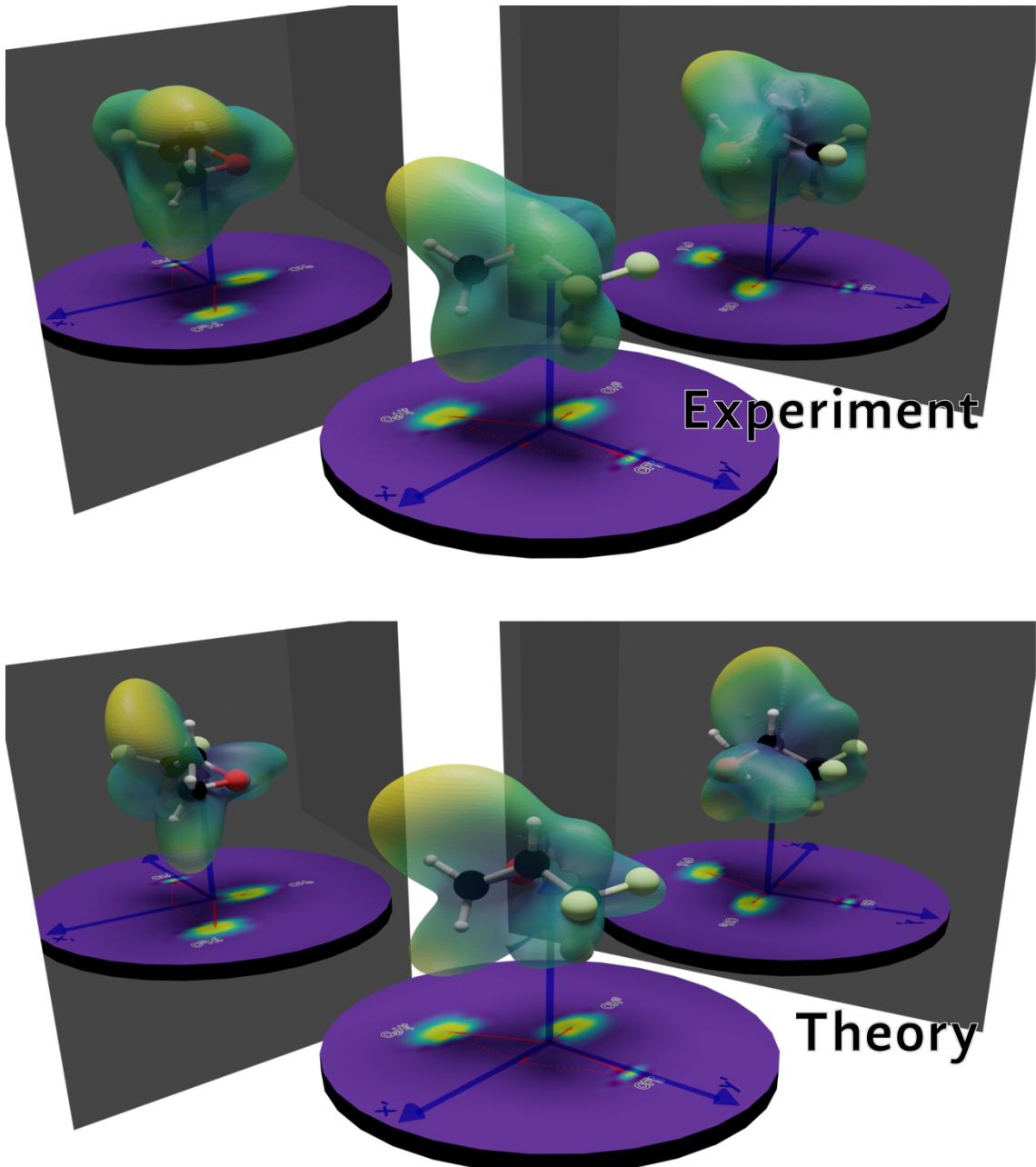
Figure 5.16: 3D sketches in Cartesian coordinates from Figure 5.14 of the experimental (top) and theoretical (bottom) PA-MFPAD of R-TFMOx at 11.7 eV and 11.5 eV respectively. The molecule is oriented according to the MF (x', y', z') shown as a blue system of reference on the disk at the bottom. The PA-MFPADs should share their centre of mass with the origin of the MF, but it is translated along the z' axis for the sake of clarity. Within the validity of the axial-recoil approximation, the two C and the O atoms lie on the x'-y' plane.
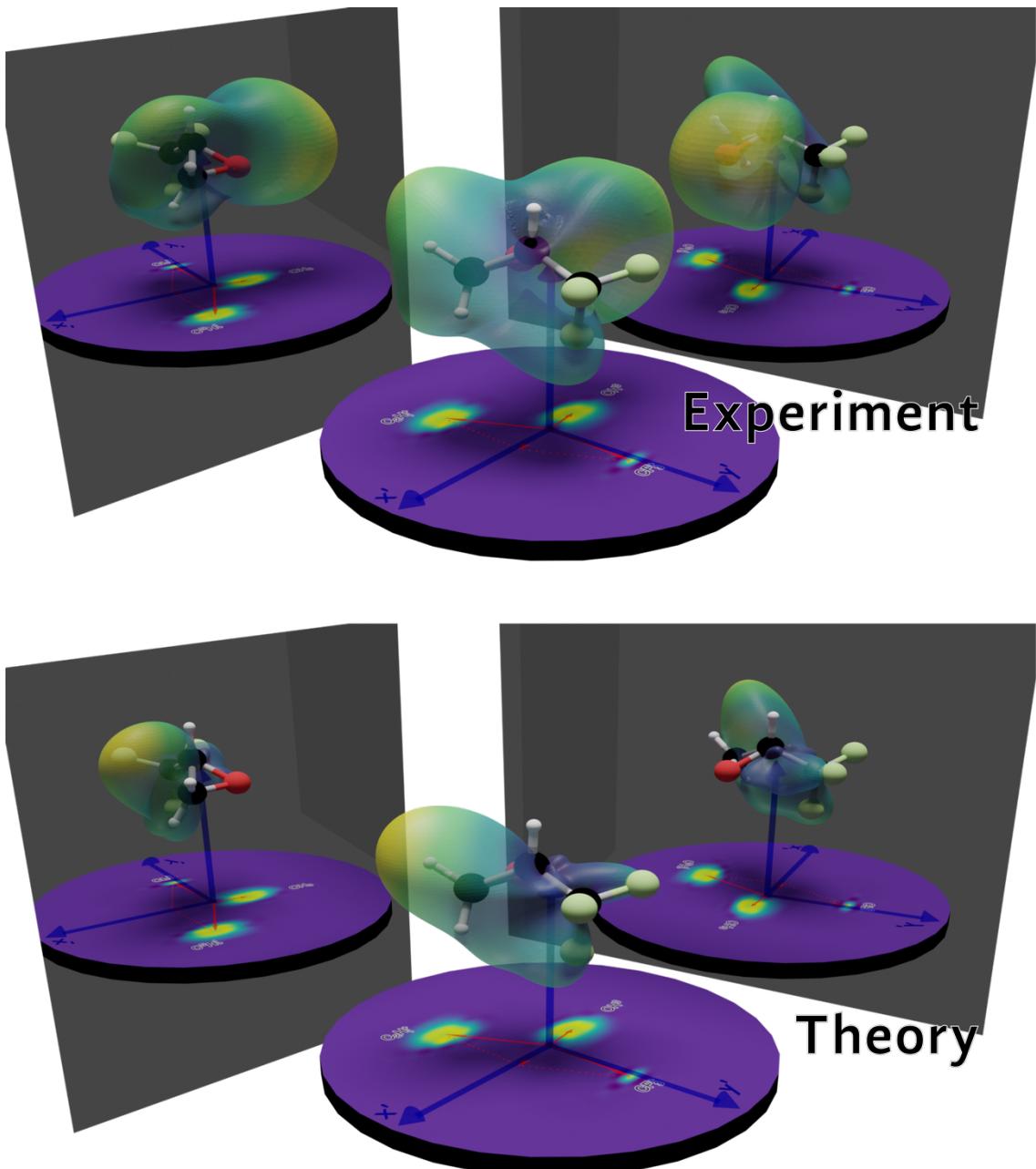
Figure 5.17: 3D sketches in Cartesian coordinates from panel e) of Figure 5.21 of the experimental (top) and theoretical (bottom) PA-MFPAD of R-TFMOx at 3.1 eV. The molecule is oriented according to the MF (x', y' z') shown as a blue system of reference on the disk at the bottom. The PA-MFPADs should share their centre of mass with the origin of the MF, but it is translated along the z' axis for the sake of clarity. Within the validity of the axial-recoil approximation , the two C and the O atoms lie on the x'-y' plane.

In Figure 5.18, the PA-MFPAD for CH9 and CH12 recorded at a photoelectron energy of 11.7 eV are presented; both PA-MFPADs show similar features with respect to CH11, but do not match the theoretical predictions shown in the second panel of Figure 5.14. The mismatch arises from an uncertainty in the definition of the MF in CH9 and CH12 due to the molecule's rotation prior to the breakup, and it confirms the breakdown of the axial-recoil approximation for CH9 and CH12. Although MFPADs and PECD can be expected for the former breakups, just CH11 will be considered further because of the promising comparison with the theoretical calculations and the MOx dataset.
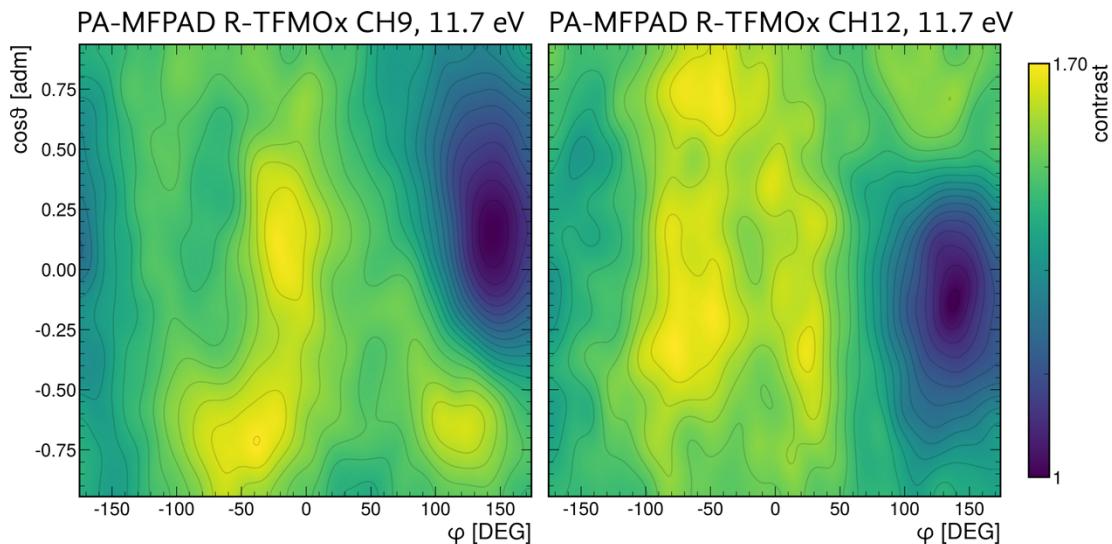
Figure 5.18: PA-MFPAD of CH9 and CH12 at 11.7 eV for R-TFMOx. The photon energy corresponds to a photon energy of 11.7 eV. Both PA-MFPADs are the sum of LCP and RCP polarization for both enantiomers and a final sum of R and S enantiomer flipped along $\cos\theta = 0$ axis. The constrast is lower than CH11.

Figure 5.19 shows the comparison between the experimental and theoretical PA-MFPAD of R-TFMOx and S-MOx from reference [156] at an electron energy of 11.7 eV and 11.5 eV, respectively. The theoretical calculations are performed with the single-centre (SC) in the RCHF approximation for MOx and FCHF for TFMOx. Most of the features at $\varphi < 120°$ are the same, at roughly the same photoelectron energy, in both molecules (i.e., the oxirane ring), but there is a large difference in the region $\varphi > 120°$ (i.e., the substitutional group). As previously mentioned, the latter area is associated with the CH_2 and oxirane ring that is identical across the two molecules, and the former one belongs to the different substitutional groups (namely CF_3 and CH_3), and the chiral carbon C. For TFMOx, the shape of the ring

is skewed, and the contrast is reduced compared to MOx by a factor of 1.5, a behaviour correctly predicted by the theory. The theoretical predictions in the region $\varphi > 120°$ retain a peak for both molecules, suggesting a lack of predicting-power for the complex scattering phenomenon in that region of the molecule.
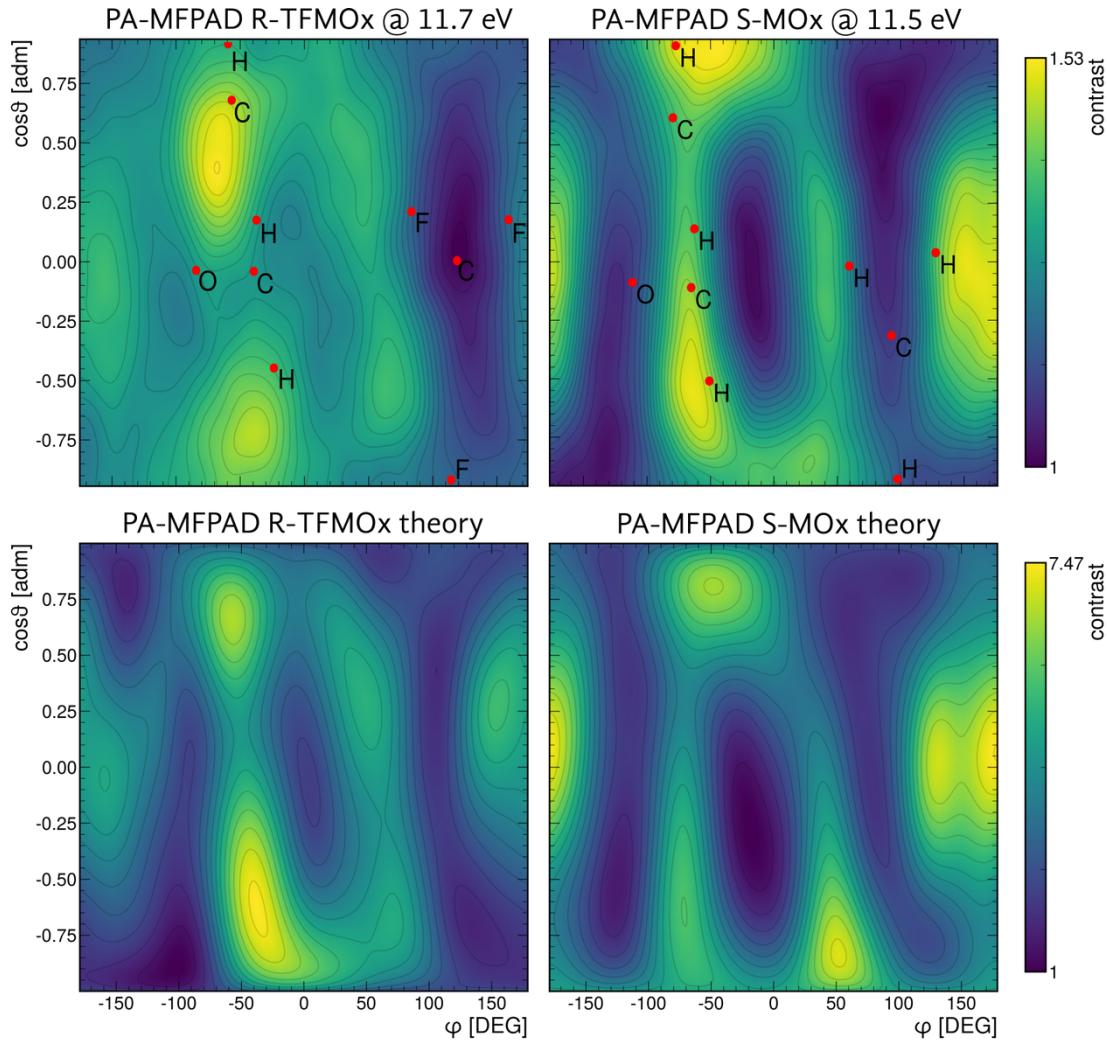
Figure 5.19: experimental (top) and theoretical (bottom) PA-MFPAD comparison between R-TFMOx CH11 at 11.7 eV (left) and S-MOx at 11.5 eV (right) adapted and reprocessed from reference [156]. Both PA-MFPADs are the sum of LCP and RCP polarization and the adapted (i.e., flipped) enantiomers, as previously described. The main discrepancy between the two distributions is the area at $\varphi > 120°$, where the substitutional groups CF_3 and CH_3 are located. Note the lower contrast within the ring structure at (0°,0) of R-TFMOx compared to S-MOx, and the higher contrast of theoretical calculations compared to experimental data (e.g., 4 times higher). The position of the R-TFMOx atoms is taken from Figure 5.11 and the one of S-MOx is obtained in the same way, therefore omitted.

The difference in interference patterns of PA-MFPAD between CH_4 and CF_4 molecules at low photoelectron energies has been reported in a theoretical work by E. Plésiat et al. [96]. In particular, remarkable changes in the emission distribution occur preferably from between the atoms at low energies, to along the bond at higher energies. A similar behaviour at low electron energies $(0-12\,\text{eV})$ has been confirmed for a $C_2H_2F_2$ molecule in a recent work by A. Menssen at al. [159]. The former systems are highly symmetrical and smaller compared to MOx and TFMOx. Therefore, it is much more challenging to directly assign features in the PA-MFPAD to geometrical features of the latter molecules because of the more complex interference patterns and the abundance of more complex vibrational modes. From the PA-MFPAD of Figure 5.19, the rigid oxirane ring seems to have a fingerprint visible on both the experimental data, and the theoretical predictions across the two molecular systems. Striking differences occur in the difference of contrast around $(0°, 0)$, and the different distributions around $(50°, 0.5)$; for TFMOx, the emission direction associated to CF_3 shows a depletion in the experimental data, but with large discrepancies with the theoretical predictions. The mismatch between experimental results and theoretical predictions could originate from the fact that the calculations are performed for one fixed geometry and no averaging o molecular vibrational mode has been performed. In general, the PA-MFPAD of larger molecules show features that cannot be assigned to individual bonds or scattering centres, but rather to collective interferences.

Experimentally, subsets of data are selected, with respect to the MF, according to 72 photon directions identified by $(\varphi_{ph}, \theta_{ph})$. The angle θ_{ph} is measured by convention with respect to z-axis in the LF, therefore, after the gating, the z'-axis is aligned along the light propagation direction. Theoretically, the photoelectron emission is directly calculated in the MF, each rotated by $(\varphi_{ph}, \theta_{ph})$ with respect to z-axis in the LF. Each computed MFPAD is therefore rotated back to the LF using the rotational matrix (B.13) using the Euler angles $\alpha = \varphi_{ph}$ and $\beta = \theta_{ph}$, thus the z'-axis is aligned to the z-axis in the LF i.e., the light propagation direction.
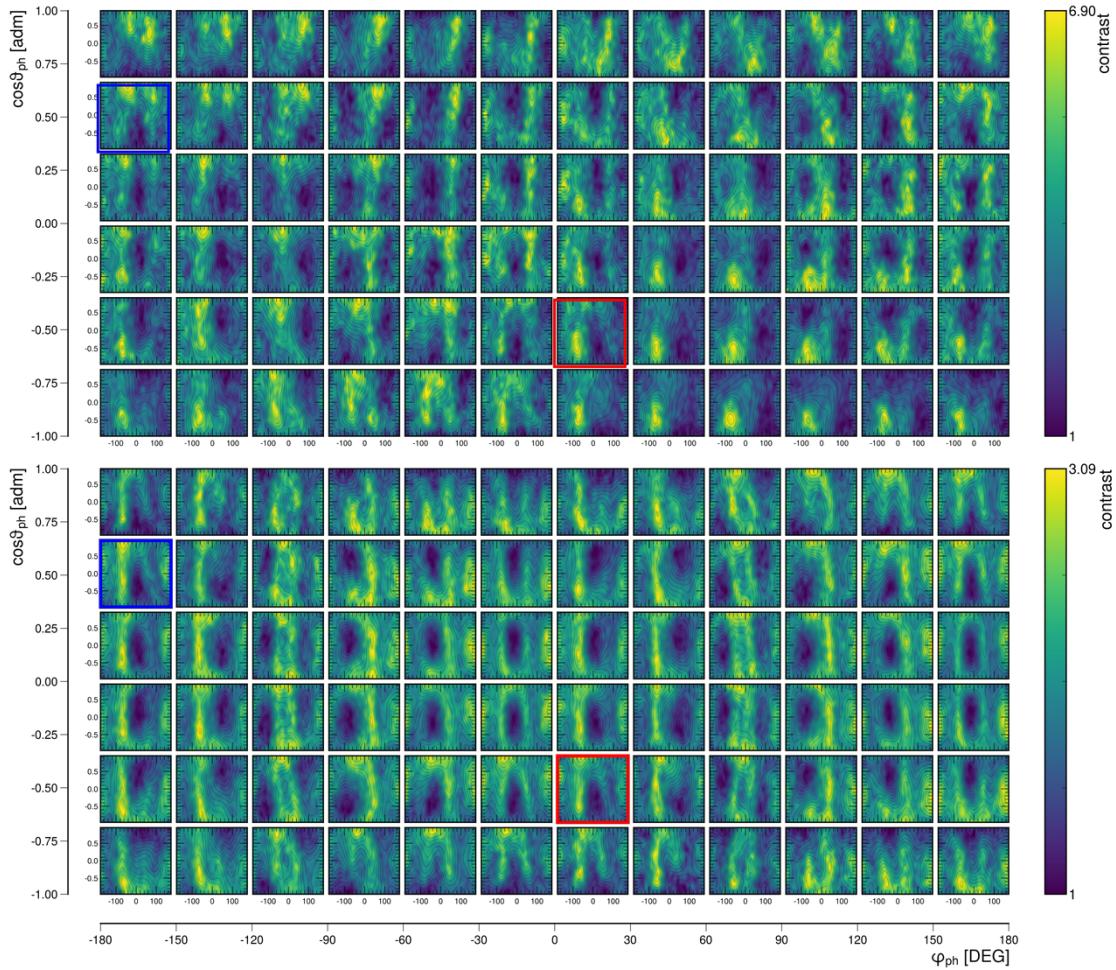
Figure 5.20: comparison of 72 the MFPADs of S-TFMOx (top) and R-MOx (bottom) at 11.7 eV and 11.5 eV respectively. The S-MOx data are adapted and reprocessed from [160]. Single MPFADs have higher contrast compared to the PA-MFPAD.

The fully-differential comparison of MFPADs for fixed-in-space S-TFMOx and R-MOx (adapted from [160]) for all light's propagation directions is shown in Figure 5.20 for 11.7 and 11.5 eV, respectively. The integration over all panels results in the respective PA-MFPADs of Figure 5.19. As already shown for CO in chapter 3.3, for each light's propagation direction the interference patters should be dominated by a toroid due to the photon spin with two minima orthogonal to the polarization plane corresponding the direction of the incoming photon (φ_{ph}, $\cos\theta_{ph}$). Figure 5.20 shows, however, a more complex behaviour: for some light's direction, there is just a single minimum moving according to $\cos\theta_{ph}$ (i.e., columns), and φ_{ph} (i.e., rows) as shown in the close up for two opposite helicities in Figure 5.24. Moreover, for most of the light directions, the same minimum seems to be more sensitive to $\cos\theta_{ph}$ rather than to φ_{ph}, especially for

$\varphi_{ph} = \pm 180°$. The latter observations hold in a consistent way for both systems (e.g., top panels S-TFMOx, bottom panels R-MOx in Figure 5.20). The remaining interference patterns surrounding each minimum across the two systems are similar just for some directions of the incident light, suggesting a different molecular potential. In particular, the area with $\varphi > 120°$ shows a relative minimum for S-TFMOx constant for all values of $\cos\theta_{ph}$, suggesting that the F atoms are reducing or hindering the interference of photoelectrons for all light's propagation directions, although not consistently reproduced by theory.

A comparison between experimental results and theoretical predictions for the five electron energies e.g., 3 eV, 4 eV, 6.1 eV, 8.2 eV, 11.7 eV is reported in Figure 5.21. As already observed for 11.7 eV electron energy, most of the features within $-120° < \varphi < 120°$ associated with the oxirane ring are correctly reproduced by the theory at all energies. In particular, it is possible to notice the progressive fading out of the area around $(50°, 0.5)$ for decreasing photoelectron energy. For $\varphi > 120°$ the peak associated with the CF_3 fragment is not correctly reproduced by theory: for the three highest energies is absent in the experimental data, but present in theoretical one, and vice-versa for the last two energies, where an inversion occurs. From the latter two energies a similar discrepancy is present for the area $\varphi < -120°$ too. The match between the experimental and calculated PA-MFPAD is overall satisfactory, but the experimental data show an area at $\varphi = 150°$ in the proximity of the CF_3 substitutional group of low interference for all energies which is not well reproduced by theory, especially at very low energies. The theoretical calculations with the HF-RCHF method are not accurate at low energies, and probably overestimate constructive interference patters in the proximity of the large F electron clouds.
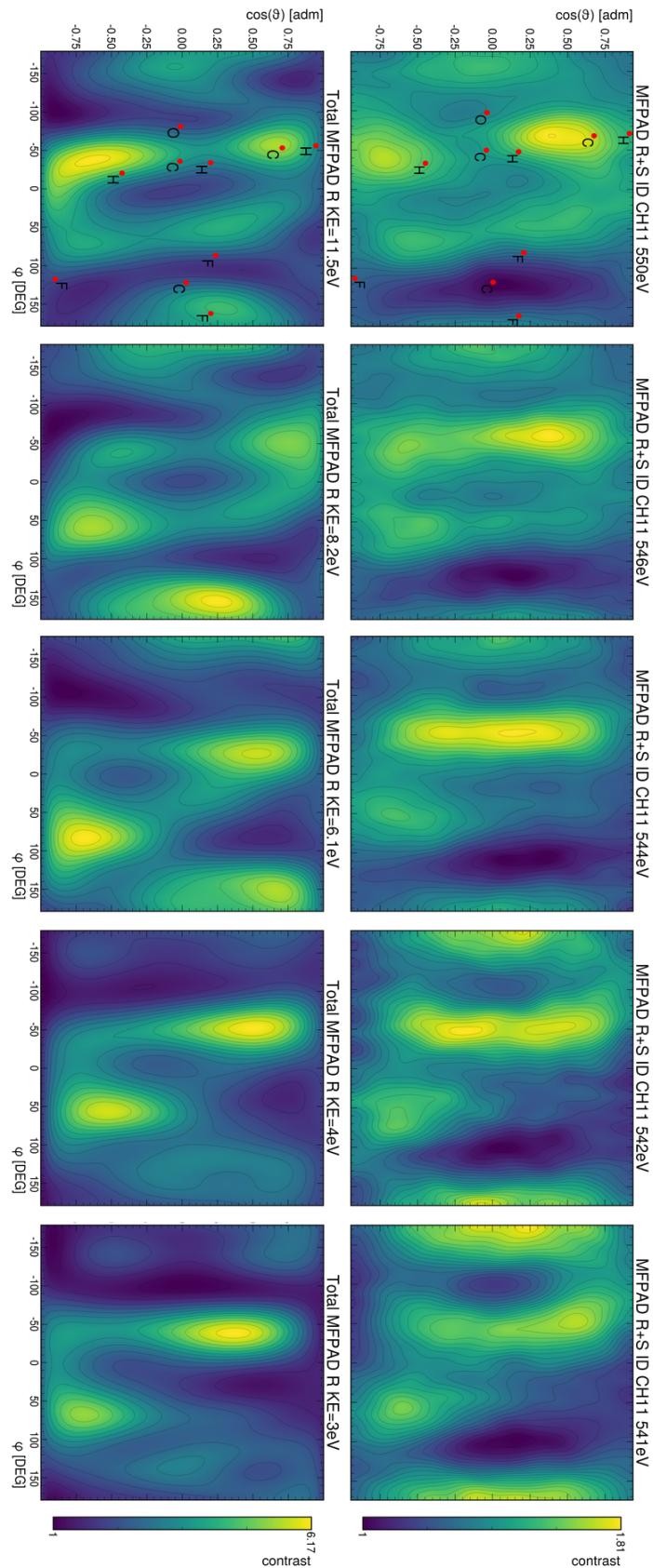
Figure 5.21: PA-MFPADs for R-TFMOx at multiple photoelectron energies. Right column: experimental data for CH11 created as a sum of LCP and RCP polarization, and the adapted enantiomers, as previously described (lower contrast). Left column: theoretical predictions (higher contrast). Position of atoms from Figure 5.11.

113

As previously mentioned, two PA-MFPADs of a chiral molecule are symmetric around $\cos\theta = 0$ upon switching light polarization or enantiomer. To quantitatively view the topological changes in the PA-MFPAD induced by chiral effects, contrast maps can be used. A contrast map is the normalized difference of two PA-MFPAD upon the change of light helicity and/or enantiomer. As for the PECD differential maps, a contrast map is computed using equation (5.2), but the β Euler angle is substituted by the φ angle as defined in equation (3.18). In contrast to differential PECD, a contrast map is independent from the the light's propagation direction. The results reported in Figure 5.22 show a perfect inversion symmetry around $\cos\theta = 0$, for both theoretical and experimental histograms at all energies, confirming the chiral nature of the investigated molecule; it is worth highlighting the profound difference in symmetry compared to the differential PECD maps of chapter 5.2, due to the integration over all light's propagation directions. The main features shown in the contrast maps are qualitatively predicted by theory, but there are differences in the absolute position of some peaks in the area $\varphi <$ 50°. The progressive fading of a peak in the area $\varphi > 0°$ for increasing energy is quantitatively well described. The magnitude of the contrast is roughly 3 times larger for the theoretical calculation; the latter can be explained by an artificial enhancement of chiral effects by theory due to a limited modelling of nuclear dynamics and a reduction of the chiral effect by the use of incomplete breakup channels which are more prone to noise resulting in uncertainties in the MF definition.
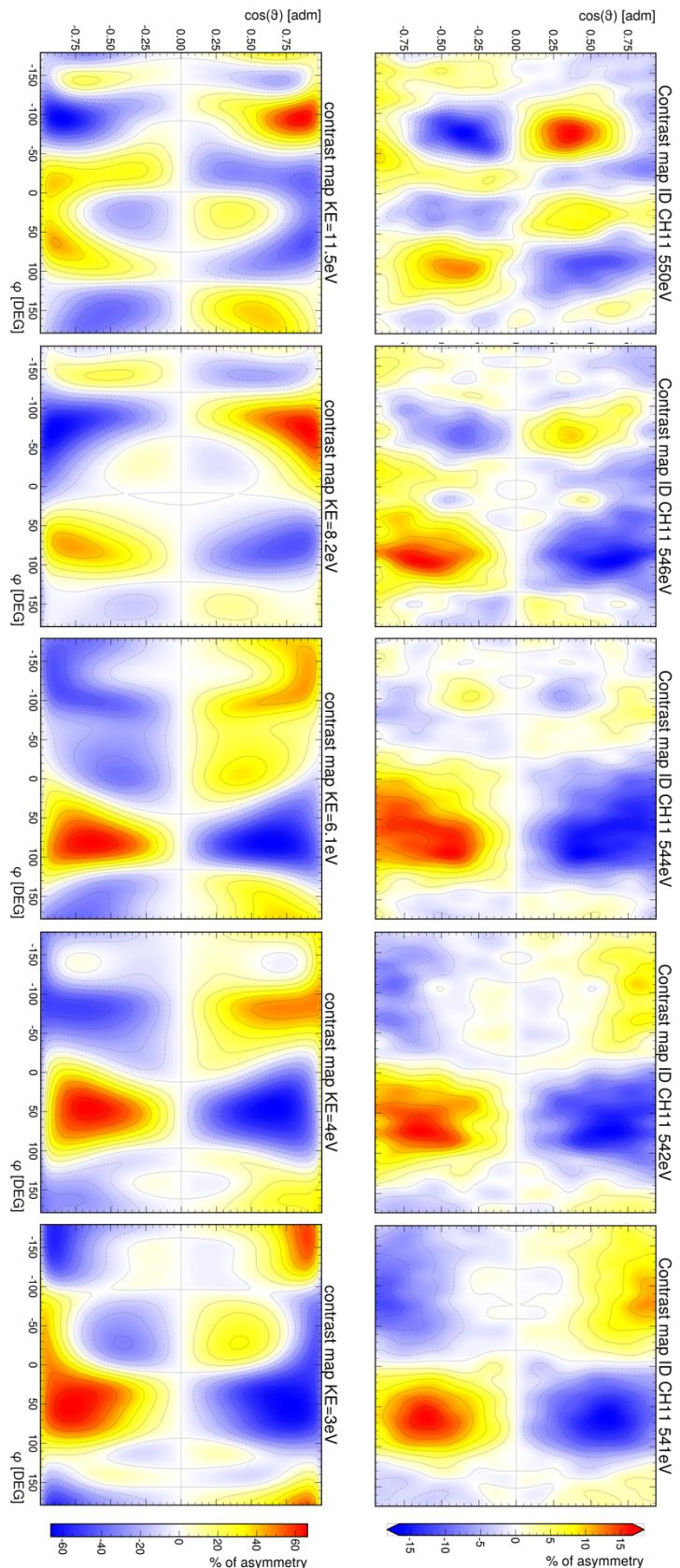
Figure 5.22: contrast maps of PA-MFPADs for R-TFMOx at multiple photoelectron energies. Right column: experimental data for CH11 created as a sum of LCP and RCP polarization, and the adapted enantiomers, as previously described. Left column theoretical. Note the scale of the theoretical data is three times the experimental one.

5.3.4   Polyatomic fully-differential PECD

Differential PECD, defined in equation (5.2), has been shown to be a very sensitive tool to study the photoelectron scattering on the molecular potential. As described in the previous chapter, it can be used complementary to PA-MFPADs and MFPADs for fixed-in-space molecules, to further probe the molecular structure. Completely orienting a molecule in space gives the possibility to arbitrary select a relative orientation of the molecule with respect to the light's propagation direction, therefore giving access to a set of single MFPADs (as already shown in Figure 5.20), and their correspondent fully-differential PECD. Using an arbitrary convention, the molecule is kept fixed and the light direction rotates, called a passive description of the system, equivalent to keeping the light source fixed and rotating the molecule's orientation. The light's propagation direction is described as a function of the two emission angles (φ_{ph}, θ_{ph}) in the LF according to the convention of spherical coordinates described in appendix B.6. In order to evaluate the fully-differential PECD, an electron interference pattern (i.e., a MFPAD) is rotated according to the associated light's propagation direction coordinates using the equation (B.13) assigning to the Euler angles the values $\alpha = \varphi_{ph}$, $\beta = \theta_{ph}$, therefore aligning to the z'-axis in the MF to the light's propagation direction. The rotated single MFPADs are used to compute the normalized difference as function of the usual spherical coordinates for electrons θ, φ in the MF upon switching light's helicity (i.e., fully-differential PECD effect), as described in equation (5.5) using the usual convention for the light's polarization p (e.g., +1 = LCP, see chapter 3.2).

$$PECD_{\theta_{ph},\varphi_{ph}}\left(cos\theta,\varphi\right)=\frac{I_{+1}^{\theta_{ph},\varphi_{ph}}\left(\theta,\varphi\right)-I_{-1}^{\theta_{ph},\varphi_{ph}}\left(\theta,\varphi\right)}{I_{+1}^{\theta_{ph},\varphi_{ph}}\left(\theta,\varphi\right)+I_{-1}^{\theta_{ph},\varphi_{ph}}\left(\theta,\varphi\right)}=\frac{I_{\theta_{ph},\varphi_{ph}}\left(\theta,\varphi\right)-I_{\theta_{ph}+\pi,\varphi_{ph}+\pi}\left(\theta,\varphi\right)}{I_{\theta_{ph},\varphi_{ph}}\left(\theta,\varphi\right)+I_{\theta_{ph}+\pi,\varphi_{ph}+\pi}\left(\theta,\varphi\right)} \quad (5.5)$$

The angles of inclination of the light are divided in 72 bins in constant steps of $\Delta cos\theta_{ph} = 1/3$ and $\Delta\varphi_{ph} = 30°$ in the domains $\theta_{ph} \in [0 , \pi]$ and $\varphi_{ph} \in [-\pi, \pi]$, respectively, to increase statistics; the coordinates are indicated on the external axis in all the following figures with 72 panels. Experimental data are presented in comparison to *ab initio* theoretical performed using the single centre (SC) FCHF

method for all photoelectron energies e.g., 3 eV, 4 eV, 6.1 eV, 8.2 eV, and 11.7 eV. An inversion of the light's propagation direction in the MF is equivalent to an inversion of the light helicity which corresponds to the combined transformation of the photon coordinates of $\varphi_{ph} \rightarrow \varphi_{ph}+180°$, followed by the mirroring $\cos\theta_{ph} \rightarrow -\cos\theta_{ph}$, as shown in the second term of equation (5.5). The former transformation holds for the positions of two panels highlighted by blue and red squares in all the following 72 MFPADs and 72 PECD histograms. A swap of enantiomer is equivalent to a reflection about $\cos\theta_i = 0$, where i indicates a reflection for both the photon (i.e., 72 light's directions θ_{ph}) and the photoelectron coordinates (i.e., θ within each panel).
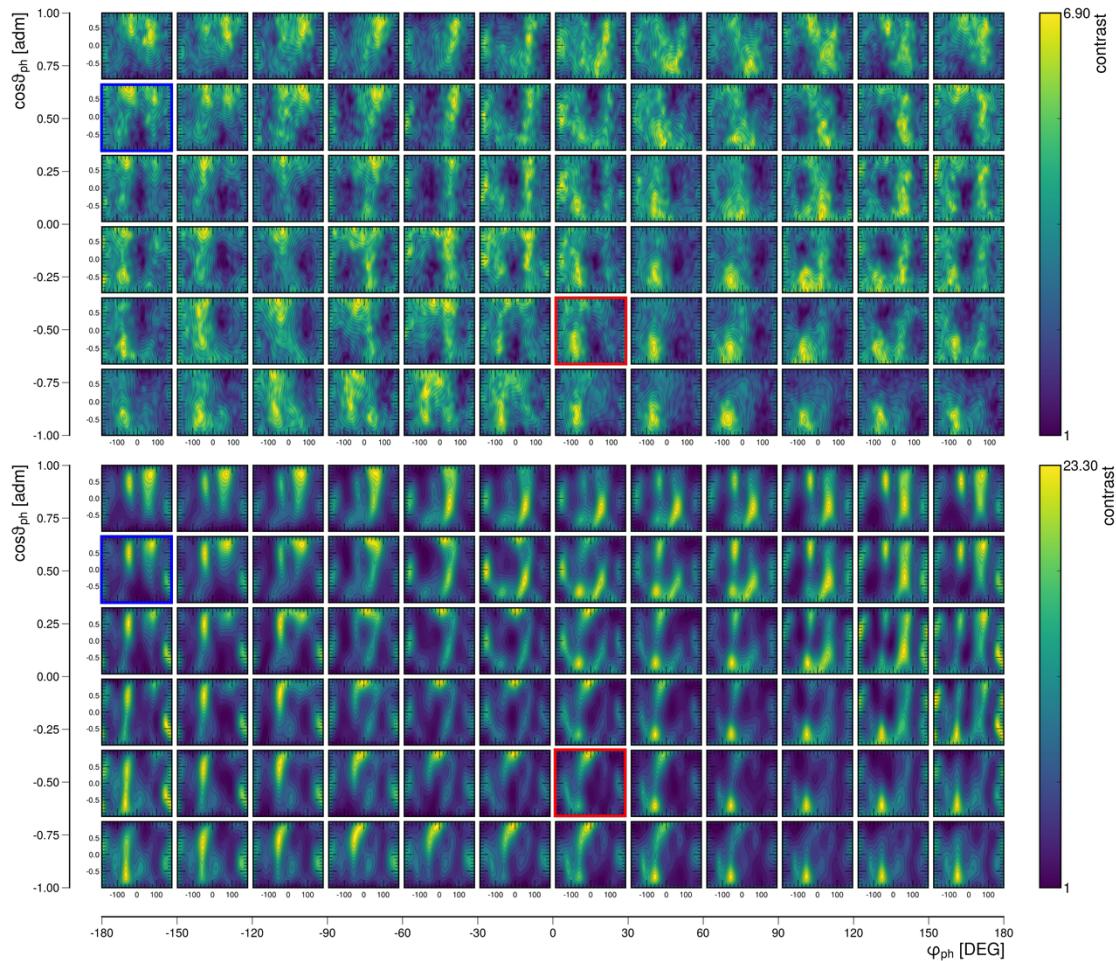
Figure 5.23: comparison of the 72 MFPADs for S-TFMOx at 11.7 eV (top panel, experimental) and 11.5 eV (bottom panel, theoretical). The highlighted panels in blue and red at (-180°, 0.75) and (0°, -0.75) respectively are two examples of opposite light helicity. Single MPFADs have higher contrast compared to the PA-MFPAD for both experimental data and theoretical predictions.

The comparison between theoretical and experimental single MFPADs for the S-TFMOx at 11.7 eV photoelectron energy is shown in Figure 5.23 for all light directions. The PA-MFPADs in Figure 5.14 are the integration over all light directions of the single MFPADs of Figure 5.23. The resolution of the experimental data of each single MFPAD is limited to 36×18 due to signal-to-noise considerations, and the arbitrary chosen resolution for each theoretical MFPAD is 200×100. The minima and the most prominent features are correctly reproduced by theory for all light's directions, but the limited resolution of the experimental data limits the possibility to fully resolve smaller features (e.g., series of multiple vertical lines in all single MFPADs for φ_{ph} = 150°). Within each MFPAD, the peak at φ > 120° associated to the CF_3 group is consistently present at all light directions in the theoretical predictions, but absent in the experimental data. In general, the MFPAD minimum (sometimes minima) in each panel move vertically along $\cos\theta$ upon changing θ_{ph} and keeping φ_{ph} fixed, but it shows a periodic vertical oscillation upon changing φ_{ph} and keeping θ_{ph} fixed, thus suggesting a correlation of the MFPAD features with the direction of the incoming photon. To investigate the robustness of the former observation, a close-up of the MFPAD for two opposite helicities along the same light directions from Figure 5.23 is given in Figure 5.24 along with their 3D representation in Cartesian coordinates. The panels selected are the number 4 and 37, blue frame LCP at (-180°, 0.75), and red frame RCP at (0°, -0.75) across this work, respectively. The minimum associated to the incoming photon direction remains constant at (0°, -0.75) for both panels, suggesting the occurrence of more complex interference phenomena compared to simpler molecules as the previously mentioned CO [93], CH_4, CF_3, and $C_2H_2F_2$ [159]. As remarked above, most of the features are well predicted by the theory, and some of the most prominent occur in the polarization plane, but not a systematic way.
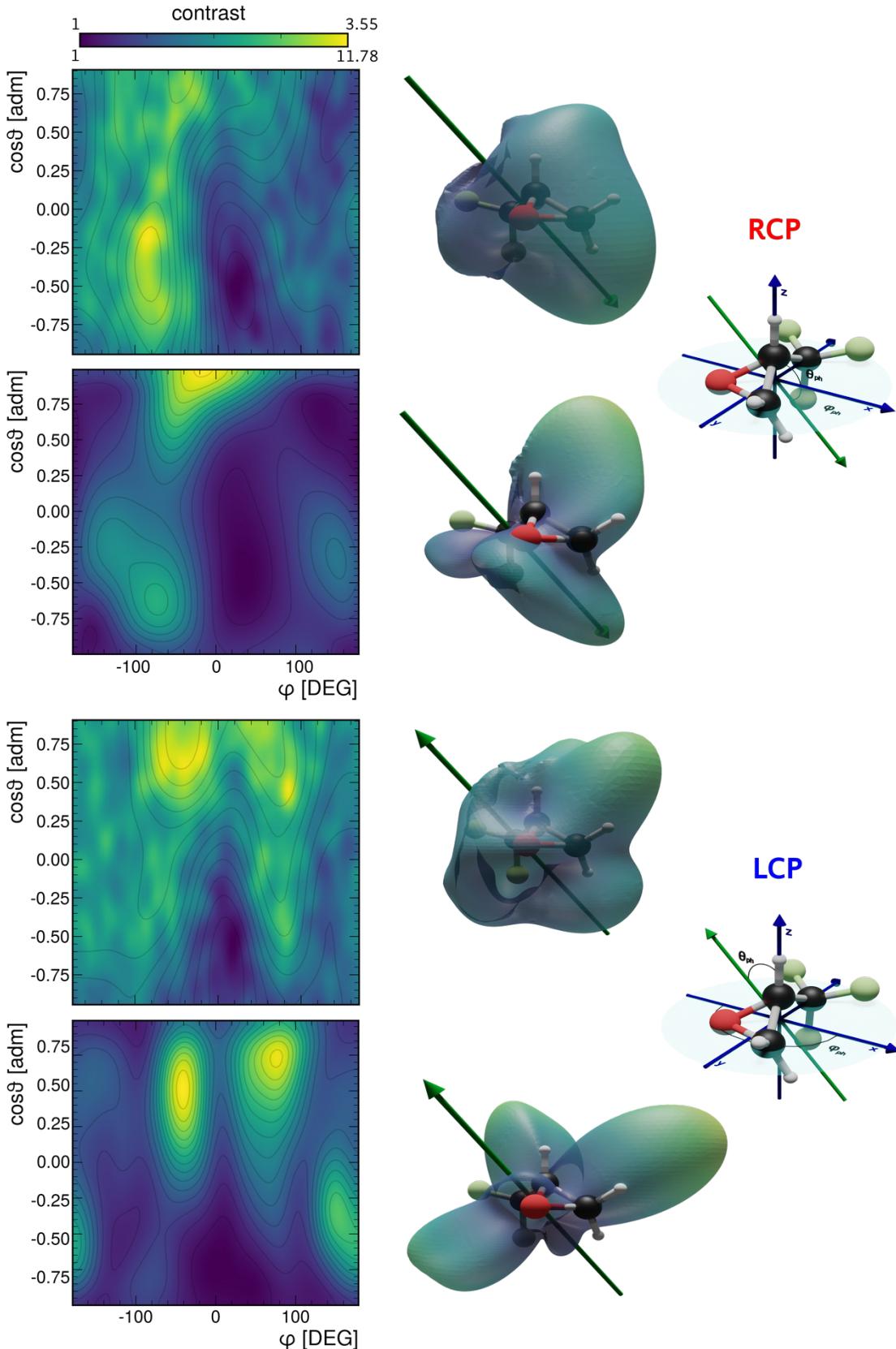
Figure 5.24: comparison of experimental (upper panels) and theoretical (lower panels) 2D and 3D MFPADs of S-TFMOx for opposite helicities along two identical directions identified in Figure 5.23 with blue and red frames represented in the 3D sketches by a green arrows. Top: RCP helicity (i.e., red frame, (0°, -0.75) panel 37). Bottom: LCP helicity (i.e., blue frame, (-180°, 0.75) panel 4). Directions sketched in the third column.
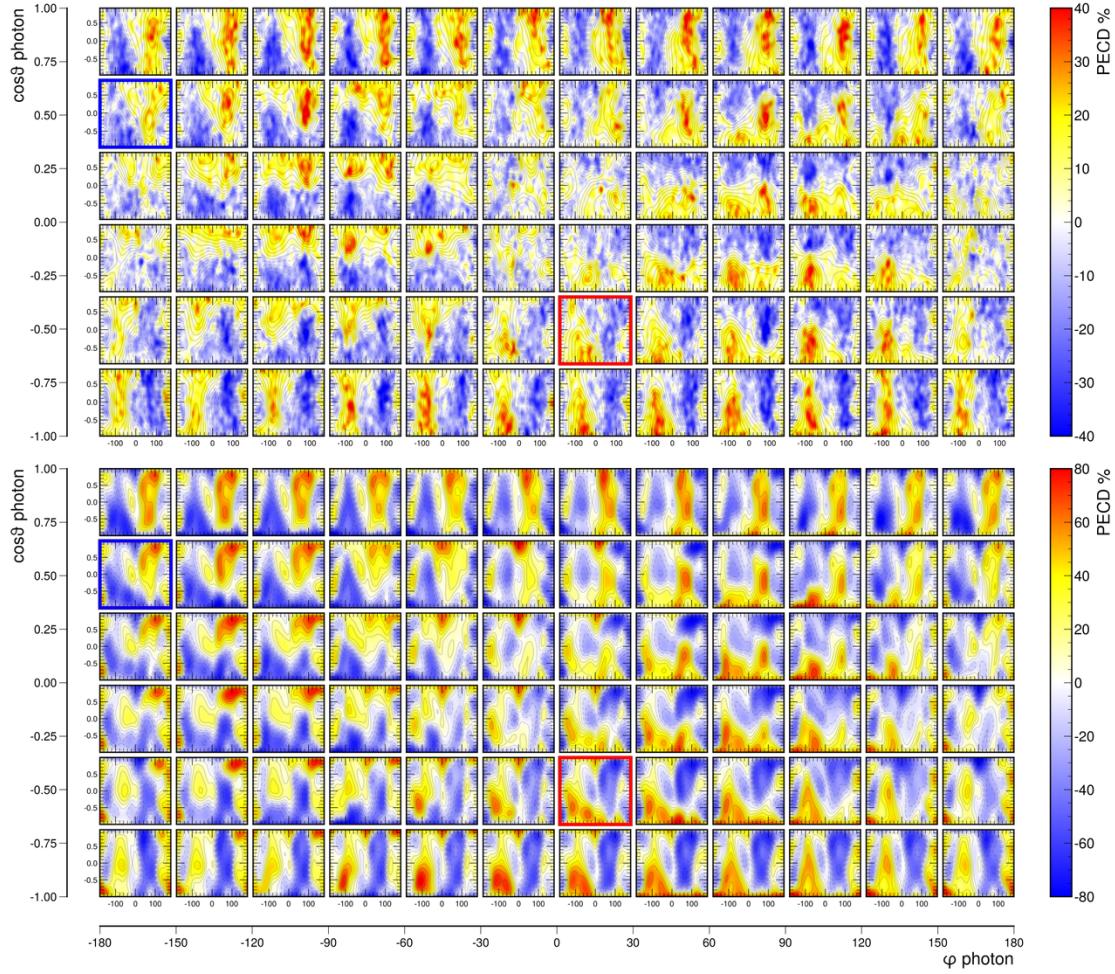
Figure 5.25: comparison of fully-differential PECD for S-TFMOx at 11.7 eV (top panel, experimental) and 11.5 eV (bottom panel, theoretical) calculated with equation (5.5) using the convention +1 = LCP for photon's polarization. The two highlighted panels are two examples of same light's propagation direction and opposite helicities, resulting in opposite values of PECD. The panels at opposite values of $\cos\theta_{ph}$ represent opposite light's propagation direction with the same helicity, thus resulting in areas of opposite PECD; both observations confirm the presence of a chiral effect.

It is possible to calculate the fully-differential PECD for each light direction, as shown in Figure 5.25 in comparison with theoretical predictions. The swap of light's helicity highlighted by the red and blue squares shows perfectly inverted values of PECD, due to its definition; the inversion of photon direction keeping the same helicity (i.e., along columns) shows a progressive qualitative inversion of PECD sign along $\cos\theta_{ph}$. Qualitatively, the agreement between experimental data and theoretical prediction is very good for all light directions within the limits of the experimental resolution; quantitatively, the experimental PECD values are half the theoretical ones. As discussed previously, the difference can be explained considering a simultaneous underestimation of the PECD effect from the

experimental data due to the MF definition and, among other factors, both the resolution of the apparatus, and a simultaneous overestimation from the theoretical prediction due to the use of a frozen geometry. For some light direction, the fully-differential PECD shows values 50% higher than the integrated PECD with a target molecule just oriented in space presented in 5.2.2, showing a dramatic increase for a fixed-in-space molecule. In general, integrating the fully-differential PECD along both the photonic coordinate φ_{ph}, and the electronic coordinates φ results in 1D PECD i.e., solely a function of $\cos\theta$, for 6 light directions described by $\cos\theta_{ph}$ i.e., Euler angle β according to the convention used (see appendix B.6). Ideally, the results of the former procedure from a polyatomic system should resemble the results for a diatomic one presented in chapter 5.3.3, net of small rotations of the MF before integration, and the use of the same convention for the Euler angles.
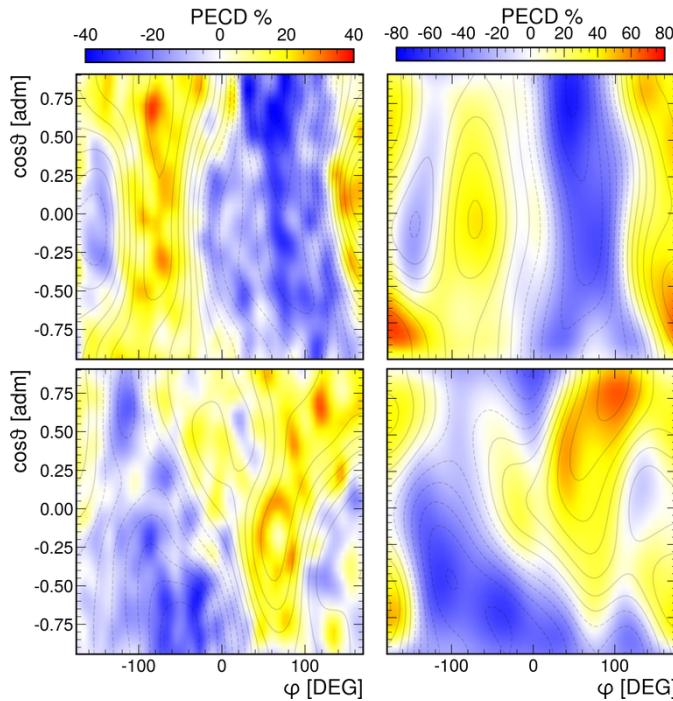

Figure 5.26: comparison of fully-differential PECD for S-TFMOx at 11.7 eV (experimental, left column) and 11.5 eV (theoretical, right column) for two opposite light's propagation direction with the same helicity, namely the top panels of photon coordinates (0°, -1), and the bottom panels (0°, 0.75). Note both the inversion of sign of most features upon inverting direction, and the intensity difference between experimental data and theoretical predictions of a factor 2.

Figure 5.26 shows a close up of two panels of Figure 5.25 with opposite propagation direction and same helicity, namely (0°, -1) for the top panels, and

(0°, 0.75) for the bottom ones: as observed previously, the sign of PECD inverts upon inverting light's propagation direction and the experimental distribution is overall matching the theoretical predictions.
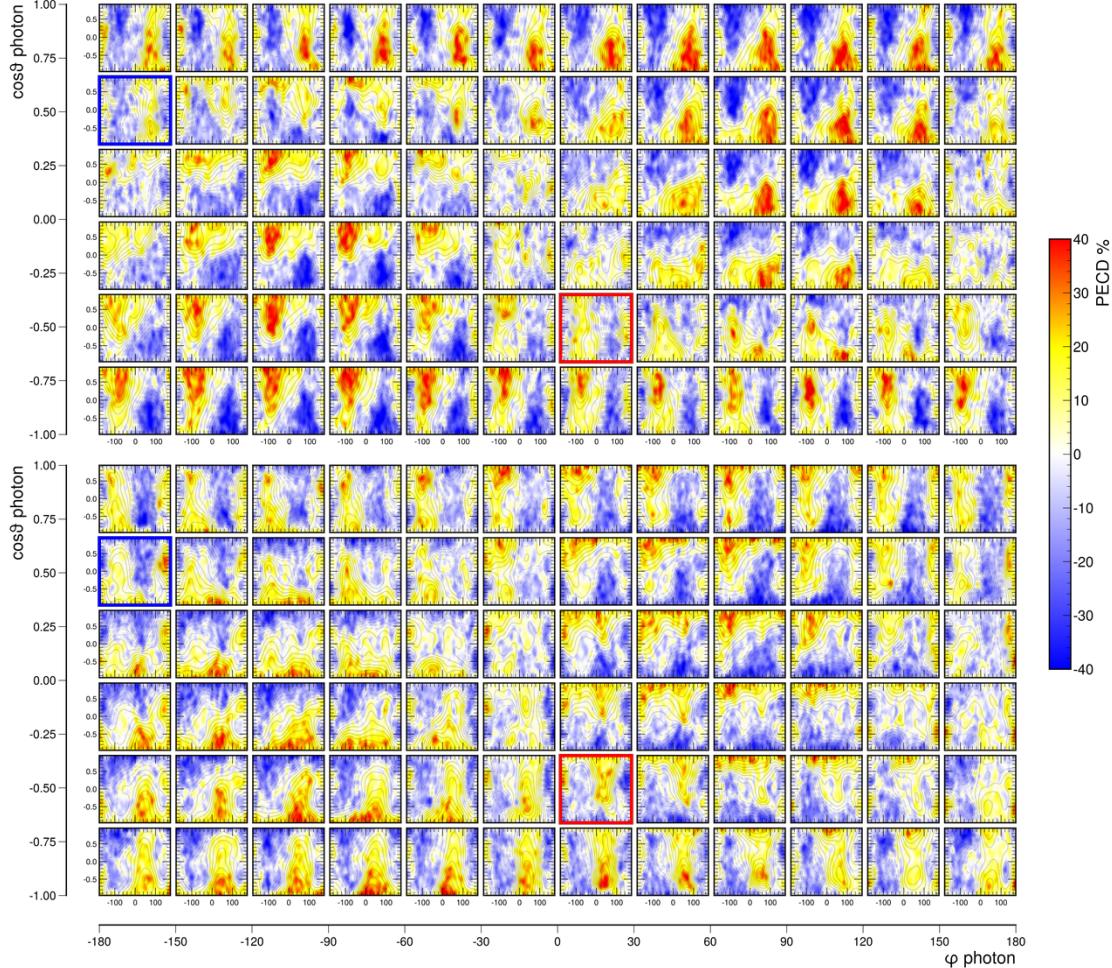
Figure 5.27: comparison of fully-differential PECD for R-TFMOx at 11.7 eV (top panel) and S-MOx at 11.5 eV (bottom panel) using equation (5.5). Note the inversion in sign of the main features across all light's directions. The S-MOx data are adapted and reprocessed from [160].

It is possible to compare the fully-differential PECD of R-TFMOx at 11.7 eV with the S-MOx at 11.5 eV photoelectron energy, extending the results for the diatomic ionization breakup of chapter 5.2.2. As usual, the comparison has to be conducted between opposite descriptors ensuring the comparison of identical spatial configurations due to the CIP rule (see appendix B.3). The MOx data were recorded during the already cited experiment from M. Tia et al. [74], and a more detailed analysis focussed on a polyatomic breakup at 11.5 eV photoelectron energy was recently published by K. Fehre et al. [160] from which the following data were reprocessed.

Figure 5.27 shows the comparison between TFMOx and MOx using the fully-differential PECD computed with equation (5.5). Within each system, each PECD map shows the typical symmetry PECD($\pi-\theta$, $\pi-\varphi$) = $-$PECD(θ, φ); across the two systems the main features are qualitatively the same, although inverted in sign across all light's directions, confirming the results shown for a diatomic breakup and randomly oriented molecular of chapter 5.2. The quantitative difference between the two systems are more evident for intermediate light's directions -0.25 < $\cos\theta_{ph}$ < 0.25 where the PECD signal of R-TFMOx is higher than S-MOx, suggesting a stronger scattering effect of the heavier and larger CF_3 group compared to CH_3. In general, the intensity of the PECD effect is comparable between the two system at around 40%, half of the theoretical predictions as shown in the lower panel of Figure 5.25 for S-TFMOx, and for S-MOx in [160]. It is important to remark that an inversion of enantiomer will not invert the sign of the fully-differential PECD, but flip the histograms with respect to $\cos\theta$ = 0 line, as already mentioned, and the inversion is more evident for larger values of $|\cos\theta_{ph}|$. A complete comparison between the fully-differential PECD for R- and S-TFMOx at 11.7 eV photoelectron energy is shown in Figure B.11 in the appendix B.7.

$$PECD_6(cos\theta) = \frac{b_1^{|+1|}P_1(cos\theta) + 1/2 \cdot b_3^{|+1|}P_3(cos\theta) + 1/4 \cdot b_5^{|+1|}P_5(cos\theta)}{\left[1 - 1/2 \cdot b_2^{|\pm1|}P_2(cos\theta) - 1/4 \cdot b_4^{|\pm1|}P_4(cos\theta) - 1/8 \cdot b_6^{|\pm1|}P_6(cos\theta)\right]} \quad (5.6)$$

Both the MFPADs and the correspondent fully-differential PECD have been computed for all five photoelectron energies. An alternative and concise way of visualizing the fully-differential PECD is described in the followings: for each light's propagation direction, each MFPAD can be integrated over the electronic coordinate φ, and the normalized difference along the electronic coordinate θ is computed between the two different helicities using the equation (5.5). For each photon propagation direction, the resulting 1D distributions can be interpolated using the PECD defined equation (5.6). Thus, for each photon energy, it is possible to compute 72 values of the dichroic parameter b_1, as well as higher values. The equation (5.6) is obtained calculating the PADs from the general equation (3.16) , including partials waves up to l = 6, and computing the usual

normalized difference. As already described in chapter 3.2, the odd terms of the expansion add up in the numerator upon switching polarization due the algebraic sum and vice-versa for the even term in the denominator.

In Figure 5.28 an example of the just mentioned integration and interpolation procedure is shown for the experimental and theoretical data of R-TFMOx at 11.7 eV and 11.5 eV electron energy, respectively. The steeper the curve, the higher b_1 parameter, where the slope determines its sign. As expected, the PECD distributions across all light's propagation directions are opposite upon swapping helicity (i.e., the transformation $\varphi_{ph} \rightarrow \varphi_{ph}+180°$) and upon changing photon propagation direction (i.e., $\cos\theta_{ph} \rightarrow -\cos\theta_{ph}$), in accordance with previous results. It is worth to remark that for the photoelectron energies lower than 11.7 eV, only the R enantiomer has been measured.

The obtained dichroic parameters b_1 are plotted for each light's propagation direction and for each energy as shown in percentage in Figure 5.29. Most of the features are correctly predicted by theory, although the absolute location of some relative maxima (and minima) is not: the main differences are visible at 11.5 eV, and 8.2 eV where the theoretical distribution seems to be shifted along φ_{ph} and skewed along the $\cos\theta_{ph}$ axis. As previously mentioned, the amplitude of the asymmetry is overestimated by the theoretical predictions, and it is roughly a factor 2 larger than the experimental values. The complete list of PECD histograms as the one reported in Figure 5.27 is given in appendix B.7 for R-TFMOx at all photoelectron energies. The absolute location of the features remains constant across the energies. As already mentioned, higher order of the radial dipole matrix elements b_i for i > 1 can be computed, although not presented in this work. The greater the order, the higher the sensitivity towards the variability of the data, thus requiring a larger number of valid events.
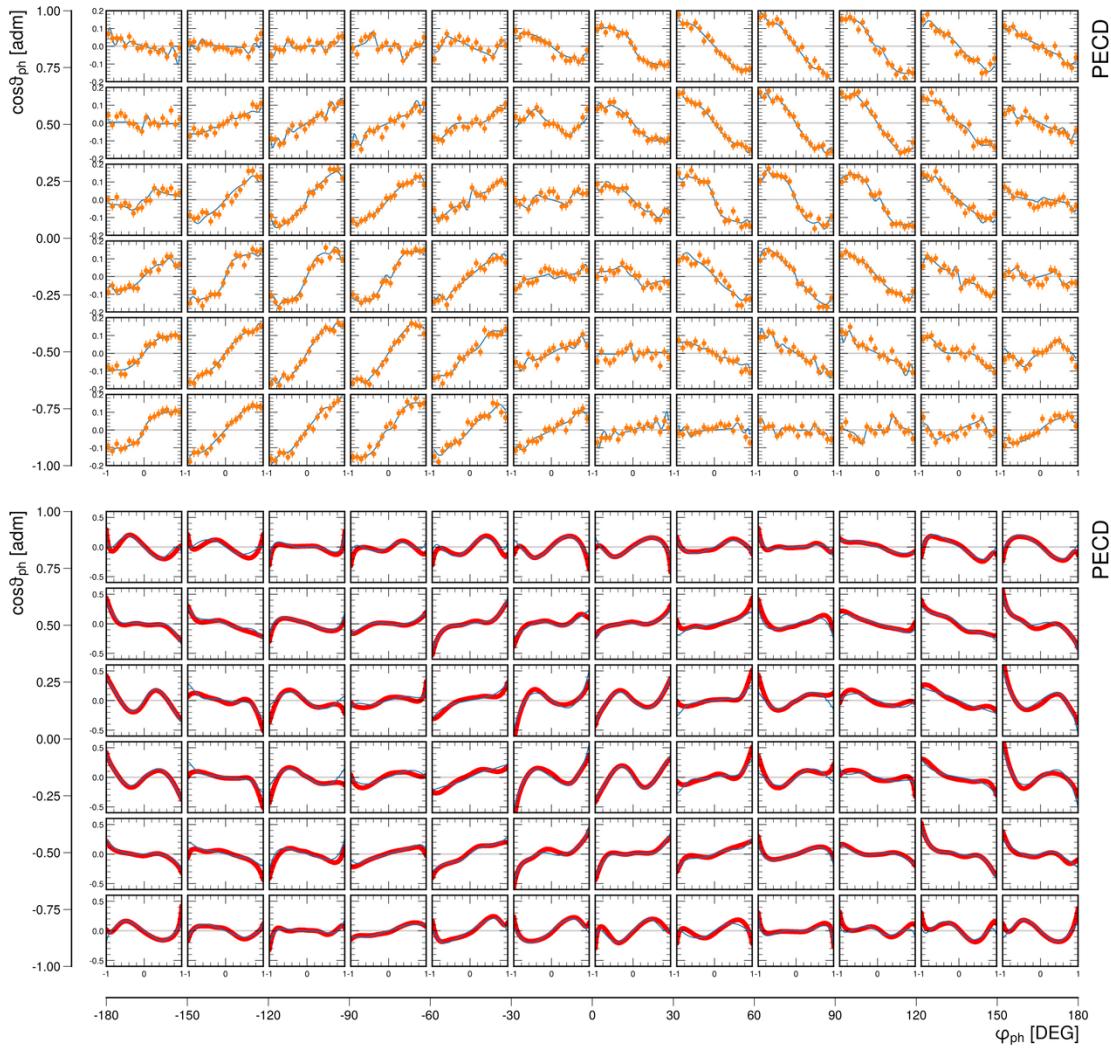
Figure 5.28: comparison of $PECD_6(\cos\theta)$ interpolations calculated with equation (5.6) for R-TFMOx experimental (top) and theoretical (bottom) data at 11.7 eV and 11.5 eV respectively. The outer axis refer to photon coordinates. Note the difference in scale of the $PECD_6(\cos\theta)$ axis between experimental data and theoretical predictions.
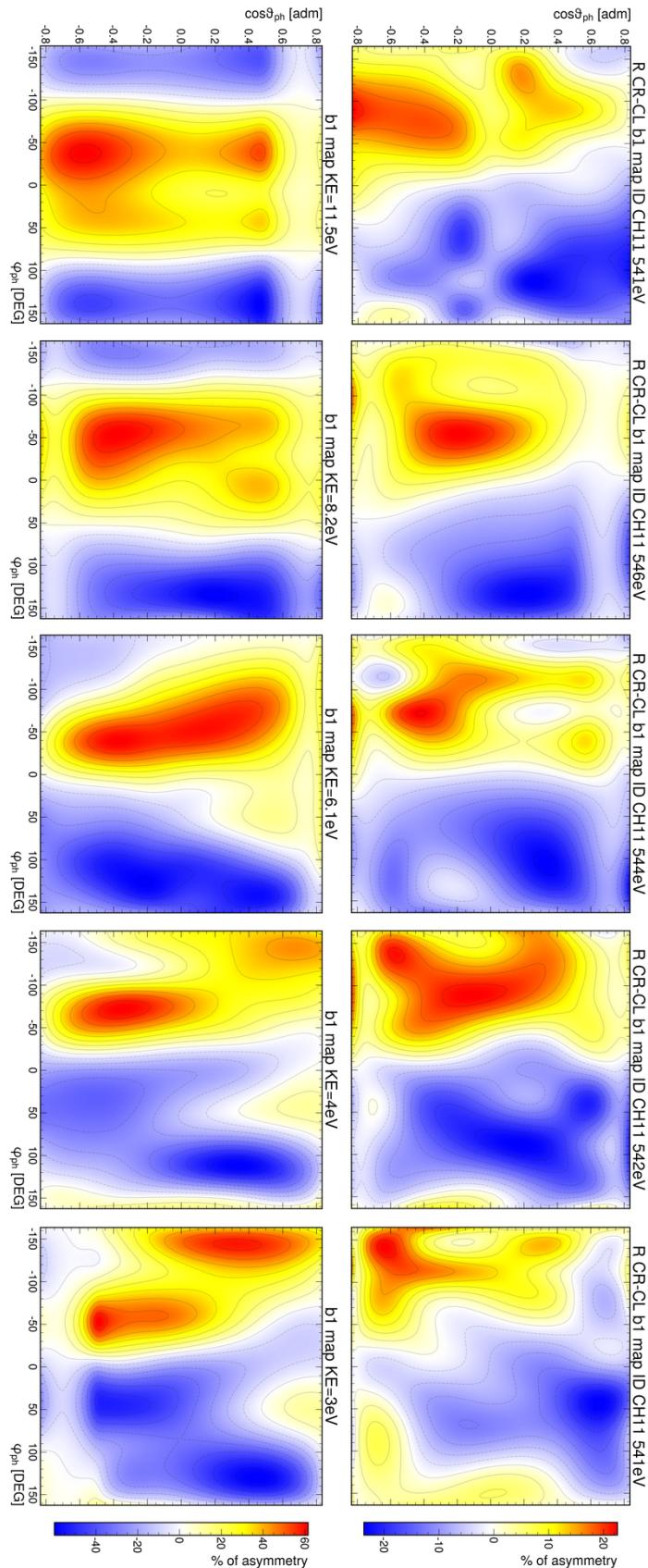
Figure 5.29: comparison of fully-differential dichroic parameter b_1 for R-TFMOx between experimental data (right column) and theoretical predictions (left column) at 11.7 eV and 11.5 eV, respectively.

6. CONCLUSIONS AND OUTLOOKS

This work demonstrates the capability of several types of MFPADs and their linked PECD to map in great detail the molecular geometry of two polyatomic chiral molecules differing in one substitutional group (e.g., TFMOx and MOx) as a function of the photoelectron energy. The study paves the way for using the photoelectron angular distribution of single molecules in gas phase as an extremely sensitive crystallography-like technique. The experiments conducted for single molecules in gas phase (i.e., without interactions) were able to assign the absolute configuration of TFMOx and MOx chiral molecules using the PECD chiroptical effects. The experimental results are in good agreement with the theoretical predictions. The results of this work confirm and refine recent findings on simple achiral and chiral molecules, setting a benchmark for the reachable complexity of the investigated molecular targets. Further developments may have large impact in the realm of fundamental physics, allowing to fully and directly characterize molecular structures, as well as probing molecular dynamics of single chiral molecules in the gas phase through the use of MFPAD emerging from (tunable) photoionization. In the field of biology, it could be possible to prove the molecular structure of extremely complex molecules, chiral in nature, such as proteins or hormones, to cite the most important, without the need of particular sample preparation or the use of references.

This work investigates the molecular frame photoelectron angular distribution (MFPAD) of the chiral molecule TFMOx in several steps of increasing degree of

details and complexity, starting from randomly oriented, to fully fixed in space, and compares it to the theoretical predictions. Furthermore, both the experimental data and the theoretical predictions are compared to another chiral system e.g., MOx to investigate the effects of the substitutional groups on the MFPAD. For both molecular systems, starting from the photoelectron emission, the PECD chiral effect has been extensively investigated as a function of the breakup channel, photoelectron energy e.g., 3 eV, 4 eV, 6.1 eV, 8.2 eV, 11.7 eV, and molecular orientation e.g., 72 directions described by θ_{ph} and ϕ_{ph} coordinates.

The PA-MFPADs have been recorded and compared to theoretical predictions. Previous studies have shown how PA-MFPAD could be used to directly probe the geometrical structure of small and highly symmetric molecules, reducing the prominence of dipolar contributions from the incoming photon's spin. The present experiments showed that PA-MFPAD is capable of imaging the molecular structure of complex polyatomic chiral molecules, too, although in a more collective way rather than for each molecular bond, probably due to the increasing complexity of the molecular potential. In particular, characteristic features linked to the rigid oxirane ring, present both in TFMOx and MOx, occur consistently across both molecular systems, in god agreement with the respective theoretical model used e.g., SC-RCHF and SC-FCHF, respectively. In the case of TFMOx, the PA-MFPAD correctly flipped around the line $\cos\theta = 0$ upon changing either helicity or enantiomer, proving it to be a sensitive tool to a chiral molecular potential. Furthermore, the PA-MFPAD showed and extremely high sensitivity to the photoelectron energy, allowing to track the evolution of interference features with a resolution of few eV (e.g., from 11.7 eV to 3.1 eV), especially in the area associated with the oxirane ring. At the low photo electron energies used in the present experiments, the link between molecular configuration and PA-MFPAD is non-trivial. Thus, an elaborated state-of-the-art theoretical model is required to interpret the observed PA-MFPAD and associated PECD maps. This work shows that the seeming disadvantage of the complex and non-trivial multiple scattering dynamics of the low energy electron comes with the benefit of enhance chiral

sensitivity. In fact, low energy electrons are very sensitive to internuclear distances and vibrational modes, which could induce phase-shifts between the scattered waves. The theoretical model used for TFMOx (e.g., SC-RCHF) takes into account the major effect of the monopole relaxation of molecular orbitals induced by the creation of the inner-shell vacancy in comparison to the model used for MOx (e.g., SC-FCHF). By contrast, both used models do not take into account an average on the most prominent vibrational modes of the molecular systems, intrinsically occurring in the experiment, but are performed for frozen (i.e., Hartree-Fock approximation), energy-optimized molecular geometries. The agreement between experimental data and theoretical predictions is overall satisfactory, confirming further the validity of the scattering from molecular potential as the main phenomenon underlying the generation of the MFPAD. For further refinements, the remaining discrepancies might arise from the fact that the calculations are not averaged over vibrational modes, but done for a fixed geometry. The latter could be especially relevant due to the size of the molecules. Furthermore, collective electron resonances at low photoelectron energies are not included in the calculations. Other sources of mismatch with the theoretical predictions could be the definition of the experimental MF using a neutral fragment, deduced by the momentum conservation, which carries uncertainty from the other two detected fragments, the non-optimized rotation between of the theoretical and experimental MF, and the intrinsic lower performances of the theoretical model at low photoelectron energies.

Taking advantage of the 4π collection solid angle for the detection of photoelectrons in the investigated energy range of the COLTRIMS apparatus, it was possible to investigate MFPADs for 72 different light's propagation directions with respect to the molecular orientation (i.e., completely fixing the target molecule in space). For both TFMOx and MOx, each single MFPAD showed similar features, and especially a similar dipolar imprinting from ionizing photon orthogonal to the light's propagation direction, as predicted by previous theoretical studies. The former features, however, are not located perfectly

orthogonally with respect to the propagation direction of the incoming photon: for each MFPAD, the observed minimum moves vertically along $\cos\theta$ upon changing θ_{ph} and keeping φ_{ph} fixed, but it shows a periodic vertical oscillation upon changing φ_{ph} and keeping θ_{ph} fixed. The latter behaviour suggests a correlation of the MFPAD features with the direction of the incoming photon, but with more complex interference phenomena compared to previously studied simpler molecules e.g., CO, CH_4, CF_3, and $C_2H_2F_2$. Due to the high sensitivity to the molecular potential, the larger scattering centres as CF_3 in TFMOx compared to the CH_3 in MOx introduces more complexity in addressing the role of each scattering centre to the overall MFPAD. Furthermore, intermediate states, numerous in large molecules, can have a strong influence on the interference patterns of the photoelectron.

The PECD phenomenon quantifies the light helicity dependence of the difference in forward-backward photoelectron emission in chiral molecules. PECD is computed from MFPAD, and it is a great tool to investigate chiral molecules, due to its high sensitivity the molecular structure and photoelectron energy. In this work, the PECD effect has been shown for both TFMOx and MOx and multiple photoelectron energies for three cases: randomly oriented molecules, oriented in space molecules (i.e., integrated-PECD), and fixed-in-space molecules (i.e., fully-differential PECD). The PECD effect for randomly oriented molecules reaches a maximum value of 2% for both molecular systems, few orders of magnitude higher than the typical signals for standard chiroptical techniques. Orienting a molecule in space shows a dramatic increase up to 20% in the integrated-PECD for specific relative angles between the photon polarization plane and the molecule: the angular distribution show a typical symmetry $PECD(\pi-\theta,\pi-\varphi) = -PECD(\theta, \varphi)$ suggesting that the maximum effect is expected y-axis of the molecule is either parallel or orthogonal to the polarization plane. Taking advantage of single MFPADs, the fully-differential PECD was computed revealing a further increase of the PECD signal for some light's propagation directions up to 45%. The chiral origin of the PECD effect is confirmed by its inversion of sign upon switching

enantiomer. Furthermore, the PECD maps for both systems show an inversion of sign upon change of light helicity, and a qualitative progressive inversion of sign upon inversion of the light direction (i.e., along the $\cos\theta_{ph}$ coordinate).

Both integral and fully-differential PECD were proven to be highly sensitivity to the photoelectron energy, too: the integral PECD shows a rearrangement of the typical symmetry for low energies, and the fully-differential PECD shows a progressive shift of maximum and minimum values of PECD to different light's propagation direction for each photoelectron energy. The latter trends were summarized by maps of the dichroic parameter b_1 as function of the light's propagation direction. The maximum intensity of PECD has a slight variation across the different energies, and it reaches its maximum at about 50% for 6 eV photoelectron energy.

The comparison between TFMOx and MOx, the latter from previous experimental campaigns, aimed at systematically quantifying the effect of a substitutional group (i.e., CF_3 and CH_3, respectively) on the MFPAD patterns and the related PECD at 11.7 eV photoelectron energy. The descriptors associated with each molecule are opposite according to the CIP rule, therefore to compare identical geometrical structures two opposite enantiomers were considered (e.g., R-TFMOx vs. S-MOx). The experiments revealed a complete sign inversion for all three types of PECD (e.g., random, partially-oriented, and fully-oriented), and a quantitative stronger effect for TFMOx, suggesting a measurable influence of the heavier scattering centres (i.e., F atoms) on the recorded scattering patterns. The trend of PECD for randomly oriented molecules and the features of integrated-PECD are very similar between the two systems, but the fully-differential PECD reveals more subtle differences as function of light's propagation direction. A possible explanation of the sign inversion is an induced phase-shift due to a complex combination of multi-scattering processes by the two molecular potentials. Phase-shift in the scattered waves can be induced both from the nature of the scattering centres, and from the interatomic distances. The

good similarity of the features observed for single MFPADs across the two molecular systems could be addressed to a prominent dipole contribution from the incoming photon, and similar dipole selection rules. The areas where theoretical predictions disagreed with experimental data in the MFPAD from fixed-in-space molecules, gave similar fully-differential PECD signal, suggesting that those features a stable upon changing the light's propagation direction and/or the light's helicity.

Several reaction channels were analysed, but discarded because of the complex interaction between charged fragments during breakup (i.e., breakdown of axial-recoil approximation), and many more were present, but not considered because of the lack of large statistical data. An increase of the detection efficiency of the apparatus can make polyatomic breakups populated enough to further test the limits of the axial-recoil approximation for the MF definition. Experiments to address the specific role of each scattering centre in combination with the oxirane ring can be designed using different substitutional groups. In particular, the influence of the distance of the scattering centres from the $O(1s)$ photoelectron emission site (i.e., the O atom in the oxirane ring) can be tested introducing a longer carbon backbone, as in Ethyloxirane. Furthermore, the influence of rotation of the substitutional groups around the C-C bond can be examined differentiating the scattering centres using a C atom substituted with three different atoms e.g., halogens. The fingerprint of the oxirane ring in the photoelectron interference pattern could be further studied using different chiral oxirane molecules e.g., 2,3-Dimethyloxirane. More innovative experiments could address how different ionization regimes such as double ionization or participator Auger decay influences the MFPAD for chiral systems. A whole new set of experiments to explore the evolution of the ionization of chiral molecules in time using MFPADs could design using tailored ionization schemes with LASERS as photon sources.

7. ● ACKNOWLEDGMENTS

This work has been possible thanks to the support and love of my friends, family, and colleagues.

I want to express my deepest gratitude to Prof. Dr. Reinhard Dörner who gave me the opportunity to be part of his research group, and shared with me his knowledge and experience. I wish to thank Dr. Ottmar Jagutzki for his mentorship and support. I am immensely thankful to Prof. Dr. Till Jahnke for his guidance, and for his inspiring and unlimited dedication to the members of our group. I especially want to thank Dr. Kilian Fehre for having inspired most of this work, and for his exceptional support from the early stage. I would like to thank Dr. Markus Schöffler and Dr. Lothar Schmidt for their invaluable scientific advising. Thanks to Marianne Frey for her dedication and precious work. I would like to express sincere appreciation to my scientific collaborators apl. Prof. Dr. Philipp Demekhin from Kassel Universität, Dr. Achim Czasch and Dr. Sven Schößler from RoentDek, Dr. Alessandro Nicolaou, Dr. Horia Popescu, Dr. Laurent Nahon and Dr. Gustavo Garcia-Macias from the synchrotron facility SOLEIL for their essential contributions to this work. I wish to thank Dr. Claus Peter Schulz for his warm welcome and exciting time in the laboratory during my secondment at the Max Born Institute in Berlin.

Many thanks to my colleagues Isabel, Max K., Arnab, Raghu, Dimitrios, Sebastian, Daniel, Jonas, Miriam, Gregor, Max H., Florian and Sven for their care, patience and

precious help in the most difficult moments of this journey. Thank you for the thrilling time shared at beamtimes, for your scientific insights, for the funky group trips, and for the unforgettable Christmas parties. A special thank to Maksim for his wise words, generous help, and empathy. I want to express warm thanks to my fellow ESRs Dhirendra, Hassan, Prabhash, Jennifer, Constant, Jacqueline, Ayse, Rim, Federico, Mikhail, and Isabel who shared with me exciting and stressful moments during experiments and retreats. I am proud of having been part with you of the ASPIRE Innovative Training Network. I have been learning so much from each of you, and I am very grateful you were part of my professional and personal development. I wish you success and happiness for the next stage of your journey.

I want to share my joy and gratitude for having friends who support me constantly, with patience and love during my journey. Finding and getting to know them were the most amazing presents I could have ever received. When I am with them, I can be myself and vulnerable. When I am with them, I feel at home. Thank you, Ame, for inspiring me to live up to my ideals, with determination, one laughter at a time. I am looking forward to each of the next million talks on how to make this world a better place (yes, we do know it best). Thank you, Miriam Ester Monakong Escobar, for remembering me every day to keep the heart ahead of the intellect (and sometimes of the whole brain), and to embrace self-love when into the shitstorm. Thank you, Tere, for the light you shine, and for sharing your passion for the beautiful discoveries of life, unconditionally. Thank you, Tommaso, for *gently* questioning one by one all the founding values of our society (with a strong focus on the religious ones), I am having great fun doing it together. With Maria Teresa di Calcutta, to the Moon!!1! Thank you, Noe, for being so generous with your love, and for reminding me to get into adventures with curiosity and faith in ourselves; *ti voglio bene*, aka I *amish* you! Thank you, Sara, for being my biggest fan: your words of encouragement reminding me about my strengths were crucial every single time. You are a source of constant inspiration, and I deeply admire you. Namaste, Tommie, for accompany me through our beautiful

spiritual journey. Thank you, Jana, for having welcomed me into your life with enthusiasm, and for being always up for dreamy adventures *"I don't accessorise. I'm Howard Moon. There's a simple truth to me."*. Thank you Maus, Richi and Cami for the truly beautiful and crazy years together as a big family in Milan. I am missing you, and I am looking forward celebrating again with you! *Viva, ora e per sempre, Piazza Monte(spazio)Titano!!* Thank you, Michi, Albi, Giamma, Luca, Chiara e Miccia for being my roots for 20 years. I want to thank you, Berni, for the special time spent together. I wish you all the strength and luck to make your dreams come true. Thanks to all of you, my dear friends, for the endless conversations trying to give meaning to our impermanent time here, or simply for being and growing together. You are my role models,v*i amo pasticcini miei.*

Lastly, my family deserves endless gratitude and love. I want to thank my father for teaching me integrity, honesty, and humbleness, and my mother for teaching me resilience and how to cultivate a critical mind, but above all for her endless love. Thank you for being always open to question and discuss openly your values and believes. Thank you for always believing in me, and for the strength and freedom you gave me with your support.

This work has been entirely produced using open-source software packages. I am indebted to the communities of volunteers behind their development and constant maintenance. Thank you to make these alternatives available, powerful and free for everyone, our freedom depends on your dedication.

A. *ALPHABETICAL INDEX*

B. *APPENDIX*

B.1 Stoke´s parameter for polarization

In 1822, A. Fresnel discovered that a linearly polarised wave can be though as a superimposition of two coherent circularly polarised waves of opposite helicity and equal amplitude, and the orientation of the resulting polarization plane is equal relative phase between the two circularly polarised waves.
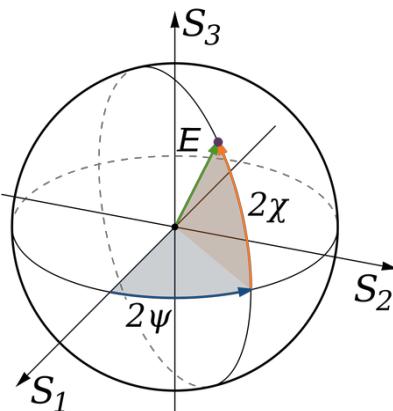
Figure B.1: The Poincaré sphere is the parametrisation of the last three Stokes' parameters in spherical coordinates. Image reproduced from Wikipedia.

A convenient way to mathematically describe the polarization state of an electro-magnetic field has been introduced by G. G. Stokes in 1852 by the mean of four quantities called Stokes parameters [161]. For partial-polarization for a quasi-monochromatic wave, it is possible to describe the Stoke parameters S_n in spherical coordinates ψ and χ as in Figure B.1

$$
\begin{aligned}
S_0 &= E_0 \\
S_1 &= E_0 \cdot P \cdot \cos(2\psi)\cos(2\chi) \\
S_2 &= E_0 \cdot P \cdot \sin(2\psi)\cos(2\chi) \\
S_3 &= E_0 \cdot P \cdot \sin(2\chi) \\
P &= (S_1^2 + S_2^2 + S_3^2)^{1/2} / S_0
\end{aligned}
\tag{B.1}
$$

with the degree of polarization $0 \leq P \leq 1$.

For the present work, it is possible to assume $P \approx 1$, because of the high degree of polarization and high level of monochromatic photons that synchrotron facilities can deliver, therefore

$$S = \begin{pmatrix} S_0 \\ S_1 \\ S_2 \\ S_3 \end{pmatrix} \tag{B.2}$$

where S_0 gives the total intensity, S_1 gives the excess in intensity transmitted by an analyser which accepts linear polarization with an azimuth $\theta = 0$ over that transmitted by an analyser which accepts linear polarization with an azimuth $\theta = \pi/2$. S_2 has a similar interpretation with respect to the azimuths $\theta = \pi/4$ and $\theta = 3\pi/4$. S_3 is the excess in intensity transmitted by a device which accepts right-circularly polarized light over that transmitted by a device which accepts left-circularly polarized light.

Pure states of CPL are therefore coded as $S = \begin{pmatrix} 1 \\ 0 \\ 0 \\ \pm 1 \end{pmatrix}$ for left (+) and right (-), respectively.

B.2 Derivation of Lagrangian coefficient

The approach used in the following derivation follows the review of I. Powis and the reader is welcome to refer to [80] for greater details.

Following from chapter 3.2, it is possible to compute the differential cross-section for emission of photoelectrons into solid angle in the laboratory frame for random molecular orientation and an axis of cylindrical symmetry defined by the photon polarization described by the equation (B.3).

$$\frac{d\sigma}{d\Omega} = \frac{\sigma}{4\pi} I_p(\theta) = \sum_j b_j^p P_j(cos\theta) \qquad \text{(B.3)}$$

Within the non-relativistic electric dipole approximation E1 and using the Hartree-Fock approximation (i.e., frozen cores), the differential cross-section about a direction **k** as a function of the incoming photon frequency ω and polarization $\hat{e}$, is equal to the square of the transition matrix V_{in}, and can be expressed as

$$\frac{d\sigma(\omega)}{d\hat{\boldsymbol{k}}} \cong \frac{\boldsymbol{k}}{\pi\omega} \left| \langle \psi_{n,k} | \hat{e} \cdot \boldsymbol{x} | \psi_i \rangle \right|^2 = \left| V_{in} \right|^2 \qquad \text{(B.4)}$$

for a wave function describing an electron within the final state *n* free electron in the continuum with momentum **k** , and the initial state *i* molecular orbital of energy ϵ_i. It is possible use an expansion of normalized partial waves for the photoelectron wave function in the continuum using the spherical harmonics Y_{lm} of angular momentum *l* and its projection in the molecular frame *m*, and σ_l is the Coulomb phase shift, as shown in equation (B.5).

$$\psi_{\boldsymbol{k}}(\boldsymbol{r}) = \sum_{lm} i^l e^{-i\sigma_l} Y^*_{lm}(\hat{k}) \psi_{lm}(\boldsymbol{r}) \qquad \text{(B.5)}$$

The transition matrix element V^v_{lm} will be therefore expressed as functions of the momentum vector $\hat{\boldsymbol{k}}'$ along the recoil direction

$$V_{\mathrm{lm}}^{v} = (-i)^{l} e_{v}^{l} f_{v}^{\mathrm{lm}} Y_{\mathrm{lm}}^{*}(\hat{\boldsymbol{k}}') \tag{B.6}$$

with e_{v}^{l} spherical tensor component of the photon momentum vector, f_{v}^{lm} radial transition amplitudes for the electron from the bound i to the l-m partial wave, for the photon momentum projection v in the MF. It is now possible to rotate the system of reference to the LF using a rotation $\boldsymbol{R}$ by the use of a rotation matrix $D_{pv}^{l}(\boldsymbol{R})$. Introducing p, the photon momentum projection in LF (i.e., polarization in the LF), the rotated matrix element will therefore be

$$V_{\mathrm{lm}}^{p} = \sum_{v\mu} (-i)^{l} D_{\mathrm{pv}}^{l}(\boldsymbol{R}) e_{v}^{l} f_{v}^{\mathrm{lm}} [D_{\mu\mathrm{m}}^{l}(\boldsymbol{R}) \cdot Y_{\mathrm{l}\mu}^{*}(\hat{k})]^{*} . \tag{B.7}$$

Inserting the latter equation into (B.1), and considering two interfering partial waves with angular momentum l, m, v, and l', m', v' , a product of rotation matrices with the same argument $\boldsymbol{R}$ appears, that can be substituted with a Cleabsch-Gordon (GC) series . It is therefore possible to carry out the integral of the GC over all molecular orientations, implementing simplifications due to the orthonormality relationships of the rotations which end up into a series of delta functions. The sum on μ $\sum_{\mu} (-1)^{\mu} \langle l'\mu, l-\mu | j0 \rangle Y_{\mathrm{l}'\mu}(\hat{k}) Y_{\mathrm{l}\mu}^{*}(\hat{k}) \propto P_{j} \cos(\theta)$ reduces to a delta function proportional to the Legendre polynomial P_{j}, with the polar angle θ considered respect to the light's propagation direction in the LF. Finally, combining all together into equation (B.3) returns the equation

$$\begin{aligned}
\frac{d\sigma(\omega,p)}{d\hat{\boldsymbol{k}}} = 2\pi \sum_{j} \sum_{lmv,l'm'v'} & (-i)^{l-l'} (-1)^{p-m-v} e^{i(\sigma_{l}-\sigma_{l'})} \frac{\sqrt{((2l'+1)(2l+1))}}{(2j+1)} \\
& \times \langle 1-p, 1p | j0 \rangle \langle 1-v', 1v | jv-v' \rangle \\
& \times \langle l'0, l0 | j0 \rangle \langle l'-m', lm | jm-m' \rangle \\
& \times [e_{v'}^{l} f_{v'l'm'}]^{*} e_{v'}^{l} f_{v'l'm'} \delta_{v'-v, m'-m} \cdot P_{j}(cos\theta)
\end{aligned} \tag{B.8}$$

with the explicit $B_{j}^{\{p\}}$ coefficients and the Legendre polynomials $P_{j}(\cos\theta)$.

B.3 Cahn Ingold Prelog (CIP) rule

The Cahn, Ingold and Prelog (CIP) system is a nomenclature system used to completely and unequivocally name a stereoisomer of a molecule. The main goal is to assign the descriptor labels R (from Latin *rectus*) and S (from Latin *sinister*) to the molecular structure models selecting therefore the handedness. The following procedure is coded since 1974 into the IUPAC rules for organic nomenclature [162], [163].

After the identification of chiral centres (e.g., the second C atom in the backbone for both TFMOx and MOx, marked with a star in Figure B.3) it is possible to assign priorities from high (1) to low (4) for a chiral C. First, evaluate the atomic number (Z) of the closest atoms (i.e., distance 1) directly attached to the considered chiral centre: the higher the atomic number Z, the higher the priority. If there are atoms with equal Z, the atoms at a distance 2 from the chiral centre should be considered. At the earliest difference, the group containing the substitutional atom with the highest Z receives higher priority. This process is repeated recursively, when atoms at the same distance from the considered chiral centre have equal Z. Each chiral centre has eventually a descriptor. Because of the sequential rule, in both TFMOx and MOx the lowest priority atom is H (i.e., number 4), the highest is O (i.e., number 1) and the two C atoms is to be further determined. In particular, the priority is inverted between TFMOx and MOx: in the former (H, H, O) < (F, F, F), in the latter (H, H, H) < (H, H, O).

After priorities have been assigned, the molecule is rotated in space so that the group with the lowest priority (i.e., number 4) points away from the observer (e.g., the H atom of the chiral centre for both TFMOx and MOx). Looking at the chiral centre, the sense of rotation of a curve passing through the groups in *ascending* priority order distinguishes the chiral centre type: a clockwise sense of rotation gives a R centre, and a counter-clockwise sense of rotation gives a S centre.

144

Along with the descriptors R and S, the optical rotation (+) or (-) could be added. The optical rotation of an optically active (chiral) molecule is defined experimentally as the rotation of the electric field in the polarization plane of a linearly polarized monochromatic light, seen from an observer who looks at the source of the radiation. (+) identifies a dextrorotary (clockwise) rotation and (-) a levorotary anticlockwise rotation. The optical rotation does not have a direct correlation to the absolute molecular structure, therefore it is not strictly correlated to the descriptors R and S.
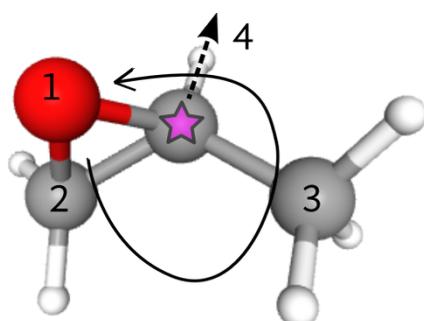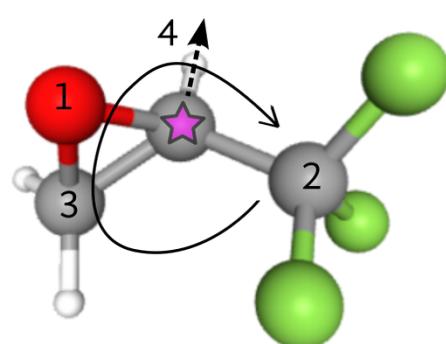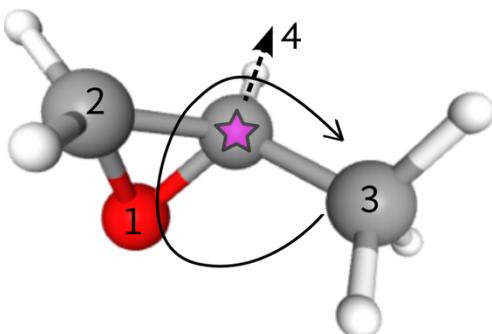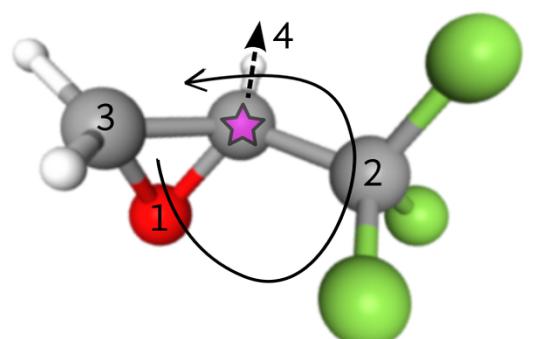
Figure B.2: comparison of descriptors' assignment procedure for MOx and TFMOx. The chiral C atom is marked with a star, each substitutional group has an assigned priority from 1 (highest) to 4 (lowest) based on their atomic number Z. The dashed arrow points away from the viewer and it associated with the atom with the lowest priority (i.e., number 4 for the H atom at the chiral centre for both molecules).

Another common nomenclature, still relevant for carbohydrates and amminoacids, is the Fisher projection developed by Emil Fischer in 1891. The method based on a convention consists in projecting the 3D structure of an oriented molecule on a plane and assign one of the two descriptor D (short for Latin *dextro*) or L (short for Latin *laevo*).

B.4 Propagation of errors

A normalized difference is used to quantify an asymmetry between two distributions by the difference of counts normalized to the total sum. If R is the number of events of a first Poisson distribution and L the number of a second Poisson distribution the asymmetry is then given by $\epsilon = \dfrac{R-L}{R+L}$.

The error can be derived using the chain rule for derivation and introducing the covariance

$$\sigma^2(\epsilon) = \left(\frac{\partial \epsilon}{\partial R}\right)^2 \sigma_R^2 + \left(\frac{\partial \epsilon}{\partial L}\right)^2 \sigma_L^2 + 2cov(R,L)\frac{\partial \epsilon}{\partial R}\frac{\partial \epsilon}{\partial L} \quad . \tag{B.9}$$

The covariance is exactly 0 since the measurements are designed to be completely independent. The errors on R and L are now given by the Poisson distribution, so that $\sigma_R^2 = R$ and $\sigma_L^2 = L$ and $N_{tot} = R+L$, therefore the error becomes

$$\sigma^2(\epsilon) \simeq \frac{4L^2}{N_{tot}^4}\sigma_R^2 + \frac{4R^2}{N_{tot}^4}\sigma_L^2 = 4\frac{RL}{N_{tot}^3} \quad . \tag{B.10}$$

If the number of counts of the two distribution differ just a little such that $R \simeq L \simeq N_{tot}/2$, it is possible to simplify equation (B.10) with

$$\sigma^2(\epsilon) \simeq \sqrt{\frac{1}{N_{tot}}} \quad . \tag{B.11}$$

B.5 Data treatment for plotting
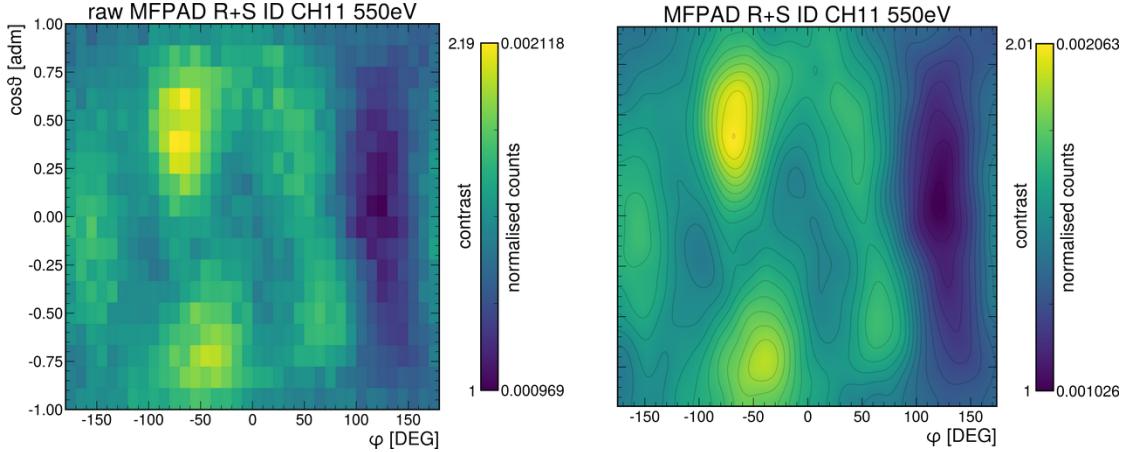
Figure B.3: comparison of PA-MFPAD before and after data treatment; left raw as exported from LMF2ROOT resolution 36x18; right final data treatment with level curves resolution 1000x500. The histograms in this work are further processed dividing by the minimum showing the contrast in colour scale.

The workflow for the post-processing data analysis starts with the calculation of momentum vectors from *.lmf* files using the software *LMF2ROOT v3.38* and ROOT library *ROOT 5.34/36 (2016)* that exports aggregated data in *.root* files. A typical raw histogram for a PA-MFPAD with dimension (36, 18) is shown on the left of Figure B.3. In this work, all histograms are processed using libraries based on *Python v3.8*. A histogram of interest is extracted from each *.root* file using the *Uproot v4* library which generates three *Numpy* arrays of dimension x (36, 1), y (18, 1) and counts (36, 18), respectively. The counts vector is normalized to its total sum. A 2D B-spline is created using the *Scipy* library interpolating the imported counts, and it is evaluated on a denser grid of dimension (1000, 500) within the same limits of the original x and y data. The resulting vector of the interpolation is processes with a 2D Gaussian filter of $\sigma_x = 8$ and $\sigma_y = 4$ from which the level curves are extracted too. The interpolated vector is plotted using the *Matplotlib* library and the level curves are added as overlay layer. The result of the treatment is shown in right plot of Figure B.3 for PA-MFPAD of R-TFMOx for the CH11 reaction channel at 11.7 eV, where the two helicity and the two enantiomers are combine together according to the symmetry rules mentioned in chapter 5.3.3. The presented method keeps the contrast (i.e., the difference

between the absolute maximum and minimum) within few percentages compare to the original values i.e., 2.1, therefore the colour scales are used interchangeability. As a final normalization, each histogram is divided by its minimum value, thus the minimum value is 1 and the maximum value is the contrast.

A pseudocode for the plotting procedure is given in the followings: the full version of the code is available in a repository on the archive.

```python
import uproot
import numpy as np
import scipy as sp
import matplotlib as mpl
import matplotlib.pyplot as plt

x,y,counts = np.array(file[location].to_numpy(),dtype=object)

xnew = np.arange(x.min(), x.max(), 0.001)

ynew = np.arange(y.min(), y.max(), 0.05)

Xn, Yn = np.meshgrid(xnew, ynew)

f = interpolate.bisplrep(x,y,counts)

Zn = interpolate.bisplev(Xn[0,:],Yn[:,0],f).T

plt.pcolormesh(Xn, Yn, Zn, shading = 'gouraud')

plt.contour(Xn, Yn, gaussian_filter(Zn, sigma = [4,8]), alpha=0.1)
```

B.6 System of reference and rotation
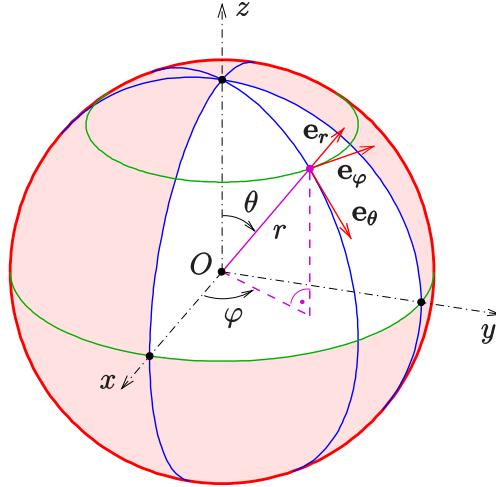
Figure B.4: representation of the Cartesian system of reference with physics convention for spherical coordinates (φ, θ) in the laboratory frame (LF). Image adapted from Wikipedia.

In the laboratory frame (LF), according to the convention adopted, the x-axis is the photon propagation direction, the y-axis is the molecular beam direction and the z-axis is the tof direction. The x-y plane is therefore parallel to the detector plane and to the polarization plane for circularly polarized photons. In the molecular frame MF

The physics convention for spherical coordinates is used in this work. A vector **r** from the origin O with length ||**r**|| is described by the polar angle θ, the angle with respect to polar z-axis, defined in the domain $[0, \pi]$, and the azimuthal angle φ, the angle of rotation from the initial meridian x-y plane, with a domain $(\pi, -\pi)$, as shown in Figure B.4. The transformation from Cartesian to spherical coordinates is described in the set of equations (B.12).

$$\varphi = atan2\left(\boldsymbol{r}_y, \boldsymbol{r}_x\right)$$
$$\theta = \cos^{-1}\left(\frac{\boldsymbol{r}_z}{\sqrt{\boldsymbol{r}_x + \boldsymbol{r}_y + \boldsymbol{r}_z}}\right) \tag{B.12}$$

The Euler angles are used to describe a 3D rotation in the Cartesian coordinate frames are by convention defined as shown in Figure B.5.
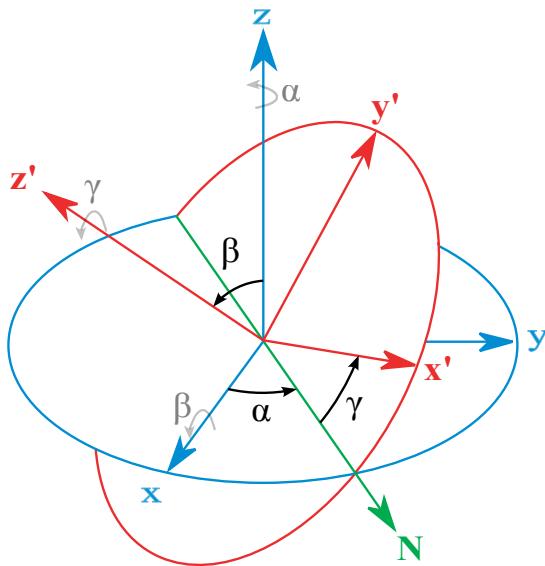
Figure B.5: Classic Euler angles geometrical definition. The xyz (fixed) system is shown in blue, the x'y'z' (rotated) system is shown in red. The line of nodes (N) is shown in green, the angles are reported both as plain angles (black) and rotation around the axis (grey). The convention shown here is the $z_1y_2x_3$.

To conveniently rotate the molecules from the molecular frame (MF) to the LF according to a photon direction expressed in spherical coordinates, the most commonly used convention *zxz'* (i.e., intrinsic) was chosen. A rotation around an axis can be described by a rotational matrix e.g., A, B and C for the rotation around the z-axis of an angle $\alpha \in [0, 2\pi]$, around the x-axis of an angle $\beta \in [0, \pi]$, and around the z'-axis of an angle $\gamma \in [0, 2\pi]$, respectively. The three linearly independent rotations can be subsequently combined (i.e., multiplied) into a general rotational matrix R reported in equation B.13. If the angle $\gamma = 0$, the *single* spherical coordinates can be translated directly into Euler angles $\alpha = \varphi$ (i.e., rotation around the z-axis) and $\beta = \theta$ (i.e., rotation around the x-axis).

$$R_{YPR} = R_x(\gamma)\, R_y(\beta)\, R_z(\alpha) =$$

$$= \begin{pmatrix} \cos\gamma\,\cos\beta & \sin\gamma\,\cos\beta & -\sin\beta \\ \cos\gamma\,\sin\beta\,\sin\alpha - \sin\gamma\,\cos\alpha & \sin\gamma\,\sin\beta\,\sin\alpha + \cos\gamma\,\cos\alpha & \cos\beta\,\sin\alpha \\ \cos\gamma\,\sin\beta\cos\alpha + \sin\gamma\,\sin\alpha & \sin\gamma\,\sin\beta\cos\alpha - \cos\gamma\,\sin\alpha & \cos\beta\,\cos\alpha \end{pmatrix} \quad \text{(B.13)}$$

B.7 Fully-differential PECD for multiple photoelectron energies

As a complementary to the dichroic parameter b_1 representation of Figure 5.29:, the fully-differential PECD experimental histograms for R-TFMOx channel CH11 for all sub-breakup channels at all photoelectron energies are presented in the Figure B.6, Figure B.7, Figure B.8, Figure B.9, and Figure B.10 along with the respective theoretical predictions. Figure B.11 shows a comparison of PECD between S- and R-TFMOx at energy 11.7 eV in the top and bottom panel, respectively: for each photon direction, there is a flip in PECD values between the two enantiomers, according to the symmetry rule $\cos\theta \rightarrow -\cos\theta$ for the electronic coordinates. The effect is stronger for larger values of $|\cos\theta_{ph}|$.
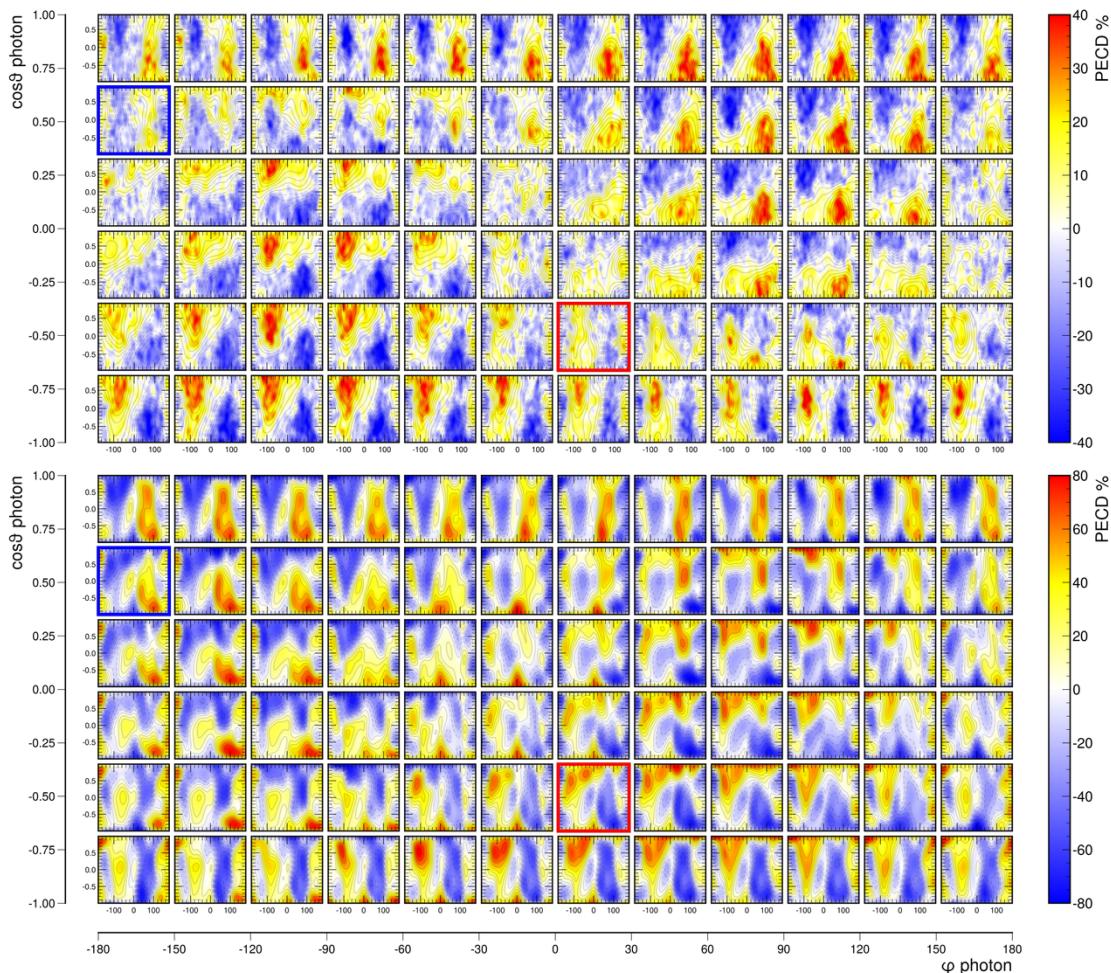
Figure B.6: comparison of fully-differential PECD for R-TFMOx at 11.7 eV (top panel, experimental) and 11.5 eV (bottom panel, theoretical). PECD calculated using the equation (3.21).
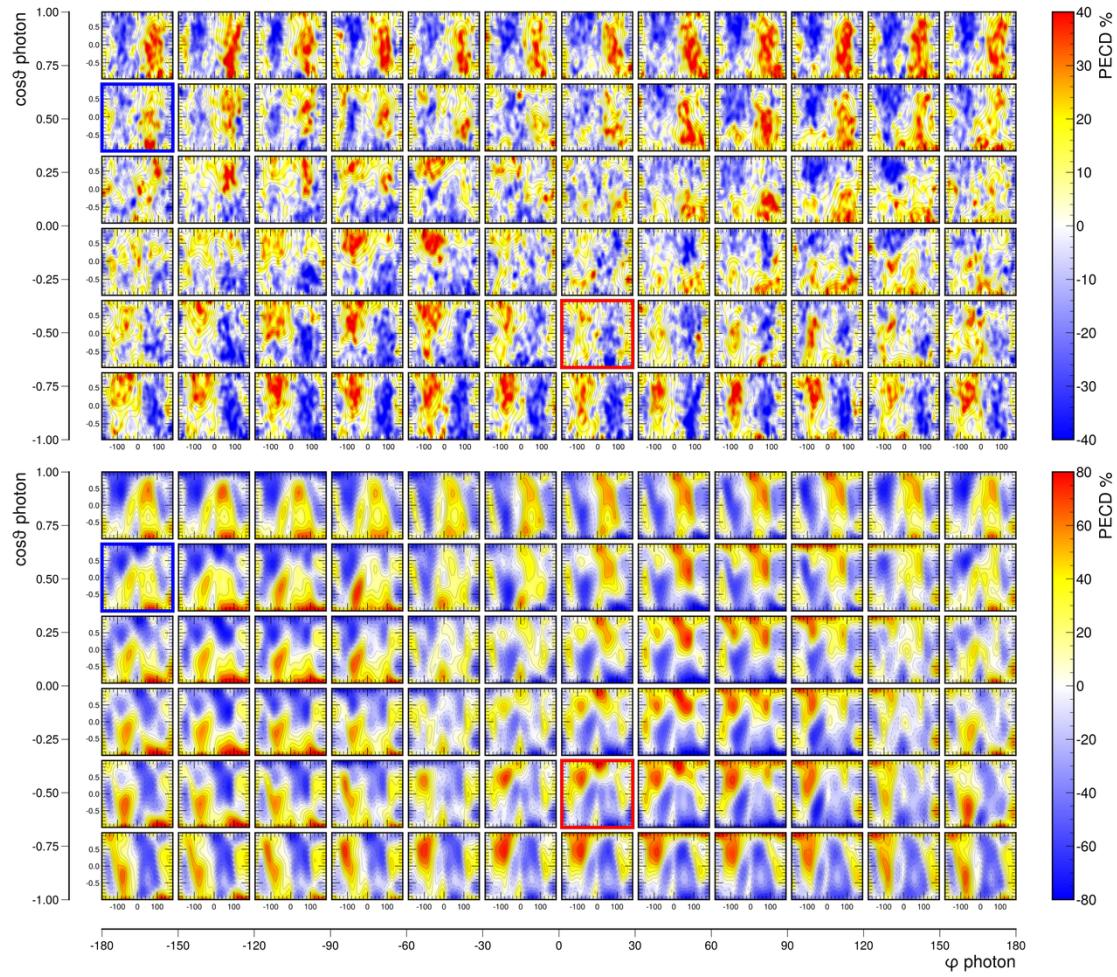
Figure B.7: comparison of fully-differential PECD for R-TFMOx at 8.1 eV (top panel, experimental) and 8.2 eV (bottom panel, theoretical). PECD calculated using the equation (3.21).
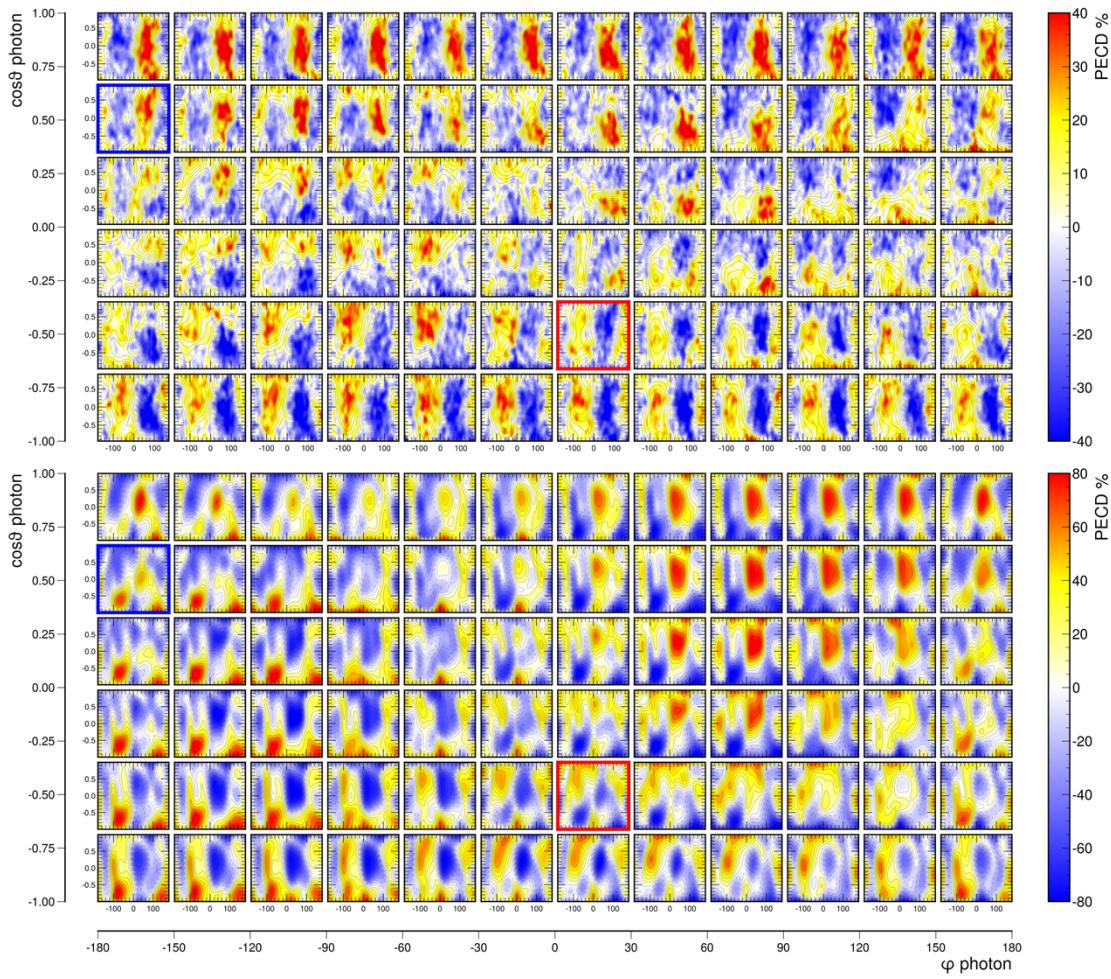
Figure B.8: comparison of fully-differential PECD for R-TFMOx at 6.1 eV (top panel, experimental) and 6 eV (bottom panel, theoretical). PECD calculated using the equation (3.21).
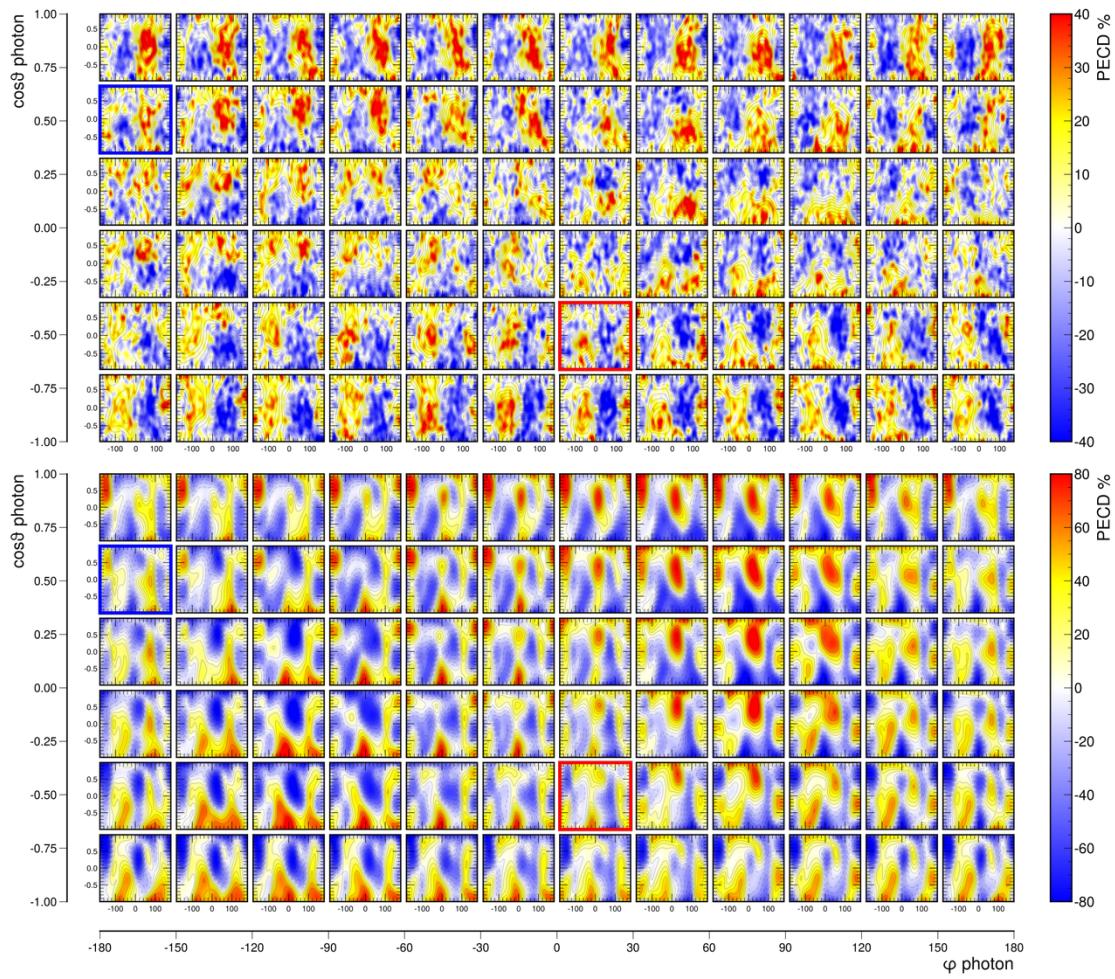
Figure B.9: comparison of fully-differential PECD for R-TFMOx at 4.1 eV (top panel, experimental) and 4 eV (bottom panel, theoretical). PECD calculated using the equation (3.21).
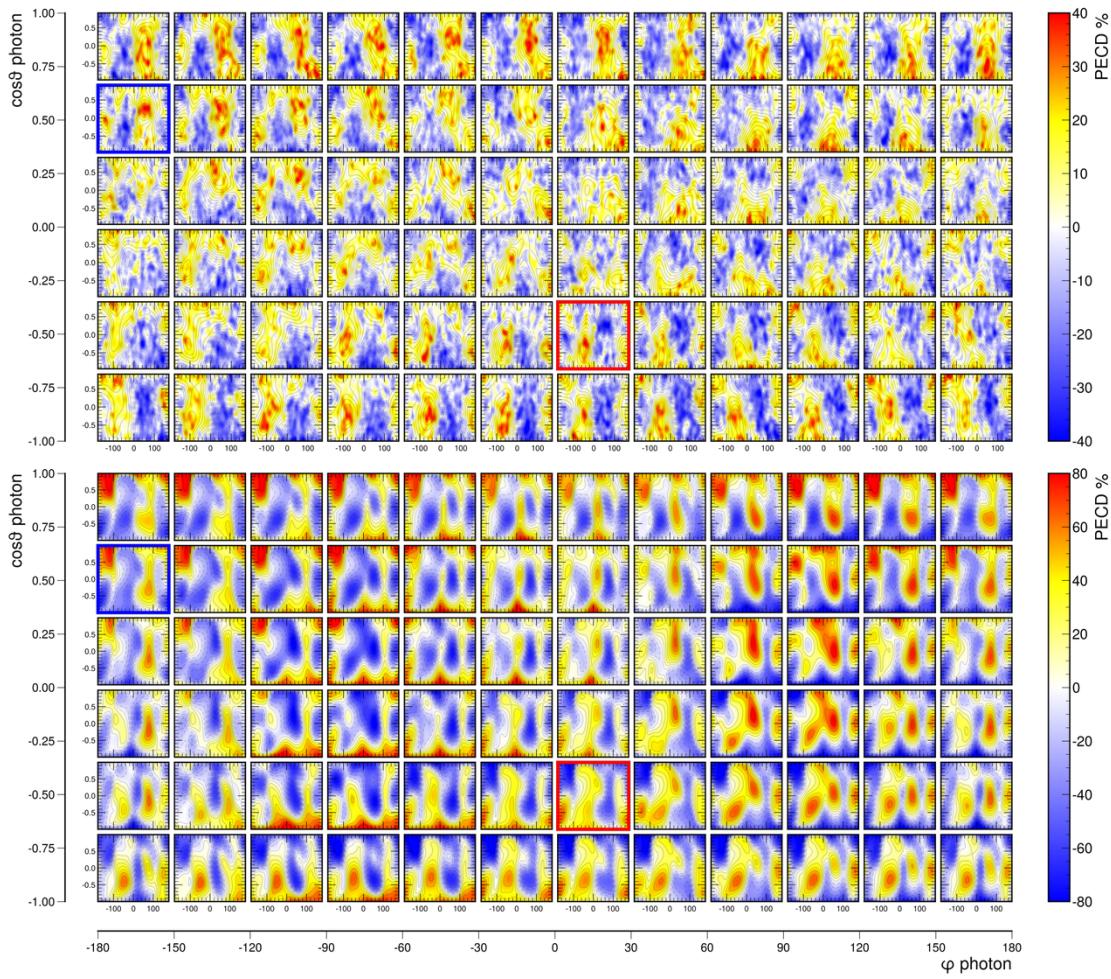
Figure B.10: comparison of fully-differential PECD for R-TFMOx at 3.1 eV (top panel, experimental) and 3 eV (bottom panel, theoretical). PECD calculated using the equation (3.21).
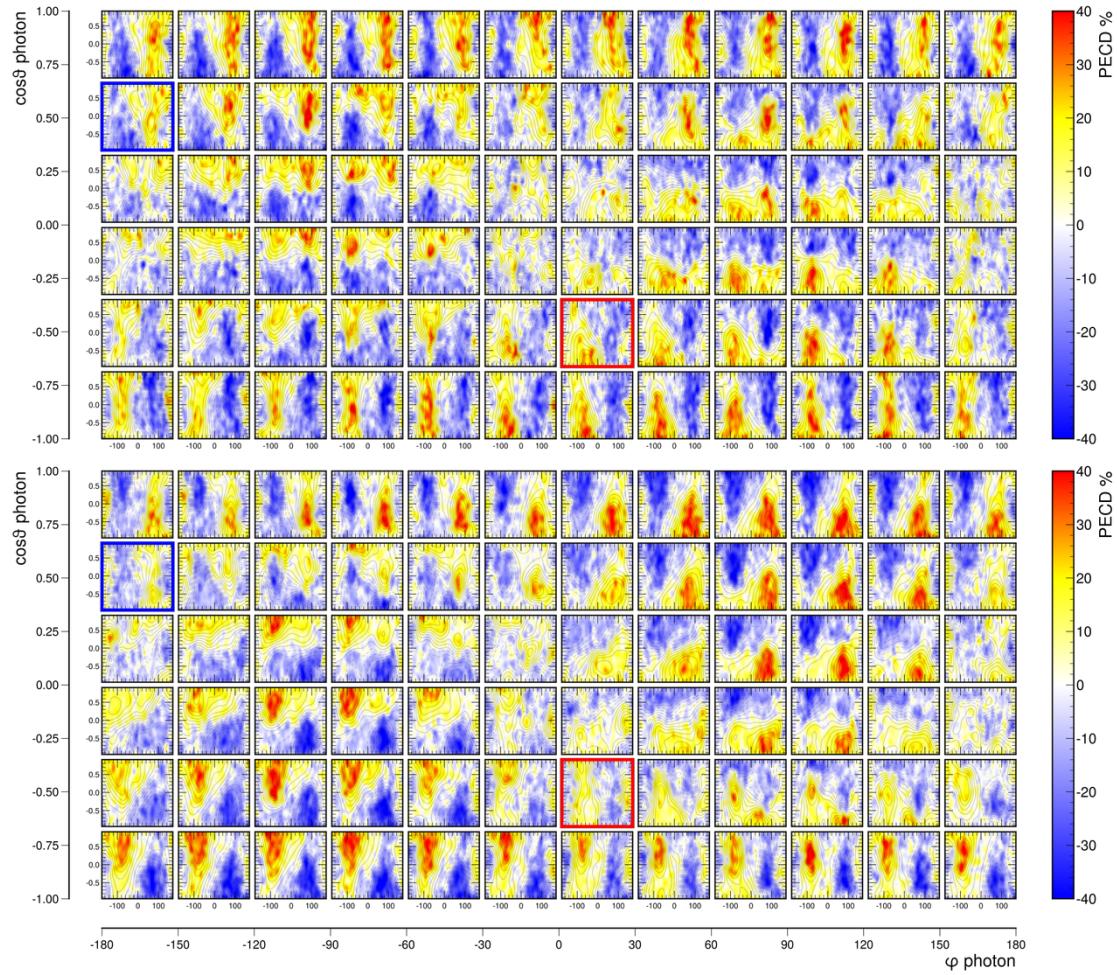
Figure B.11: fully-differential PECD for S- and R-TFMOx at 11.7 eV, top and bottom panel, respectively. Experimental results. Note in each panel for each enantiomer, the mirroring around $\cos\vartheta = 0$ upon the change of $\cos\theta_{ph}$; the effect is more visible for larger values of $|\cos\theta_{ph}|$. For each light's propagation direction, the values of PECD are mirrored around $\cos\vartheta = 0$ upon changing enantiomer; the effect is stronger for larger values of $|\cos\theta_{ph}|$. PECD calculated using the equation (3.21).

B.8 Newton plots for multiple photoelectron energies

Figure B.12 shows the Newton plots with side projections for all photoelectron energies for R-TFMOx, breakup CH11, and all sub-breakup combined. The influence of the energy on the distributions (i.e., definition of MF) is negligible.
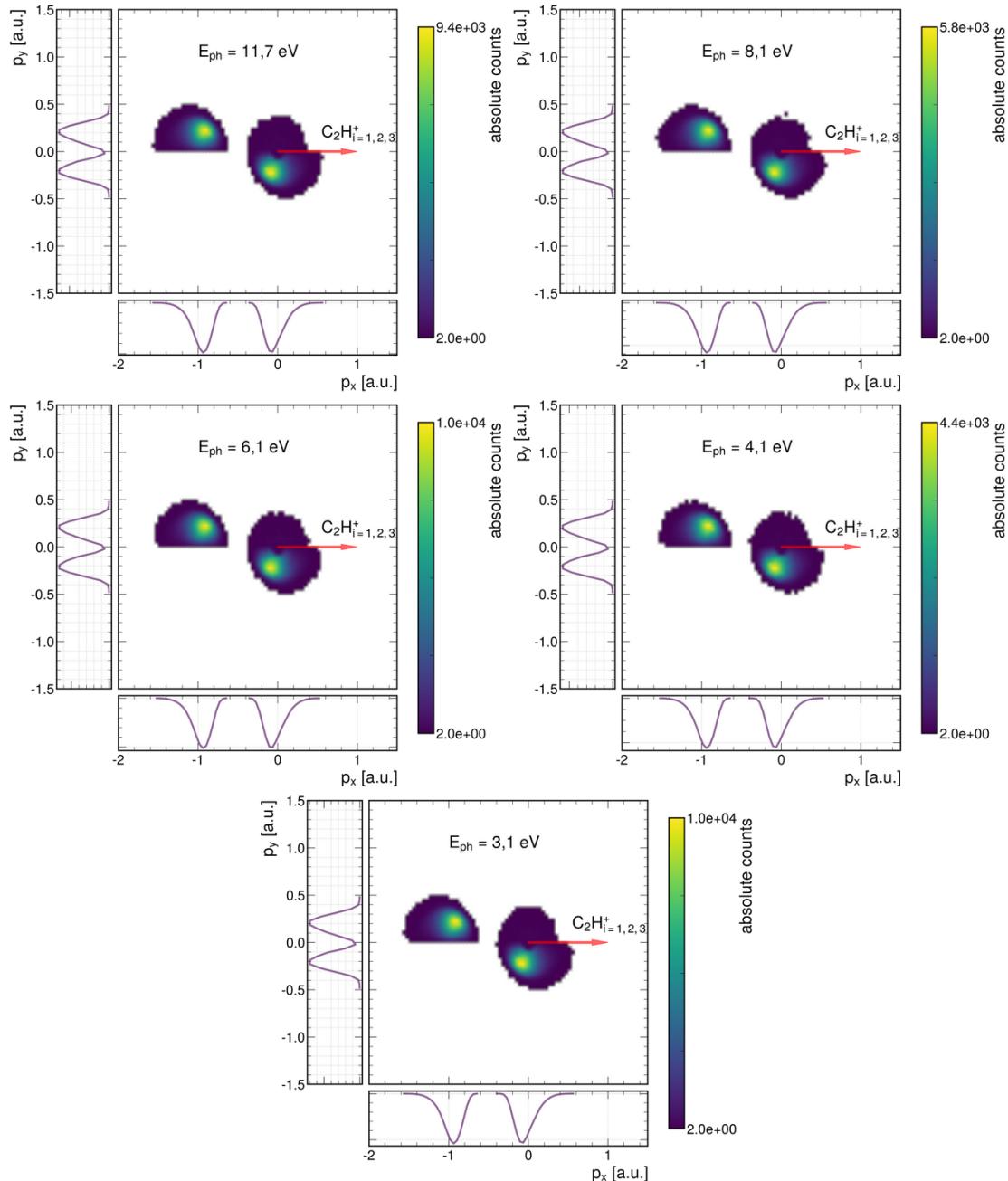
Figure B.12: Newton plots R-TFMOx for CH11 all PIPICO lines combined for multiple photoelectron energies with projections; note the peaks position remains constant for all five photoelectron energies.

B.9 Hexanode position calculation

An hexanode delay line (DL) has three-layers. The time value u_i for each wire is calculated as the time difference of arrival at the two opposite sides of each wire time a the conversion factor f_i to convert from time (ns) to position (mm) as shown in the set of equation (B.14). The exact f_i values are unique for each hexanode and are determined by a self-calibration routine; a shift factor w_{offset} is usually required for the w layer in order to obtain consistent values for all equations B.14, and its values is also returned from the self-calibration routine.

$$
\begin{aligned}
u &= (u_1 - u_2) \cdot f_u \\
v &= (v_1 - v_2) \cdot f_v \\
w &= (w_1 - w_2) \cdot f_w + w_{offset}
\end{aligned}
\tag{B.14}
$$

The location of an impinging particle in Cartesian coordinates (x, y) is calculated as from the internal coordinate frame u, v, and w, and due to the over-determined (redundant) system generated from three layers, any combination of pairs from the set of equations (B.15) can be used. O_x and O_y are arbitrary offsets. The third layer is redundant and is used for event resorting purposes.

$$
\begin{aligned}
x_{uv} &= u + O_x \\
y_{uv} &= \frac{1}{\sqrt{3}} (u - 2v) + O_y \\
x_{uw} &= x_{uv} \\
y_{uw} &= \frac{1}{\sqrt{3}} (2w - u) + O_y \\
x_{vw} &= (w + v) + O_x \\
y_{vw} &= \frac{1}{\sqrt{3}} (w - v) + O_y
\end{aligned}
\tag{B.15}
$$

Thus, the x-direction is defined parallel to the u-plane; the definition of the direction of the y-coordinate follows from the geometric arrangement of the wire windings. The convention used dictates that the detector image corresponds to the image of a viewer looking from *outside* to *inside* of the experimental chamber.

B.10 HPLC and NMR Purity analysis
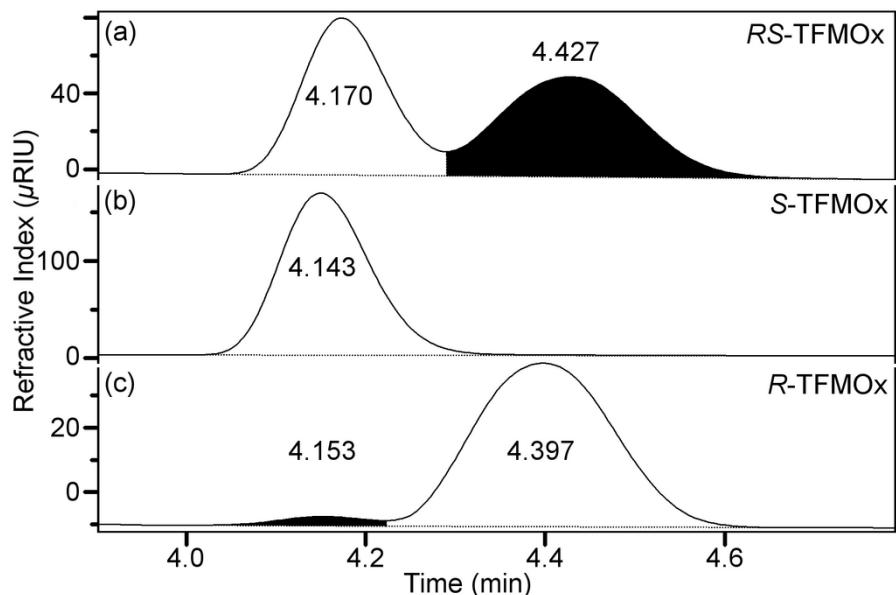
Figure B.13: Ratio of enantiomers present in the samples of racemic RS-TFMOx (a) and its S- and R-enantiomers (b and c, respectively) as experimentally determined using HPLC. Image reproduced from [154].

Nuclear magnetic resonance (NMR) spectroscopy is used to verify the purity of commercial samples (SynQuest Laboratories): RS-mixture and pure S- or R-TFMOx enantiomers. The ^{1}H- ,^{13}C- and ^{19}F-NMR-data were recorded with Varian VNMRS-500 MHz or MR-400 MHz spectrometers at T_R. Chemical shifts were referenced to residual protic impurities in the solvent (^{1}H) or the deuterio solvent itself (^{13}C), and reported relative to external $Si(CH_3)_4$(^{1}H, ^{13}C) or $C_6H_5CF_3$(^{19}F). The NMR-shifts were assigned based on 2D-NMR (HSQC) spectra. After integration of the fluorine NMR signal, the chemical purity is higher than 96% for the RS-TFMOx mixture and higher than 96% or 98% for the S-TFMOx or R-TFMOx enantiomers, respectively. An High-performance liquid chromatography (HPLC) CHIRALPAK IG (4.6 mm × 250 mm) chiral analytical column was used to estimate the enantiomeric purity of the samples. The RS-TFMOx mixture is racemic within margins of error (S-TFMOx : R-TFMOx = 0.49 : 0.51), and the enantiopure S-TFMOx or R-TFMOx have an enantiomeric excess of approximately 95%, as shown in Figure B.13.

C. *BIBLIOGRAPHY*

[1] J. D. Watson and F. H. C. Crick, 'Molecular Structure of Nucleic Acids: A Structure for Deoxyribose Nucleic Acid', *Nature*, vol. 171, no. 4356, pp. 737–738, Apr. 1953, doi: https://doi.org/10.1038/171737a0.

[2] W. T. Kelvin, *The molecular tactics of a crystal*. Oxford, Clarendon Press, 1894. Accessed: Mar. 23, 2021. [Online]. Available: http://archive.org/details/moleculartactic00kelvgoog

[3] P. Cintas, 'Tracing the Origins and Evolution of Chirality and Handedness in Chemical Language', *Angew. Chem. Int. Ed.*, vol. 46, no. 22, pp. 4016–4024, May 2007, doi: https://doi.org/10.1002/anie.200603714.

[4] M. J. Longo, 'Detection of a dipole in the handedness of spiral galaxies with redshifts z~0.04', *Phys. Lett. B*, vol. 699, no. 4, pp. 224–229, May 2011, doi: https://doi.org/10.1016/j.physletb.2011.04.008.

[5] P. Carlsson, N. A. Warner, I. G. Hallanger, D. Herzke, and R. Kallenborn, 'Spatial and temporal distribution of chiral pesticides in Calanus spp. from three Arctic fjords', *Environ. Pollut.*, vol. 192, pp. 154–161, Sep. 2014, doi: https://doi.org/10.1016/j.envpol.2014.05.021.

[6] S. Mason, 'The origin of chirality in nature', *Trends Pharmacol. Sci.*, vol. 7, pp. 20–23, Jan. 1986, doi: https://doi.org/10.1016/0165-6147(86)90235-X.

[7] W. A. Bonner, 'The origin and amplification of biomolecular chirality', *Orig. Life Evol. Biosphere J. Int. Soc. Study Orig. Life*, vol. 21, no. 2, pp. 59–111, 1991, doi: https://doi.org/10.1007/BF01809580.

[8] W. A. Bonner, J. Mayo Greenberg, and E. Rubenstein, 'The Extraterrestrial Origin of the Homochirality of Biomolecules – Rebuttal to a Critique', *Orig. Life Evol. Biosph.*, vol. 29, no. 2, pp. 215–219, Mar. 1999, doi: https://doi.org/10.1023/A:1006544203107.

[9] H. D. Flack, 'Louis Pasteur's discovery of molecular chirality and spontaneous resolution in 1848, together with a complete review of his

crystallographic and chemical work', *Acta Crystallogr. A*, vol. 65, no. 5, pp. 371–389, Sep. 2009, doi: https://doi.org/10.1107/S0108767309024088.

[10] G. Vantomme and J. Crassous, 'Pasteur and chirality: A story of how serendipity favors the prepared minds', *Chirality*, vol. 33, no. 10, pp. 597–601, 2021, doi: https://doi.org/10.1002/chir.23349.

[11] T. Yoshimura and N. Esak, 'Amino acid racemases: Functions and mechanisms', *J. Biosci. Bioeng.*, vol. 96, no. 2, pp. 103–109, Jan. 2003, doi: https://doi.org/10.1016/S1389-1723(03)90111-3.

[12] J. C. Brookes, A. P. Horsfield, and A. M. Stoneham, 'Odour character differences for enantiomers correlate with molecular flexibility', *J. R. Soc. Interface*, vol. 6, no. 30, pp. 75–86, Jan. 2009, doi: https://doi.org/10.1098/rsif.2008.0165.

[13] E. Brenna, C. Fuganti, and S. Serra, 'Enantioselective perception of chiral odorants', *Tetrahedron Asymmetry*, vol. 14, no. 1, pp. 1–42, Jan. 2003, doi: https://doi.org/10.1016/S0957-4166(02)00713-9.

[14] L. A. Nguyen, H. He, and C. Pham-Huy, 'Chiral Drugs: An Overview', *Chiral Drugs*, vol. 2, no. 2, pp. 85–100, 2006.

[15] J. H. Kim and A. R. Scialli, 'Thalidomide: The Tragedy of Birth Defects and the Effective Treatment of Disease', *Toxicol. Sci.*, vol. 122, no. 1, pp. 1–6, Jul. 2011, doi: https://doi.org/10.1093/toxsci/kfr088.

[16] E. Pichersky, J. P. Noel, and N. Dudareva, 'Biosynthesis of Plant Volatiles: Nature's Diversity and Ingenuity', *Science*, vol. 311, no. 5762, pp. 808–811, Feb. 2006, doi: https://doi.org/10.1126/science.1118510.

[17] W. Song, M. Staudt, I. Bourgeois, and J. Williams, 'Laboratory and field measurements of enantiomeric monoterpene emissions as a function of chemotype, light and temperature', *Biogeosciences*, vol. 11, no. 5, pp. 1435–1447, Mar. 2014, doi: https://doi.org/10.5194/bg-11-1435-2014.

[18] K. Mori, 'Chirality and insect pheromones', *CHIRALITY*, vol. 10, pp. 578–586, 1998.

[19] R. M. Silverstein, 'Chirality in insect communication', *J. Chem. Ecol.*, vol. 14, no. 11, pp. 1981–2004, Nov. 1988, doi: https://doi.org/10.1007/BF01014245.

[20] J. A. Switzer, H. M. Kothari, P. Poizot, S. Nakanishi, and E. W. Bohannan, 'Enantiospecific electrodeposition of a chiral catalyst', *Nature*, vol. 425, no. 6957, pp. 490–493, Oct. 2003, doi: https://doi.org/10.1038/nature01990.

[21] G. Long *et al.*, 'Chiral-perovskite optoelectronics', *Nat. Rev. Mater.*, vol. 5, no. 6, pp. 423–439, Jun. 2020, doi: https://doi.org/10.1038/s41578-020-0181-5.

[22] R. Neier, 'A Two-Catalyst Photochemistry Route to Homochiral Rings', *Science*, vol. 344, no. 6182, pp. 368–369, Apr. 2014, doi: https://doi.org/10.1126/science.1252965.

[23] T. R. Harvey *et al.*, 'Probing Chirality with Inelastic Electron-Light Scattering', *Nano Lett.*, vol. 20, no. 6, pp. 4377–4383, Jun. 2020, doi: https://doi.org/10.1021/acs.nanolett.0c01130.

[24] M. Sozzi, *Discrete symmetries and CP violation: from experiment to theory*. Oxford; New York: Oxford University Press, 2008.

[25] J. Mun *et al.*, 'Electromagnetic chirality: from fundamentals to nontraditional chiroptical phenomena', *Light Sci. Appl.*, vol. 9, no. 1, Art. no. 1, Sep. 2020, doi: https://doi.org/10.1038/s41377-020-00367-8.

[26] K. Fehre *et al.*, 'Enantioselective fragmentation of an achiral molecule in a strong laser field', *Sci. Adv.*, vol. 5, no. 3, p. eaau7923, Mar. 2019, doi: https://doi.org/10.1126/sciadv.aau7923.

[27] L. D. Barron, *Molecular light scattering and optical activity*. Cambridge, UK; New York: Cambridge University Press, 2004. Accessed: Feb. 18, 2021. [Online]. Available: http://proxy.uqtr.ca/login.cgi?action=login&u=uqtr&db=ebsco&ezurl=http://search.ebscohost.com/login.aspx?direct=true&scope=site&db=nlebk&AN=174086

[28] T. D. Lee and C. N. Yang, 'Question of Parity Conservation in Weak Interactions', *Phys. Rev.*, vol. 104, no. 1, pp. 254–258, Oct. 1956, doi: https://doi.org/10.1103/PhysRev.104.254.

[29] M. Quack, 'How Important is Parity Violation for Molecular and Biomolecular Chirality?', *Angew. Chem. Int. Ed.*, vol. 41, no. 24, pp. 4618–4630, Dec. 2002, doi: https://doi.org/10.1002/anie.200290005.

[30] D. W. Rein, 'Some remarks on parity violating effects of intramolecular interactions', *J. Mol. Evol.*, vol. 4, no. 1, pp. 15–22, Mar. 1974, doi: https://doi.org/10.1007/BF01732768.

[31] V. S. Letokhov, 'On difference of energy levels of left and right molecules due to weak interactions', *Phys. Lett. A*, vol. 53, no. 4, pp. 275–276, Jun. 1975, doi: https://doi.org/10.1016/0375-9601(75)90064-X.

[32] A. Guijarro and M. Yus, *The Origin of Chirality in the Molecules of Life: A Revision from Awareness to the Current Theories and Perspectives of this Unsolved Problem*. Cambridge: Royal Society of Chemistry, 2008. doi: https://doi.org/10.1039/9781847558756.

[33] C. S. Wu, E. Ambler, R. W. Hayward, D. D. Hoppes, and R. P. Hudson, 'Experimental Test of Parity Conservation in Beta Decay', *Phys. Rev.*, vol. 105, no. 4, pp. 1413–1415, Feb. 1957, doi: https://doi.org/10.1103/PhysRev.105.1413.

[34] J. H. Christenson, J. W. Cronin, V. L. Fitch, and R. Turlay, 'Evidence for the $2\ensuremath{\pi}$ Decay of the K_{2}^{0} Meson', *Phys. Rev. Lett.*, vol. 13, no. 4, pp. 138–140, Jul. 1964, doi: https://doi.org/10.1103/PhysRevLett.13.138.

[35] J. M. Bijvoet, A. F. Peerdeman, and A. J. van BOMMEL, 'Determination of the Absolute Configuration of Optically Active Compounds by Means of X-Rays', *Nature*, vol. 168, no. 4268, pp. 271–272, Aug. 1951, doi: https://doi.org/10.1038/168271a0.

[36] J. Haesler, I. Schindelholz, E. Riguet, C. G. Bochet, and W. Hug, 'Absolute configuration of chirally deuterated neopentane', *Nature*, vol. 446, no. 7135, Art. no. 7135, Mar. 2007, doi: https://doi.org/10.1038/nature05653.

[37] J. Labuta *et al.*, 'NMR spectroscopic detection of chirality and enantiopurity in referenced systems without formation of diastereomers', *Nat. Commun.*, vol. 4, no. 1, Art. no. 1, Jul. 2013, doi: https://doi.org/10.1038/ncomms3188.

[38] I. Ilisz, R. Berkecz, and A. Péter, 'Application of chiral derivatizing agents in the high-performance liquid chromatographic separation of amino acid enantiomers: A review', *J. Pharm. Biomed. Anal.*, vol. 47, no. 1, pp. 1–15, May 2008, doi: https://doi.org/10.1016/j.jpba.2007.12.013.

[39] P. Fischer, D. S. Wiersma, R. Righini, B. Champagne, and A. D. Buckingham, 'Three-Wave Mixing in Chiral Liquids', *Phys. Rev. Lett.*, vol. 85, no. 20, pp. 4253–4256, Nov. 2000, doi: https://doi.org/10.1103/PhysRevLett.85.4253.

[40] M. D. Marshall, H. O. Leung, K. Wang, and M. D. Acha, 'Microwave Spectrum and Molecular Structure of the Chiral Tagging Candidate, 3,3,3-Trifluoro-1,2-epoxypropane and Its Complex with the Argon Atom', *J. Phys. Chem. A*, vol. 122, no. 19, pp. 4670–4680, May 2018, doi: https://doi.org/10.1021/acs.jpca.8b02550.

[41] D. Patterson, M. Schnell, and J. M. Doyle, 'Enantiomer-specific detection of chiral molecules via microwave spectroscopy', *Nature*, vol. 497, no. 7450, Art. no. 7450, May 2013, doi: https://doi.org/10.1038/nature12150.

[42] L. Rosenfeld, 'Quantenmechanische Theorie der natürlichen optischen Aktivität von Flüssigkeiten und Gasen', *Z. Für Phys.*, vol. 52, pp. 161–174, 1929.

[43] P. C. Sercel, Z. V. Vardeny, and A. L. Efros, 'Circular dichroism in non-chiral metal halide perovskites', *ArXiv200700073 Cond-Mat*, Jul. 2020, Accessed: Feb. 08, 2021. [Online]. Available: http://arxiv.org/abs/2007.00073

[44] X. Zambrana-Puyalto, X. Vidal, and G. Molina-Terriza, 'Angular momentum-induced circular dichroism in non-chiral nanostructures', *Nat. Commun.*, vol. 5, no. 1, Art. no. 1, Sep. 2014, doi: https://doi.org/10.1038/ncomms5922.

[45] M. K. Hargreaves, 'Optical Rotatory Dispersion: Its Nature and Origin', *Nature*, vol. 195, no. 4841, pp. 560–566, Aug. 1962, doi: https://doi.org/10.1038/195560a0.

[46] P. J. Stephens, 'Theory of vibrational circular dichroism', *J. Phys. Chem.*, vol. 89, no. 5, pp. 748–752, Feb. 1985, doi: https://doi.org/10.1021/j100251a006.

[47] C. Brouder and M. Hikam, 'Multiple-Scattering Theory of Magnetic-X-Ray Circular-Dichroism', *Phys. Rev. B*, vol. 43, no. 5, pp. 3809–3820, Feb. 1991, doi: https://doi.org/10.1103/PhysRevB.43.3809.

[48] D. Venus, 'Interrelation of Magnetic-Dichroism Effects Seen in the Angular-Distribution of Photoelectrons from Surfaces', *Phys. Rev. B*, vol. 49, no. 13, pp. 8821–8829, Apr. 1994, doi: https://doi.org/10.1103/PhysRevB.49.8821.

[49] L. Alagna *et al.*, 'X-Ray Natural Circular Dichroism', *Phys. Rev. Lett.*, vol. 80, no. 21, pp. 4799–4802, May 1998, doi: https://doi.org/10.1103/PhysRevLett.80.4799.

[50] P. Cintas, 'Chirality of Living Systems: A Helping Hand from Crystals and Oligopeptides', p. 7, 2002.

[51] M. E. Couprie, 'New generation of light sources: Present and future', *J. Electron Spectrosc. Relat. Phenom.*, vol. 196, pp. 3–13, Oct. 2014, doi: https://doi.org/10.1016/j.elspec.2013.12.007.

[52] B. Ritchie, 'Theory of the angular distribution for ejection of photoelectrons from optically active molecules and molecular negative ions. II', *Phys. Rev. A*, vol. 14, no. 1, pp. 359–362, Jul. 1976, doi: https://doi.org/10.1103/PhysRevA.14.359.

[53] B. Ritchie, 'Theory of the angular distribution of photoelectrons ejected from optically active molecules and molecular negative ions', *Phys. Rev. A*, vol. 13, no. 4, pp. 1411–1415, Apr. 1976, doi: https://doi.org/10.1103/PhysRevA.13.1411.

[54] N. A. Cherepkov, 'Circular dichroism of molecules in the continuous absorption region', *Chem. Phys. Lett.*, vol. 87, no. 4, pp. 344–348, Apr. 1982, doi: https://doi.org/10.1016/0009-2614(82)83600-2.

[55] S. Beaulieu *et al.*, 'Universality of photoelectron circular dichroism in the photoionization of chiral molecules', *New J. Phys.*, vol. 18, no. 10, p. 102002, Oct. 2016, doi: https://doi.org/10.1088/1367-2630/18/10/102002.

[56] S. Beaulieu *et al.*, 'Multiphoton photoelectron circular dichroism of limonene with independent polarization state control of the bound-bound and bound-continuum transitions', *J. Chem. Phys.*, vol. 149, no. 13, p. 134301, Oct. 2018, doi: https://doi.org/10.1063/1.5042533.

[57] K. Fehre *et al.*, 'Angular streaking in strong field ionization of chiral molecules', *Phys. Rev. Res.*, vol. 1, no. 3, p. 033045, Oct. 2019, doi: https://doi.org/10.1103/PhysRevResearch.1.033045.

[58] G. A. Garcia, L. Nahon, M. Lebech, J. C. Houver, D. Dowek, and I. Powis, 'Circular dichroism in the photoelectron angular distribution from randomly oriented enantiomers of camphor', *J. Chem. Phys.*, vol. 119, no. 17, pp. 8781–8784, Nov. 2003, doi: https://doi.org/10.1063/1.1621379.

[59] L. Nahon, G. A. Garcia, C. J. Harding, E. Mikajlo, and I. Powis, 'Determination of chiral asymmetries in the valence photoionization of camphor enantiomers by photoelectron imaging using tunable circularly polarized light', *J. Chem. Phys.*, vol. 125, no. 11, p. 114309, Sep. 2006, doi: https://doi.org/10.1063/1.2336432.

[60] G. A. Garcia, L. Nahon, C. J. Harding, and I. Powis, 'Chiral signatures in angle-resolved valence photoelectron spectroscopy of pure glycidol enantiomers', *Phys. Chem. Chem. Phys.*, vol. 10, no. 12, pp. 1628–1639, 2008, doi: https://doi.org/10.1039/b714095a.

[61] G. A. Garcia, H. Soldi-Lose, L. Nahon, and I. Powis, 'Photoelectron Circular Dichroism Spectroscopy in an Orbitally Congested System: The Terpene Endoborneol', *J. Phys. Chem. A*, vol. 114, no. 2, pp. 847–853, Jan. 2010, doi: https://doi.org/10.1021/jp909344r.

[62] M. Tia *et al.*, 'Chiral Asymmetry in the Photoionization of Gas-Phase Amino-Acid Alanine at Lyman-α Radiation Wavelength', *J. Phys. Chem. Lett.*, vol. 4, no. 16, pp. 2698–2704, Aug. 2013, doi: https://doi.org/10.1021/jz4014129.

[63] G. A. Garcia, H. Dossmann, L. Nahon, S. Daly, and I. Powis, 'Photoelectron circular dichroism and spectroscopy of trifluoromethyl- and methyl-oxirane: a comparative study', *Phys. Chem. Chem. Phys.*, vol. 16, no. 30, p. 16214, Jun. 2014, doi: https://doi.org/10.1039/C4CP01941E.

[64] G. A. Garcia, L. Nahon, S. Daly, and I. Powis, 'Vibrationally induced inversion of photoelectron forward-backward asymmetry in chiral molecule photoionization by circularly polarized light', *Nat. Commun.*, vol. 4, p. 2132, Jul. 2013, doi: https://doi.org/10.1038/ncomms3132.

[65] L. Nahon *et al.*, 'Determination of accurate electron chiral asymmetries in fenchone and camphor in the VUV range: sensitivity to isomerism and enantiomeric purity]', *Phys. Chem. Chem. Phys.*, vol. 18, no. 18, pp. 12696–12706, May 2016, doi: https://doi.org/10.1039/c6cp01293k.

[66] S. Turchini *et al.*, 'Conformational Sensitivity in Photoelectron Circular Dichroism of 3-Methylcyclopentanone', *ChemPhysChem*, vol. 14, no. 8, pp. 1723–1732, Jun. 2013, doi: https://doi.org/10.1002/cphc.201200975.

[67] L. Nahon, G. A. Garcia, H. Soldi-Lose, S. Daly, and I. Powis, 'Effects of dimerization on the photoelectron angular distribution parameters from chiral camphor enantiomers obtained with circularly polarized vacuum-ultraviolet radiation', *Phys. Rev. A*, vol. 82, no. 3, p. 032514, Sep. 2010, doi: https://doi.org/10.1103/PhysRevA.82.032514.

[68] S. Daly, I. Powis, G. A. Garcia, H. Soldi-Lose, and L. Nahon, 'Photoionization of epichlorohydrin enantiomers and clusters studied with circularly polarized vacuum ultraviolet radiation', *J. Chem. Phys.*, vol. 134, no. 6, p. 064306, Feb. 2011, doi: https://doi.org/10.1063/1.3536500.

[69] I. Powis, C. J. Harding, G. A. Garcia, and L. Nahon, 'A valence photoelectron imaging investigation of chiral asymmetry in the photoionization of fenchone and camphor', *Chemphyschem*, vol. 9, no. 3, pp. 475–483, Feb. 2008, doi: https://doi.org/10.1002/cphc.200700748.

[70] S. Beaulieu *et al.*, 'Probing ultrafast dynamics of chiral molecules using time-resolved photoelectron circular dichroism', *Faraday Discuss.*, vol. 194, pp. 325–348, 2016, doi: https://doi.org/10.1039/c6fd00113k.

[71] A. Comby *et al.*, 'Relaxation Dynamics in Photoexcited Chiral Molecules Studied by Time-Resolved Photoelectron Circular Dichroism: Toward Chiral Femtochemistry', *J. Phys. Chem. Lett.*, vol. 7, no. 22, pp. 4514–4519, Nov. 2016, doi: https://doi.org/10.1021/acs.jpclett.6b02065.

[72] A. Comby *et al.*, 'Real-time determination of enantiomeric and isomeric content using photoelectron elliptical dichroism', *Nat. Commun.*, vol. 9, no. 1, p. 5212, Dec. 2018, doi: https://doi.org/10.1038/s41467-018-07609-9.

[73] V. Ulrich *et al.*, 'Giant Chiral Asymmetry in the C 1 *s* Core Level Photoemission from Randomly Oriented Fenchone Enantiomers', *J. Phys. Chem. A*, vol. 112, no. 16, pp. 3544–3549, Apr. 2008, doi: https://doi.org/10.1021/jp709761u.

[74] M. Tia *et al.*, 'Observation of Enhanced Chiral Asymmetries in the Inner-Shell Photoionization of Uniaxially Oriented Methyloxirane Enantiomers', *J. Phys. Chem. Lett.*, vol. 8, no. 13, pp. 2780–2786, Jul. 2017, doi: https://doi.org/10.1021/acs.jpclett.7b01000.

[75] B. Ritchie, 'Theoretical studies in photoelectron spectroscopy. Molecular optical activity in the region of continuous absorption and its characterization by the angular distribution of photoelectrons', *Phys. Rev. A*,

vol. 12, no. 2, pp. 567–574, Aug. 1975, doi: https://doi.org/10.1103/PhysRevA.12.567.

[76] R. Parzynski, *Acta Phys Pol. A*, vol. 57, no. 49, 1980.

[77] R. Dubs, S. Dixit, and V. Mckoy, 'Circular-Dichroism in Photoelectron Angular-Distributions from Oriented Linear-Molecules', *Phys. Rev. Lett.*, vol. 54, no. 12, pp. 1249–1251, 1985, doi: https://doi.org/10.1103/PhysRevLett.54.1249.

[78] C. Westphal, J. Bansmann, M. Getzlaff, and G. Schonhense, 'Circular-Dichroism in the Angular-Distribution of Photoelectrons from Oriented Co Molecules', *Phys. Rev. Lett.*, vol. 63, no. 2, pp. 151–154, Jul. 1989, doi: https://doi.org/10.1103/PhysRevLett.63.151.

[79] T. Jahnke *et al.*, 'Multicoincidence studies of photo and Auger electrons from fixed-in-space molecules using the COLTRIMS technique', *J. Electron Spectrosc. Relat. Phenom.*, vol. 141, no. 2–3, pp. 229–238, Dec. 2004, doi: https://doi.org/10.1016/j.elspec.2004.06.010.

[80] I. Powis, 'Photoelectron spectroscopy and circular dichroism in chiral biomolecules: L-alanine', *J. Phys. Chem. A*, vol. 104, no. 5, pp. 878–882, Feb. 2000, doi: https://doi.org/10.1021/jp9933119.

[81] T. Jahnke *et al.*, 'Circular dichroism in K-shell ionization from fixed-in-space CO and N_2 molecules', *Phys. Rev. Lett.*, vol. 88, no. 7, p. 073002, Feb. 2002, doi: https://doi.org/10.1103/PhysRevLett.88.073002.

[82] Stuart A. Rice, *Advances in chemical physics*, vol. 138. John Wiley & Sons, Inc., 2008. [Online]. Available: https://onlinelibrary.wiley.com/doi/10.1002/9780470259474.ch5

[83] T. Kitamura, T. Nishide, H. Shiromaru, Y. Achiba, and N. Kobayashi, 'Direct observation of "dynamic" chirality by Coulomb explosion imaging', *J. Chem. Phys.*, vol. 115, no. 1, pp. 5–6, Jul. 2001, doi: https://doi.org/10.1063/1.1383793.

[84] M. Pitzer, 'How to determine the handedness of single molecules using Coulomb explosion imaging', *J. Phys. B At. Mol. Opt. Phys.*, vol. 50, no. 15, p. 153001, Aug. 2017, doi: https://doi.org/10.1088/1361-6455/aa77a9.

[85] J. J. Sakurai and J. Napolitano, *Modern Quantum Mechanics*, 2nd ed. Cambridge: Cambridge University Press, 2017. doi: https://doi.org/10.1017/9781108499996.

[86] J. Cooper and R. N. Zare, 'Angular Distribution of Photoelectrons', *J Chem Phys*, vol. 48, no. 942, p. 3, 1968, doi: https://doi.org/10.1063/1.1668742.

[87] I. Powis, 'Photoelectron Circular Dichroism in Chiral Molecules', in *Advances in Chemical Physics, Vol 138*, vol. 138, S. A. Rice, Ed. Hoboken: John Wiley & Sons Inc, 2008, pp. 267–329. doi: https://doi.org/10.1002/9780470259474.ch5.

[88] K. L. Reid, 'Photoelectron angular distributions', *Annu. Rev. Phys. Chem.*, vol. 54, pp. 397–424, 2003, doi: https://doi.org/10.1146/annurev.physchem.54.011002.103814.

[89] D. Dill, 'Fixed-molecule photoelectron angular distributions', *J. Chem. Phys.*, vol. 65, no. 3, pp. 1130–1133, Aug. 1976, doi: https://doi.org/10.1063/1.433187.

[90] J. L. Hansen, H. Stapelfeldt, D. Dimitrovski, M. Abu-samha, C. P. J. Martiny, and L. B. Madsen, 'Time-Resolved Photoelectron Angular Distributions from Strong-Field Ionization of Rotating Naphthalene Molecules', *Phys. Rev. Lett.*, vol. 106, no. 7, p. 073001, Feb. 2011, doi: https://doi.org/10.1103/PhysRevLett.106.073001.

[91] P. Lablanquie *et al.*, 'Experimental and theoretical investigation of the spectroscopy and dynamics of multiply charged CO cations', *Phys. Rev. A*, vol. 40, no. 10, pp. 5673–5689, Nov. 1989, doi: https://doi.org/10.1103/PhysRevA.40.5673.

[92] K. L. Reid, 'Photoelectron angular distributions: developments in applications to isolated molecular systems', *Mol. Phys.*, vol. 110, no. 3, pp. 131–147, 2012, doi: https://doi.org/10.1080/00268976.2011.640292.

[93] A. Landers *et al.*, 'Photoelectron Diffraction Mapping: Molecules Illuminated from Within', *Phys. Rev. Lett.*, vol. 87, no. 1, p. 013002, Jun. 2001, doi: https://doi.org/10.1103/PhysRevLett.87.013002.

[94] F. Ota, K. Yamazaki, D. Sébilleau, K. Ueda, and K. Hatada, 'Theory on polarization-averaged core-level molecular-frame photoelectron angular distributions: I. A Full-potential method and its application to dissociating carbon monoxide dication', *ArXiv200900853 Phys.*, Nov. 2020, Accessed: Jul. 02, 2021. [Online]. Available: http://arxiv.org/abs/2009.00853

[95] J. B. Williams *et al.*, 'Imaging Polyatomic Molecules in Three Dimensions Using Molecular Frame Photoelectron Angular Distributions', *Phys. Rev. Lett.*, vol. 108, no. 23, p. 233002, Jun. 2012, doi: https://doi.org/10.1103/PhysRevLett.108.233002.

[96] E. Plésiat, P. Decleva, and F. Martín, 'Relationship between polarization-averaged molecular-frame photoelectron angular distributions and geometry', *Phys. Rev. A*, vol. 88, no. 6, p. 063409, Dec. 2013, doi: https://doi.org/10.1103/PhysRevA.88.063409.

[97] H. Fukuzawa *et al.*, 'Probing molecular bond-length using molecular-frame photoelectron angular distributions', *J. Chem. Phys.*, vol. 150, no. 17, p. 174306, May 2019, doi: https://doi.org/10.1063/1.5091946.

[98] K. Fehre *et al.*, 'Enantiosensitive Structure Determination by Photoelectron Scattering on Single Molecules', *ArXiv210103375 Phys.*, Jan. 2021, Accessed: Jun. 13, 2021. [Online]. Available: http://arxiv.org/abs/2101.03375

[99] G. Kastirke *et al.*, 'Photoelectron Diffraction Imaging of a Molecular Breakup Using an X-Ray Free-Electron Laser', *Phys. Rev. X*, vol. 10, no. 2, p. 021052, Jun. 2020, doi: https://doi.org/10.1103/PhysRevX.10.021052.

[100] M. S. Schuurman and A. Stolow, 'Dynamics at Conical Intersections', *Annu. Rev. Phys. Chem.*, vol. 69, no. 1, pp. 427–450, Apr. 2018, doi: https://doi.org/10.1146/annurev-physchem-052516-050721.

[101] D. W. Chandler and P. L. Houston, 'Two-dimensional imaging of state-selected photodissociation products detected by multiphoton ionization', *J. Chem. Phys.*, vol. 87, no. 2, pp. 1445–1447, Jul. 1987, doi: https://doi.org/10.1063/1.453276.

[102] R. N. Zare, 'Photoejection dynamics', *Mol Photochem*, vol. 4, no. 1, 1972, Accessed: Feb. 10, 2021. [Online]. Available: http://web.stanford.edu/group/Zarelab/publinks/zarepub60.pdf

[103] D. H. Bilderback, P. Elleaume, and E. Weckert, 'Review of third and next generation synchrotron light sources', *J. Phys. B At. Mol. Opt. Phys.*, vol. 38, no. 9, pp. S773–S797, May 2005, doi: https://doi.org/10.1088/0953-4075/38/9/022.

[104] E. J. N. Wilson, 'Fifty Years of Synchrotrons', p. 5.

[105] H. Wiedemann, *Synchrotron Radiation*. Berlin, Heidelberg: Springer Berlin Heidelberg, 2003. doi: https://doi.org/10.1007/978-3-662-05312-6.

[106] K. Holldack *et al.*, 'Single bunch X-ray pulses on demand from a multi-bunch synchrotron radiation source', *Nat. Commun.*, vol. 5, no. 1, p. 4010, Sep. 2014, doi: https://doi.org/10.1038/ncomms5010.

[107] H. S.- Schrepping, J. Viefhaus, A. Wefer, and T. Wroblewski, 'Commissioning of the APPLE II undulator', p. 9, 2002.

[108] L. Nahon *et al.*, 'DESIRS: a state-of-the-art VUV beamline featuring high resolution and variable polarization for spectroscopy and dichroism at SOLEIL', *J. Phys. Conf. Ser.*, vol. 425, no. 12, p. 122004, Mar. 2013, doi: https://doi.org/10.1088/1742-6596/425/12/122004.

[109] G. Geloni, E. Saldin, E. Schneidmiller, and M. Yurkov, 'Transverse coherence properties of X-ray beams in third-generation synchrotron radiation sources', *Nucl. Instrum. Methods Phys. Res. Sect. Accel. Spectrometers Detect. Assoc. Equip.*, vol. 588, no. 3, pp. 463–493, Apr. 2008, doi: https://doi.org/10.1016/j.nima.2008.01.089.

[110] B. W. J. McNeil and N. R. Thompson, 'X-ray free-electron lasers', *Nat. Photonics*, vol. 4, no. 12, pp. 814–821, Dec. 2010, doi: https://doi.org/10.1038/nphoton.2010.239.

[111] 'SEXTANTS | French national synchrotron facility'. https://www.synchrotron-soleil.fr/en/beamlines/sextants (accessed May 06, 2021).

[112] M. Sacchi *et al.*, 'The SEXTANTS beamline at SOLEIL: a new facility for elastic, inelastic and coherent scattering of soft X-rays', *J. Phys. Conf. Ser.*, vol. 425, no. 7, p. 072018, Mar. 2013, doi: https://doi.org/10.1088/1742-6596/425/7/072018.

[113] T. Vogt *et al.*, 'From (γ,2e) to (γ,eR): Kinematically Complete Experiments with Coltrims', in *Coincidence Studies of Electron and Photon Impact Ionization*, C. T. Whelan and H. R. J. Walters, Eds. Boston, MA: Springer US, 1997, pp. 127–136. doi: https://doi.org/10.1007/978-1-4757-9751-0_15.

[114] M. Kircher *et al.*, 'Kinematically complete experimental study of Compton scattering at helium atoms near the threshold', *Nat. Phys.*, vol. 16, no. 7, pp. 756–760, Jul. 2020, doi: https://doi.org/10.1038/s41567-020-0880-2.

[115] M. Kunitski *et al.*, 'Observation of the Efimov state of the helium trimer', *Science*, vol. 348, no. 6234, pp. 551–555, May 2015, doi: https://doi.org/10.1126/science.aaa5601.

[116] J. Voigtsberger *et al.*, 'Imaging the structure of the trimer systems 4He3 and 3He4He2', *Nat. Commun.*, vol. 5, no. 1, p. 5765, Dec. 2014, doi: https://doi.org/10.1038/ncomms6765.

[117] A. Schottelius *et al.*, 'Crystal growth rates in supercooled atomic liquid mixtures', *Nat. Mater.*, vol. 19, no. 5, pp. 512–516, May 2020, doi: https://doi.org/10.1038/s41563-020-0613-z.

[118] S. Grundmann *et al.*, 'Zeptosecond birth time delay in molecular photoionization', *Science*, vol. 370, no. 6514, pp. 339–341, Oct. 2020, doi: https://doi.org/10.1126/science.abb9318.

[119] S. Eckart *et al.*, 'Sideband Modulation by Sub-Cycle Interference', *Phys. Rev. A*, vol. 102, no. 4, p. 043115, Oct. 2020, doi: https://doi.org/10.1103/PhysRevA.102.043115.

[120] S. Eckart *et al.*, 'Direct Experimental Access to the Nonadiabatic Initial Momentum Offset upon Tunnel Ionization', *Phys. Rev. Lett.*, vol. 121, no. 16, p. 163202, Oct. 2018, doi: https://doi.org/10.1103/PhysRevLett.121.163202.

[121] X. Ding *et al.*, 'Threshold photodissociation dynamics of NO_2 studied by time-resolved cold target recoil ion momentum spectroscopy', *J. Chem. Phys.*, vol. 151, no. 17, p. 174301, Nov. 2019, doi: https://doi.org/10.1063/1.5095430.

[122] G. Kastirke *et al.*, 'Double Core-Hole Generation in O 2 Molecules Using an X-Ray Free-Electron Laser: Molecular-Frame Photoelectron Angular Distributions', *Phys. Rev. Lett.*, vol. 125, no. 16, p. 163201, Oct. 2020, doi: https://doi.org/10.1103/PhysRevLett.125.163201.

[123] S.-G. Chen *et al.*, 'Photon Momentum Transfer in Single-Photon Double Ionization of Helium', *Phys. Rev. Lett.*, vol. 124, no. 4, p. 043201, Jan. 2020, doi: https://doi.org/10.1103/PhysRevLett.124.043201.

[124] R. Dörner *et al.*, 'Fully Differential Cross Sections for Double Photoionization of He Measured by Recoil Ion Momentum Spectroscopy', *Phys. Rev. Lett.*, vol. 77, no. 6, pp. 1024–1027, Aug. 1996, doi: https://doi.org/10.1103/PhysRevLett.77.1024.

[125] F. Trinter *et al.*, 'Resonant Auger decay driving intermolecular Coulombic decay in molecular dimers', *Nature*, vol. 505, no. 7485, pp. 664–666, Jan. 2014, doi: https://doi.org/10.1038/nature12927.

[126] B. Gaire *et al.*, 'Auger decay and subsequent fragmentation pathways of ethylene following K -shell ionization', *Phys. Rev. A*, vol. 92, no. 1, p. 013408, Jul. 2015, doi: https://doi.org/10.1103/PhysRevA.92.013408.

[127] M. Kircher *et al.*, 'Recoil-Induced Asymmetry of Nondipole Molecular Frame Photoelectron Angular Distributions in the Hard X-ray Regime', *Phys. Rev. Lett.*, vol. 123, no. 24, p. 243201, Dec. 2019, doi: https://doi.org/10.1103/PhysRevLett.123.243201.

[128] L. Kaiser *et al.*, 'Angular emission distribution of O 1s photoelectrons of uniaxially oriented methanol', *J. Phys. B At. Mol. Opt. Phys.*, vol. 53, no. 19, p. 194002, Oct. 2020, doi: https://doi.org/10.1088/1361-6455/aba3d3.

[129] M. Pitzer *et al.*, 'Direct Determination of Absolute Molecular Stereochemistry in Gas Phase by Coulomb Explosion Imaging', *Science*, vol.

341, no. 6150, pp. 1096–1100, Sep. 2013, doi: https://doi.org/10.1126/science.1240362.

[130] J. Ullrich, R. Moshammer, A. Dorn, R. D rner, L. P. H. Schmidt, and H. Schmidt-B cking, 'Recoil-ion and electron momentum spectroscopy: reaction-microscopes', *Rep. Prog. Phys.*, vol. 66, no. 9, pp. 1463–1545, Sep. 2003, doi: https://doi.org/10.1088/0034-4885/66/9/203.

[131] R. Dörner *et al.*, 'From Atoms to Molecules', in *Many-Particle Quantum Dynamics in Atomic and Molecular Fragmentation*, vol. 35, J. Ullrich and V. Shevelko, Eds. Berlin, Heidelberg: Springer Berlin Heidelberg, 2003, pp. 245–260. doi: https://doi.org/10.1007/978-3-662-08492-2_14.

[132] D. W. Chandler, P. L. Houston, and D. H. Parker, 'Perspective: Advanced particle imaging', *J. Chem. Phys.*, vol. 147, no. 1, p. 013601, May 2017, doi: https://doi.org/10.1063/1.4983623.

[133] R. Dörner *et al.*, 'Cold Target Recoil Ion Momentum Spectroscopy: a "momentum microscope" to view atomic collision dynamics', *Phys. Rep.*, vol. 330, no. 2–3, pp. 95–192, Jun. 2000, doi: https://doi.org/10.1016/S0370-1573(99)00109-X.

[134] L. Fechner, *High-Resolution Experiments on Strong-Field Ionization of Atoms and Molecules*. Cham: Springer International Publishing, 2016. doi: https://doi.org/10.1007/978-3-319-32046-5.

[135] G. Kastirke, 'Konstruktion und Aufbau einer UHV-tauglichen COLTRIMS-Kammer', 2014.

[136] W. Gerlach and O. Stern, 'Der experimentelle Nachweis der Richtungsquantelung im Magnetfeld', *Z. Phys.*, vol. 9, pp. 349–352, Dec. 1922, doi: https://doi.org/10.1007/BF01326983.

[137] A. S. Palau, S. D. Eder, T. Kaltenbacher, B. Samelin, G. Bracco, and B. Holst, 'A modified time-of-flight method for precise determination of high speed ratios in molecular beams', *Rev. Sci. Instrum.*, vol. 87, no. 2, p. 023102, Feb. 2016, doi: https://doi.org/10.1063/1.4941336.

[138] G. Tejeda, B. Maté, J. M. Fernández-Sánchez, and S. Montero, 'Temperature and Density Mapping of Supersonic Jet Expansions Using Linear Raman Spectroscopy', *Phys. Rev. Lett.*, vol. 76, no. 1, pp. 34–37, Jan. 1996, doi: https://doi.org/10.1103/PhysRevLett.76.34.

[139] K. Fehre *et al.*, 'Closed-loop recycling of rare liquid samples for gas-phase experiments', *Rev. Sci. Instrum.*, vol. 92, no. 2, p. 023205, Feb. 2021, doi: https://doi.org/10.1063/5.0037836.

[140] W. C. Wiley and I. H. McLaren, 'Time-of-Flight Mass Spectrometer with Improved Resolution', *Rev. Sci. Instrum.*, vol. 26, no. 12, pp. 1150–1157, Dec. 1955, doi: https://doi.org/10.1063/1.1715212.

[141] D. J. Ruggieri, 'Microchannel Plate Imaging Detectors', *IEEE Trans. Nucl. Sci.*, vol. 19, no. 3, pp. 74–84, 1972, doi: https://doi.org/10.1109/TNS.1972.4326705.

[142] O. Jagutzki, 'MCP Delay Line Detector Manual'. RoentDek Handels GmbH, 2021. [Online]. Available: http://www.roentdek.com/manuals/

[143] K. Fehre *et al.*, 'Absolute ion detection efficiencies of microchannel plates and funnel microchannel plates for multi-coincidence detection', *Rev. Sci.*

Instrum., vol. 89, no. 4, p. 045112, Apr. 2018, doi: https://doi.org/10.1063/1.5022564.

[144] 'MANUAL - HAMAMATSU'. https://seltokphotonics.com/upload/iblock/86d/86d305a4985dda3cef76 839a7588a795.pdf (accessed Feb. 23, 2021).

[145] 'RoentDek Handels GmbH - Time and Position sensitive MCP Delay Line Detectors'. http://www.roentdek.com/manuals/ (accessed Mar. 20, 2021).

[146] S. E. Sobottka and M. B. Williams, 'Delay line readout of microchannel plates', *IEEE Trans. Nucl. Sci.*, vol. 35, no. 1, pp. 348–351, Feb. 1988, doi: https://doi.org/10.1109/23.12740.

[147] L. J. Frasinski, K. Codling, and P. A. Hatherly, 'Covariance Mapping: A Correlation Method Applied to Multiphoton Multiple Ionization', *Science*, vol. 246, no. 4933, pp. 1029–1031, Nov. 1989, doi: https://doi.org/10.1126/science.246.4933.1029.

[148] L. J. Frasinski, M. Stankiewicz, K. J. Randall, P. A. Hatherly, and K. Codling, 'Dissociative photoionisation of molecules probed by triple coincidence; double time-of-flight techniques', *J. Phys. B At. Mol. Phys.*, vol. 19, no. 23, pp. L819–L824, Dec. 1986, doi: https://doi.org/10.1088/0022-3700/19/23/002.

[149] M. Lundqvist, D. Edvardsson, P. Baltzer, and B. Wannberg, 'Doppler-free kinetic energy release spectrum of', *J. Phys. B At. Mol. Opt. Phys.*, vol. 29, no. 8, pp. 1489–1499, Apr. 1996, doi: https://doi.org/10.1088/0953-4075/29/8/013.

[150] T. Weber *et al.*, 'K-shell photoionization of CO and N_2: is there a link between the photoelectron angular distribution and the molecular decay dynamics?', *J. Phys. B At. Mol. Opt. Phys.*, vol. 34, no. 18, pp. 3669–3678, Sep. 2001, doi: https://doi.org/10.1088/0953-4075/34/18/305.

[151] R. G. Houlgate, K. Codling, G. V. Marr, and J. B. West, 'Angular distribution and photoionization cross section measurements on the 3p and 3s subshells of argon', *J. Phys. B At. Mol. Phys.*, vol. 7, no. 17, pp. L470–L473, Dec. 1974, doi: https://doi.org/10.1088/0022-3700/7/17/003.

[152] S. A. Galitskiy, A. N. Artemyev, K. Jänkälä, B. M. Lagutin, and Ph. V. Demekhin, 'Hartree-Fock calculation of the differential photoionization cross sections of small Li clusters', *J. Chem. Phys.*, vol. 142, no. 3, p. 034306, Jan. 2015, doi: https://doi.org/10.1063/1.4905722.

[153] Ph. V. Demekhin, A. Ehresmann, and V. L. Sukhorukov, 'Single center method: A computational tool for ionization and electronic excitation studies of molecules', *J. Chem. Phys.*, vol. 134, no. 2, p. 024113, Jan. 2011, doi: https://doi.org/10.1063/1.3526026.

[154] G. Nalin *et al.*, 'Photoelectron circular dichroism of O 1s-photoelectrons of uniaxially oriented trifluoromethyloxirane: energy dependence and sensitivity to molecular configuration', *Phys. Chem. Chem. Phys.*, vol. 23, no. 32, pp. 17248–17258, Aug. 2021, doi: https://doi.org/10.1039/D1CP02462K.

[155] M. Ilchen *et al.*, 'Emitter-site-selective photoelectron circular dichroism of trifluoromethyloxirane', *Phys. Rev. A*, vol. 95, no. 5, p. 053423, May 2017, doi: https://doi.org/10.1103/PhysRevA.95.053423.

[156] K. Fehre *et al.*, 'Enantiosensitive Structure Determination by Photoelectron Scattering on Single Molecules', *ArXiv210103375 Phys.*, Jan. 2021, Accessed: Feb. 12, 2021. [Online]. Available: http://arxiv.org/abs/2101.03375

[157] U. Ablikim *et al.*, 'Identification of absolute geometries of cis and trans molecular isomers by Coulomb Explosion Imaging', *Sci. Rep.*, vol. 6, no. 1, p. 38202, Dec. 2016, doi: https://doi.org/10.1038/srep38202.

[158] N. Neumann *et al.*, 'Fragmentation Dynamics of CO_2^{3+} Investigated by Multiple Electron Capture in Collisions with Slow Highly Charged Ions', *Phys. Rev. Lett.*, vol. 104, no. 10, p. 103201, Mar. 2010, doi: https://doi.org/10.1103/PhysRevLett.104.103201.

[159] A. Menssen *et al.*, 'Molecular frame photoelectron angular distributions for core ionization of ethane, carbon tetrafluoride and 1,1-difluoroethylene', *J. Phys. B At. Mol. Opt. Phys.*, vol. 49, no. 5, p. 055203, Mar. 2016, doi: https://doi.org/10.1088/0953-4075/49/5/055203.

[160] K. Fehre *et al.*, 'Fourfold Differential Photoelectron Circular Dichroism', *ArXiv210614170 Phys.*, Jun. 2021, Accessed: Jul. 15, 2021. [Online]. Available: http://arxiv.org/abs/2106.14170

[161] G. G. Stokes, *On the composition and resolution of streams of polarized light from different sources*. Cambridge: Cambridge Philosophical Society, 1852.

[162] R. S. Cahn, C. Ingold, and V. Prelog, 'Specification of Molecular Chirality', *Angew. Chem. Int. Ed. Engl.*, vol. 5, no. 4, pp. 385–415, 1966, doi: https://doi.org/https://doi.org/10.1002/anie.196603851.

[163] H. A. Favre and W. H. Powell, *Nomenclature of Organic Chemistry*. 2013. doi: https://doi.org/10.1039/9781849733069.

[164] F. Marteau, C. Benabderrahmane, P. Berteaud, F. Briquez, P. Brunelle, and L. Chapuis, 'Development and Installation of Insertion Devices at SOLEIL', 2009, p. 3.

[165] T. Jahnke, 'vom Fachbereich Physik der Johann Wolfgang Goethe-Universität als Dissertation angenommen.', 2015.

[166] D. A. Dahl, 'simion for the personal computer in reflection', *Int. J. Mass Spectrom.*, vol. 200, no. 1–3, pp. 3–25, Dec. 2000, doi: https://doi.org/10.1016/S1387-3806(00)00305-5.